

**Search for the Minimal Supersymmetric Standard  
Model Neutral Higgs Bosons (A/H) decaying to  
 $\tau^+\tau^-$  in  $pp$  Collisions at  $\sqrt{s} = 13$  TeV with the  
ATLAS Detector**

by

Samina Jabbar

A thesis submitted in partial fulfillment of the requirements for the degree  
of  
Doctor of Philosophy

Department of Physics  
University of Alberta

© Samina Jabbar, 2017

# Search for the Minimal Supersymmetric Standard Model Neutral Higgs Bosons (A/H) decaying to $\tau^+\tau^-$ in $pp$ Collisions at $\sqrt{s} = 13$ TeV with the ATLAS Detector

## ABSTRACT

This thesis presents results of a search for the neutral Higgs bosons (A/H) of the Minimal Supersymmetric Standard Model (MSSM) performed using the data corresponding to an integrated luminosity of  $3.21 \text{ fb}^{-1}$  from proton-proton collisions at the centre of mass energy  $\sqrt{s} = 13$  TeV recorded by the ATLAS detector at the LHC. Two primary MSSM neutral Higgs production modes, gluon-gluon fusion and in association with b-quarks, are considered. The analysis presented here searches for events where the neutral Higgs bosons decay to a  $\tau^+\tau^-$  pair with one  $\tau$  decaying to leptons ( $e/\mu$ ) and the other  $\tau$  decaying to hadrons. The data are in good agreement with the background predicted by the Standard Model and the results provide an upper limit on the production cross section times branching fraction of the scalar boson decay to  $\tau^+\tau^-$  as a function of the boson mass. The results are also interpreted in the  $m_h^{mod+}$  MSSM benchmark scenario to derive exclusion limits on the  $m_{A/H} - \tan\beta$  plane.

## PREFACE

The search presented in this thesis is based on the experimental apparatus and data of the ATLAS Experiment at the Large Hadron Collider (LHC). The analysis is performed within the ATLAS collaboration, a group of nearly 3000 individuals from over 175 institutions in 38 countries who work together to build and run the ATLAS detector. The material presented here is dependent on others work, therefore where applicable sources are referenced by citing published papers or otherwise public reports, internal notes and/or documentation pages.

All figures and tables for which a reference is not indicated in the caption represent my own work, except tables [A.1](#) to [A.8](#) in the appendix that list the Monte Carlo samples that are already appeared in the internal ATLAS note. Chapter [3](#) describes the design and subcomponents of the ATLAS detector along with the ATLAS trigger system. I contributed to the ATLAS tau trigger (described in section [3.3.1](#)) for authorship qualification within the ATLAS collaboration. I was responsible for the validation of Run-2 tau trigger which involved maintaining and testing the software, and monitoring nightly validation results.

The main analysis presented in chapters [5](#), [6](#) and [7](#) was conducted within the ATLAS MSSM Higgs to tau tau group where I was a leading members of the analysis team. My contributions in the analysis include: signal selection cutflow for data and Monte Carlo samples (tables [5.3](#) and [5.4](#)); background estimation through factor factor calculation in the W+jets control region and the associated systematics (described in section [5.4.2](#) and [6.1.2](#)) and validation of the signal region (section [5.5](#)). In addition, I derived the uncertainties due to modelling of the Monte Carlo b-associated MSSM Higgs signal samples (section [6.4.1](#)). Those parts of the analysis which were implemented by other members were also recomputed by me as a cross check before ATLAS published the results.

The analysis is published in European Physical Journal C ([Eur. Phys. J. C76 \(2016\) 585](#)) in August 2016, in which a combined search in  $\tau_{lep}\tau_{had}$  and  $\tau_{had}\tau_{had}$  together with  $Z'$  decaying to a pair of taus are presented.

*Dedicated To:*

*My Parents  
Abdul Jabbar (Late) and Safia,*

*§*

*My Loving Son  
Muhammad Waleed*

## ACKNOWLEDGMENTS

A huge thanks must go to my supervisor, Dr. Roger Moore, for his invaluable guidance throughout the course of PhD. His consistent support and key suggestions helped me complete this thesis. I would also like to thank our ATLAS Alberta group team leader, Dr. Doug Gingrich, and the other team members: Dr. James Pinfeld, Xiaohu Sun, Asif Saddique, Francesc Vives Vaque, Aatif Imtiaz Butt, Kingsley Emelideme, Nooshin Dehghanian and Andrew Karamaoun for providing an excellent research environment. My special thanks goes to our postdoctoral fellow Patrick Czdowski who has been a constant source of help along the way.

Many thanks to everyone in the HBSM and tau groups whom I have had the opportunity to work with. Among them, I am specially thankful to Nikolaos Rompotis, Matthew Beckingham, Lei Zhang, Lorenz Hauswald, Allison Mccarn, Pier-Olivier and Daniele Zanzi.

I am also thankful to my friends in Pakistan and Canada for their moral support and wonderful company. Last but not least, I would like to thank my parents, parents-in-law, siblings and husband, Rashid Haroon, for their continuous support and always expecting best from me.

---

# Table of Contents

List of Abbreviations . . . . .	xii
List of Figures . . . . .	xvii
List of Tables . . . . .	xxv
<b>1 Introduction . . . . .</b>	<b>1</b>
<b>2 Theoretical Framework: The Standard Model and Beyond . . . . .</b>	<b>4</b>
2.1 The Standard Model . . . . .	5
2.1.1 Fundamental Particles and the Interactions . . . . .	5
2.1.2 Tau Lepton . . . . .	7
2.2 The Relativistic Quantum Mechanics . . . . .	9
2.2.1 The Klein-Gordon Equation . . . . .	9
2.2.2 The Dirac Equation . . . . .	10
2.3 Mathematical Framework for the Standard Model . . . . .	12
2.3.1 Quantum Electrodynamics (QED) . . . . .	13
2.3.2 Quantum Chromodynamics (QCD) . . . . .	15
2.3.3 Weak Interactions . . . . .	17
2.3.4 Unification of Electromagnetic and Weak Interaction . . . . .	19
2.3.5 Glashow-Weinberg-Salam Model . . . . .	19
2.3.6 Spontaneous Symmetry Breaking and the Higgs Mechanism . . . . .	22

2.4	Higgs Discovery at the LHC . . . . .	25
2.5	Problems in the Standard Model . . . . .	27
2.5.1	The Hierarchy Problem . . . . .	27
2.5.2	Dark Matter . . . . .	28
2.6	Supersymmetry (SUSY) . . . . .	29
2.6.1	Chiral and Gauge Supermultiplets . . . . .	30
2.6.2	SUSY Breaking . . . . .	31
2.6.3	Motivations for Supersymmetry . . . . .	32
2.7	Higgs Sector in the MSSM . . . . .	34
2.7.1	SUSY Benchmark Scenarios . . . . .	35
2.7.2	MSSM Higgs Production and Decay Modes . . . . .	37
2.8	Neutral MSSM Higgs Searches at the ATLAS Experiment . . . . .	39
<b>3</b>	<b>The ATLAS Experiment at the LHC . . . . .</b>	<b>43</b>
3.1	The Large Hadron Collider (LHC) . . . . .	43
3.1.1	The LHC Experiments . . . . .	44
3.1.2	The LHC Beam Parameters . . . . .	46
3.2	The ATLAS Detector . . . . .	46
3.2.1	Design . . . . .	47
3.2.2	Coordinate System . . . . .	47
3.2.3	Components . . . . .	47
3.3	The ATLAS Trigger System . . . . .	58
3.3.1	Tau Trigger at the ATLAS Experiment . . . . .	60
3.3.2	b-Jet Triggering at the ATLAS Experiment . . . . .	64
3.4	The LHC Computing Facilities . . . . .	66
3.5	The Monte Carlo (MC) Simulation in ATLAS Experiment . . . . .	67

<b>4</b>	<b>Monte Carlo Simulation and Object Reconstruction . . . . .</b>	<b>68</b>
4.1	Monte Carlo Event Generation . . . . .	68
4.1.1	Signal Samples . . . . .	69
4.1.2	Monte Carlo Background Samples . . . . .	70
4.2	Data Samples . . . . .	71
4.3	Detector Simulation . . . . .	72
4.4	Object Reconstruction . . . . .	72
4.4.1	Track Reconstruction . . . . .	73
4.4.2	Vertexing . . . . .	73
4.4.3	Cluster Reconstruction . . . . .	74
4.4.4	Electron Reconstruction . . . . .	75
4.4.5	Jet Reconstruction . . . . .	75
4.4.6	Tau Reconstruction . . . . .	76
4.4.7	Muon Reconstruction . . . . .	80
4.4.8	Missing Transverse Energy . . . . .	80
4.4.9	b-tagging . . . . .	81
<b>5</b>	<b>Events Selection and the Background Estimation for <math>A/H \rightarrow \tau_{lep}\tau_{had}</math> . . . . .</b>	<b>88</b>
5.1	Pre-selection . . . . .	88
5.2	Event Selection . . . . .	92
5.3	Di-tau Mass Reconstruction . . . . .	94
5.4	Background Estimation . . . . .	95
5.4.1	Background Estimation Through Simulation . . . . .	95
5.4.2	Data-Driven Background Estimation: The Combined Fake Factor Method . . . . .	97
5.5	Validation of the Signal Region . . . . .	109

<b>6</b>	<b>Systematic Uncertainties</b>	<b>111</b>
6.1	Background Estimation Systematics	111
6.1.1	QCD Fake Factors	111
6.1.2	W+Jets/Top Fake Factors	112
6.1.3	Systematic uncertainties in the $r_{QCD}$ Calculations	115
6.1.4	Electron to Tau Scale Factor	117
6.2	Systematic Uncertainties on Luminosity and Theoretical Cross Section Measurements	118
6.3	Detector-related Simulation Systematics	118
6.4	Systematics Uncertainties on the Monte Carlo Modelling	124
6.4.1	Modelling of the Monte Carlo Signal Samples	124
6.4.2	Monte Carlo Top Modelling	126
6.5	Comparison of the Statistical and Systematic Errors in Fakes	126
6.6	Signal Region Yields with Full Systematics	130
<b>7</b>	<b>Statistical Procedure for Limit Settings and Results</b>	<b>137</b>
7.1	Limit Settings	137
7.1.1	Likelihood Function ( $\mathcal{L}$ )	139
7.1.2	Test Statistics	139
7.1.3	$CL_s$ Method	140
7.1.4	Exclusion Limits	141
7.2	Results	141
<b>8</b>	<b>Summary and Conclusion</b>	<b>147</b>
	<b>Bibliography</b>	<b>150</b>

Appendices . . . . . 164

A Signal and Background MC Samples . . . . . 165

---

# List of Abbreviations

**2HDM** two Higgs Doublet Model.

**AF2** ATLAS Fast simulation version 2.

**ALEPH** Apparatus for LEP PHysics.

**ALICE** A Large Ion Collider Experiment.

**AMI** ATLAS Metadata Interface.

**ATLAS** A Toroidal LHC ApparatuS.

**BDT** Boosted Decision Tree.

**BSM** Beyond Standard Model.

**CDF** Collider Detector at Fermilab.

**CERN** European Organisation for Nuclear Research.

**CL** Confidence Level.

**CMD** Cosmic Microwave Background.

**CMS** Compact Muon Solenoid.

**CPU** Central Processing Unit.

**CSC** Cathode Strip Chamber.

**DAQ** Data AcQuisition.

**DELPHI** DEtector with Lepton, Photon and Hadron Identification.

**DID** Dataset IDentification.

**ECAL** Electromagnetic CALorimeter.

**EF** Event Filter.

**EM** ElectroMagnetic.

**EWSB** ElectroWeak Symmetry Breaking.

**FCAL** Forward CALorimeter.

**FF** Fake Factor.

**FT** Flavour Tagging.

**GEANT** GEometry ANd Tracking.

**GRLs** Good Run Lists.

**GUT** Grand Unified Theory.

**HCAL** Hadronic CALorimeter.

**HERWIG** Hard Emission Reactions With Interfering Gluons.

**HL-LHC** High Luminosity Lagre Hadron Collider.

**HLT** High Level Trigger.

**IBL** Insertable B-Layer.

**ID** IDentification or Inner Detector.

**IP** Impact Parameter.

**JVF** Jet Vertex Fraction.

**JVT** Jet Vertex Tagger.

**KG equation** Klein-Gordon equation.

**L1** Level 1.

**L2** Level 2.

**LAr** Liquid Argon.

**LBL** Lawrence Berkeley Laboratory.

**LEP** Large Electron-Positron collider.

**LHC** Large Hadron Collider.

**LHCb** Large Hadron Collider-beauty.

**LHCf** Large Hadron Collider-forward.

**LINAC** LINear ACcelerator.

**LLR** Log Likelihood Ratio.

**LO** Leading Order.

**LS1** Long Shutdown-1.

**LSP** Lightest SUSY Particle.

**MC** Monte Carlo.

**MDTs** Muon Drift Tubes.

**ME** Matrix Element.

**MMC** Missing Mass Calculator.

**MoEDAL** Monopole and Exotics Detector At the LHC.

**MOSAIC** Matrix-element Oriented SAMpling Calculator.

**MSSM** Minimal Supersymmetric Standard Model.

**mSUGRA** minimal Super GRAvity.

**MV** Multi-Variate.

**NLO** Next-to-Leading Order.

**NNLO** Next-to-Next-to-Leading Order.

**OPAL** Omni-Purpose Apparatus for LEP.

**PDF** Parton Distribution Function.

**pMSSM** phenomenological Minimal Supersymmetric Standard Model.

**PMTs** PhotoMultiplier Tubes.

**POWHEG** POsitive Weight Hardest Emission Generator.

**PS** Proton Synchrotron or Parton Shower.

**PSB** Proton Synchrotron Booster.

**QCD** Quantum ChromoDynamics.

**QED** Quantum ElectroDynamics.

**QFD** Quantum Field Theory.

**RDOs** Raw Data Objects.

**ROI** Region Of Interest.

**ROS** Read-Out-System.

**RPCs** Resistive Plate Chambers.

**RQM** Relativistic Quantum Mechanics.

**SCT** Semi-Conductor Tracker.

**SHERPA** Simulation for High-Energy Reactions of PArticles.

**SIPS** Signed Impact Parameter Significance.

**SLAC** Stanford Linear Accelerator Center.

**SM** Standard Model.

**SPEAR** Stanford Positron Electron Accelerating Ring.

**SPS** Super Proton Synchrotron.

**SSB** Spontaneous Symmetry Breaking.

**SusHi** Supersymmetric Higgs.

**SUSY** SUperSYmmetry.

**SV** Secondary Vertex.

**TES** Tau Energy Scale.

**TGCs** Thin Gap Chambers.

**TOTEM** TOTal Elastic and diffractive cross section Measurement.

**TR** Transition Radiation.

**TRT** Transition Radiation Tracker.

**VEV** Vacuum Expectation Value.

**WIMPs** Weakly Interacting Massive Particles.

**WLCG** Worldwide LHC Computing Grid.

**XML** eXtensible Markup Language.

---

# List of Figures

1.1	The reconstructed invariant mass distribution of $\gamma\gamma$ showing a resonance around 125 GeV/c <sup>2</sup> [4] . . . . .	2
2.1	Fundamental Particles in the Standard Model . . . . .	6
2.2	Feynman diagram of tau production . . . . .	7
2.3	Feynman diagrams of Common tau decays . . . . .	8
2.4	Feynman Vertex factor in QED . . . . .	14
2.5	Feynman Vertex factor in QCD . . . . .	16
2.6	Feynman representation of 3- and 4-gluon interaction . . . . .	17
2.7	The mexican hat potential for $\mu^2 < 0$ [27] . . . . .	22
2.8	The observed local $p_0$ -value, the probability of background to produce a signal-like excess, as a function of the Higgs mass, $m_H$ . [30] . . . . .	26
2.9	Feynman diagram for the Higgs boson quadratic mass corrections with a single fermion loop (a) and for a single scalar boson loop (b) . . . . .	28
2.10	Convergence of coupling constants $\alpha$ at GUT scale a) in SM b) in MSSM . . . . .	33
2.11	Branching ratios for the MSSM neutral CP-even Higgs boson (H) with $\tan\beta=3$ (left) and $\tan\beta=30$ (right) with fixed values of other SUSY parameters [41]. . . . .	39
2.12	b-associated production of a neutral MSSM Higgs boson . . . . .	39
2.13	gluon-gluon fusion production of a neutral MSSM Higgs boson . . . . .	40
2.14	Common Feynman diagrams for the Higgs production and the decay modes at the LHC . . . . .	40
2.15	95% confidence level exclusion limit of $\phi \rightarrow \tau\tau$ in the $m_A$ - $\tan\beta$ plane, in 2011 (a) [42] and 2012 search (b) [43] . . . . .	42

3.1	The CERN accelerator chain [46]. . . . .	45
3.2	Computer generated cut-away view of the ATLAS detector showing its various components [75]. . . . .	48
3.3	A schematic view of the Inner Detector showing its various components [59].	51
3.4	A schematic view of the ATLAS inner detector [60]. . . . .	52
3.5	The ATLAS calorimeter system [63]. . . . .	55
3.6	A schematic view of the barrel accordion electromagnetic calorimeter [65].	56
3.7	A schematic view of the muon spectrometer [69]. . . . .	58
3.8	The ATLAS trigger system in Run-2 showing a single high level trigger (HLT) [70]. . . . .	60
3.9	A tau decay to three charged pions and a neutral pion [72]. . . . .	61
3.10	The trigger towers used in the L1 tau trigger ( [73]) . . . . .	62
3.11	The energy weighted shower width of tau and the QCD jets in the calorimeter $R_{cal}$ inside the calorimeter [128]. . . . .	63
3.12	The tau trigger efficiency as a function of the offline $p_T$ . The $p_T$ thresholds for L1, L2 and EF are 11 GeV/c, 20 GeV/c and 20 GeV/c respectively [74].	64
3.13	A schematic view of a b-hadron decay with displaced secondary vertex [77].	65
4.1	Distribution of identification variables for tau leptons and QCD jets (a) $f_{EM}^{track-HAD}$ (b) $f_{track}^{EM}$ (c) $m_{EM+track}$ (d) $p_T^{EM+track}/p_T$ for one-prong (top plots) and (e) $f_{EM}^{track-HAD}$ (f) $f_{track}^{EM}$ (g) $m_{EM+track}$ (h) $p_T^{EM+track}/p_T$ for three-prong (bottom plots) ( [127]) . . . . .	79
4.2	The light-jet rejection versus b-jet efficiency with and without the IBL ( [130]) . . . . .	82
4.3	Schematic view of the workflow of MV2 algorithm ( [130]) . . . . .	83
4.4	Final discriminant of IP3D algorithm for b-, c- and light-flavoured jets in $t\bar{t}$ events ( [131]) . . . . .	84

4.5	Properties of the secondary vertices reconstructed by the SV algorithm for b-, c- and light-flavoured jets in $t\bar{t}$ events: (a) the invariant mass, (b) the number of tracks, (c) number of 2-track vertices, (d) transverse decay length, (e) 3D decay length significance, and (f) the energy fraction of tracks in the secondary vertex to all tracks reconstructed within the jet ( [131]) . . . . .	85
4.6	Properties of the decay topology and secondary vertices reconstructed by the JetFitter algorithm for b-, c- and light-flavoured jets in $t\bar{t}$ events: (a) the number of 1-track vertices, (b) the number of vertices with at least two tracks, (c) the number of tracks from vertices with at least two tracks, (d) the average flight length significance of the reconstructed vertices, (e) the invariant mass of tracks fitted to one or more displaced vertices, and (f) the energy fraction of tracks in the secondary vertex to all tracks reconstructed within the jet ( [131]) . . . . .	86
4.7	The output of MV2c20 for b-, c- and light-flavour jets in $t\bar{t}$ events ( [131]). In MV2c20 algorithm, the BDT training is performed assigning b-jets as signal and a mixture of 80% light-flavour jets and 20% c-jets as background.	87
4.8	a) The light-flavour jet rejection b) c-jet rejection versus b-jet efficiency for Run-1 and Run-2 default taggers ( [131]) . . . . .	87
5.1	Scale factor for electron faking 3- prong $\tau_{had}$ as a function of leading $\tau_{had}$ $\eta$	97
5.2	Scale factor for electron faking 1- prong $\tau_{had}$ as a function of leading $\tau_{had}$ $\eta$ . Monte Carlo simulation has large mis-modelling near $\eta > 2.3$ , therefore events with $\tau_{had}$ $\eta > 2.3$ are vetoed in the signal region. . . . .	97
5.3	Fake factors from the W+jets control region in the b-veto category for 1-prong (left) and 3-prong (right) taus. The error bars correspond to statistical uncertainties only. . . . .	101
5.4	Fake factors from the W+jets control region before the b-veto/b-tag (the inclusive category) for 1-prong (left) and 3-prong (right) taus. The error bars correspond to statistical uncertainties only. . . . .	101

5.5	Fake factors from the QCD control region in the b-veto category for 1-prong (left) and 3-prong (right) taus. The error bars correspond to statistical uncertainties only. . . . .	103
5.6	Fake factors from the QCD control region in the b-tag category for 1-prong (left) and 3-prong (right) taus. The error bars correspond to statistical uncertainties only. . . . .	103
5.7	Fake factors from the fake lepton control region in the electron channel for the b-veto and b-tag categories. The error bars correspond to statistical uncertainties only. The unusual behaviour near $\eta = 1.5$ correspond to the transition region between the barrel and endcap electromagnetic calorimeters at $1.37 <  \eta  < 1.52$ . . . . .	105
5.8	Fake factors from the fake lepton control region in the muon channel with $p_T < 55$ GeV/c (left) and $p_T > 55$ GeV/c (right) for the b-veto and b-tag categories. The error bars correspond to statistical uncertainties only. Due to low statistics in lepton control region with muon $p_T > 55$ GeV/c, fake factors in only one bin are considered . . . . .	105
5.9	Ratio plots of the parametrization test on FF(QCD) as a function of $\Delta\phi(e/\mu, E_T^{miss})$ in electron and muon channels and for 1- and 3- prong taus. . . . .	106
5.10	Ratio plots of the parametrization test on FF(W+jets) as a function of $\Delta\phi(\tau_{had}, E_T^{miss})$ in electron and muon channels and for 1- and 3- prong taus. . . . .	106
5.11	The fraction of QCD multijet events ( $r_{QCD}$ ) in the b-veto category for the electron and muon channels. . . . .	108
5.12	The fraction of QCD multijet events ( $r_{QCD}$ ) in the b-tag category for the electron and muon channels. . . . .	108
5.13	Distribution of the transverse momentum ( $p_T$ ) of the tau candidate in the signal region, in the b-veto category for the electron (left) and the muon (right) channel . . . . .	110

5.14	Distribution of the transverse momentum ( $p_T$ ) of the tau candidate in the signal region, in the b-tag category for the electron (left) and the muon (right) channel . . . . .	110
6.1	QCD fake factors for 1- and 3-prong taus in the b-veto category. The error bars show the statistical error while the shaded regions show the systematic error. . . . .	113
6.2	QCD fake factors for 1- and 3-prong taus in the b-tag category. The error bars show the statistical error while the shaded regions show the systematic error. . . . .	113
6.3	The W+jets fake factors for 1- and 3-prong taus in the b-veto category. The error bars show the statistical error while the shaded regions show the systematic error. . . . .	116
6.4	The W+jets fake factors for 1- and 3-prong taus in the b-tag category. The error bars show the statistical error while the shaded regions show the systematic error. . . . .	116
6.5	The $r_{QCD}$ shape in the b-veto category. The error bars show the statistical error while the shaded regions show the systematic error. . . . .	117
6.6	The $r_{QCD}$ shape in the b-tag category. The error bars show the statistical error while the shaded regions show the systematic error. . . . .	117
6.7	Comparison between the statistical (error bars) and the systematic (shaded region) uncertainties associated with the data-driven fake estimation in the signal region is provided in the b-veto category for the electron (left) and the muon (right) channel. . . . .	128
6.8	Comparison between the statistical (error bars) and the systematic (shaded region) uncertainties associated with the data-driven fake estimation in the signal region is provided in the b-tag category for the electron (left) and the muon (right) channel. . . . .	128

6.9	Comparison between the data and the predicted background in the signal region is provided in the b-veto category for the electron (left) and the muon (right) channel. Statistical errors are shown as error bars and the systematic errors are shown as the shaded region. . . . .	129
6.10	Comparison between the data and the predicted background in the signal region is provided in the b-tag category for the electron (left) and the muon (right) channel. Statistical errors are shown as error bars and the systematic errors are shown as the shaded region. . . . .	129
6.11	Distribution of the transverse momentum ( $p_T$ ) of the tau candidate in the signal region, in the b-veto category for the electron (left) and the muon (right) channel. The error bars show the statistical uncertainties and the shaded region shown the total error (statistical plus systematic) on the fake estimation in the signal region. . . . .	133
6.12	Distribution of the transverse momentum ( $p_T$ ) of the tau candidate in the signal region, in the b-tag category for the electron (left) and the muon (right) channel. The error bars show the statistical uncertainties and the shaded region shown the total error (statistical plus systematic) on the fake estimation in the signal region. . . . .	133
6.13	Distribution of the transverse momentum ( $p_T$ ) of the lepton ( $e/\mu$ ) candidate in the signal region, in the b-veto category for the electron (left) and the muon (right) channel. The error bars show the statistical uncertainties and the shaded region shown the total error (statistical plus systematic) on the fake estimation in the signal region. . . . .	134
6.14	Distribution of the transverse momentum ( $p_T$ ) of the lepton ( $e/\mu$ ) candidate in the signal region, in the b-tag category for the electron (left) and the muon (right) channel. The error bars show the statistical uncertainties and the shaded region shown the total error (statistical plus systematic) on the fake estimation in the signal region. . . . .	134

6.15	Distribution of the visible mass ( $m_{\tau,e/\mu}$ ) of the lepton ( $e/\mu$ ) and the tau candidate in the signal region, in the b-veto category for the electron (left) and the muon (right) channel. The error bars show the statistical uncertainties and the shaded region shown the total error (statistical plus systematic) on the fake estimation in the signal region. . . . .	135
6.16	Distribution of the visible mass ( $m_{\tau,e/\mu}$ ) of the lepton ( $e/\mu$ ) and the tau candidate in the signal region, in the b-tag category for the electron (left) and the muon (right) channel. The error bars show the statistical uncertainties and the shaded region shown the total error (statistical plus systematic) on the fake estimation in the signal region. . . . .	135
6.17	Distribution of the missing transverse energy ( $E_T^{miss}$ ) in the signal region, in the b-veto category for the electron (left) and the muon (right) channel. The error bars show the statistical uncertainties and the shaded region shown the total error (statistical plus systematic) on the fake estimation in the signal region. . . . .	136
6.18	Distribution of the missing transverse energy ( $E_T^{miss}$ ) in the signal region, in the b-tag category for the electron (left) and the muon (right) channel. The error bars show the statistical uncertainties and the shaded region shown the total error (statistical plus systematic) on the fake estimation in the signal region. . . . .	136
7.1	Distribution of the total invariant mass ( $m_T^{tot}$ ) in the signal region. Each category is shown separately. The shaded region shows the uncertainties (statistical plus systematics) in the total fake estimation in the signal region. . . . .	138
7.2	The 95% CL upper limit on the $m_{A/H} - \tan \beta$ plane of the MSSM parameter space in the $m_h^{mod+}$ scenario. The b-tag category (a) and the b-veto category (b) are shown separately. . . . .	142
7.3	The 95% CL upper limit on the $m_{A/H} - \tan \beta$ plane of the MSSM parameter space in the $m_h^{mod+}$ scenario. The limits are obtained from the inclusive (before b-tag and b-veto requirement) analysis. . . . .	143

7.4	Comparison of the 95% CL upper limits on $m_{A/H} - \tan \beta$ the plane of the MSSM parameter space in the $m_h^{max}$ scenario with LEP, Tevatron and the ATLAS Run-1 exclusion limits. . . . .	144
7.5	CMS exclusion limits in the $m_{A/H} - \tan \beta$ plan (in the $m_h^{max}$ (see section 2.7.1)) for the combined analysis ( $\tau_{lep}\tau_{had} + \tau_{had}\tau_{had}$ ) using Run-1 data [160].	144
7.6	Comparison of the exclusion limits in the $m_{A/H} - \tan \beta$ plan (in the hMSSM scenario (see section 2.7.1)) for the combined ( $\tau_{lep}\tau_{had} + \tau_{had}\tau_{had}$ ) Run-2 $H/A \rightarrow \tau\tau$ search with the 2015 data [161]. . . . .	145
7.7	The 95% CL upper limit on the production cross section times branching ratio to $\tau_{lep}\tau_{had}$ of a single scalar boson produced via gluon-gluon fusion or b-associated production. Each category is shown separately. . . . .	146

---

# List of Tables

2.1	Chiral supermultiplets in the Minimal Supersymmetric Standard Model.	30
2.2	Gauge supermultiplets in the Minimal Supersymmetric Standard Model.	31
3.1	The designed and the achieved LHC beam parameters in 2012 [52,53]. . . .	46
4.1	Electron ID levels and summary of cuts (details in [125]). . . . .	76
5.1	List of control regions used in the analysis for b-veto and b-tag categories and in the electron and muon channels. . . . .	89
5.2	List of triggers used in the electron and the muon channel. The electron and muon trigger conditions are provided in [132] and [133] . . . . .	90
5.3	The electron channel cutflow in the signal region. The uncertainties provided are only statistical. . . . .	93
5.4	The muon channel cutflow in the signal region. The uncertainties provided are only statistical. . . . .	94
5.5	W+jets control region composition for the electron and muon channel in the b-veto category. The remainder corresponds to the multijet background that is estimated through data. . . . .	99
5.6	W+jets control region composition for the electron and muon channel in the b-tag category. The remainder corresponds to the multijet background that is estimated through data. . . . .	100
5.7	The QCD control region composition for the electron and muon channel in the b-veto category. The uncertainty shown here are only statistical. The remaining events are QCD multijets. . . . .	102

5.8	The QCD control region composition for the electron and muon channel in the b-tag category. The uncertainty shown here are only statistical. The remaining events are QCD multijets. . . . .	102
5.9	The fake lepton control region composition for the electron and muon channel in the b-veto category. The remainder corresponds to the QCD multijet background that is estimated through data. . . . .	102
5.10	The fake lepton control region composition for the electron and muon channel in the b-tag category. The remainder corresponds to the QCD multijet background that is estimated through data. . . . .	104
6.1	The relative difference between the Monte Carlo W+jets events in the signal region over the anti- $\tau_{had}$ region to the W+jets control region fake factors calculated through the Monte Carlo samples. The error provided here are statistical . . . . .	114
6.2	The effect of the detector related systematic uncertainties in the Monte Carlo samples used for the background estimation in the b-veto category. The effect on the normalization is shown in %. . . . .	121
6.3	The effect of the detector related systematic uncertainties in the Monte Carlo samples used for the background estimation in the b-tag category. The effect on the normalization is shown in %. . . . .	121
6.4	The effect of the detector related systematic uncertainties in the Monte Carlo samples used for the signal in the b-veto category. The effect on the normalization is shown in %. . . . .	122
6.5	The effect of the detector related systematic uncertainties in the Monte Carlo samples used for the signal in the b-tag category. The effect on the normalization is shown in %. . . . .	123
6.6	Uncertainties (given in %, variations are $\pm$ ) on the signal acceptance of the gluon-gluon fusion and the b-associated signal in the b-veto and b-tag category . . . . .	125
6.7	The signal region yields in the b-veto category for the electron and muon channels with full systematics. . . . .	131

6.8	The signal region yields in the b-tag category for the electron and muon channels with full systematics. . . . .	132
A.1	List of MC15 ggH signal samples used in the analysis. . . . .	165
A.2	List of MC15 bbH signal samples used in the analysis. . . . .	165
A.3	List of MC15 W+jets samples used in the analysis . . . . .	166
A.4	List of MC15 W+jets samples used in the analysis . . . . .	167
A.5	List of MC15 $Z/\gamma^*(\rightarrow ee/\mu\mu)$ +jets samples used in the analysis . . . . .	168
A.6	List of MC15 single top and $t\bar{t}$ samples used in the analysis . . . . .	168
A.7	List of MC15 diboson samples used in the analysis . . . . .	169
A.8	List of MC15 $Z/\gamma^*(\rightarrow \tau\tau)$ +jets samples used in the analysis . . . . .	169

---

# CHAPTER 1

## Introduction

The Standard Model of particle physics is a theoretical framework of quantum field theory and so far is the most complete description of fundamental particles and their interactions. The last discovered Standard model particle, the Higgs boson, was first predicted in 1964 by Peter Higgs [1–3]. His work showed that adding a doublet of complex scalar fields can lead to spontaneous symmetry breaking in the electroweak sector and explain why the W and Z bosons are massive particles. This process is known as the “Higgs Mechanism”.

The observation of a new particle was announced by the ATLAS and the CMS experiments [4, 5] on 4<sup>th</sup> July, 2012. Subsequent studies performed in both ATLAS and CMS confirmed that the new particle is compatible with the Standard Model Higgs boson [6–8]. The discovery of the Higgs boson was realized by detecting a resonance around 125 GeV/ $c^2$  in the invariant mass spectrum of diphotons (figure 1.1). This completed the particle content of the Standard Model and marked the beginning of a new era in particle physics.

Despite the great success of the Standard Model, it fails to explain, among other things, the presence of dark matter [9], gravity [10] and the matter-antimatter asymmetry of the universe [11]. In addition, the mass of the Higgs boson is quadratically divergent at high energies which leads to the “Hierarchy Problem”. The Standard Model lacks any mechanism that can explain the huge difference between the planck (where effects from quantum gravity become important) and the electroweak energy scales. A proposed solution to this problem is provided by supersymmetry [12] which is a symmetry between fermions and bosons.

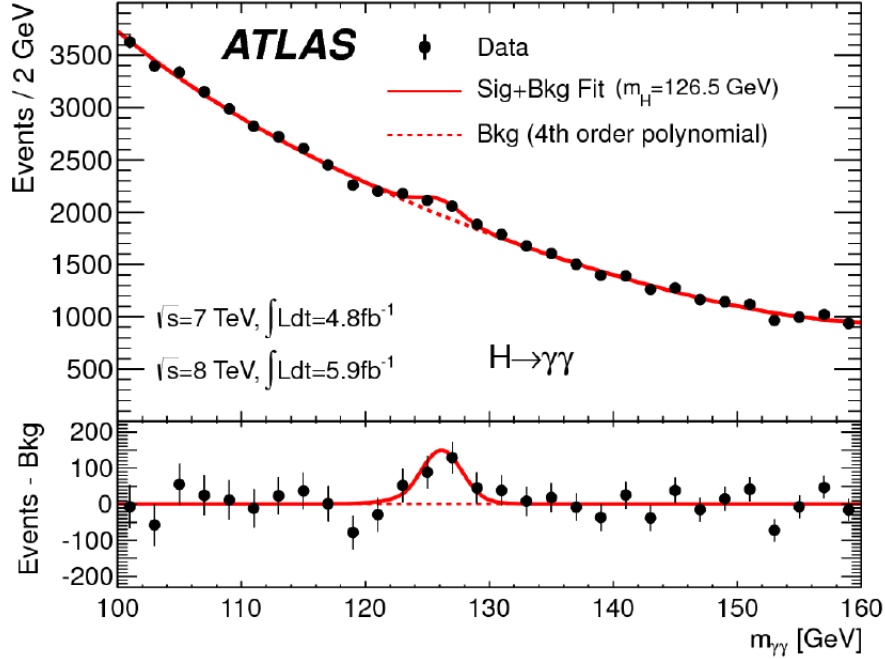


Fig. 1.1: The reconstructed invariant mass distribution of  $\gamma\gamma$  showing a resonance around  $125 \text{ GeV}/c^2$  [4]

Supersymmetry can be achieved through an extension to the Standard Model. The minimal extension possible is called the Minimal Supersymmetric Standard Model (MSSM) [13]. The MSSM uses a two-Higgs-doublet model (2HDM) in the extended Higgs sector. In a 2HDM, there are five Higgs bosons: one lightest CP even Higgs ( $h$ ), one heavy CP even Higgs ( $H$ ), one heavy CP odd Higgs ( $A$ ) and two charged Higgs ( $H^\pm$ ). In this thesis, the search for the heavy neutral MSSM Higgs bosons ( $A/H$ ) decaying into a tau pair is performed, where the MSSM Higgs boson is produced via gluon-gluon fusion or in association with b-quarks. The MSSM Higgs boson search is done where one tau decays into leptons ( $l = e/\mu$ ) and the other tau decays into hadrons. The theories that serve as the motivation of this thesis are presented in chapter 2 such as the Standard Model, the Higgs mechanism, supersymmetry and the minimal supersymmetric standard model.

The analysis is performed using the data collected by the ATLAS experiment [14] which is one of the two general-purpose detectors at the Large Hadron Collider (LHC). The ATLAS experiment investigates a wide range of physics, such as the original search for the Standard Model Higgs boson; precision measurements of the Standard Model; and

searches for new physics like supersymmetry, extra dimensions and dark matter. Details of the LHC and the ATLAS detector are provided in chapter 3. The data used in the analysis were collected in 2015 as part of the second run of the LHC and corresponds to integrated luminosity of  $3.21 \text{ fb}^{-1}$  at a centre of mass energy of 13 TeV.

Monte Carlo simulated signal and background samples play an important role in the data analysis to estimate background and to study the detector response to the signal. In the ATLAS experiment, events generated during real collision as well as from Monte Carlo simulation are both reconstructed to physics objects using the same dedicated algorithms. Chapter 4 summarizes the Monte Carlo simulation, lists the data and the simulated samples used in the analysis and the techniques used in the ATLAS detector to reconstruct physics objects.

The Standard Model physics can produce events which look like the signal and detector effects can also add to this background. Chapter 5 describes the detailed selection criteria applied to discriminate the potential MSSM Higgs boson (H/A) events from these backgrounds. Chapter 6 provides description of the systematic errors and their effects on the results. Finally the implications of the results for the theory is discussed in chapter 7

---

## CHAPTER 2

# Theoretical Framework: The Standard Model and Beyond

*“From the earliest times, man’s dream has been to comprehend the complexity of nature in terms of as few unifying concepts as possible”*

Abdus Salam

The aim of the particle physics is to describe the most fundamental particles of the universe and the interactions between these particles. The Standard Model (SM) of the particle physics is the most current theoretical description of the known fundamental particles and their interactions. So far, the results from the Standard Model are in good agreement with the experimental observations. However, there exist reasons to suppose that the Standard Model is not the ultimate theory and one can look beyond the Standard Model to explain certain phenomena that remain as open questions such as the nature of dark matter and the infamous hierarchy problem. Such an effort to look beyond the Standard Model resulted in a theory called Supersymmetry (SUSY) which attempts to answer these open questions.

This chapter provides a brief description of the evolution of relativistic quantum mechanics and an overview of the quantum field theory which provides the mathematical framework to the Standard Model of particle physics. It also summarizes the motivations for looking beyond the Standard Model and the reasons to introduce Supersymmetry.

## 2.1 The Standard Model

The Standard Model is a relativistic quantum field theory that provides a mathematical framework to study fundamental particles and their interactions. According to the Standard Model, the universe is composed of fundamental particles and these particles interact via three fundamental forces of nature: the electromagnetic, the strong and the weak force. The Standard Model does not include gravity. Electromagnetic and weak interactions were combined into the electroweak interaction by Glashow in 1960 [16] and expanded by Weinberg [17] and Abdus Salam [18] to incorporate the Higgs mechanism.

### 2.1.1 Fundamental Particles and the Interactions

There are two classes of fundamental particles: matter and forces. The matter particles are called fermions and they carry  $\frac{1}{2}$ -integer spin. The force carriers, vector bosons, are particles that mediate the fundamental forces of the Standard Model. All these particles have spin-1. Apart from these particles, the Standard Model also contains a scalar boson, the Higgs boson, which has spin-0 and gives masses to W, Z bosons and to fermions. In 2012, both ATLAS and CMS announced the discovery of a particle whose characteristics are consistent with the Standard Model Higgs [4,5] as described in section 2.4. Figure 2.1 shows the fundamental particles in the Standard Model.

Fermions obey the Pauli Exclusion Principle and therefore can not co-exist in the same state at the same time. The fundamental fermions are classified into two categories, quarks and leptons, on the basis of how they interact and what charges they carry. Quarks carry electric, colour as well as weak isospin charges and are the only fermions that interact via all three forces of the SM. Quarks can not usually be isolated due to the gluonic field between them that does not decrease as they separate, an effect known as colour confinement. Therefore only colour neutral bound states of those quarks, called hadrons, typically exist in nature. An exception is the top quark which decays too rapidly to form bound states and so only exists as a “bare” quark. Hadrons are further classified as mesons (quark antiquark pair) and baryons (three quarks). Leptons are divided into charged and neutral categories. The charged leptons carry electric and weak charges so they interact via the electromagnetic and weak forces whereas neutrinos



the  $W$  and  $Z$  masses, the electromagnetic and the weak force merge into a single force, the electroweak force.

### 2.1.2 Tau Lepton

The tau lepton is the heaviest of all known leptons with a mass of  $1.77 \text{ GeV}/c^2$ . It was first detected by Martin Lewis Perl and his colleagues between 1974 and 1977 in a series of experiments conducted at SLAC's  $e^+e^-$  collider ring, called SPEAR, using the magnetic detector of Lawrence Berkeley National Laboratory (LBL). At the LHC, the common modes of tau production are  $W^\pm \rightarrow \tau^\pm \nu^\mp$ ,  $Z \rightarrow \tau^+ \tau^-$ ,  $\gamma \rightarrow \tau^+ \tau^-$  and  $H \rightarrow \tau^+ \tau^-$  with the Feynman diagrams<sup>1</sup> shown in figure 2.2.

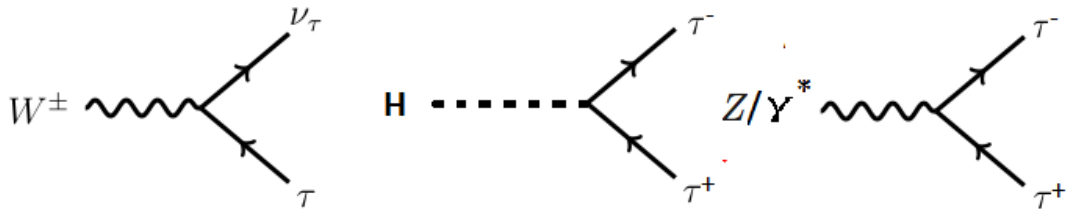


Fig. 2.2: Feynman diagram of tau production

Tau is the only lepton whose decay products can be hadrons, called the hadronic decays. The other leptons do not have necessary mass to do so. Feynman diagrams showing common tau decays are shown in figure 2.3

The branching ratios for the leptonic tau ( $\tau^-$ ) decays are [19]

- 17.83% for  $\tau \rightarrow \nu_\tau e^- \bar{\nu}_e$
- 17.41% for  $\tau \rightarrow \nu_\tau \mu^- \bar{\nu}_\mu$

---

<sup>1</sup>The calculation of probability amplitudes in quantum field theory involves large and complicated integrals however they may be represented in a pictorial form. A Feynman diagram is a graphical representation of a perturbative contribution to the transition amplitude. It represents quantum field theory processes in terms of particle paths. The particle paths are represented by lines in the diagram with the type of line indicating the type of particle. A point where a line connects to another line is an interaction vertex. At interaction vertices particles meet and interact by emitting or absorbing new particles, scattering or changing types. For more details on Feynman diagrams and their rules see [21]

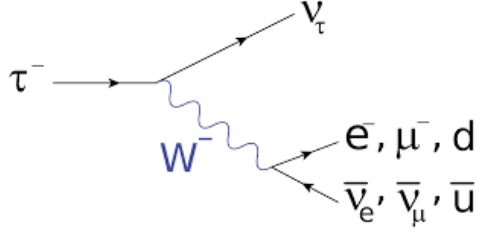


Fig. 2.3: Feynman diagrams of Common tau decays

The remaining tau decays are hadronic. The branching ratios for common hadronic tau ( $\tau^-$ ) decays are [19]:

- 25.52% for  $\tau \rightarrow \nu_\tau \pi^- \pi^0$
- 10.83% for  $\tau \rightarrow \nu_\tau \pi^-$
- 9.31% for  $\tau \rightarrow \nu_\tau \pi^- \pi^+ \pi^-$
- 9.30% for  $\tau \rightarrow \nu_\tau \pi^- 2\pi^0$
- 4.62% for  $\tau \rightarrow \nu_\tau \pi^- \pi^+ \pi^- \pi^0$
- 1.05% for  $\tau \rightarrow \nu_\tau \pi^- 3\pi^0$

Taus decay to one or three charged hadrons predominantly with the branching ratio for tau decay to five or more charged hadrons being very small ( $< 10^{-3}$ ). Tau decay to one charged hadron is termed as 1-prong and to three charged hadrons is termed as a 3-prong decay due to the number of tracks observed in the detector.

The tau plays an important role in particle physics. It couples to the Higgs boson more strongly than any other lepton (section 2.3.6) and therefore  $H \rightarrow \tau^+ \tau^-$  is an important decay channel of the Higgs boson whose evidences have been found [20] confirming its coupling with the Standard Model fermions. The tau also plays significant role in the searches of new physics such as Supersymmetry (see section 2.6).

## 2.2 The Relativistic Quantum Mechanics

In modern colliders such as the Large Hadron Collider (LHC) at CERN, particles are accelerated to a speed close to the speed of light. Therefore a theoretical framework to describe subatomic particles propagating relativistically is needed. Relativistic quantum mechanics (RQM) provides a mathematical formulation of the quantum mechanical aspects in the relativistic regime. The Klein-Gordon (KG) and the Dirac equations form basis of RQM.

### 2.2.1 The Klein-Gordon Equation

In special relativity the product of any two 4-vectors is invariant therefore Lorentz invariance of the quantity  $p^\mu p_\mu$ , where  $p^\mu = (E, \vec{p})$  is the 4-momentum, provides a relation between energy and momentum. In the system of natural units where  $c = 1$ ,  $\hbar = 1$  this gives:

$$p^\mu p_\mu = E^2 - p^2 = m^2 \quad (2.1)$$

To take quantum mechanics into account, we replace energy and momentum with their respective operators,  $\hat{E} = i\frac{\partial}{\partial t}$  and  $\hat{p} = -i\Delta$ , acting on a wave function. In covariant form,  $\hat{p}_\mu = i(\frac{\partial}{\partial t}, \Delta) = i\partial_\mu$ . The above equation becomes:

$$(\partial_\mu \partial^\mu + m^2)\Psi(x^\nu) = 0 \quad (2.2)$$

where  $\Psi(x^\nu)$  is a complex scalar function. This partial differential equation is known as the Klein-Gordon equation. The free particle solution of the KG equation is  $\Psi(x^\nu) = Ne^{i(\vec{p}\cdot\vec{x}-Et)}$  where  $E = \pm\sqrt{\vec{p}^2 + m^2}$  and  $N$  is the normalization factor.

The Klein Gordon equation gave negative probability densities,  $\rho = 2E |N|^2$  with  $E = -\sqrt{\vec{p}^2 + m^2}$ , and as there was no interpretation of negative energy at that time, the KG equation was rejected [15] until Dirac derived his equation and provided an interpretation of negative energy.

## 2.2.2 The Dirac Equation

The problem of negative probability density led Dirac to think of another equation, an equation which is first order in space and time. Dirac started with the same energy-momentum equation that Oskar Klein and Walter Gordon used to derive KG equation i.e.,  $E^2 = p^2 + m^2$  and then tried to factorise it:

$$\begin{aligned} E^2 - p^2 - m^2 &= p^\kappa p_\kappa - m^2 = p_0^2 - p_1^2 - p_2^2 - p_3^2 - m^2 \\ &= \gamma^\mu \gamma^\nu p_\mu p_\nu - m^2 \\ &= (\gamma^\mu p_\mu - m)(\gamma^\nu p_\nu + m) = 0 \end{aligned} \quad (2.3)$$

where  $\gamma^\mu$  are 4-dimensional matrices called gamma matrices. To satisfy the above equation, the gamma matrices must hold following characteristics:

$$(\gamma^0)^2 = 1 \quad (2.4)$$

$$(\gamma^1)^2 = (\gamma^2)^2 = (\gamma^3)^2 = -1 \quad (2.5)$$

$$\{\gamma^\mu \gamma^\nu + \gamma^\nu \gamma^\mu\} = 2g_{\mu\nu} \quad (2.6)$$

Equation 2.3 implies that either

$$(\gamma^\mu p_\mu - m) = 0 \quad (2.7)$$

or

$$(\gamma^\nu p_\nu + m) = 0 \quad (2.8)$$

The Dirac equation can be taken as either of the above two equations giving two possible types of solutions: one for matter and one for anti-matter. Replacing the momentum with its operator acting on the wave function  $\Psi(x^\nu)$  gives:

$$(i\gamma^\mu \partial_\mu - m)\Psi(x^\nu) = 0 \quad (2.9)$$

This is the covariant form of the Dirac Equation. The solution  $\Psi(x^\nu)$  is a 4-element column vector, of plane waves, called a Dirac spinor.

$$\Psi(x_\nu) = \begin{bmatrix} \Psi(x_1) \\ \Psi(x_2) \\ \Psi(x_3) \\ \Psi(x_4) \end{bmatrix}$$

Equation 2.6 implies that the gamma matrices are anti-commuting. The three  $2 \times 2$  Pauli matrices  $\sigma^j$  are also anti-commuting matrices. So one representation of the gamma matrices, called the Dirac basis, is:

$$\gamma^0 = \begin{bmatrix} I & 0 \\ 0 & -I \end{bmatrix}$$

,

$$\gamma^j = \begin{bmatrix} 0 & \sigma^j \\ -\sigma^j & 0 \end{bmatrix}$$

where  $I$  and  $0$  are  $2 \times 2$  identity and null matrices respectively.

Through the equation of continuity, the probability density calculation leads to:

$$\rho = \bar{\Psi}\gamma^0\Psi = \Psi^\dagger\gamma^0\Psi = \sum_{i=1}^4 |\psi_i|^2 \quad (2.10)$$

which gives a positive definite number.

The negative energy states in the Dirac equation were initially explained by “the Dirac Sea” which is a theoretical model of vacuum as an infinite sea of electron with negative energy [15]. Since electrons obey the Pauli exclusion principle, no other electron could fall into them. When energy supplied, the negative energy electron can lift to high energy state leaving a hole. The hole in the Dirac sea was interpreted as a positive energy elec-

tron with a reversed charge. In 1932, Carl Anderson [22] discovered a positively charged particle with all properties same as predicted for the electron. It was named as positron.

As bosons do not obey Pauli exclusion principle, the Dirac interpretation of negative energy does not work for them. The Feynman interpretation is a more general interpretation which is based on the concept that positive energy states propagate forward in time ( $e^{-ip^\mu x^\mu} = e^{-i(\vec{p}\cdot\vec{x}+Et)}$ ) whereas the negative energy states propagate only backwards in time ( $e^{-i(\vec{p}\cdot\vec{x}+(-E)(-t))}$ ). In this interpretation, the emission of a negative energy particle with momentum  $p^\mu$  is interpreted as the absorption of a positive energy antiparticle with momentum  $-p^\mu$ .

There exist two solutions of the Dirac equation for particles and antiparticles both. This leads to the conclusion that the Dirac equation describes spin-1/2 particles such as quarks and leptons. Whereas, the Klein-Gordon equation successfully describes spin 0 particles in relativistic quantum field theory.

## 2.3 Mathematical Framework for the Standard Model

Standard Model is a relativistic quantum field theory in which particles are treated as fields such as  $\phi(\vec{x}, t)$ . The interaction between particles are actually the interaction between their underlying fields. The Euler-Lagrange equation (in equation 2.11) gives the equation of motion of the system.

$$\partial_\mu \left( \frac{\partial \mathcal{L}}{\partial(\partial_\mu \phi)} \right) - \frac{\partial \mathcal{L}}{\partial \phi} = 0 \quad (2.11)$$

where  $\mathcal{L}$  is the lagrangian density (where the lagrangian  $L = \int \mathcal{L} d^3x$ ). The free Dirac and Klein-Gordon lagrangian are given in equation 2.12 and 2.13 respectively.

$$\mathcal{L}_{Dirac} = i\bar{\Psi}\gamma^\mu\partial_\mu\Psi - m\bar{\Psi}\Psi \quad (2.12)$$

$$\mathcal{L}_{KG} = \frac{1}{2}\partial_\mu\phi\partial^\mu\phi - \frac{1}{2}m^2\phi^2 \quad (2.13)$$

QFT is a gauge theory which means the lagrangian is invariant under certain local transformations applied to the field. To make the lagrangian invariant, the interaction terms are included in the free lagrangian.

In the Standard Model, all types of interactions between particles are described in a local phase symmetry based on  $SU(3)_C \times SU(2)_L \times U(1)_Y$ . Here  $SU(3)_C$  subgroup describes Quantum Chromodynamics and  $SU(2)_L \times U(1)_Y$  subgroup describes electroweak interactions. The Lagrangian of the Standard Model ( $\mathcal{L}_{SM} = \mathcal{L}_{QCD} + \mathcal{L}_{EW} + \mathcal{L}_{Higgs}$ ) is invariant under local phase transformations based on  $SU(3)_C \times SU(2)_L \times U(1)_Y$ . The corresponding conserved quantities are colour charge in QCD and hypercharge and weak isospin in EW interactions.

### 2.3.1 Quantum Electrodynamics (QED)

QED describes the interaction between photons and the charged fermions. As stated before, the local phase invariance brings interactions into the theory. The Dirac Lagrangian given in equation 2.12 must be locally phase invariant under the transformation to the field  $\Psi \rightarrow \Psi' = e^{ie\Theta(x_\mu)}\Psi$ , where  $\Theta(x_\mu)$  is the phase transformation. The free Dirac lagrangian is not invariant under such transformation. Therefore, an electromagnetic potential  $A^\mu = (V, \vec{A})$  is introduced which is invariant under gauge transforms:

$$A^\mu \rightarrow A^{\mu'} = A^\mu + \partial^\mu\Theta(x^\mu) \quad (2.14)$$

Furthermore, the derivative  $\partial^\mu$  is replaced with a covariant derivative  $D^\mu$  such that:

$$D^\mu = \partial^\mu + ieA^\mu \quad (2.15)$$

This makes the lagrangian local phase invariant. The introduction of a gauge field brings the interaction term  $e\bar{\Psi}\gamma_\mu A^\mu\Psi$  which is the coupling of the gauge field  $A^\mu$  (the EM field) and the matter field  $\Psi$  (fermionic field). Each interaction term has an incoming fermion (or outgoing antifermion), an outgoing fermion (or incoming antifermion) and a photon

(such interactions are represented by the Feynman vertex as in figure 2.4). The strength of interaction is described by a coupling constant. The loop corrections to Feynman diagrams bring a divergence in the calculations. This divergence is absorbed through a running coupling constant. In QED, the running coupling constant is defined as:

$$\alpha(Q^2) = \frac{e^2(Q^2)}{4\pi} = \frac{\alpha(0)}{1 - \frac{\alpha(0)}{3\pi} \ln \frac{Q^2}{m^2}} \quad (2.16)$$

where  $e$  is the effective charge of an electron,  $m$  is the mass of electron,  $\alpha(0) = \frac{e^2(0)}{4\pi}$  and  $Q^2$  is the momentum squared. The strength of interaction increases at short distances.

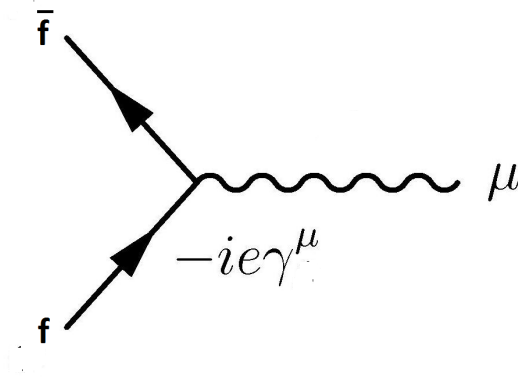


Fig. 2.4: Feynman Vertex factor in QED

The QED lagrangian is [23]:

$$\mathcal{L}_{QED} = -\frac{1}{4}F_{\mu\nu}F^{\mu\nu} + \bar{\Psi}(i\gamma_\mu D^\mu - m)\Psi \quad (2.17)$$

The kinetic energy term of the photon,  $-\frac{1}{4}F_{\mu\nu}F^{\mu\nu}$  where  $F^{\mu\nu} = \partial^\mu A^\nu - \partial^\nu A^\mu$ , describes the propagation of photon and is also invariant under local phase transformation. The explicit mass term  $\frac{1}{2}m_\gamma^2 A_\mu A^\mu$  in the lagrangian breaks the local phase invariance which requires the gauge boson of QED to be massless.

### 2.3.2 Quantum Chromodynamics (QCD)

QCD is a gauge theory that provides a framework to describe the interactions between particles that have a colour charge and interact through strong interactions. The three colour charges are: red, green and blue. Gluons, the force carriers of QCD, have eight possible states each of which carry both a colour and an anti-colour charge.

QCD has two distinct properties:

- **Confinement:** In QCD, the force carriers themselves carry colour charge. Unlike QED where the electric field between electric charges weakens as they are separated, the gluon field between quarks increases and forms a narrow tube. At some point, the energy in the gluon field between these quarks is sufficient to create another quark-antiquark pair. This is why quarks are generally always bounded in the form of hadrons and no free quark, except for the top quark, is ever observed.
- **Asymptotic Freedom:** In the vicinity of an electric charge, the vacuum becomes polarized. Getting closer and closer to the central charge, the effective charge increases (as shown in equation 2.22). In QCD, where the force carriers also carry charge, the polarization of virtual gluons also contribute in the effective charge seen by a second quark brought closer to a central quark. The effective charge decreases when getting close to a quark because there is less charge field to observe. Therefore at short distances, quarks interact weakly.

There exists an exact gauge symmetry, called  $SU(3)$ , that acts on the different colours of the quarks mediated by the gluons. Each gluon state has a corresponding  $3 \times 3$  matrix (one of the 8 Gell-Mann matrices). These matrices are the generators of the QCD symmetry ( $SU(3)$ ).

The QCD lagrangian is [24]

$$\begin{aligned}
\mathcal{L} = & -\frac{1}{4}(\partial^\mu G_a^\nu - \partial^\nu G_a^\mu)(\partial_\mu G_\nu^a - \partial_\nu G_\mu^a) + \sum_f \bar{q}_f^\alpha (i\gamma^\mu \partial_\mu - m_f) q_f^\alpha \\
& + g_s G_a^\mu \sum_f (\bar{q}_f^\alpha \gamma_\mu \left(\frac{\lambda^a}{2}\right)_{\alpha\beta} q_f^\beta) - \frac{g_s}{2} f^{abc} (\partial^\mu G_a^\nu - \partial^\nu G_a^\mu) G_\mu^b G_\nu^c \\
& - \frac{g_s^2}{4} f^{abc} f_{ade} G_b^\mu G_c^\nu G_\mu^d G_\nu^e
\end{aligned} \tag{2.18}$$

where  $q_f^\alpha$  is a quark field of colour  $\alpha$  and flavour  $f$ ,  $G_a^\mu$  are eight different gauge bosons (the gluons),  $g_s$  is the strength of strong interaction,  $\lambda^a$  are eight generators of the SU(3) algebra (the Gell-Mann matrices) and  $f^{abc}$  is the SU(3) structure constant such that  $[\lambda^a, \lambda^b] = 2if^{abc}\lambda^c$ . The structure constant in SU(3) is given as:

$$f^{123} = 1 \tag{2.19}$$

$$f^{147} = -f^{156} = f^{246} = f^{257} = f^{345} = -f^{367} = \frac{1}{2} \tag{2.20}$$

$$f^{458} = f^{678} = \frac{\sqrt{3}}{2} \tag{2.21}$$

and all other are zero.

The interaction term  $\frac{g_s}{2}(\bar{q}\gamma^\mu\lambda^a q)G_a^\mu$  is represented by the Feynman vertex (in figure 2.5):

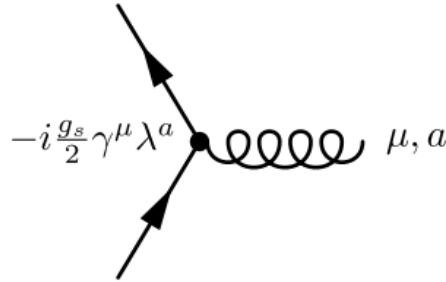


Fig. 2.5: Feynman Vertex factor in QCD

The running coupling constant in QCD is defined as:

$$\alpha(Q^2) = \frac{g_s^2(Q^2)}{4\pi} = \frac{\alpha(\mu)}{1 + \frac{\alpha(\mu)}{12\pi}(33 - 2f) \ln \frac{Q^2}{\mu^2}} \tag{2.22}$$

where  $f$  is the number of active quark flavours, and  $\mu$  is an arbitrary scale large enough to make perturbation valid.

QCD is a non-abelian gauge theory (the gluon field terms do not commute) therefore, unlike photons, gluons self interact. The 3- and 4- gluon interaction terms are represented by the Feynman diagrams (figure 2.6)

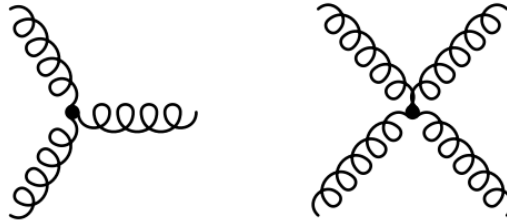


Fig. 2.6: Feynman representation of 3- and 4-gluon interaction

### 2.3.3 Weak Interactions

The weak interaction is mediated by massive bosons ( $W^\pm$  and  $Z$ ). All fermions interact through the weak interactions. The force is called weak because at low energies its strength ( $\alpha_W = 10^{-5}$ ) is several orders of magnitude less than that of the electromagnetic force below  $\sim 100$  GeV. The gauge bosons ( $W^\pm$  and  $Z$ ) mediate the weak interaction between fermions with the weak isospin quantum number. The weak isospin is defined as:

$$I_3 = Q - \frac{Y_W}{2} \quad (2.23)$$

where  $Q$  is the charge and  $Y_W$  is the weak hypercharge which is -1 for leptons and +1/3 for quarks.

The weak interaction is unique in a number of respects:

- Only left handed fermions and right handed anti-fermions interact weakly ( $I_3 = 0$  for right handed fermions/left handed anti-fermions).

- Change of flavour of quarks is possible in the weak interaction.
- Force carriers ( $W^\pm$  and  $Z$ ) have significant masses.
- It also violates important symmetries. To understand this, C, P and T symmetries are summarized below.

### C, P, and T Symmetries

Charge conjugation (C) refers to the transformation of a particle into an antiparticle. The electromagnetic and the strong interactions are invariant under such a transformation. A left-handed neutrino would transform it into a left-handed antineutrino under charge conjugation, which does not interact in the Standard Model therefore the weak interaction violates C-symmetry.

Parity is the behavior of a physical system, or a mathematical function that describes such a system, under reflection. A parity operator ( $\hat{P}$ ) flips the signs of the spatial coordinates:

$$\hat{P}\psi(x) = \psi(-x) \tag{2.24}$$

The operator  $\hat{P}^2$ , which reverses the parity of a state twice, leaves the space-time invariant. This means:

$$\hat{P}\psi(x) = P\psi(x) \tag{2.25}$$

$$\hat{P}^2\psi(x) = \psi(x) \tag{2.26}$$

This implies that the eigenstates of parity are either even or odd ( $P = \pm 1$ ). A scalar is a physical quantity with  $P = 1$  whereas a pseudoscalar is a quantity that behaves like a scalar except with  $P = -1$ . A vector has  $P = -1$  whereas a pseudovector behaves like a vector but with  $P = 1$ .

Parity is conserved in the electromagnetic and the strong interactions. The weak interaction acts only on left handed particles and since the mirror image of a left handed particle is a right handed therefore the weak interaction violates parity. The weak interaction also violates CP symmetry, the symmetry under simultaneous C- and P-transformations. The CP violation was discovered in 1964 in the decays of neutral kaons [25]. CP-violation is one of the requirements to explain the matter-antimatter asymmetry in the nature.

Time reversal transformation flips only the time coordinate:

$$(\vec{x}, t) \xrightarrow{T} (\vec{x}, -t) \quad (2.27)$$

CPT symmetry is a symmetry of physical laws under simultaneous transformations of charge conjugation (C), parity (P) and time reversal (T). All known fundamental interactions obey CPT symmetry.

### 2.3.4 Unification of Electromagnetic and Weak Interaction

Glashow, Weinberg and Salam in their independent work combined the electromagnetic and weak interaction into a unified force, the electroweak force. Glashow developed a gauge theory that includes four massless gauge bosons and massless fermions. Weinberg and Salam then independently showed that through the spontaneous symmetry breaking (SSB) proposed by Peter Higgs, the three bosons could acquire mass along with the fermions. The details are given below:

### 2.3.5 Glashow-Weinberg-Salam Model

The electroweak theory has  $SU(2)_L \times U(1)_Y$  symmetry. The  $SU(2)_L$  is a symmetry for the weak isospin and has three generators  $T^i = \frac{1}{2}\tau^i (i = 1, 2, 3)$  where  $\tau^i$  are the Pauli matrices. The gauge fields for this symmetry are  $W_\mu^i$ . The  $U(1)_Y$  is a symmetry of the weak hypercharge ( $Y_W = 2(Q - T_3)$ ). The gauge field for  $U(1)_Y$  is  $B_\mu$ .

The left and right handed fermions are represented differently in the electroweak theory. Left handed fermions are represented as SU(2) doublets whereas the right handed fermions are represented as singlet:

$$q_L = \begin{pmatrix} u \\ d \end{pmatrix}_{L,m}, l_L = \begin{pmatrix} \nu \\ e \end{pmatrix}_{L,m} \quad (2.28)$$

and

$$u_{mR}, d_{mR}, \nu_{mR}, e_{mR} \quad (2.29)$$

Here,  $q$  and  $l$  represent quarks and leptons respectively, and  $m$  represents the family of fermions ( $m=1,2,3$ ). The wave function for left and right handed fermions is taken as  $\psi_L$  and  $\psi_R$  respectively.

A complex scalar field is included:

$$\phi = \frac{1}{\sqrt{2}} \begin{pmatrix} \phi_1 + i\phi_2 \\ \phi_3 + i\phi_4 \end{pmatrix} \quad (2.30)$$

where  $\phi_{1,2,3,4}$  are real.

The  $SU(2)_L \times U(1)_Y$  remains invariant under following transformations [26]:

$$\phi \rightarrow e^{i\alpha(x)_i \frac{\tau_i}{2} + i\beta(x)Y} \phi \quad (2.31)$$

$$\psi_L \rightarrow e^{i\alpha(x)_i \frac{\tau_i}{2} + i\beta(x)Y} \psi_L \quad (2.32)$$

$$\psi_R \rightarrow e^{i\beta(x)Y} \psi_R \quad (2.33)$$

$$W_\mu^i = W_\mu^i - \frac{1}{g} \partial_\mu \alpha_i - \epsilon_{ijk} \alpha^j W_\mu^k \quad (2.34)$$

$$B_\mu = B_\mu - \frac{1}{g'} \partial_\mu \beta \quad (2.35)$$

where  $g$  and  $g'$  are the weak isospin and hypercharge coupling,  $Y$  is the weak hypercharge,  $\alpha(x)$  and  $\beta(x)$  are the phases for SU(2) and U(1) parts of SU(2) $\times$ U(1) respec-

tively, and  $\epsilon_{ijk}$  is the Levi-Civita tensor. The electroweak lagrangian can be written as:

$$\mathcal{L} = \mathcal{L}_{gauge} + \mathcal{L}_f + \mathcal{L}_\phi + \mathcal{L}_{Yuk} \quad (2.36)$$

The gauge part of the lagrangian describes the propagation of the gauge bosons [26]:

$$\mathcal{L}_{gauge} = -\frac{1}{4}W_{\mu\nu}^i W^{\mu\nu i} - \frac{1}{4}B_{\mu\nu} B^{\mu\nu} \quad (2.37)$$

where  $i = 1, 2, 3$ ,  $W_{\mu\nu}^i = \partial_\mu W_\nu^i - \partial_\nu W_\mu^i - g\epsilon_{ijk}W_\mu^j W_\nu^k$  and  $B_{\mu\nu} = \partial_\mu B_\nu - \partial_\nu B_\mu$  are the field strength tensors [26].

The fermionic part of the lagrangian which includes kinetic energy terms of left and right handed fermions is [26]:

$$\begin{aligned} \mathcal{L}_f = \sum_m & (\bar{q}_{m,L} i\gamma^\mu D_\mu q_{m,L} + \bar{l}_{m,L} i\gamma^\mu D_\mu l_{m,L} + \bar{u}_{m,R} i\gamma^\mu D_\mu u_{m,R} \\ & + \bar{d}_{m,R} i\gamma^\mu D_\mu d_{m,R} + \bar{\nu}_{m,R} i\gamma^\mu D_\mu \nu_{m,R} + \bar{e}_{m,R} i\gamma^\mu D_\mu e_{m,R}) \end{aligned} \quad (2.38)$$

where

$$D_\mu \psi_L = \left( \partial_\mu + i\frac{g}{2}\tau^i W_\mu^i + ig'Y B_\mu \right) \psi_L \quad (2.39)$$

$$D_\mu \psi_R = (\partial_\mu + ig'Y B_\mu) \psi_R \quad (2.40)$$

The scalar part of the lagrangian is:

$$\mathcal{L}_\phi = (D^\mu \phi)^\dagger (D_\mu \phi) - V(\phi) \quad (2.41)$$

where  $D_\mu \phi = \left( \partial_\mu + i\frac{g}{2}\tau^i W_\mu^i + i\frac{g'}{2}Y B_\mu \right) \phi$  is the gauge covariant derivative.

### 2.3.6 Spontaneous Symmetry Breaking and the Higgs Mechanism

In the Higgs mechanism, the potential of the scalar field in the lagrangian (equation 2.41) is taken as  $V(\phi) = \mu^2 \phi^\dagger \phi + \lambda(\phi^\dagger \phi)^2$  with  $\lambda > 0$  to satisfy gauge invariance and vacuum stability. The Higgs field,  $\phi$  is given in eq. 2.30. If  $\mu^2 > 0$ , the potential has a minimum at  $\phi = 0$ . For spontaneous symmetry breaking, we are interested in the  $\mu^2 < 0$ . For this, the potential has a “Mexican hat” shape as shown in figure 2.7 and has a continuum of absolute minima. The degeneracy in the ground state forces the system to choose one of these equivalent states and consequently breaks the symmetry. It is the ground state that breaks the symmetry. The equation of motion of the system and the lagrangian preserve the symmetry.

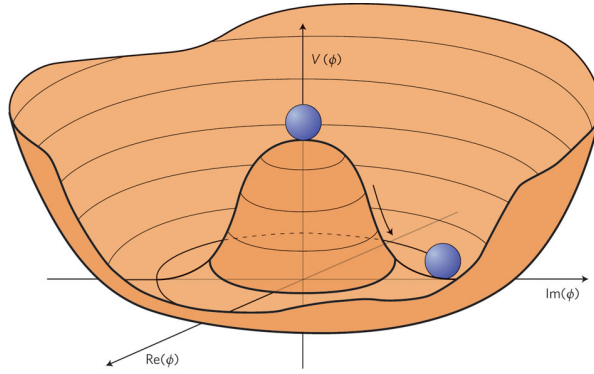


Fig. 2.7: The mexican hat potential for  $\mu^2 < 0$  [27]

The Yukawa interaction part of the lagrangian describes the Higgs coupling to the fermions:

$$\mathcal{L}_{\text{Yuk}} = - \sum_f c_f (\bar{\psi}_L \phi^\dagger \psi_R + \bar{\psi}_R \phi \psi_L) \quad (2.42)$$

In Higgs mechanism, we are interested in those parts of the electroweak lagrangian that include a complex scalar field ( $\mathcal{L}_\phi$ ) and its interactions ( $\mathcal{L}_{\text{Yuk}}$ ) with gauge fields and fermions. That is:

$$\mathcal{L}_{\text{Higgs}} = (D^\mu \phi)^\dagger (D_\mu \phi) - V(\phi) + \sum_f c_f (\bar{\psi}_L \phi^\dagger \psi_R + \bar{\psi}_R \phi \psi_L) \quad (2.43)$$

Out of all equivalent vacuum states of the Higgs field, one can choose:

$$\phi = \frac{1}{\sqrt{2}} \begin{pmatrix} 0 \\ \nu \end{pmatrix} \quad (2.44)$$

where  $\nu = \sqrt{\frac{-\mu^2}{\lambda}}$  and the three out of four degrees of freedom in the Higgs field are taken zero ( $\phi_1 = \phi_2 = \phi_4 = 0$ ) and  $\phi_3 = \nu$ . The excitation around the vacuum state is considered.

Now, the Higgs field can be written as:

$$\phi = \frac{1}{\sqrt{2}} \begin{pmatrix} 0 \\ \nu + H \end{pmatrix} \quad (2.45)$$

where H is a scalar field and  $\langle |H| \rangle = 0$ . Substituting the Higgs field (from eqn. 2.45) in the kinetic part of the Higgs lagrangian gives:

$$(D^\mu \phi)^\dagger (D_\mu \phi) = \left( \frac{g^2 \nu^2}{8} \right) (W_\mu^{1^2} + W_\mu^{2^2}) + \frac{\nu^2}{8} \begin{pmatrix} W_\mu^3 & B_\mu \end{pmatrix} \begin{pmatrix} g^2 & -gg' \\ -gg' & g'^2 \end{pmatrix} \begin{pmatrix} W^{3,\mu} \\ B^\mu \end{pmatrix} + \text{H terms} \quad (2.46)$$

The charged gauge bosons  $W_\mu^\pm$  are a mixture of SU(2) states [26]

$$W_\mu^\pm = \frac{W_\mu^1 \mp iW_\mu^2}{\sqrt{2}} \quad (2.47)$$

and the  $Z_\mu$  and  $A_\mu$  are a rotation of the  $W_\mu^3$  and  $B_\mu$  [26]

$$\begin{pmatrix} Z_\mu \\ A_\mu \end{pmatrix} = \begin{pmatrix} \cos \theta_w & -\sin \theta_w \\ \sin \theta_w & \cos \theta_w \end{pmatrix} \begin{pmatrix} W_\mu^3 \\ B_\mu \end{pmatrix} \quad (2.48)$$

where  $\theta_w = \tan^{-1}(\frac{g'}{g})$  is the Weinberg mixing angle.

Substituting eqn. 2.47 and 2.48 in eqn. 2.46, gives mass terms for gauge bosons:

$$\begin{aligned}
M_Z &= \frac{\nu}{2} \sqrt{g^2 + g'^2}, \\
M_W &= \frac{g\nu}{2}, M_\gamma = 0
\end{aligned}
\tag{2.49}$$

The excitations along the three degrees of freedom that are taken zero in the Higgs field correspond to three massless bosons (the Goldstone bosons). It can thus be said that the three massless gauge bosons “ate” the three massless Goldstone bosons to become massive bosons and gained longitudinal polarization states. The perturbation along the remaining degree of freedom is considered as a massive particles (the Higgs boson).

The measured masses of  $M_Z$  and  $M_W$  are [28]:

$$M_Z = 91.1875 \pm 0.0021 \text{ GeV}/c^2, \quad M_W = 80.398 \pm 0.025 \text{ GeV}/c^2 \tag{2.50}$$

From these experimental values, the electroweak mixing angle is:

$$\sin^2 \theta_W = 0.223 \tag{2.51}$$

The mass of the Higgs can be calculated from the Higgs potential:

$$V(\phi) = \frac{\mu^2}{2} \begin{pmatrix} 0 & \nu + H \end{pmatrix} \begin{pmatrix} 0 \\ \nu + H \end{pmatrix} + \frac{\lambda}{4} \left| \begin{pmatrix} 0 & \nu + H \end{pmatrix} \begin{pmatrix} 0 \\ \nu + H \end{pmatrix} \right|^2 = \lambda\nu^2 H^2 + \dots
\tag{2.52}$$

which gives  $m_H = \sqrt{2\lambda\nu}$ . The Higgs mass depends on two parameters:  $\lambda$  and  $\nu$ . The value of  $\nu$  can be related to the fermi constant  $G_F$ :

$$\nu = \frac{1}{\sqrt{\sqrt{2}G_F}} \sim 246 \text{ GeV} \tag{2.53}$$

with  $G_F = (1.166371 \pm 0.000006) \times 10^{-5} \text{ GeV}^{-2}$  [26]. The free parameter  $\lambda$  sets the value of the Higgs boson mass that can not be constrained theoretically.

Lastly, the Yukawa interaction part of the Higgs lagrangian yields the masses of fermions. From equation 2.42, splitting the lagrangian for leptons and quarks and solving the leptonic part for electron (the quark part follows the similar procedure):

$$\mathcal{L}_{\text{Yuk}} = - [\bar{l}_L g_e \phi l_R + h.c.] + \mathcal{L}_{\text{Yuk}}(q) \quad (2.54)$$

$$\mathcal{L}_{\text{Yuk}}(l) = -g_e \begin{pmatrix} \bar{\psi}_{\nu,L} & \bar{\psi}_{e,L} \end{pmatrix} \begin{pmatrix} 0 \\ \frac{\nu+H}{\sqrt{2}} \end{pmatrix} (\psi_{e,R}) + h.c. = -\frac{g_e \nu}{\sqrt{2}} \bar{\psi}_e \psi_e - \frac{g_e}{\sqrt{2}} \bar{\psi}_e \psi_e h \quad (2.55)$$

Which leads to the electron mass  $m_e = -\frac{g_e \nu}{\sqrt{2}}$ . While the Higgs mechanism can also give masses to neutrinos it is not the only possible mechanism for neutrino masses.

The Higgs coupling to fermions and the gauge bosons can also be calculated by considering only terms proportional to  $\bar{\psi}_f \psi_f H$  and  $V^\mu V_\mu H$  respectively, where  $V_\mu$  are the gauge fields of electroweak theory. For the Higgs self coupling calculations, terms proportional to  $H^3$  and  $H^4$  are considered.

## 2.4 Higgs Discovery at the LHC

In 2012, both ATLAS and CMS presented evidence for the discovery of a new particle consistent with the Standard Model Higgs boson. In ATLAS experiment, these searches for the Higgs boson were performed in  $H \rightarrow \gamma\gamma$ ,  $H \rightarrow ZZ^* \rightarrow 4l$ ,  $H \rightarrow WW^* \rightarrow e\nu\mu\nu$  channels based on an integrated luminosity of 5.8-5.9  $\text{fb}^{-1}$  of  $pp$  collision data recorded between April and June 2012 at a centre-of-mass energy of 8 TeV. These results were combined with the earlier results of searches in  $H \rightarrow WW$ ,  $H \rightarrow ZZ$ ,  $H \rightarrow b\bar{b}$  and  $H \rightarrow \tau^+\tau^-$  using 4.6-4.8  $\text{fb}^{-1}$  of 2011  $pp$  collision data at a centre-of-mass energy of 7 TeV [29]. The Higgs boson production processes considered in Run-1 were gluon fusion ( $gg \rightarrow H$ ), vector-boson fusion ( $qq \rightarrow qqH$ ) and the associated production with vector bosons ( $qq \rightarrow WH, ZH$ ). A small contribution from the associated production with a pair of top quarks was also considered only in  $H \rightarrow \gamma\gamma$  analysis. The results and measurements excluded a mass range of 111-559  $\text{GeV}/c^2$  with 95% confidence level except for masses in the range 122-131  $\text{GeV}/c^2$  in which an excess of events was observed.

The results showed a  $5.9\sigma$  excess in the  $H \rightarrow \gamma\gamma$ ,  $H \rightarrow ZZ^* \rightarrow 4l$ ,  $H \rightarrow WW^* \rightarrow e\nu\mu\nu$  channels which exceeds the  $5\sigma$  limit to claim a discovery. The ATLAS collaboration published the best estimate of the Higgs boson mass of [29]:

$$m_H = 126.0 \pm 0.4(\text{stat}) \pm 0.4(\text{sys.}) \text{ GeV}/c^2 \quad (2.56)$$

No excess was observed in  $H \rightarrow \tau^+\tau^-$  and  $H \rightarrow b\bar{b}$  with 2011 and early 2012 data. The results were later updated to full 2012 dataset which consisted of an integrated luminosity of  $20.7 \text{ fb}^{-1}$  at a centre-of-mass energy of 8 TeV. The results for  $H \rightarrow \tau^+\tau^-$  searches considered all combinations of hadronic and leptonic tau decays. An excess of events over the expected background was found with a significance of  $4.5\sigma$  [20]. This provided evidence for the direct coupling of the recently discovered Higgs boson to fermions.

The observed probability at the ATLAS experiment as a function of the Higgs boson mass is shown in the figure 2.8.

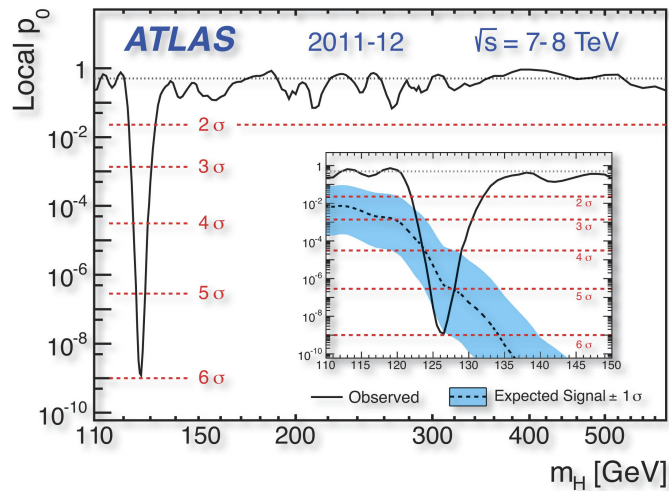


Fig. 2.8: The observed local  $p_0$ -value, the probability of background to produce a signal-like excess, as a function of the Higgs mass,  $m_H$ . [30]

In CMS, the Higgs searches were performed in its five decay channels:  $H \rightarrow \gamma\gamma$ ,  $WW$ ,  $ZZ$ ,  $\tau^+\tau^-$  and  $b\bar{b}$  using data recorded at the centre-of-mass energy of 7 and 8 TeV. The best estimate of the Higgs mass from the CMS collaboration is [31]:

$$m_H = 125.7 \pm 0.3(\text{stat.}) \pm 0.3(\text{syst.}) \text{ GeV}/c^2 \quad (2.57)$$

The combined data samples of the ATLAS and CMS are used for the measurement of Higgs boson mass in  $H \rightarrow \gamma\gamma$  and  $H \rightarrow ZZ \rightarrow 4l$  channels. The combined Higgs boson mass from both experiments is [32]:

$$m_H = 125.09 \pm 0.21(\text{stat.}) \pm 0.11(\text{syst.}) \text{ GeV}/c^2 \quad (2.58)$$

The discovered boson decays into two photons so it can not be a spin-1 particle as stated by the Landau-Yang-Theorem [33]. The studies of spin (J) and parity (P) quantum number of the Higgs boson have been made using statistical distributions of the decay products ( $WW^* \rightarrow e\nu\mu\nu$ ,  $ZZ^* \rightarrow 4l$ ). Details of the study can be found in [6, 7]. The results favour  $J^P = 0^+$  of the new boson which is consistent with the Standard Model predictions of the  $J^P$  of the Higgs boson.

## 2.5 Problems in the Standard Model

The Standard Model of particle physics provides successful description of presently known phenomena. Although no hints of any significant structure different from the Standard Model are seen at the Large Hadron Collider with 8 TeV energy, there exist support for theories beyond the Standard Model due to some open questions it fails to answer such as the existence of dark matter, neutrino oscillations, matter-antimatter asymmetry etc. These unanswered issues keep particle physicists busy in looking beyond the Standard Model.

The main problems in the Standard Model are discussed in the following sections:

### 2.5.1 The Hierarchy Problem

The hierarchy problem refers to the radiative corrections to Higgs mass that bring a divergence into the calculations. The mass of Higgs gets a correction from both fermion and vector boson loops as it couples with both. If the SM holds to high energies, these

corrections lead to unnatural and very large corrections. Since fundamental particles obtain mass through the Higgs field, this problem is indirectly related to other fundamental particles as well.



Fig. 2.9: Feynman diagram for the Higgs boson quadratic mass corrections with a single fermion loop (a) and for a single scalar boson loop (b)

The correction to the Higgs mass  $m_H^2$  from a loop containing Dirac fermions (figure 2.9 (a)) leads to a correction [12]:

$$\Delta m_H^2 = -\frac{|\lambda_f|^2}{8\pi^2} \Lambda_{UV}^2 + \dots \quad (2.59)$$

here  $\lambda_f$  is the dimensionless coupling to fermion and  $\Lambda_{UV}$  is the ultraviolet momentum cut-off parameter used to regulate the loop integral.

The corrections to the Higgs mass from a loop containing a scalar S (figure 2.9 (b)) gives [12]:

$$\Delta m_H^2 = \frac{|\lambda_S|}{16\pi^2} (\Lambda_{UV}^2 - 2m_S^2 \ln(\Lambda_{UV}/m_S) + \dots) \quad (2.60)$$

here  $\lambda_S$  is the dimensionless coupling to scalar and  $m_S$  is mass of the scalar.  $\Lambda$  is of the order of GUT (or Planck) scale (the scale where new physics must appear) where as the scale of electroweak energy is about 100 GeV.

Supersymmetry provides a possible solution to this problem which is summarized in section 2.6.3.

## 2.5.2 Dark Matter

In 1933, a swiss astronomer Fritz Zwicky measured the mass of a galactic cluster using the speed of the galaxies. He applied the virial theorem [34] which relates the velocity

of orbiting objects to the amount of gravitational force acting on them. Isaac Newton's theory tells us that gravitational force is proportional to the masses of the objects involved, so Zwicky was able to calculate the total mass of a galactic cluster from his measured galactic velocities. He then compared the results with the mass calculated from the light the galaxies shed. He realised that there was far more mass than what was visible. This unknown matter generated gravitational field without emitting light and so was named dark matter. This observation was later backed up by the rotation curves of spinning galaxies which plot the measured speed of visible stars in that galaxy versus their radial distance from the centre of that galaxy. The rotation curve of stars in spinning galaxies were in contradiction with the curve obtained through Newton's law. This was as if stars were not rotating around the visible mass but around many unknown centres, all providing additional gravitational attraction. Other evidence for dark matter is gravitational lensing<sup>2</sup> and the cosmic microwave background (CMB)<sup>3</sup>. It is now believed that roughly 27% of the universe is made up of dark matter while baryonic matter accounts for only 5% [9].

Dark matter does not interact electromagnetically. It reveals its presence through gravitational effects. If dark matter also interacts weakly, it would likely be composed of weakly interacting massive particles (WIMPs) and the Standard Model does not include any matter compatible astronomical observations.

## 2.6 Supersymmetry (SUSY)

SUSY is a symmetry between bosons and fermions. A SUSY transformation turns a fermionic state into a bosonic state and vice versa. The transformation operator  $Q$ , an anti-commuting operator, is a complex spinor such that:

---

<sup>2</sup>In an empty space, the light moves in a straight path whereas in the presence of massive object, light bends when passing a massive object and follows the curvature. Gravitational lensing refers to bending of light from the source as it travels towards the observer. This provides strong evidence of the presence of dark matter and produces the maps of dark matter distribution in the universe.

<sup>3</sup>CMB is referred as the oldest light in our universe that is left over from the time of recombination in Big Bang cosmology. Scientists can tell how much dark matter exist by studying the CMB.

$$\begin{aligned}
Q | \text{Boson} \rangle &= | \text{Fermion} \rangle \\
Q | \text{Fermion} \rangle &= | \text{Boson} \rangle
\end{aligned}
\tag{2.61}$$

$Q^\dagger$  is also a symmetry operator. Both  $Q$  and  $Q^\dagger$  carry spin angular momentum 1/2. Therefore, SUSY is a spacetime symmetry.

The Minimal Supersymmetric Standard Model (MSSM) is a minimal extension to the Standard Model that realizes Supersymmetry. It is minimal in the sense that it includes minimum number of new particle states for a consistent theory.

### 2.6.1 Chiral and Gauge Supermultiplets

Supermultiplets are the single-particle states of a supersymmetric theory. Each supermultiplet contains both the boson and the fermion states that are the superpartner of each other. Two categories of the supermultiplets exist: the chiral supermultiplets and the gauge supermultiplets. The chiral supermultiplets contain those particles whose left-handed parts transform differently under the gauge group than their right-handed parts. All SM fermions have this property so they are members of chiral supermultiplets. Their spin-0 superpartners (called sfermions: squark ( $\tilde{q}$ ) and slepton ( $\tilde{l}$ )) ('s' prefix before the name and tilde ( $\sim$ ) on the symbol) are also included in the chiral supermultiplets. The chiral supermultiplets in the SUSY are given in the table 2.1 [12]:

Particles	Spin-0	Spin-1/2
squarks, quarks ( $\times 3$ families)	$\tilde{u}, \tilde{d}$ $(\tilde{u}_L, \tilde{d}_L), (\tilde{u}_R, \tilde{d}_R)$	$u, d$ $(u_L, d_L), (u_R, d_R)$
sleptons, leptons ( $\times 3$ families)	$\tilde{e}, \tilde{\nu}$ $(\tilde{e}_L, \tilde{\nu}_L), \tilde{e}_R$	$e, \nu$ $(e_L, \nu_L), e_R$
Higgs, Higgsinos	$H_u = (H_u^+, H_u^0)$ $H_d = (H_d^0, H_d^-)$	$\tilde{H}_u = (\tilde{H}_u^+, \tilde{H}_u^0)$ $\tilde{H}_d = (\tilde{H}_d^0, \tilde{H}_d^-)$

Table 2.1: Chiral supermultiplets in the Minimal Supersymmetric Standard Model.

The Higgs scalar boson also resides in the chiral supermultiplet. It turns out that one chiral supermultiplet for Higgs is not enough. One reason is that if we have one chiral

supermultiplet, the electroweak gauge symmetry will suffer a gauge anomaly and would be inconsistent as a quantum theory. This gauge anomaly can be canceled by considering two Higgs supermultiplets. Another reason is that the fermionic superpartner of the Higgs chiral supermultiplets have weak hypercharge  $Y = \pm 1/2$ . From the structure of supersymmetric theories, only a  $Y = 1/2$  Higgs chiral supermultiplet can have Yukawa coupling to up-type quarks (up, charm, top) and only a  $Y = -1/2$  Higgs chiral supermultiplet can have Yukawa coupling to down-type quarks (down, strange, bottom) plus to the charged leptons (electron, muon, tau). Therefore, two Higgs chiral supermultiplets ( $H_u$  and  $H_d$ ) are needed. The fermionic partner of these are called Higgsinos ( $\tilde{H}_u$  and  $\tilde{H}_d$ ).

The gauge bosons of the Standard Model and their fermionic superpartners (called gauginos) must reside in the gauge supermultiplets. The gauge supermultiplets are given in the table 2.2 [12]:

Particles	Spin-1/2	Spin-1
gluino, gluon	$\tilde{g}$	$g$
winos, W bosons	$\tilde{W}^\pm, \tilde{W}^0$	$W^\pm, W^0$
Bino, B boson	$\tilde{B}^0$	$B^0$

Table 2.2: Gauge supermultiplets in the Minimal Supersymmetric Standard Model.

After the electroweak symmetry breaking, the neutral gauge bosons ( $W^0$  and  $B^0$ ) of the electroweak gauge symmetry mix to give mass eigenstates  $Z^0$  and  $\gamma$ . Their respective superpartners, zino and photino, are obtained from the gauge mixtures of  $\tilde{W}^0$  and  $\tilde{B}^0$ . In addition, gauge mixing of neutral Higgsinos with  $\tilde{W}^0$  and  $\tilde{B}^0$  give four neutral states called neutralinos, often labelled as  $\tilde{X}_1^0, \tilde{X}_2^0, \tilde{X}_3^0$  and  $\tilde{X}_4^0$ .

The chiral and gauge supermultiplets make the particle content of the Minimal Supersymmetric Standard Model.

## 2.6.2 SUSY Breaking

If SUSY is unbroken, the masses of superpartners will be exactly the same as their corresponding SM partner (e.g. the mass of selectron will be  $0.511 \text{ MeV}/c^2$ ) and therefore

they would have been detected easily a long time ago. As superpartners of the Standard Model have not been discovered yet, this clearly implies that SUSY is a broken symmetry in the vacuum state chosen by nature. Additionally, it must be broken in such a way that the masses of superpartners are larger than the corresponding Standard Model particles. The masses of superpartners must not be very high otherwise we would lose our successful solution to the Hierarchy Problem. The masses of few lightest superpartners should be  $\lesssim 1\text{TeV}/c^2$  in order for MSSM scalar potential give a Higgs vacuum expectation value that results in the known masses of W and Z bosons from the Standard Model [12] without fine tuning. We consider “soft” supersymmetry breaking. With soft susy breaking (SSB) mechanism one can avoid further fine tuning of the Higgs mass. In soft SUSY breaking, divergent SUSY breaking terms must not rise stronger than logarithmically. As a consequence, 105 new parameters, in addition to the existing Standard Model parameters, must be introduced into the theory. These are necessary because the exact symmetry breaking mechanism is not known.

### 2.6.3 Motivations for Supersymmetry

The motivation for SUSY is the Hierarchy Problem which is solved by SUSY. It also provides a possible candidate for the dark matter and leads to the gauge coupling unification. These motivations are the primary reasons why SUSY is the most favoured candidate of a new theory to be discovered at the Large Hadron Collider. These motivations for SUSY are discussed below.

The original motivation for Supersymmetry is the infamous ‘Hierarchy Problem’. SUSY could be a solution to this problem. As stated before, SUSY relates fermions with bosons and vice versa. SUSY stabilizes the hierarchy problem in such a way that the radiative corrections to Higgs mass are cancelled by the terms correspond to the superpartners and they do not drag  $m_H$  upto a high scale  $\Lambda_{UV}$  (figure 2.9). This cancellation is natural if SUSY is visible at a scale not much greater than the order of a few TeV. Although the divergent terms in the quantum correction to Higgs mass are cancelled by the corresponding superpartner, a small correction remains being at the order of the electroweak mass scale due to difference in the masses of the SM and the SUSY particles.

SUSY phenomenology depends on whether R-parity is conserved or violated. R-parity is defined as:

$$P_R = (-1)^{3(B-L)+2s} \quad (2.62)$$

where  $s$  is spin,  $B$  and  $L$  are the Baryon and Lepton number of the particle respectively. All the Standard Model particles have even R-parity ( $P_R = +1$ ) while all the SUSY particles have odd R-parity ( $P_R = -1$ ).

If R-parity is conserved, SUSY particles, which have odd R-parity, are produced in pairs and the decays of each SUSY particle must involve an odd number of lighter SUSY particles. The lightest SUSY particle (LSP) can not decay into anything and remains stable. A decay of the LSP to SM particles would not conserve R-parity and is therefore forbidden. If R-parity is conserved, possible candidates for dark matter are the lightest sneutrino, the lightest neutralino and the gravitino [12].

An interesting side effect of SUSY is the unification of fundamental coupling constants at the Grand Unified Theory (GUT) scale independent of parameter. In the Standard Model, this is not the case (figure 2.10).

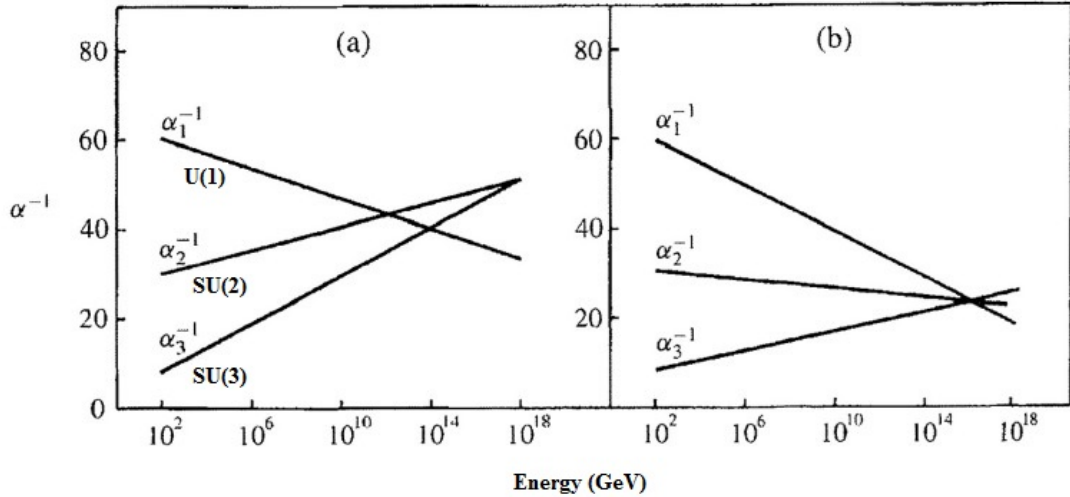


Fig. 2.10: Convergence of coupling constants  $\alpha$  at GUT scale a) in SM b) in MSSM

## 2.7 Higgs Sector in the MSSM

In the minimal extension of the Standard Model at least two Higgs doublets are required to provide coupling to both up-like and down-like fermions. Therefore the Higgs sector in the MSSM is described with a 2 Higgs Doublet Model (2HDM). The two Higgs fields in MSSM are:

$$\begin{aligned} H_u &= \begin{pmatrix} H_u^+ \\ H_u^0 \end{pmatrix} \quad (Y = +1/2) \\ H_d &= \begin{pmatrix} H_d^0 \\ H_d^- \end{pmatrix} \quad (Y = -1/2) \end{aligned} \tag{2.63}$$

The  $H_u$  couples with up-type fermions while  $H_d$  couples with the down-type fermions. When the Higgs potential is minimized, the Higgs doublets acquire the vacuum expectation value:

$$\begin{aligned} \langle H_u \rangle &= \frac{1}{\sqrt{2}} \begin{pmatrix} 0 \\ \nu_u \end{pmatrix} \\ \langle H_d \rangle &= \frac{1}{\sqrt{2}} \begin{pmatrix} \nu_d \\ 0 \end{pmatrix} \end{aligned} \tag{2.64}$$

where the vacuum expectation values add up quadratically to the SM value, that is:  $\sqrt{\nu_u^2 + \nu_d^2} = \nu \sim 246$  GeV. These nonzero vacuum expectation values (VEVs) of the Higgs doublets give masses to particles in the MSSM. The vacuum expectation values of the Higgs doublets are related to the known mass of the Z boson and the electroweak gauge coupling.

The two complex Higgs doublets have eight degrees of freedom. Three degrees of freedom become the polarization states of the  $W^\pm$  and Z bosons while the remaining five yield the physical Higgs bosons: two CP even neutral scalars ( $h$ ,  $H$ ), one CP odd neutral scalar ( $A$ ), and a charge +1 scalar ( $H^+$ ) and its conjugate charge -1 scalar ( $H^-$ ).

The SUSY breaking calculations (for details see [13]) lead to the following relations:

$$M_{H^\pm}^2 = M_A^2 + M_W^2 \quad (2.65)$$

$$M_{H,h}^2 = \frac{1}{2}(M_A^2 + M_Z^2 \pm \sqrt{(M_A^2 + M_Z^2)^2 - 4M_Z^2 M_A^2 \cos^2(2\beta)}) \quad (2.66)$$

Equation 2.65 and 2.66 implies that:

- $M_h < \min(M_Z, M_A) < M_H$ . This means the mass of the lightest Higgs of the MSSM has mass less than mass of the Z boson. This is ruled out after the discovery of the Higgs boson at 125 GeV/c<sup>2</sup> but the relation holds at the tree level.  $M_h$  gets radiative corrections mainly from the top and stop loop corrections which push the upper bound to  $M_h < 140$  GeV/c<sup>2</sup> [36].
- $M_{H^\pm} > M_W$ .
- If  $M_A \gg M_Z$ ,  $M_H^2 = M_A^2 + M_Z^2 \sin^2(2\beta)$  so  $m_A$  and  $m_H$  are almost degenerate in mass (as they differ by a factor of  $(\frac{m_z}{m_A} \sin(2\beta))^2 \approx 1.5 \times 10^{-2}$  for  $\tan\beta=10$  and  $m_A = 150$  GeV/c<sup>2</sup>) and thus would be hard to distinguish in detectors.
- Masses of charged Higgs bosons depend on  $M_A$  and  $M_W$  where as the masses of neutral Higgs bosons depend on  $M_A$ ,  $\tan\beta$  and  $M_Z$ . Therefore, all the Higgs sector parameters at tree level are determined by just two unknown parameters:  $\tan\beta$  and  $M_A$ , where  $\tan\beta = \frac{\nu_u}{\nu_d}$ .

The Higgs masses as well as their coupling to fermions and gauge bosons get large radiative corrections. These radiative correction mainly arise from the top/stop sector. For large values of  $\tan\beta$ , radiative corrections also arise from bottom/sbottom and tau/stau sector. Once radiative corrections are taken in to account, the Higgs sector of MSSM gets sensitive to more soft SUSY breaking parameters.

### 2.7.1 SUSY Benchmark Scenarios

Experimentally, it is difficult to deal with 105 free parameters. However, they can be reduced to 22 by imposing well motivated constraints such as requiring that the SUSY

breaking parameters do not introduce new sources of CP-violation, no flavour changing neutral currents, and the first and second generation universality. This formulation of MSSM that has 22 parameters is called “phenomenological MSSM (pMSSM)” [38]. The 22 parameters of pMSSM are:

- $\tan \beta$  : the ratio of the vacuum expectation values of the two Higgs doublets
- $M_H, M_A$  : the mass of the CP even and odd Higgs boson
- $M_1, M_2, M_3$  : the bino, wino, and gluino mass parameters
- $m_{\tilde{q}}, m_{\tilde{u}_R}, m_{\tilde{d}_R}, m_{\tilde{l}}, m_{\tilde{e}_R}$  : the mass parameters for the first generation of squarks and sleptons
- $A_u, A_d, A_e$  : the trilinear couplings of the first generation of squarks and sleptons
- $m_{\tilde{Q}}, m_{\tilde{t}_R}, m_{\tilde{b}_R}, m_{\tilde{L}}, m_{\tilde{\tau}_R}$  : the mass parameters of the third generation of squarks and sleptons
- $A_t, A_b, A_\tau$  : the trilinear couplings of the third generation of squarks and sleptons

Two additional parameters are defined that can be written in terms of the above parameters, i.e., the stop mixing parameter  $X_t = A_t - \mu \cot \beta$  (Higgsino mass parameter  $\mu$  is fixed during electroweak symmetry breaking), which gives the amount of mixing between left and right-handed stops when computing the stop mass eigenstates, and the SUSY scale  $M_S = \sqrt{m_{\tilde{t}_1, \tilde{t}_2}}$  that represent the scale where supersymmetry breaks, usually taken to be around 1 TeV to avoid imposing excessive fine tuning into the model.

SUSY benchmark scenarios are used to set the parameter values. In these scenarios, only  $M_A$  and  $\tan \beta$  are varied while other SUSY parameters are kept fixed to particular values chosen from the interpretation of the MSSM Higgs phenomenology. The most relevant scenarios to this thesis are summarized below (details are provided in [37]):

- $m_h^{max}$ : In this scenario, the stop mixing parameter  $X_t$  is chosen such as to maximize the mass of the lightest MSSM Higgs, h, yielding  $m_h \sim 135$  GeV/c<sup>2</sup> for high values of  $\tan \beta$  and  $M_S \sim 2$  TeV/c<sup>2</sup>. After the discovery of Higgs boson with mass of

about  $125.5 \text{ GeV}/c^2$ , the predicted values of  $m_h$  are incompatible for the majority of the parameter space. In spite of that,  $m_h^{max}$  scenario has been studied and remains as a reference MSSM benchmark scenario.

- $m_h^{mod}$ : After the discovery of Higgs boson with mass of about  $125.5 \text{ GeV}/c^2$ , which is compatible with the predictions of the Standard Model and the Higgs sector of Minimal Supersymmetric Standard Model (MSSM), the existing SUSY benchmark scenarios are modified in such a way that the light CP-even Higgs boson is interpreted as the LHC signal of the Higgs boson in large parts of the  $M_A - \tan \beta$  plane.  $m_h^{mod}$  is a modified form of the  $m_h^{max}$  scenario that gives a lighter  $m_h$  prediction consistent with the observed value in the large region of the parameter space available. The lower  $m_h$  values are achieved by reducing the radiative corrections to the Higgs mass from the mixing in the stop sector. The specific term whose reduction gives the lower  $m_h$  prediction is  $\frac{X_t}{M_{SUSY}}$ , which can be positive or negative thus giving two benchmarks  $m_h^{mod+}$  and  $m_h^{mod-}$ . For this thesis, the Monte Carlo simulated signal samples are generated using the benchmark scenario  $m_h^{mod+}$ . The exclusion limits on  $\tan \beta - M_{A/H}$  plan presented in chapter 7 use the cross sections and branching ratios of  $M_{A/H}$  at various values of  $\tan \beta$  that are derived using the parameter values provided by the  $m_h^{mod+}$  scenario.
- hMSSM: In this scenario, those dominant radiative corrections to the MSSM Higgs mass that introduce a dependence on SUSY parameters are traded against the observed Higgs mass of  $125 \text{ GeV}/c^2$  allowing to describe the entire Higgs sector with only two input parameters ( $m_A$  and  $\tan \beta$ ). This simple approach reopens the low  $\tan \beta$  region at the cost of considering the SUSY breaking scale high, i.e,  $M_S \gg 1 \text{ TeV}$  [39].

## 2.7.2 MSSM Higgs Production and Decay Modes

MSSM Higgs production and decay modes depend on the SUSY parameter values. The Yukawa coupling of the neutral Higgs to the fermions relative to the Standard Model are given as [41]

$$hb\bar{b} (h\tau^+\tau^-) : -\frac{\sin(\alpha)}{\cos(\beta)} = (\sin(\beta - \alpha) - \tan \beta \cos(\beta - \alpha)) \quad (2.67)$$

$$ht\bar{t} : \frac{\cos(\alpha)}{\sin(\beta)} = (\sin(\beta - \alpha) + \cot \beta \cos(\beta - \alpha)) \quad (2.68)$$

$$Hb\bar{b} (H\tau^+\tau^-) : \frac{\cos(\alpha)}{\cos(\beta)} = (\cos(\beta - \alpha) + \tan \beta \sin(\beta - \alpha)) \quad (2.69)$$

$$Ht\bar{t} : \frac{\sin(\alpha)}{\sin(\beta)} = (\cos(\beta - \alpha) - \cot \beta \sin(\beta - \alpha)) \quad (2.70)$$

$$Abb\bar{b} (A\tau^+\tau^-) : \gamma_5 \tan(\beta) \quad (2.71)$$

$$Att\bar{t} : \gamma_5 \cot(\beta) \quad (2.72)$$

where  $\alpha$  is the mixing angle between the weak and the mass eigenstates of the neutral Higgs bosons and  $\gamma_5$  ( $=i\gamma_0\gamma_1\gamma_2\gamma_3$ ) indicates a pseudoscalar coupling.

For large values of  $\tan \beta$ , Higgs coupling to b-quarks and other down type fermions is significantly enhanced with respect to the Standard Model resulting in increased branching fraction to tau leptons and b quarks. Figure 2.11 shows the branching ratios for the MSSM neutral CP-even Higgs boson (H) with low and high  $\tan \beta$  values i.e.  $\tan \beta=3$  and  $\tan \beta=30$  respectively.

In the SM, Higgs decays to ZZ, WW are important with  $m_H < 160 \text{ GeV}/c^2$ . In the MSSM, these decays are slightly suppressed for  $H^0$  and  $h^0$  and even absent for  $A^0$  (in CP conserving models), and the decays to  $\tau^+\tau^-$  are enhanced. The Higgs decay to second generation of fermions  $\mu^+\mu^-$  and third generation quarks  $b\bar{b}$  are also promising but the Higgs decay to  $b\bar{b}$  has huge QCD background therefore it is less accessible experimentally. The b-associated Higgs production (Feynman diagrams are shown in figure 2.12) is particularly enhanced for large values of  $\tan\beta$  (equations 2.67,2.69, 2.71) [41] as compared to gluon-gluon fusion production (figure 2.13) and offers improved background reduction.

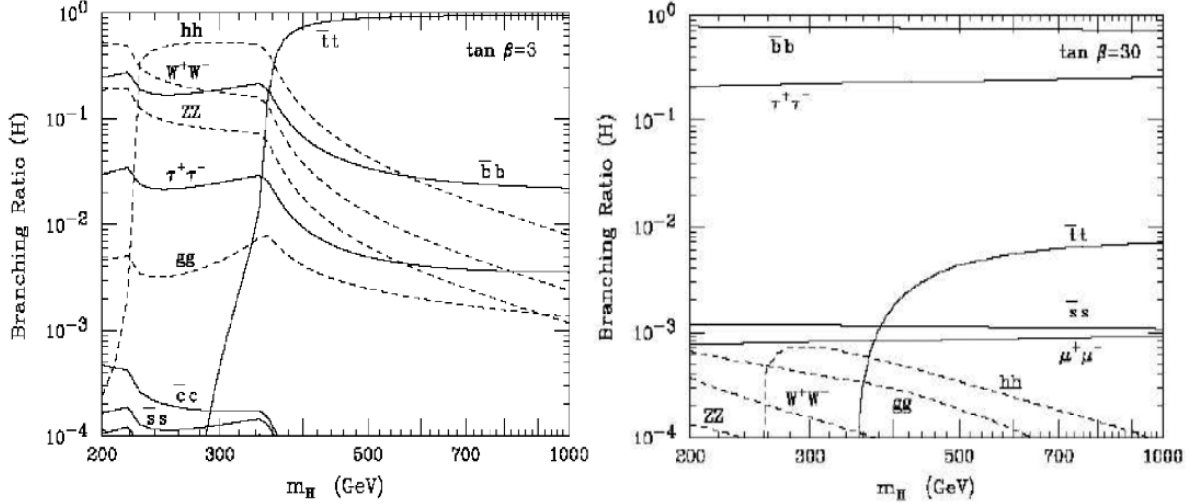


Fig. 2.11: Branching ratios for the MSSM neutral CP-even Higgs boson (H) with  $\tan\beta=3$  (left) and  $\tan\beta=30$  (right) with fixed values of other SUSY parameters [41].

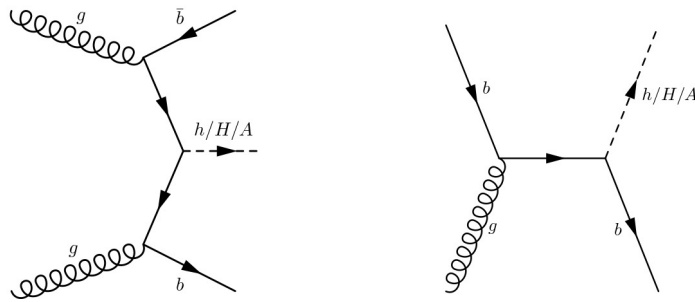


Fig. 2.12: b-associated production of a neutral MSSM Higgs boson

## 2.8 Neutral MSSM Higgs Searches at the ATLAS Experiment

At the ATLAS experiment, the most important production mode of the neutral MSSM Higgs are the b-associated production and the gluon-fusion [43]. The cross section of both processes increases with  $\tan\beta$ . The presence of b-tagged jets in the final state decreases the background. The common decay modes of the neutral Higgs are  $\phi \rightarrow b\bar{b}$  and  $\phi \rightarrow \tau^+\tau^-$  (where  $\phi = h, H, A$ ). Figure 2.14 shows common Feynman diagrams of the Higgs production and the decay modes:

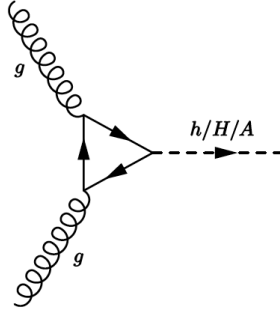


Fig. 2.13: gluon-gluon fusion production of a neutral MSSM Higgs boson

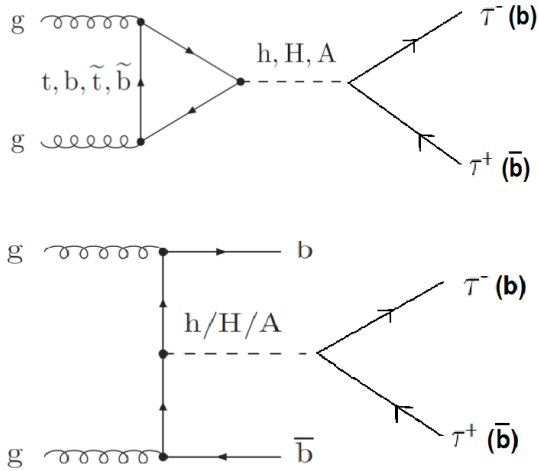


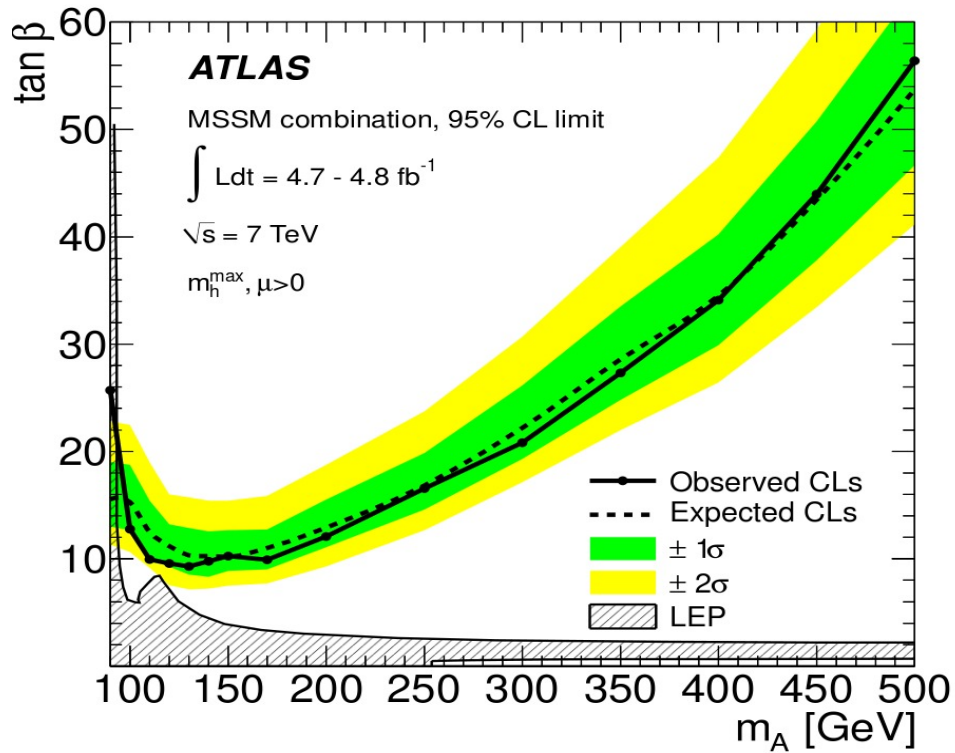
Fig. 2.14: Common Feynman diagrams for the Higgs production and the decay modes at the LHC

The searches for  $\phi \rightarrow \tau^+\tau^-$  divide the analysis into three sub-channels: the  $\tau_{lep}\tau_{lep}$  where both taus decay into leptons, the  $\tau_{lep}\tau_{had}$  in which one tau decays into leptons and the other into hadrons, and the  $\tau_{had}\tau_{had}$  where both taus are decaying into hadrons.

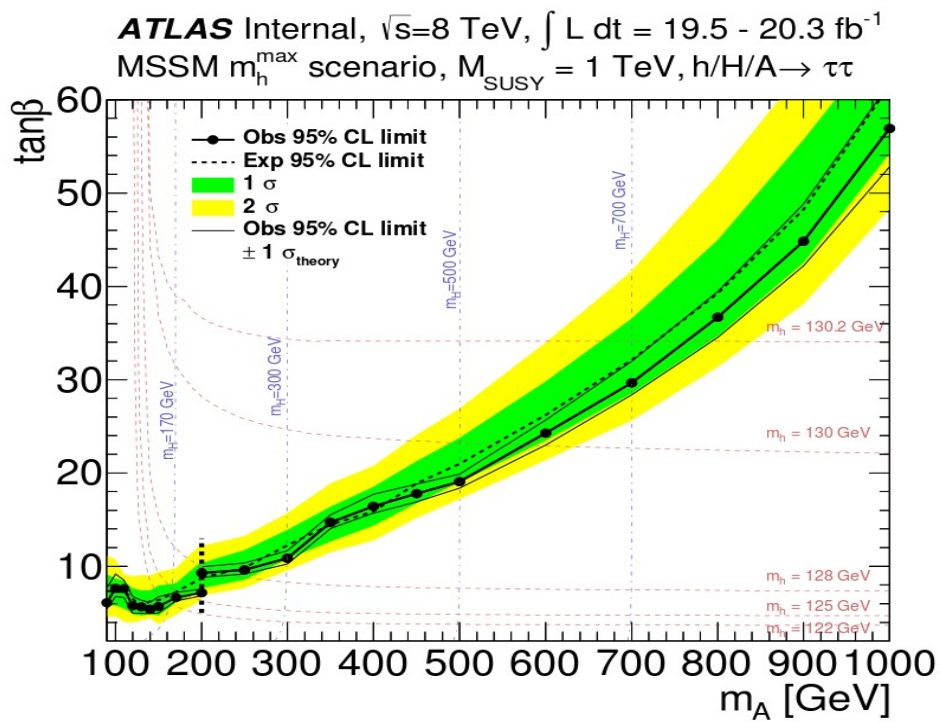
In 2011, ATLAS used  $4.7\text{-}4.8 \text{ fb}^{-1}$  of  $\sqrt{s} = 7 \text{ TeV}$  collision data to perform the analysis (for detail see [42]). In 2012, a similar analysis was made using an integrated luminosity of  $19.5\text{-}20.3 \text{ fb}^{-1}$  with  $\sqrt{s} = 8 \text{ TeV}$  data (for detail see [43]). No significant excess over the expected background was observed and the exclusion limits are derived using the modified frequentist method called  $CL_s$  [44]. The 95% confidence level exclusion limits on  $\tan \beta$  as a function of  $m_A$  provided by the search  $\phi \rightarrow \tau\tau$  in 2011 and 2012 are shown

in the figure 2.15.

In this thesis, the search for  $\phi \rightarrow \tau\tau$  will be presented with  $\sqrt{s}= 13$  TeV collision data that corresponds to an integrated luminosity of  $3.21 \text{ fb}^{-1}$ . Out of three sub-channels, the search will focus on the  $\tau_{lep}\tau_{had}$  channel with or without b-tagged jets in the final state.



(a)



(b)

Fig. 2.15: 95% confidence level exclusion limit of  $\phi \rightarrow \tau\tau$  in the  $m_A$ - $\tan \beta$  plane, in 2011 (a) [42] and 2012 search (b) [43]

---

## CHAPTER 3

# The ATLAS Experiment at the LHC

Particle accelerators are used to probe the high energy frontier and allows scientists to look beyond our current understanding of nature and search for new particles such as the Higgs boson and the superpartners of the Standard Model particles. In accelerators, particles are smashed together which creates a cascade of other particles. The identification of these particles is accomplished by the detector components and using software reconstruction techniques. The Large Hadron Collider located at the European Organization for Nuclear Research (CERN) is designed to meet the requirements of the new physics that may arise at the scale of several TeV. The ATLAS detector is one of the four major detectors at the LHC and was specifically designed with the goal of discovering the Higgs boson and studying scenarios beyond the Standard Model. The chapter introduces the accelerator complex of the LHC, summarizes the ATLAS detector and its various components and gives a brief overview of the trigger system of the ATLAS experiment.

### 3.1 The Large Hadron Collider (LHC)

The world's largest particle accelerator, the Large Hadron Collider, is situated at CERN about 100 metres beneath the border between France and Switzerland. The accelerator ring was built between 1998 and 2008. The tunnel was previously used as the Large Electron-Positron (LEP) Collider and has a circumference of 27 km.

The accelerator is designed to accelerate and collide protons and heavy ions. A series of accelerators accelerate particles to higher energies and push protons to speed near

to the speed of light. In 2012, with 8 TeV, protons acquired nearly 99.999997% of the speed of light. Each machine boosts the energy of particles before injecting into the next machine in row. The first collision in the LHC was recorded on 23<sup>rd</sup> November 2009, three days after the beams first circulated with the injection energy of 450 GeV per beam. On 30<sup>th</sup> March 2010, the first collision took place between two 3.5 TeV beams, setting a world record for the highest energy man made particle collision. By the end of 2012, the energy of each beam was 4 TeV for protons and 2.76 TeV per nucleon for lead nuclei. The LHC went into shutdown for upgrades at the end of 2012 with reopening as planned in early 2015. In Run-2, the energy of each beam reached up to 6.5 TeV giving a centre of mass energy of 13 TeV and providing a new window for potential discoveries, further studies on the Higgs boson and the unresolved mysteries such as the Dark Matter.

In the LHC, protons are obtained from hydrogen gas. An electric field is used that strips off electrons from the hydrogen atoms and leaves only protons. The journey of protons in LHC starts from a linear accelerator called LINAC2, where they accelerate up to 50 MeV. From here, they are injected into the first circular accelerator, the Proton Synchrotron Booster (PSB). In the PSB, the protons accelerate to 1.4 GeV before feeding into the Proton Synchrotron (PS). The PS raises the energy from 1.4 to 25 GeV. From the PS, these protons are injected into the Super Proton Synchrotron (SPS) that increases the energy up to 450 GeV. The beams are finally injected into the main LHC ring in bunches [45]. Figure 3.1 shows the CERN accelerator chain. In the main ring, the beams circulate in two evacuated pipes. The radio-frequency cavities generating electric field are used to accelerate the beams. Several superconducting dipole magnets operating at a temperature of 1.9 K are used to bend these beams in the circular path whereas quadrupole magnets are used to focus the beams.

### 3.1.1 The LHC Experiments

The beams collide at four distinct points along the circumference of the accelerator. At these collision points four experiments ATLAS (A Toroidal LHC ApparatuS), ALICE (A Large Ion Collider Experiment), CMS (Compact Muon Solenoid) and LHCb (LHC-beauty) are present. ATLAS and CMS are two general purpose detectors that take the advantage of high energy available at the LHC to discover high energy particles

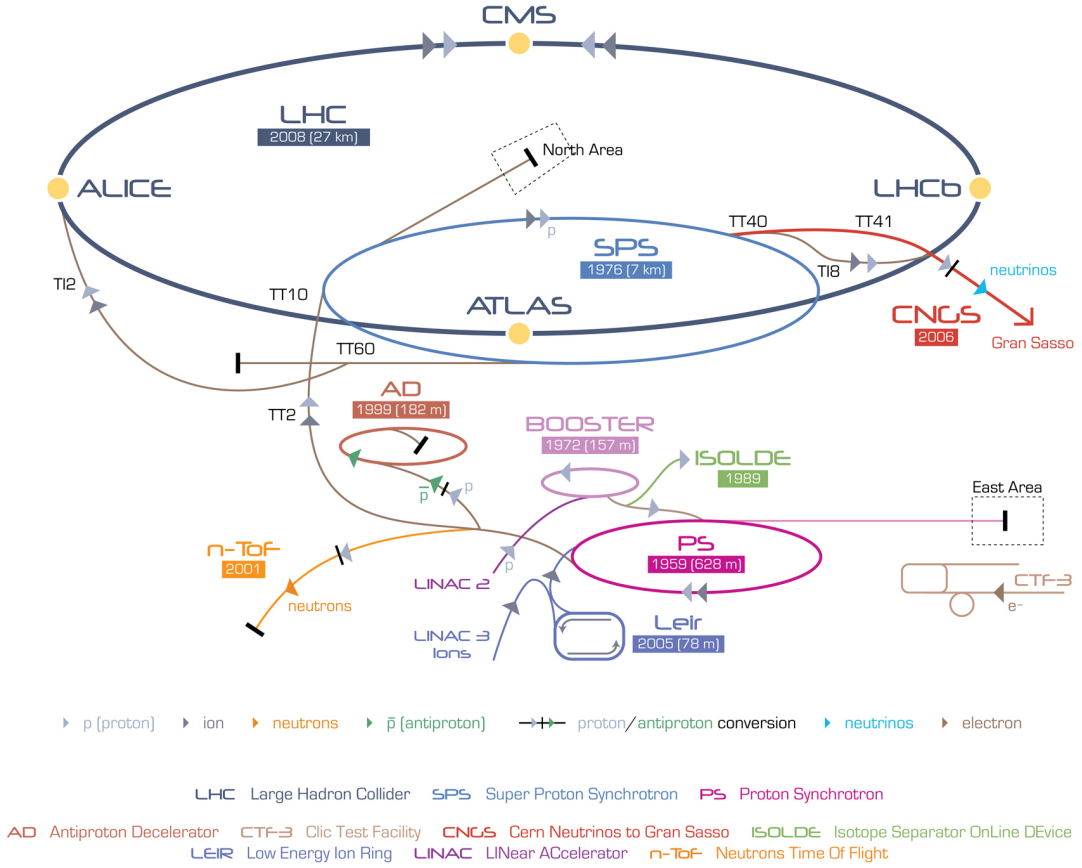


Fig. 3.1: The CERN accelerator chain [46].

which are not observable in lower energy accelerators. The main targets are the Higgs physics, beyond the Standard Model (BSM) particles and the precision measurement of Electroweak Symmetry Breaking (EWSB) [14, 48]. The ALICE experiment studies quark gluon plasma, mainly through Pb-Pb collisions [49] and the LHCb experiment is designed to investigate CP symmetry violation and the rare decays of B hadrons [50].

In addition to these four detectors, three additional smaller detectors were also built sharing interaction points with previously said detectors. The TOTEM (TOTAl Elastic and diffractive cross section Measurement) detector shares the interaction point with the CMS detector, LHCf (Large Hadron Collider forward) with ATLAS and MoEDAL (Monopole and Exotics Detector At the LHC) with the LHCb detector. The TOTEM experiment aims at measurement of total cross section, elastic scattering, and diffractive processes. The LHCf detector is designed to study the particles generated in the

“forward” region of collisions, almost directly in line with the colliding beams and the MoEDAL experiment primarily searches for the magnetic monopoles.

### 3.1.2 The LHC Beam Parameters

In Run-2, the LHC aimed at a luminosity of  $1 \times 10^{34} \text{ cm}^{-2}\text{s}^{-1}$  whereas in 2015 the peak luminosity reached upto  $5.1 \times 10^{33} \text{ cm}^{-2}\text{s}^{-1}$ . Furthermore the design specified 2,808 bunches with  $1.15 \times 10^{11}$  particles in each bunch and a 25 ns bunch spacing. The actual number of bunches in each beam in 2015 were 2,244 with almost  $1.1 \times 10^{11}$  particles in each bunch and the bunch spacing was 25 ns [51]. Due to the high luminosity of the LHC, instead of one proton interaction per bunch crossing several interactions take place. In 2015 an average of 25 interactions took place per bunch crossing. This important effect is called pileup. There are two types of pileup effects at the LHC. The in-time pileup corresponds to the multiple interactions in one bunch crossing, whereas the out-of-time pileup refers to the overlap of signals between bunch crossings [52].

The comparison of beam parameters between design, 2012 and 2015 run is made in table 3.1:

Parameters	Design	2012 Run	2015 Run
Beam Energy (TeV)	7	4	6.5
Bunch Spacing (ns)	25	50	25
Number of Bunches	2808	1374	2244
Number of Particles per bunch	$1.15 \times 10^{11}$	$1.5 \times 10^{11}$	$1.1 \times 10^{11}$
Stored Beam energy (MJ)	362	143	277
Peak Luminosity ( $\text{cm}^{-2} \text{ s}^{-1}$ )	$1 \times 10^{34}$	$7.7 \times 10^{33}$	$5.1 \times 10^{33}$

Table 3.1: The designed and the achieved LHC beam parameters in 2012 [52, 53].

## 3.2 The ATLAS Detector

The increased energy, luminosity, multiplicities and the need of precision measurements at the LHC have set new standards for detector design. The ATLAS detector is one of the two multipurpose detectors built to probe p-p and Pb-Pb collisions. It provides a

platform for the precision measurements of the Standard Model parameters and explore the physics beyond the Standard Model.

### 3.2.1 Design

The ATLAS detector is roughly cylindrical with an almost  $4\pi$  solid angle coverage. It is 44 metres long and has diameter of 25 metres making it the largest detector at the LHC. The detector weighs about 7,000 tons [14]. Figure 3.2 shows the schematic view of the ATLAS detector and its various sub-components.

### 3.2.2 Coordinate System

The ATLAS makes use of right hand coordinate system  $(x,y,z)$  with the interaction point at the origin. The beam direction defines the  $z$  axis whereas the  $(x,y)$  plane is transverse to the beam direction. The positive  $x$ -axis points from interaction point to the centre of the LHC ring and the positive  $y$ -axis points upward.  $(r,\phi)$  form the transverse plane in terms of the cylindrical coordinates where  $\phi$  is the angle around the beam axis and  $\theta$  is the angle from the beam axis. It is common practice to use pseudorapidity ( $\eta = -\ln(\tan(\frac{\theta}{2}))$ ) which is the massless limit of the rapidity  $y = \frac{1}{2} \ln \frac{(E+P_z)}{(E-P_z)}$  instead of polar angle as the particles from collisions are roughly uniformly distributed in this variable. The distance  $\Delta R$  in  $(\eta, \phi)$  plane is defined as  $\Delta R = \sqrt{(\Delta\eta)^2 + (\Delta\phi)^2}$ .

The transverse momentum  $p_T = p \sin(\theta)$ , transverse energy  $E_T = E \sin(\theta)$  and the missing  $E_T^{miss}$  in the transverse plane are taken into account for further calculations.

### 3.2.3 Components

Several layers of the ATLAS detector allow excellent particle identification. After the collision of the beams, a cascade of particles pass through the inner detector which tracks charged particles, the electromagnetic and hadronic calorimeter measure energy deposition, and finally the muon spectrometer identifies muons. Tracking detectors focus on position resolution and measuring particle momentum while calorimeters have

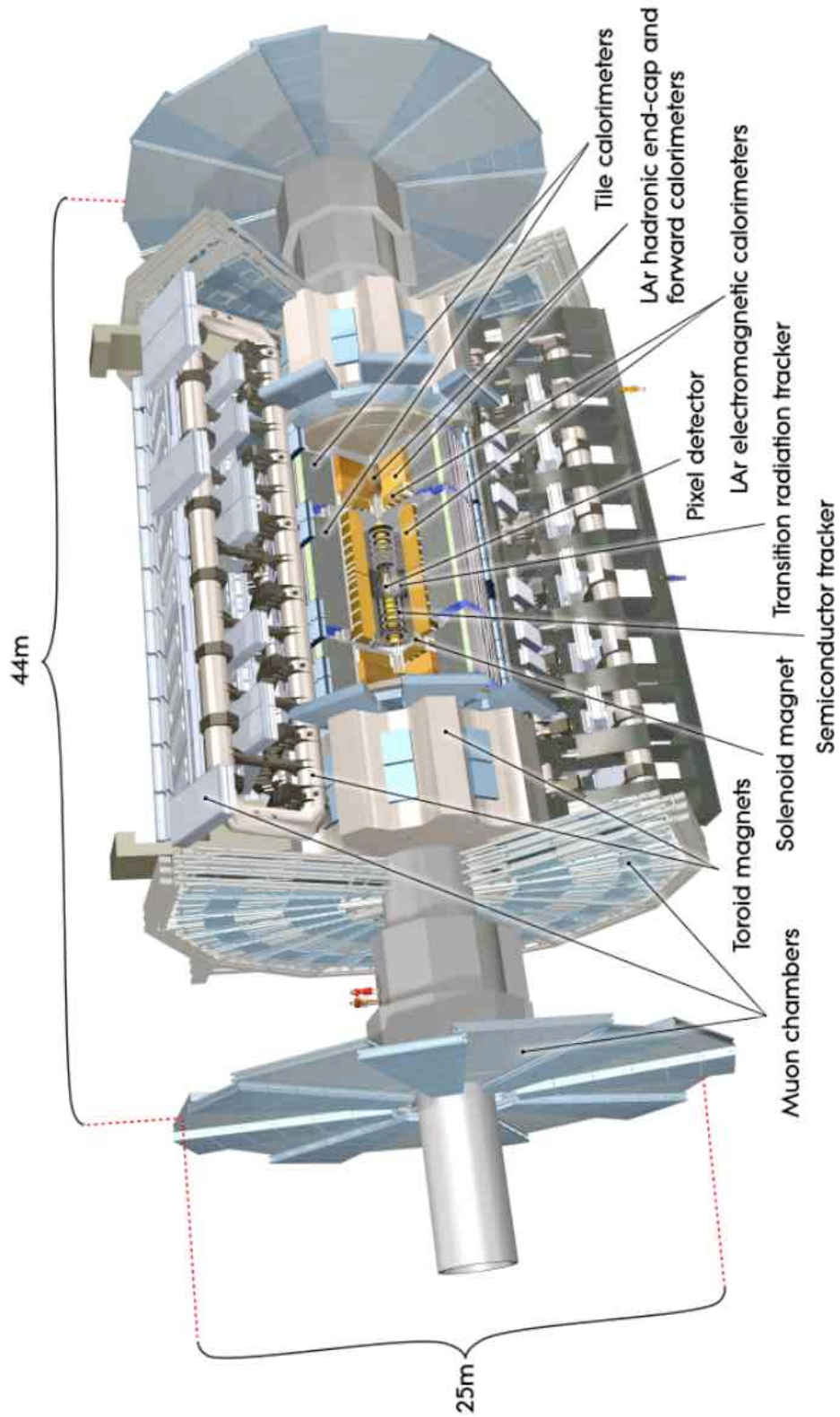


Fig. 3.2: Computer generated cut-away view of the ATLAS detector showing its various components [75].

good energy resolution. The only SM particle not detected in this detector is neutrino. It's presence is inferred by measuring the momentum imbalance among the detected particles.

A brief introduction of sub-systems of the ATLAS detector is given below:

## The Magnetic System

The ATLAS detector has two types of superconducting magnetic Systems, the solenoid system and the toroidal system [54].

A solenoid magnet located between the inner detector and the electromagnet calorimeter provides a magnetic field parallel to the beam axis. The strength of magnetic field is 2 tesla in the central region [55]. The magnetic field of the solenoid allows the inner detector to measure the momentum of the charged particles. The charged particles change their course due to the presence of a magnetic field. The curvature of their paths are used to determine the momentum of these particles via the Lorentz Force ( $\vec{F} = q(\vec{v} \times \vec{B})$ ).

The choice of the solenoid field configuration and the strength of magnetic field prevents the low energy particles from reaching the calorimeters and reduces the potential background.

Three large air-core toroidal magnets, two dedicated to the endcap and one for the barrel, lie just outside the hadronic calorimeter providing a magnetic field for the muon spectrometer. The endcap toroidal magnets are attached with the barrel magnets at each end and line up with the central solenoid. The endcap toroidal magnets consists of eight coils placed in a common cryostat [56]. The barrel toroidal magnet also consists of eight coils that are each immersed in their own cryostat [57]. The strength of the magnetic field is around 4 tesla. Similar to the solenoid magnet, it also provides a magnetic field necessary to measure the momentum of muons [14].

## The Inner Detector

The Inner Detector (ID) is used to reconstruct tracks of particles to measure their momentum and to find the location of primary and secondary vertices. It is 5.3 m long, has diameter of 2.5 m and covers  $|\eta| < 2.5$  [58]. It consists of three subsystems: the silicon pixel detector providing precision measurements of position and momentum, a microstrip Semi-Conductor Tracker (SCT) giving a good momentum resolution (equation 3.1) and a tracking resolution of the order of 10 $\mu$ m, and a Transition Radiation Tracker (TRT) for large number of tracking points ( $\sim 30$  hits/track in the barrel) to reconstruct tracks, placed in the superconducting solenoid magnet that provides a magnetic field of 2 tesla necessary to bend the charged particles.

In the presence of magnetic field parallel to z-axis, the trajectory of a charged particle forms an arc in xy plane due to the Lorentz force  $\vec{F} = q(\vec{E} + \vec{v} \times \vec{B})$ , represented by a helix. There are five measured parameters:

- $p_T$ : transverse momentum of the particle ( $p_T = p \sin \theta$ )
- $\phi$ : azimuthal angle of the track ( $\tan \phi = p_y/p_x$ )
- $d_0$ : transverse impact parameter that is defined as the distance of the closest approach of the track to the primary vertex in the transverse plane
- $\theta$ : polar angle ( $\cot \theta = p_z/p_T$ )
- $z_0$ : longitudinal impact parameter that is the z-coordinate at the point of closest approach

The interaction of particles with the components of the inner detector provides a series of discrete points which allow reconstruction of the tracks. These points help to determine if the particles are coming out of a primary collision or from the decay of very short lived particles. They also help to determine types of particles, their charge and momentum. The momentum resolution depends on the length of the reconstructed tracks, strength of the magnetic field and the momentum of particle P itself. The inner

detector provides a relative momentum resolution of [58]:

$$\frac{\sigma(p)}{p} = (4.83 \pm 0.16) \times 10^{-4} \text{GeV}^{-1} \times p_T \quad (3.1)$$

and a transverse impact parameter of  $10 \mu\text{m}$  for high momentum tracks.

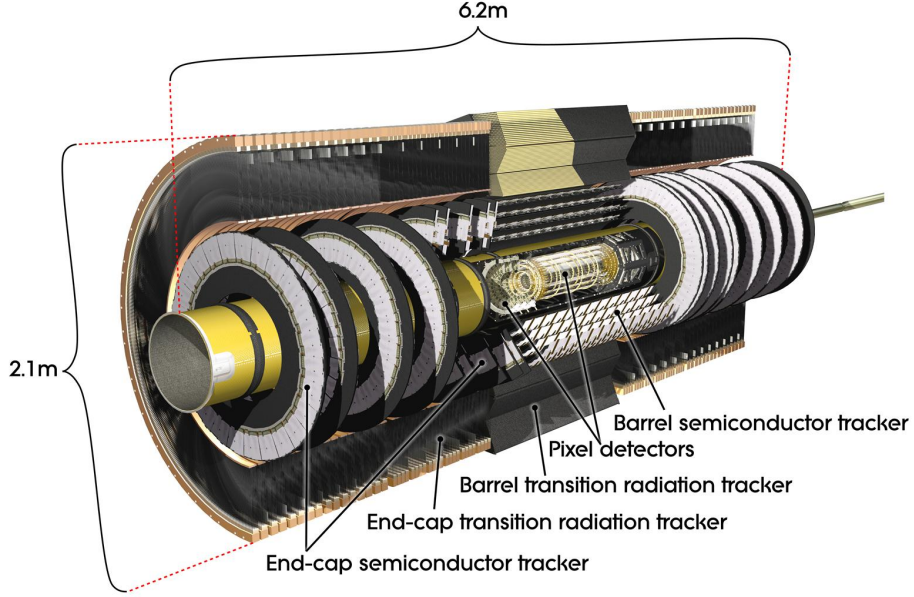


Fig. 3.3: A schematic view of the Inner Detector showing its various components [59].

The innermost tracking detector, the silicon pixel detector, is designed to provide high precision measurements, as close to the interaction point as possible, such as the ability to find the decay vertex of short lived particles like the  $b$  quarks and the tau leptons. Since the pixel detector is exposed to extreme radiation (over  $300\text{kGy}$  [61]), the material is radiation hardened. It consists of three barrel layers and two endcaps. The barrel layers are located on the concentric cylinders around the beam axis while the two endcaps are located on the disks perpendicular to the beam direction. The barrel layers are placed at  $50.5 \text{ mm}$ ,  $88.5 \text{ mm}$  and  $122.5 \text{ mm}$  away from the interaction point. Each endcap has three disc layers. The pixel layers are segmented uniformly in  $R\phi$  and  $z$ . Each track passing through three barrel layers of the pixel detector is taken into account.

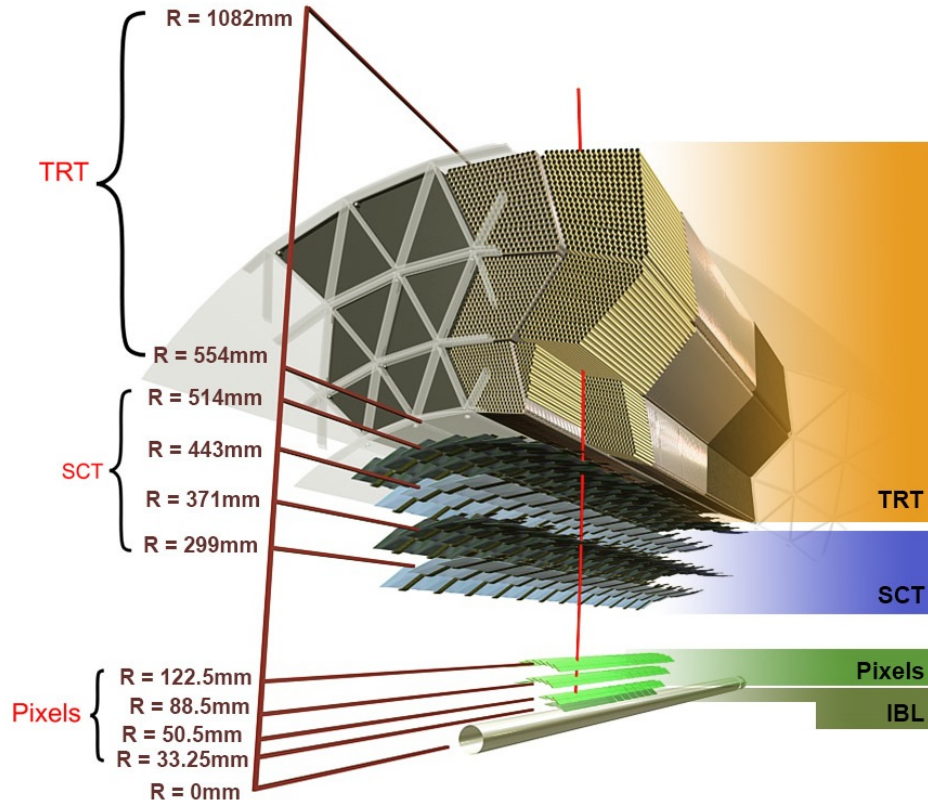


Fig. 3.4: A schematic view of the ATLAS inner detector [60].

There exist at least 80 million readout channels and approximately 1700 modules [62]. Each module is 62.4 mm long and 21.4 mm wide. Pixel modules have a resolution of 12  $\mu\text{m}$  in the  $R\phi$ -coordinate, and 110  $\mu\text{m}$  in the  $z$  coordinate [61]. These modules consist of silicon sensors. A silicon sensor acts as a diode and by applying bias voltage, the sensor forms a depletion region. As charged particles pass through the depletion region they create electron-hole pairs by ionization. As a result electrons drift to the cathode side of the sensor, where they are collected in tiny bump bonds which connect the sensor with the readout chips.

During the long shutdown-1 (LS1), one of the major upgrades for the pixel detector is the installation of a fourth layer, the Insertable B-Layer (IBL). The IBL is inserted to recover the efficiency drop and to improve the performance [62].

The second innermost detector, the Semi-Conductor Tracker, consists of 4,088 modules

of silicon strip detectors arranged in four concentric barrels (covering  $|\eta| < 1.4$ ) and two endcaps of nine disks each (covering  $1.4 < |\eta| < 2.5$ ). The four barrel layers are located at 30.0 cm, 37.3 cm, 44.7 cm and 52.0 cm from the IP. Each barrel or disk uses small-angle (40 mrad) stereo strips to measure both coordinates. One set of strips in each layer is parallel to the beam direction and measures  $R\phi$ . The stereo strips in the barrel region consist of two 6.4 cm long daisy-chained sensors with a strip pitch of  $80 \mu\text{m}$ . In the end-cap region, the SCT has a set of strips running radially and of variable pitch. The total number of readout channels in the SCT is approximately 6.3 million [14, 47]. Typically eight strip layers are crossed by each track. The spatial resolution is  $\Delta(R\phi) \times \Delta z = 16 \times 580 \mu\text{m}^2$ . The area covered by the SCT is greater than the pixel detector so it is an essential tool for momentum measurement and vertex determination.

The outermost detector, the Transition Radiation Tracker, consists of straw tubes with a 4mm diameter each, nearly 370,000 straws each with a length of 144 cm and can provide average 30 and up to 36 hits per track in the region  $|\eta| < 2.0$ . These are filled with gas mixture containing xenon ( $Xe(70\%)CO_2(27\%)O_2(3\%)$ ) [64]. A tiny gold plated tungsten wire with a diameter of  $30 \mu\text{m}$  in the centre of each straw acts as an anode for a drift-time measurement. In the barrel region, the straws are read out at both ends to minimize the down time. An average 36 hits per track are detected in the barrel region. The TRT achieves a spatial resolution of  $170 \mu\text{m}$  [14, 47, 58]. When a relativistic charged particle traverses through the boundary of two materials with different dielectric constants, the particle emits electromagnetic radiation called transition radiation (TR). This radiation is detected by the TRT in addition to the signal resulting from the charged particle tracking. The signal in the straws due to TR photons is much stronger than the one caused by the passing of charged particles. As a consequence, two independent thresholds for TR and passing particles are applied. The magnitude of TR grows with increasing velocity of the charged particles and for a fixed energy the velocity for lighter particles is higher. Therefore, the TRT allows us to distinguish between the lightest particles i.e. electrons and positrons from the heavier ones like pions and kaons.

## Calorimeters

The calorimeters are designed to measure the energy of particles. There are two types of calorimeters, the electromagnetic and the hadronic. The distinction is needed because of the different interaction behaviour between the calorimeter and electrons/photons and the calorimeter and hadrons. The electromagnetic calorimeter measures energy deposition by electrons and photons whereas the hadronic calorimeter measures energy deposition by hadrons. Hadrons can start depositing energy in the electromagnetic calorimeter therefore information from both calorimeters is used to determine energy of incident particles.

Both calorimeters provide pseudorapidity coverage up to  $|\eta| < 4.9$ . They are sampling calorimeters having absorbers and sensitive regions. When a particle hits the absorber, it interacts with the material and generates a shower. The calorimeter counts the particles of the shower that hit the sensitive region and so only a part of the energy of the shower is sampled by the calorimeter. The sampled energies are then used to calculate the full energy of the shower. A good calorimeter must have a large containment for these showers to limit the energy leakage. For this, thickness and material of the detector are important factors. Due to wide angular coverage and fine granularity, it is also possible to reconstruct missing energy from neutrinos and other non-interacting particles.

The electromagnetic calorimeter (ECAL) covering the pseudorapidity up to  $|\eta| < 3.2$  is a lead, liquid argon (LAr) sampling calorimeter with an accordion geometry [47] that provides full  $\phi$  coverage. Lead is used as an absorber while liquid argon is used to measure the energy of the shower. When electrons or photons enter the material, they mainly undergo bremsstrahlung and pair production processes. At relatively low energies, Compton scattering replaces pair production. In bremsstrahlung, electrons interact with the nuclei in the material and reduce their kinetic energy by emitting a photon. In pair production, high energy photons create particle-antiparticle pair (e.g.  $e^+e^-$ ) in the presence of a nucleus. While in Compton scattering, a photons interact with the atoms and knock out electrons. These processes keep creating new particles until there is insufficient energy left to do so. The shower deposits energy by ionization in the LAr. The deposited charge is drawn to electrodes by a high voltage field. The en-

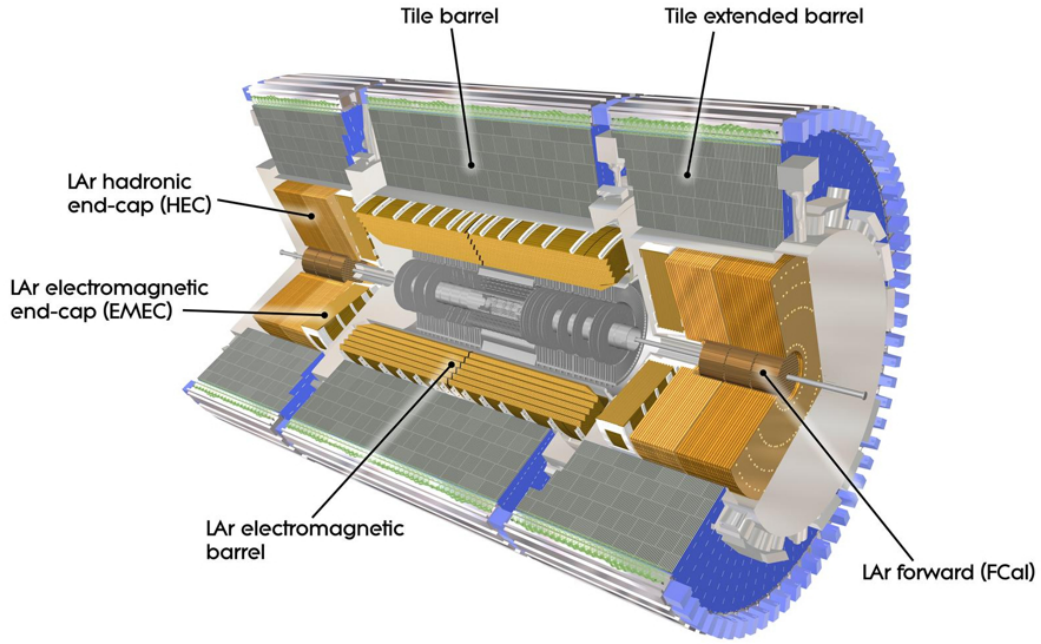


Fig. 3.5: The ATLAS calorimeter system [63].

ergy of the incoming electrons and photons is proportional the total energy of the shower.

ECAL has a barrel section with cylindrical symmetry around the beam axis with eta coverage  $|\eta| < 1.475$  and two end-caps with  $1.375 < |\eta| < 3.2$  [47]. The granularity varies with  $\eta$  and depth. The resolution in the endcap region is  $\Delta\phi \times \Delta\eta = 0.1 \times 0.1$  while in the central region  $\Delta\phi \times \Delta\eta = 0.025 \times 0.025$  is achieved. In the central region, the calorimeter has three sampling channels with varying thickness. The middle layer of the calorimeter has much fine granularity than the outer layers providing 8 times higher resolutions than the remaining layers. The thickness of the ECAL in the barrel region is  $> 24X_0$  and  $> 26X_0$  in the endcaps, where  $X_0$  is the radiation length. The particle passes through the cryostat and the soleniod before entering in the calorimeter. A presampler detector is present for  $|\eta| < 1.8$  to estimate the energy loss of the particle before entering in the calorimeter [66]. The energy resolution of EM calorimeter is [67]:

$$\frac{\sigma(E)}{E} = \frac{10\%}{\sqrt{E(\text{GeV})}} \oplus 0.7\% \quad (3.2)$$

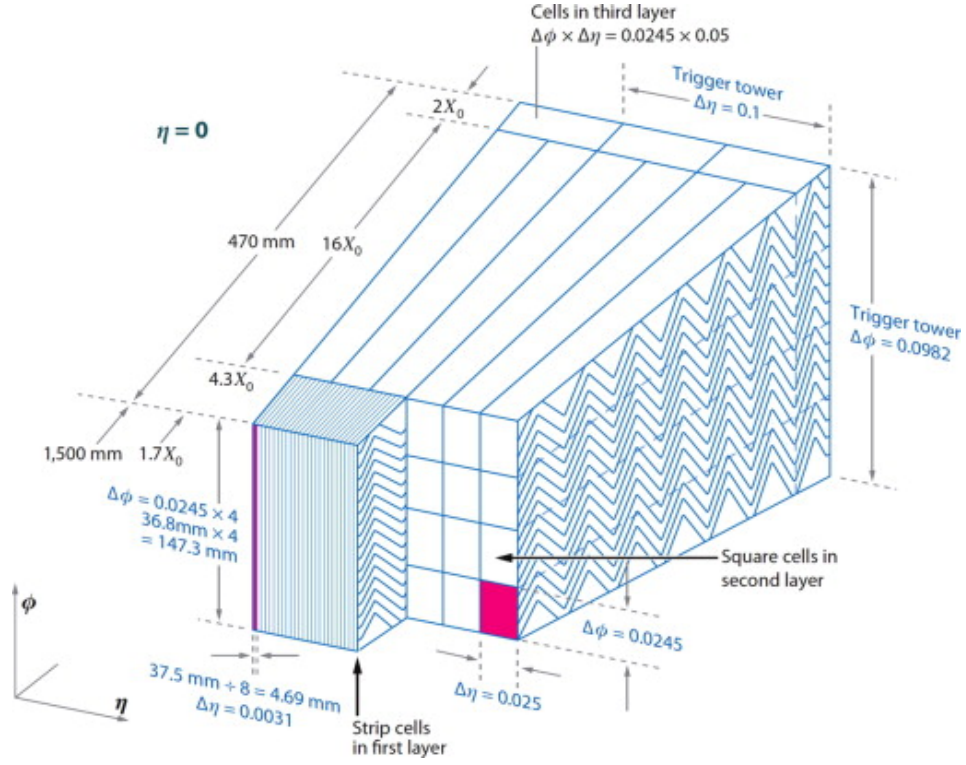


Fig. 3.6: A schematic view of the barrel accordion electromagnetic calorimeter [65].

in the barrel and endcap region.

In the hadronic calorimeter, the nature of identification is more complicated than in the ECAL due to particles interacting strongly inside the material. About half of the incident hadron energy is passed on to additional secondaries. The remainder is consumed in multiparticle production of slow particles and/or excitation of the nuclei of the detector material. The main phenomena which determine the development of the hadronic showers are: hadron production, nuclear deexcitation and the pion and the muon decays. The shower continues until the the shower energy fall below pion production threshold [124]. The hadronic calorimeter uses iron as absorber. The scintillator tiles arranged in alternating form act as the active material. Particles passing through the calorimeter initiate the shower, the scintillator material is excited by the charged particles of the shower and emits light. The light is converted into the electrical signal by photomultiplier tubes (PMTs). The hadronic endcap calorimeter covers  $1.5 < |\eta| < 3.2$ . It has a coarser granularity than the EM calorimeter, which is sufficient for the measurements of the hadronic showers. The energy resolution of HCAL is:

$$\frac{\sigma(E)}{E} = \frac{50\%}{\sqrt{E(\text{GeV})}} \oplus 3\% \quad (3.3)$$

In the very forward region, the LAr forward calorimeter (FCAL), providing pseudorapidity coverage up to  $3.1 < |\eta| < 4.9$ , is placed near the interaction point and has to withstand very high radiations. The FCAL has three layers, the first layer is for the measurements of the EM shower while the last two are for the hadronic showers. The thickness of the hadronic calorimeter at  $\eta = 0$  is about  $11 \lambda$ , where  $\lambda$  is the interaction length. This is sufficient to ensure that generally only muons pass through the hadronic calorimeter [66]. The energy resolution of FCAL is:

$$\frac{\sigma(E)}{E} = \frac{100\%}{\sqrt{E(\text{GeV})}} \oplus 10\% \quad (3.4)$$

## The Muon Spectrometer

This is the outermost detector of ATLAS detector system and covers the pseudorapidity range  $|\eta| < 2.7$ . It consists of an air-core toroidal magnet, two trigger chambers and two precision tracking chambers. The Precision tracking chambers are used to reconstruct the muon tracks. It has six layers of the Monitored Drift Tubes (MDT) (which cover  $|\eta| < 2.7$ ) and the Cathode Strip Chambers (CSC) (which cover  $2.0 < |\eta| < 2.7$ ). The MDT is made of gas ( $Ar(93\%)CO_2(7\%)$ ) filled aluminium tubes with a  $50 \mu m$  tungsten wire in its centre. The electrons produced from ionization are collected at the central wire at a potential of  $\sim 3kV$ . At the innermost plane of the endcap, the CSCs are added to the MDTs. The CSCs are the multiwire proportional chambers that have better time resolution than the MDTs and are therefore placed in the forward region ( $2.0 < |\eta| < 2.7$ ) where the background is expected to be the largest. The signals are readout using a cathode segmented into the strips [47, 68].

The toroidal magnet creates a magnetic field which deflects muons from their original course for momentum measurements. Since the precision tracking chambers require enough time to reconstruct tracks, about  $700 \mu s$ , the muon system has independent trigger chambers to generate a fast response for use in the muon trigger. These trigger chambers provide acceptance in the range  $|\eta| < 2.4$  and consist of three layers of

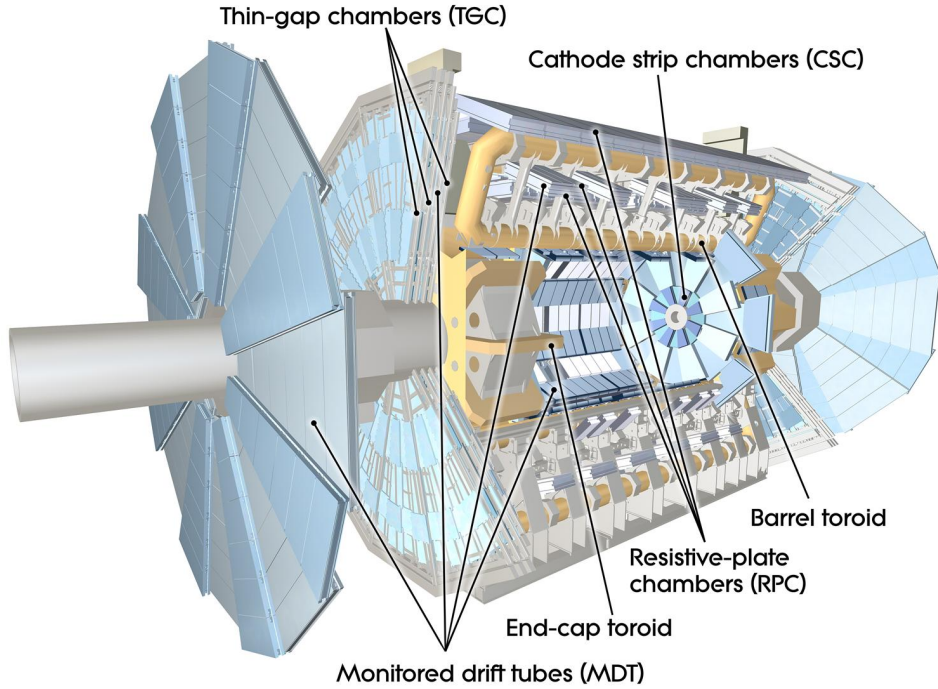


Fig. 3.7: A schematic view of the muon spectrometer [69].

Resistive Plate Chambers (RPC) in the barrel region and three layers of the Thin Gap Chambers (TGC) at the endcap region. The RPCs are gas ( $C_3H_2F_4(94.7\%)$  Iso- $C_4H_{10}(5\%)SF_6(0.3\%)$ ) filled detectors composed of two resistive plates. These plates are parallel and 2 mm apart. An electric field of about 4.5 kV/mm is applied that causes avalanches when an ionizing particle passes through the gas. The signal is readout using metal strips placed on both side of the detector. The TGCs are similar to the multi-wire proportional chambers [68]. The momentum resolution of the muon spectrometer for  $p_T(\mu) \approx 1$  TeV/c is:

$$\frac{\sigma(p_T)}{p_T} = 10\% \quad (3.5)$$

### 3.3 The ATLAS Trigger System

At the ATLAS experiment, typically 40 million events per second are generated during the collision of beams. No storage device can handle successfully the gigantic rate at

which these data are generated (greater than 1 terabit/s). To cope with this, a trigger system is designed to select only those events that are "interesting" for detailed analysis. There are two levels of trigger system, the Level-1 (L1) trigger is hardware based while the high level trigger (HLT) is software based that run over computer clusters near the ATLAS detector. In Run-1, the L1 and the HLT reduced the event rate from 40 MHz to a few hundred Hz. After the events are stored permanently, the offline event reconstruction is performed on them to obtain physics objects, such as photons, leptons and jets for physics analysis.

The Level-1 trigger is entirely hardware based and uses reduced granularity information from the calorimeter and the muon trigger chambers to identify candidates for muons, electrons, photons, tau leptons, jets and events with large missing transverse energy. It does not use tracking information from the inner detector that is why at L1 b-jets can not be identified. It also defines the Regions-of-Interest (ROI) that contain those  $\eta$  and  $\phi$  coordinates where interesting objects have been identified. The L1 passes the ROIs to the HLT for further analysis. In Run-1, the maximum L1 acceptance rate was 75kHz and the latency rate was  $2.5 \mu s$ .

During the Run-1, the software based HLT had two levels: the Level-2 (L2) and the Event Filter (EF). The L2 had access to the full detector granularity and to the data only within the ROIs seeded by the L1 whereas the EF was designed to access the full event data and process it. The L2 reduced the event rate to 3 kHz with average processing time of 40 ms. EF reduced the event rate to a few hundred Hz with latency of 4 sec.

In Run-2, the higher energy and luminosity required upgrades to the trigger system. These upgrades took advantage of improvements in the available technology. The L1 acceptance rate was increased from 75 to 100 kHz. A new HLT architecture was adopted in which L2 and EF levels were merged and run together with event builders within the same processing unit (figure 3.8). This has many advantages such as the reduction of CPUs and the network usage. In Run-2, the event rate after the HLT trigger selection is 1 kHz [70].

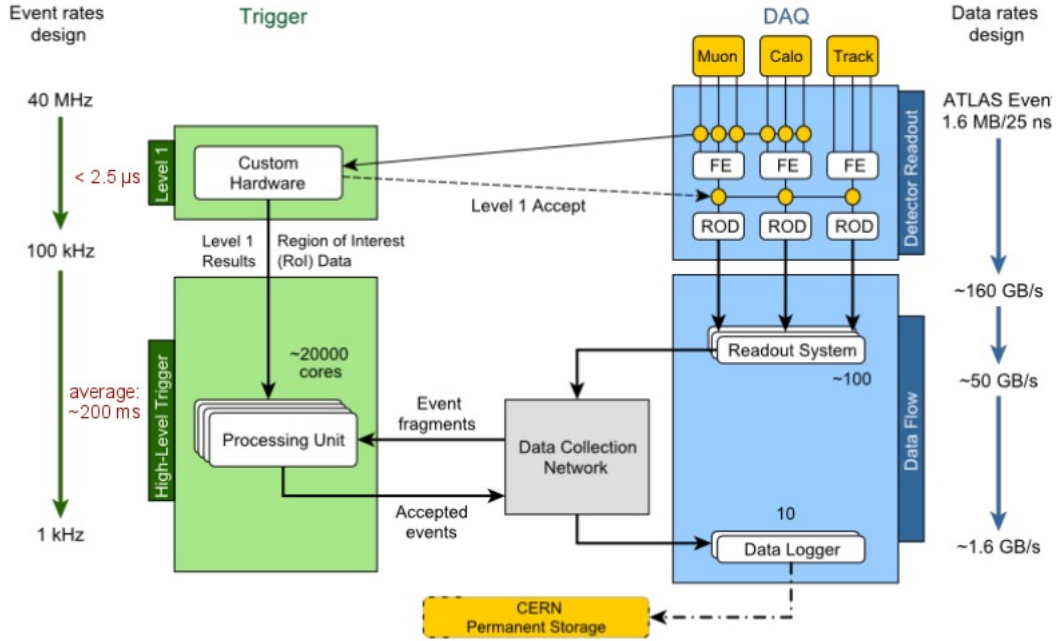


Fig. 3.8: The ATLAS trigger system in Run-2 showing a single high level trigger (HLT) [70].

The Data Acquisition (DAQ) system has also been upgraded by the use of a faster Readout System (ROS). The Read-Out-System (ROS) receives and buffers events coming from different ATLAS sub-detectors and from the level-1 trigger, and conveys to the high level trigger and the event builder via a GbE-based network. The new ROS consists of roughly 100 Linux-based 2U-high rack-mounted server PCs, each equipped with 2 PCIe I/O cards and four 10GbE interfaces [71].

### 3.3.1 Tau Trigger at the ATLAS Experiment

The tau lepton plays a significant role in particle physics both as a decay product of the Higgs boson and as a probe to new physics. As the heaviest lepton, the tau couples to the Higgs boson more strongly than any other lepton. Due to its short lifetime (nearly  $2.9 \times 10^{-13}$ s), it decays before passing through the detector. It is then detected through its decay signatures. Tau decays could be leptonic or hadronic, making it the only lepton that can decay hadronically. In the leptonic decay, it decays into an electron or a muon with two neutrinos. The hadronic decay products are most commonly one or

three charged hadrons (1-prong or 3-prong) (commonly pions) and possibly one or more neutral hadrons. Decay to five or more charged hadrons is also possible but there is a very small branching fraction ( $< 10^{-3}$ ). Figure 3.9 shows a typical tau decay to three charged pions and a neutral pion.

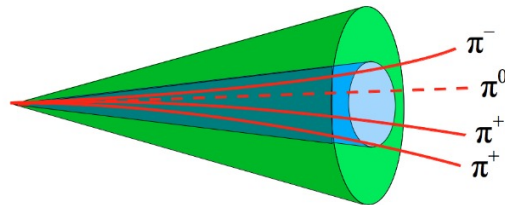


Fig. 3.9: A tau decay to three charged pions and a neutral pion [72].

The charged hadronic decay products look like a QCD jet with typically one or three tracks. Therefore QCD jets can fake taus making tau identification challenging. A dedicated hadronic tau trigger system in ATLAS uses tau identification tools developed using tracking and calorimetry capabilities to maximize the separation between true taus and the background. The main background of the hadronic tau decay is quark or gluon initiated jets because the hadrons produced through the QCD hadronization can fake a hadronic tau decay signature. However there are certain characteristics of taus that are useful to distinguish between taus and QCD jets. These are:

- (a) Low track multiplicity: Mainly one or three charged tracks from the tau decay whereas QCD jets typically have larger number of tracks.
- (b) Calorimeter cluster isolation: No track or energy deposition in the isolation cone. The cone is defined as  $0.2 \leq \Delta R = \sqrt{(\Delta\eta)^2 + (\Delta\phi)^2} \leq 0.4$  from the highest  $p_T$  track of the tau.
- (c) Narrowness: The charged tracks from the tau lepton decay are collimated in a narrow cone whereas the QCD jets are more spread out because they do not come from decay of a particle with a fixed mass.
- (d) The invariant mass of the tau ( $1.777 \text{ GeV}/c^2$ ).

The ATLAS trigger system has a hardware based level 1 tau trigger to identify regions of interest (ROI) to be investigated further in the high level trigger (HLT) where track reconstruction is performed only within the ROIs. The ROIs are selected using the trigger towers  $\Delta\eta \times \Delta\phi = 0.1 \times 0.1$  inside the electromagnetic and the hadronic calorimeter. At the level-1, taus are identified using following quantities:

- (a) the energy in  $2 \times 1$  pair of the EM tower within a  $2 \times 2$  core region
- (b) the energy in a  $2 \times 2$  group of the hadronic towers behind the EM core
- (c) the energy found in the  $4 \times 4$  isolation ring around the  $2 \times 2$  cone in both EM and hadronic calorimeter.

The isolation requirement is optional. Figure 3.10 shows the trigger towers used in the L1 tau trigger. At the level 1, relative to HLT lower thresholds on the transverse energy  $E_T$  cuts are applied. The energy is reconstructed by the sum of the energy deposited in the selected EM and the hadronic towers.

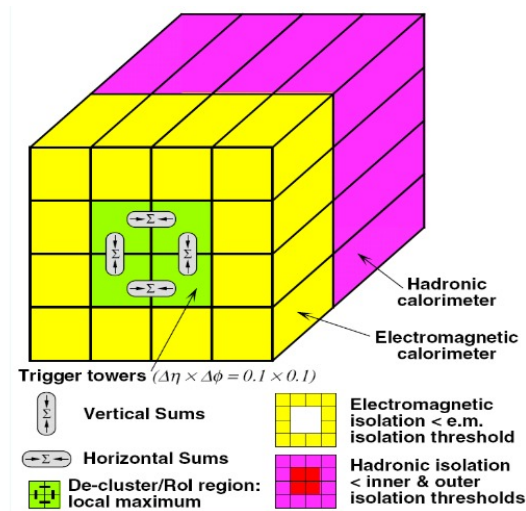


Fig. 3.10: The trigger towers used in the L1 tau trigger ( [73])

Due to greater time availability at the software based HLT, the full calorimeter granularity and the tracking information is seeded to reconstruction algorithms derived from

the offline reconstruction. The calorimeter jets with  $E_T > 10$  GeV and within the detector acceptance are used as a seed for the reconstruction of taus. The tracks within a cone of  $\Delta R < 0.4$  around the tau axis with  $|\eta| < 2.5$  and  $cp_T > 20$  GeV are considered as the tau candidates. The number of tracks within  $\Delta R < 0.2$  are further classified into 1-prong or 3-prong taus. All calorimeter clusters within  $\Delta R < 0.2$  around the 4-vector sum of the clusters associated with the jet seed are used to calculate tau energy. At the reconstruction level, no discrimination is applied on taus and QCD jets. These reconstructed taus could be QCD jets, therefore identification techniques are applied to separate them. Tau identification is based on the characteristics of narrowness and the low track multiplicity of taus. The tracks from tau decays are collimated within a narrow cone  $\Delta R < 0.2$ , therefore the energy deposited for taus in the calorimeter is also collimated in a smaller area than for jets. Figure 3.11 shows the energy weighted shower width of tau and the QCD jets in the calorimeter  $R_{cal}$ .

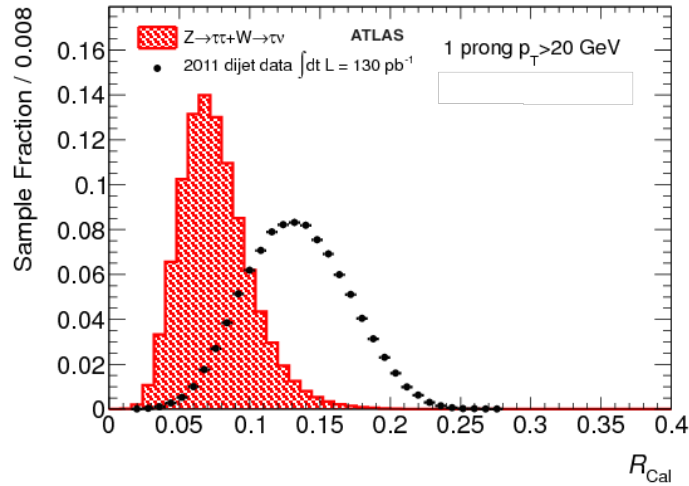


Fig. 3.11: The energy weighted shower width of tau and the QCD jets in the calorimeter  $R_{cal}$  inside the calorimeter [128].

In ATLAS, two independent approaches are used for the identification of taus. The cut-based method (applying rectangular cuts on variables) and the multivariate techniques (the likelihood method, which uses log-likelihood ratio of the signal and the background, and the Boosted Decision Trees (BDTs)). The BDTs are trained using a set of identification variables for single and multi-prong taus to find the optimal separation between signal and background in multi-dimensional phase space. Three cut values for BDT

output: the loose, the medium and the tight, are considered based on the efficiency (60%, 45% and 30% respectively) and their background rejection capabilities [128]

In Run-1, the tau trigger performance was studied using real data. Figure 3.12 shows the tau trigger efficiency as a function of the offline  $p_T$ . The trigger efficiency was measured using the tag-and-probe method in the  $Z \rightarrow \tau\tau \rightarrow (\tau_{lep}\bar{\nu}_\tau)(\tau_{had}\nu_\tau)$ . The muon from the leptonic decay of tau ( $\tau_{lep}$ ) is used to tag the event while the hadronic decay of tau ( $\tau_{had}$ ) is used to estimate the tau trigger performance [74].

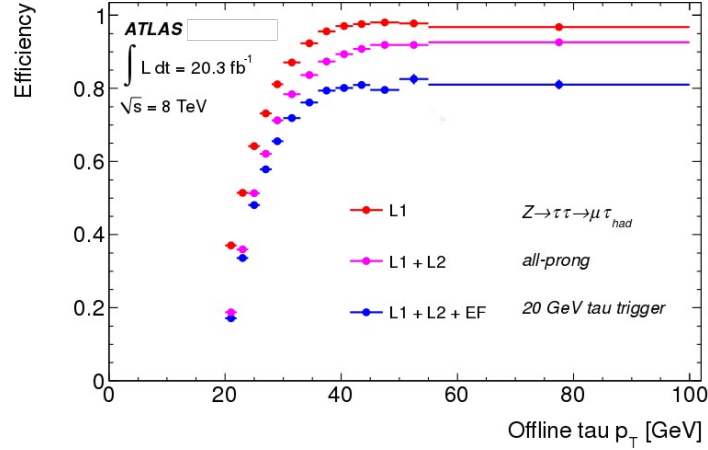


Fig. 3.12: The tau trigger efficiency as a function of the offline  $p_T$ . The  $p_T$  thresholds for L1, L2 and EF are 11 GeV/c, 20 GeV/c and 20 GeV/c respectively [74].

### 3.3.2 b-Jet Triggering at the ATLAS Experiment

The identification of jets originating from b-quarks (the b-tagging) is crucial in many physics analyses such as for the searches of new particles that couple strongly with heavy quarks for example the Higgs boson, and tagging the top quark with its decay  $t \rightarrow bW$ . The b-quarks and b-hadrons have some distinct properties that help in the identification of b-jets. These properties are:

- (a) b-hadrons have a longer lifetime (of the order of 1 ps) than those in the jets coming from c-quarks. This gives a decay length of  $\sim 3\text{mm}$  for a b-hadron of  $50\text{ GeV}/c^2$  mass. Therefore the jets originating from b-hadron decay will often be coming from a displaced secondary vertex. This means that the tracks of the b-jet will have

larger impact parameters than the ones coming from the primary vertex (see figure 3.13).

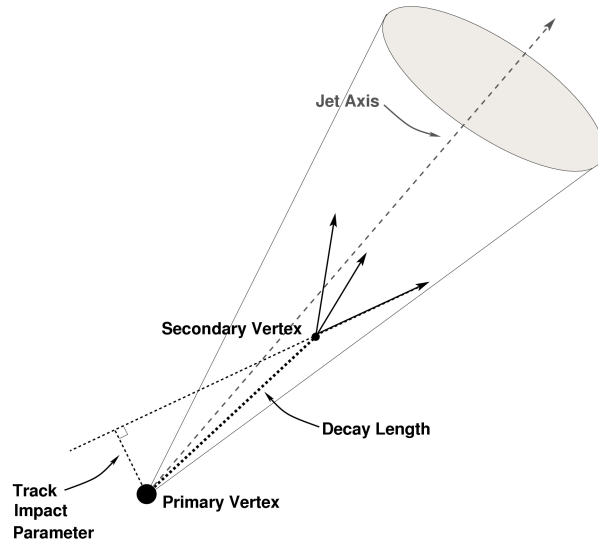


Fig. 3.13: A schematic view of a b-hadron decay with displaced secondary vertex [77].

- (b) The b-quark has higher mass ( $\approx 5 \text{ GeV}/c^2$ ) than first and second generation quarks.
- (c) B-hadrons retain about 70% of the original b-quark momentum as the fragmentation process is hard.

The presence of a secondary vertex, its associated properties and a larger impact parameter of the reconstructed tracks provide an excellent discriminator between jets originating from b-quarks and the jets coming from the lighter quarks and gluons.

The precision silicon detectors within the ATLAS detector make it possible to identify the presence of a b-jet. The b-jet triggering relies on the information from the inner detector. Therefore the identification of b-jets can only start at the HLT of the ATLAS trigger system. At L1, the calorimeter-based jet trigger provides the ROI information that is used as an input in the inner detector tracking algorithms and the b-tagging algorithms. The L1 jet trigger is a fixed-size sliding window method that sums energy in the trigger towers  $\Delta\eta \times \Delta\phi = 0.4 \times 0.4$  [76]. At the HLT, the b-jet trigger algorithm

consists of two steps: the calorimeter jet reconstruction and the b-jet identification (b-tagging). These reconstruction steps are explained in the next chapter (see [4.4.5](#) and [4.4.9](#)).

### 3.4 The LHC Computing Facilities

For a single LHC experiment, there are typically 40 million bunch crossing per second. The online selection reduces the rate to 1000 events per second which implies  $> 20$  PB per year data rate is expected. The large data volume and rate provides a unique challenge to the LHC computing facilities. A distributed computing infrastructure, the Worldwide LHC Computing Grid (WLCG), divides the computing facilities (CPU resources and storage devices) available at CERN and worldwide into tiers and enables nearly 8000 physicist to access the LHC data. The tier system is described as below [[78](#)]:

- **Tier-0:** Tier-0 is a CERN analysis facility. The raw data acquired from the detector is stored directly on the storage device at Tier-0. It is also responsible for performing the first pass at the reconstruction of the raw data into the meaningful information. The raw and the reconstructed data are exported from Tier-0 to Tier-1 and Tier-2 centres located worldwide.
- **Tier-1:** Tier-1 consists of 13 computing centres distributed worldwide. These are responsible for storing a proportional share of the data coming from Tier-0. It also does the reprocessing of the data and distributes it to the Tier-2.
- **Tier-2:** Tier-2 centres are distributed worldwide for physics analysis. These are typically group of universities and other scientific institutes that can store a large amount of data and provide computing power to perform specific data analysis. There are nearly 150 Tier-2 sites responsible of production and reconstruction of simulated events.
- **Tier-3:** Individual scientists and students can access grid through Tier-3 resources that are typically clusters in a university.

## 3.5 The Monte Carlo (MC) Simulation in ATLAS Experiment

The use of Monte Carlo simulation is important for various analyses. It provides environment to develop, test and understand the detector and its components. It is also helpful in developing techniques and strategies for analyses, estimating the uncertainties, designing and testing the reconstruction methods, and to optimize the trigger menu. MC simulation can be performed in the Athena framework [79] of the ATLAS experiment and includes following steps:

1. **Event Generation:** Various event generators such as PYTHIA [80], MC@NLO [81] and HERWIG [82] use hadronization models (e.g the Lund string, the cluster model etc) to simulate events such as the proton-proton collision. The event generators used for the analysis will be discussed in the next chapter in detail.
2. **Detector Simulation:** The information of the interactions between the particles and the detector material is used to simulate the detector. In ATLAS, GEANT4 [83] is used as a standard simulator that uses the full detector description including the dead materials, the detector noise and the effects of pileup etc.
3. **Digitization:** It refers to the process of converting the GEANT4 [83] simulated hits to the Raw Data Objects (RDOs) which are provided to the reconstruction algorithms as an input. Digitization involves simulation of the detector's readout, the front end electronics, and the conversion of these responses to the RDOs. The output format of the digitization is same for both the MC simulation and the real data.
4. **Reconstruction:** The output of the digitization process is converted into measurements associated with the particles produced during the collision. This process of reconstruction is done by dedicated algorithms. There are several steps of the reconstruction. The outcome of one reconstruction algorithm is often used by another algorithm. For physics analyses, these reconstruction algorithms are used to produce signatures of the particles. These methods are same for both the MC and the real data. The reconstruction of the objects related to the analysis are discussed in the next chapter.

---

## CHAPTER 4

# Monte Carlo Simulation and Object Reconstruction

### 4.1 Monte Carlo Event Generation

Data are compared with expectations from signal plus backgrounds to check if data agree with the theory. For these expectations, Monte Carlo simulated background samples are generated that use various physics processes which occur during the proton-proton collision and how they appear in the detector. Monte Carlo simulated signal samples are also generated to model the MSSM Higgs events. Monte Carlo event generation of physics processes consists of following major steps:

- **Parton Distribution Functions (PDFs):** Momentum distribution functions are simply called parton distribution functions. PDFs are available at leading order (LO), next-to-leading order (NLO) and next-to-next-to-leading order (NNLO) of the perturbative QCD in order to match the level of the matrix element calculations.
- **Matrix Element (ME):** This simulates the effects of primary parton collision.
- **Parton Shower (PS):** This simulates the cascade of partons that are accelerated in a scattering process. The aim is to generate large number of simulated collision events, each consisting of list of final-state particles and their momenta.
- **Hadronization:** During parton showering the interaction scale falls and strong interaction coupling rises, eventually triggering the process of hadronization in which the partons are bound into hadrons.
- **Decays:** Many hadrons produced in a collision event are unstable so the final stage of the event generation is the simulation of the hadron decays.

Event generators use several set of parameters that can be adjusted to control modelling of the properties of an events. These set of parameters are referred as “tunes”. Events in each Monte Carlo simulated sample are generated using dedicated PDFs that are tuned to model the physics of that sample accurately. The Monte Carlo samples used in the analysis are described in following sections.

### 4.1.1 Signal Samples

Two relevant production processes of the heavy neutral MSSM Higgs bosons are gluon-gluon fusion and b-associated production (Feynman diagrams in figures 2.12 and 2.13). Samples of gluon-gluon fusion production at different Higgs masses were generated using POWHEG-BOX v2 [84, 85] and interfaced to PYTHIA 8.210 [86] with the AZNLO tune [87] for the parton shower. Samples of b-associated production were also generated with same Higgs masses using the MadGraph5\_aMC@NLO 2.1.2 [88] generator and then PYTHIA 8.210 with the A14 tune [89] is used for the parton shower. The CT10 [90] and CT10nlo\_nf4 [91] PDFs are used in gluon-gluon fusion and b-associated production respectively.

The production cross sections for various MSSM scenarios are calculated using SusHi [92] in the five-flavour scheme <sup>1</sup> [93]. b-associated production in the four-flavour scheme <sup>2</sup> is also calculated (as described in ref. [94, 95]). The final b-associated production cross-section is calculated (as in ref. [96]) to match the four- and five-flavour scheme. The masses and couplings of the MSSM Higgs bosons are computed with FeynHiggs [97]. The branching fractions are calculated using the procedure described in ref. [98].

The Monte Carlo signal samples used in the analysis are listed in the tables A.1 and A.2 in appendix A.

---

<sup>1</sup>In five-flavour scheme, during cross section calculations b-quarks appear in the initial state. In addition, b-quarks appear in the leading order and next-to-leading order corrections

<sup>2</sup>In four-flavour scheme, PDFs do not include b-quarks. They only appear in the next-to-leading order corrections to the cross section calculations

## 4.1.2 Monte Carlo Background Samples

Those processes which have final states similar to the MSSM Higgs signal are considered background. These processes have hadronic tau, electron or muon and b-jets in the final state where hadronically decaying taus could be real or faked by either jets or other leptons ( $e/\mu$ ). The backgrounds that have real taus and leptons ( $e/\mu$ ) (often called 'irreducible'), include  $Z/\gamma^*(\rightarrow \tau_{had}l\nu\bar{\nu})+\text{jets}$ ,  $t\bar{t} \rightarrow \tau_{had}l\nu\bar{\nu}b\bar{b}$  and diboson ( $WW/ZZ/WZ$ ) events. The other backgrounds where an hadronic tau is faked by a jet or a lepton ( $e/\mu$ ) include W+jets and single top or  $Z/\gamma^*(\rightarrow ee/\mu\mu)+\text{jets}$  events respectively. These samples are generated using the following event generators (while the contribution of background from QCD multi-jet production is estimated through data):

1.  **$W(\rightarrow e/\mu)+\text{jets}$  and  $Z/\gamma^*(\rightarrow ee/\mu\mu)+\text{jets}$  samples:**

These samples are modelled using the POWHEG-BOX v2 generator and the events are showered with PYTHIA 8.186 [99] with the AZNLO tune. Samples where bosons are real exchange particles (on-shell bosons) and where bosons are virtual (off-shell bosons), such as Drell-Yan processes, are also generated. Tables A.3, A.4 and A.5 in appendix A lists all the W+jets and Z+jets samples used in the analysis. PHOTOS++ v3.52 [100, 101] is used to model final state QED radiations in these samples. The spin correlation effects between the W boson and its decay product are simulated with the TauSpinner [102] program. All W+jets and Z+jets samples use the CT10 PDF set and are normalized to NNLO cross sections calculated using FEWZ [103, 104].

2.  **$t\bar{t}$  and single top samples:**

The  $t\bar{t}$  and single top samples are generated using the POWHEG-BOX v2 generator with the CT10 PDF set in Wt- and s-channels. The single top samples in t-channel are produced using the POWHEG-BOX v1 generator with the four-flavour scheme for the NLO matrix element calculations together with the fixed four-flavour scheme PDF set CT10f4 [90]. The top decay is modelled with MadSpin [105]. In all top samples, PYTHIA 6.428 [106] is used as the parton shower with the CTQ6L1 PDF set and the corresponding Preugia 2012 tune [107]. PHOTOS++ v3.52 is used to model the final state QED radiations. The  $t\bar{t}$  samples are normalized to the NNLO cross section whereas the normalization of single top

samples uses an approximate NNLO calculations described in ref. [108–111]. For all samples, the top quark mass is set to 172.5 GeV/c<sup>2</sup>. The list of samples used for  $t\bar{t}$  and single top is in the table A.6 in appendix A .

### 3. Diboson samples (WW,ZZ,WZ):

The diboson samples are generated using SHERPA 2.1.1 [112] with the CT10 PDF. The samples are normalized to the NLO cross sections that SHERPA calculates. The list of diboson samples used are given in the table A.7 in appendix A .

### 4. $Z/\gamma^* \rightarrow \tau\tau$ +jets samples:

The  $Z/\gamma^* \rightarrow \tau\tau$  samples are generated with PYTHIA 8.165 [99]. The A14 tune together with the PDF set NNPDF2.3 LO [113] are used. These samples are also generated with various mass points of the off-shell boson. The list of samples used for  $Z/\gamma^* \rightarrow \tau\tau$  is provided in appendix A (see table A.8) .

The simulation of b- and c- hadron decays in all samples use EvtGen v1.2.0 [114], except those generated with SHERPA. All simulated events include effects of pileup (both in-time and out-of-time pileup as explained in section 3.1.2) by overlaying simulated minimum-bias events on each generated signal or background event. These minimum-bias events are generated with PYTHIA 8.186 using the A2 tune [115] and the MSTW2008LO PDF [116].

## 4.2 Data Samples

The data samples used in the analysis were recorded with the ATLAS detector, during 2015, using proton-proton collision from the Large Hadron Collider at a centre of mass energy of 13 TeV. The data where the new insertable B-layer (IBL) was not fully operational is not used (corresponding to 0.2 fb<sup>-1</sup> integrated luminosity). Data from the 50 ns bunch crossing configuration is also not included. The analysis only considers 25 ns bunch crossing data which gives a total integrated luminosity of 3.21 fb<sup>-1</sup>.

## 4.3 Detector Simulation

The interactions between particles and the material of the detector are modelled using GEANT4 [117] except the b-associated MSSM Higgs boson signal which uses ATLFAS-II aiming to speed up the full simulation process by reducing the steps that GEANT4 takes (for details see [118]). It was observed that MadGraph5\_aMC@NLO 2.1.2 had a bug, due to which a lot of b-associated signal events had negative weights. Therefore much larger statistics with respect to the gluon-gluon fusion samples were generated. For simulation of these large number of events, ATLFAS-II had been used and the events with negative weights were discarded during the simulation.

The particles produced by the event generators are passed through the GEANT4 or the ATLFAS-II programs. The detector simulation is performed in various steps. At each step, a particle has a specific chance of decay or to interact with the material. The energy deposited from each particle is translated into hits in the detector through the process of digitization. At this point, full event reconstruction is performed on the simulated and digitized events using identical reconstruction algorithms as are used for the real data. The common reconstruction algorithms used in the ATLAS experiment are discussed in detail in the next section.

## 4.4 Object Reconstruction

Information obtained from various components of the ATLAS detector are converted into measurements that are useful to reconstruct particles produced by the collision and interact with the detector. This process of reconstruction is done by dedicated algorithms. There are several steps of reconstruction. The outcome of one reconstruction algorithm is often used by another algorithm. The ultimate goal of these algorithms is to reconstruct particles and their properties that are used in a physics analysis.

In this analysis, the MSSM Higgs searches make use of taus, electrons, muons, jets, b-tagging and missing transverse energy to identify the potential signal events. An overview of the reconstruction steps of these particles is provided in coming sections.

### 4.4.1 Track Reconstruction

Tracks of charged particles are reconstructed inside the inner detector using two algorithms: the “inside-out” and the “outside-in”. The inside-out algorithm runs first in which the hits from the pixel and the SCT are converted into 3-dimensional space points. These 3-point seeds are then extended to the end of the inner detector to reconstruct tracks using a Kalman filter (an iterative algorithm consists of essentially a set of mathematical equations that implement a predictor-corrector type estimator that is optimal in the sense that it minimizes the estimated error covariance, when some presumed conditions are met, for details see [119]). The tracks are then re-fitted and ambiguities are resolved by removing fake tracks and overlaps.

After this, the outside-in approach is applied in which the tracks are reconstructed from the hits in the TRT, excluding hits already assigned to the tracks from the first algorithm. These are then extrapolated backward to the interaction point and hits in the SCT and the pixel detector are associated to the track. Finally, these track candidates are re-fitted using all the associated hits (for details see [120]).

### 4.4.2 Vertexing

Reconstruction of the primary vertex is divided into two steps, primary vertex finding and primary vertex fitting. In the first step, reconstructed tracks are associated with vertex candidates. Only those tracks are considered that satisfy certain quality criteria. These quality criteria includes [121]:

- $p_T > 400 \text{ MeV}/c$
- $|\eta| < 2.5$
- Number of silicon hits  $\geq 9$  if  $|\eta| \leq 1.65$  and 11 if  $|\eta| < 1.65$
- IBL hits + B-layer hits  $\geq 1$
- A maximum of 1 shared pixel hit or 2 shared SCT hits

- Pixel holes<sup>3</sup> = 0
- SCT holes  $\leq 1$

In order to reconstruct secondary vertices, secondary track candidates are selected which have  $p_T > 300$  MeV/c and a transverse impact parameter relative to the primary vertex of at least 5 mm. Tracks coming from the primary vertex are rejected in order to reduce combinatorial background. To be selected as a candidate, a primary or secondary vertex requires two tracks passing these selection criteria.

After vertex finding, an adapted fitting algorithm is used for vertex fitting which uses an iterative  $\chi^2$  minimization routine. The algorithm is repeated until all the tracks are associated with the vertices or until it is not possible to form a vertex with a lower  $\chi^2$ . The primary vertex is chosen as the one with the highest sum  $p_T^2$  of the associated tracks.

### 4.4.3 Cluster Reconstruction

Particles passing through the electromagnetic and/or the hadronic calorimeter interact with the material and produce a cascade of particles called a shower. Particles in the shower deposit energy in different calorimeter cells. A calorimeter cluster is a group of neighbouring cells whose combined energy deposition reflects the energy loss of particles in the calorimeter. The EM particles, electrons and photons, produce narrow showers inside the electromagnetic calorimeter while the hadronically interacting particles such as kaons and pions often start showering in the electromagnetic calorimeter with bulk of shower in the hadronic calorimeter. The cluster reconstruction or simply clustering is performed in both EM and hadronic calorimeters. Two algorithms are used for clustering: the sliding-window and the topological. The sliding-window approach is based on summing cells in a fixed size rectangular window which is slid across the  $\eta - \phi$  grid of the calorimeter. The position of the window is adjusted so that its contained energy is a local maximum. In topological clustering, the variable size clusters (called topoclusters) are formed starting with a seed cell and iteratively adding the cluster the neighbours of cells already in the cluster, provided that the significance of the new cells energy with

---

<sup>3</sup>A hole is counted when an active module that the track traverses does not have a corresponding hit

respect to the expected noise is above a threshold. The calorimeter clusters are used as an input for both electron and jet reconstruction [122].

#### 4.4.4 Electron Reconstruction

Electrons are reconstructed using the sliding window clusters in the pseudorapidity range  $|\eta| < 1.37$  or  $1.52 < |\eta| < 2.47$ , with the gap corresponding to the crack region between the barrel and endcaps of the EM calorimeter. These clusters must have a transverse energy  $\geq 3$  GeV and size of  $3 \times 5$  in the middle layer of the electromagnetic calorimeter. To distinguish an electron from a photon, electron clusters must be associated with a track in the inner detector. For track matching,  $0.2 \times 0.4$  in  $\Delta\eta \times \Delta\phi$  is considered around the cluster. The tracks within this should have at least three silicon hits and the requirement on  $E/p < 10$ . In order to reject electrons from the decaying particles, an isolation requirement is also needed.

The identification of electrons defines three levels with decreasing efficiency and increasing background rejection. These levels are: loose, medium and tight based on an increasingly stringent set of isolation cuts applied to reconstructed electrons (table 4.1). The loose electron identification has a low background rejection (a factor of  $\sim 5$ ) but gives high efficiency ( $\sim 87\%$ ). The medium electron identification uses additional tracking cuts and puts more constraints on the cluster-track matching. The background rejection increases by an order of magnitude and the efficiency drops to 77%. In the tight electron identification, no new cuts are added but the constraints on the cluster-track matching are increased. This gives the maximum background rejection increase by a factor of two with respect to medium identification level and the efficiency drops to 61%. ([123, 124]).

#### 4.4.5 Jet Reconstruction

ATLAS uses an anti- $k_T$  algorithm for the jet reconstruction. The topoclusters are used as input to this jet-finding algorithm. In the anti- $k_T$  algorithm, the following two

Electron ID levels	Cuts
Loose	Detector acceptance: $ \eta  < 2.47$ Shower lateral width and shape (2nd calorimeter layer) Hadronic leakage veto
Medium	Cuts from loose electron ID Veto two maxima in shower transverse profile to reject $\pi^0 \rightarrow \gamma\gamma$ Track quality cuts (number of hits in SCT and Pixel and the impact parameter) Shower width and shape (1st calorimeter layer)
Tight	Cuts from medium electron ID TRT hits Track-cluster match ( $\Delta\eta < 0.005$ , $\Delta\phi < 0.02$ ) Ratio of cluster energy to track momentum: E/p

Table 4.1: Electron ID levels and summary of cuts (details in [125]).

parameters are calculated for each pair (i,j) of topoclusters:

$$d_{ij} = \min(p_{T,i}^{2k}, p_{T,j}^{2k}) \frac{\Delta R_{ij}^2}{r^2} \quad (4.1)$$

$$d_{iB} = p_{T,i}^{2k} \quad (4.2)$$

where  $p_T$  is the transverse momentum,  $\Delta R_{ij} = \sqrt{(\phi_i - \phi_j)^2 - (\eta_i - \eta_j)^2}$ , and the jet radius  $r=0.4$  and the parameter  $k=-1$  are considered. The minimum of  $d_{ij}$  and  $d_{iB}$  is taken. If the minimum is  $d_{ij}$ , both  $i$  and  $j$  are combined into a single topocluster and if it is  $d_{iB}$ , the topocluster  $i$  is taken as a jet and removed from the list of the input. This jet-finding algorithm produces well-defined jets in  $\eta - \phi$  plane [126].

To reject jets from pileup interactions, the Jet Vertex Fraction (JVF) is calculated. It is defined as the transverse momentum of the tracks within the jet which are associated to a particular vertex, divided by the total transverse momentum of all tracks within the jet. A cut of  $JVF > 0.5$  is applied to jets within the acceptance of the tracker.

#### 4.4.6 Tau Reconstruction

Taus decay 35% of the time to an electron or a muon with two neutrinos, and 65% of the time to hadrons; usually one or three pions (or kaons) with zero, one or more neutral pions (or kaons). The leptons ( $e/\mu$ ) are indistinguishable from those produced in other processes and are reconstructed by the algorithms discussed above. Reconstruct-

tion of hadronic taus is done in the same way as jets (using an anti- $k_T$  algorithm on topoclusters) with additional requirements due to the narrowness of jets. These include:

- The jets should be within the acceptance of the tracking detector, i.e.,  $|\eta| < 2.5$ .
- Topoclusters with  $p_T > 10$  GeV/c.
- Tracks are associated with a tau candidate if they are within  $\Delta R < 0.2$  and have  $p_T > 1$  GeV/c. In addition to these requirements, the track must have at least two associated hits in the pixel+IBL detector, at least seven hits in total in the Pixel and the SCT detector
- Longitudinal and transverse impact parameters (the distance of the closest approach of the track to the primary vertex) should be with 1.5 mm and 1.0 mm respectively.

The energy of the visible hadronic tau decay products is calculated using all the calorimeter clusters within a cone of  $\Delta R = 0.2$  around the 4-vector sum of clusters associated with the tau. Contributions from particles that are not seen in the calorimeter are derived from simulation of various physics processes with hadronic taus. The calibrated tau energy depends on the pseudorapidity and the track multiplicity of the tau candidate (for details see [127]).

These hadronic tau candidates contain mainly QCD jets therefore separate identification steps are applied using discriminating variables which are based on the tracks and topoclusters in the core ( $\Delta R < 0.2$ ) and isolation ( $0.2 < \Delta R < 0.4$ ) regions around tau candidate direction. The following variables are used to distinguish between taus and jets originating from quarks and gluons [127]:

- $m_{tracks}$ : the invariant mass of the track system in the core and isolation regions
- $f_{iso}^{track}$ : the scalar sum of the  $p_T$  of tracks in isolation region divided by the sum of the  $p_T$  of all tracks associated with the tau

- $f_{leadtrack}^{-1}$ : the transverse energy sum calibrated at the EM energy scale and deposited in all cells belonging to topoclusters in the core region divided by the transverse momentum of the highest  $p_T$  charged in the core region

- $f_{cent}$ :

$$f_{cent} = \frac{\sum^{\Delta R < 0.1} E_T^{EM}}{\sum^{\Delta R < 0.2} E_T^{EM}} \quad (4.3)$$

Fraction of the total transverse energy ( $E_T$ ) of all cells in the respective regions that are associated to the tau candidate calibrated at the EM energy scale.

- $\Delta R_{max}$ : maximum distance of a track in the core region from the tau axis
- $R_{0.2}^{track}$ : the  $p_T$  weighted  $\Delta R$  distance of the associated tracks within the core region
- $p_T^{EM+track}/p_T$ : ratio of the tau  $p_T$  estimated using the vector sum of track momenta and upto two of the most energetic EM clusters in the core region ( $p_T^{EM+track}$ ) to the calorimeter only measurement of the tau  $p_T$
- $f_{track}^{EM}$ : the ratio of sum of cluster energy deposited in EM part of each topocluster to the sum of the momentum of tracks in the core region
- $f_{EM}^{track-HAD}$ : the difference between the sum of the momentum of tracks in core region and the sum of cluster energy deposited in the hadronic part of each topocluster divided by the sum of cluster energy deposited in the EM part of each topocluster
- $m_{EM+track}$ : invariant mass of the system composed of the tracks and upto two of the most energetic EM clusters in the core region
- $S_{track}^{IP}$ : the transverse impact parameter of highest  $p_T$  track in core region divided by its estimated uncertainty
- $S_T^{flight}$ : the decay length of the particle at secondary vertex in the core region divided by its estimated uncertainty

Figure 4.1 shows distributions of the identification variables ( $f_{EM}^{track-HAD}$ ,  $f_{track}^{EM}$ ,  $m_{EM+track}$ ,  $p_T^{EM+track}/p_T$ ) for one- and three-prong taus and QCD jets.

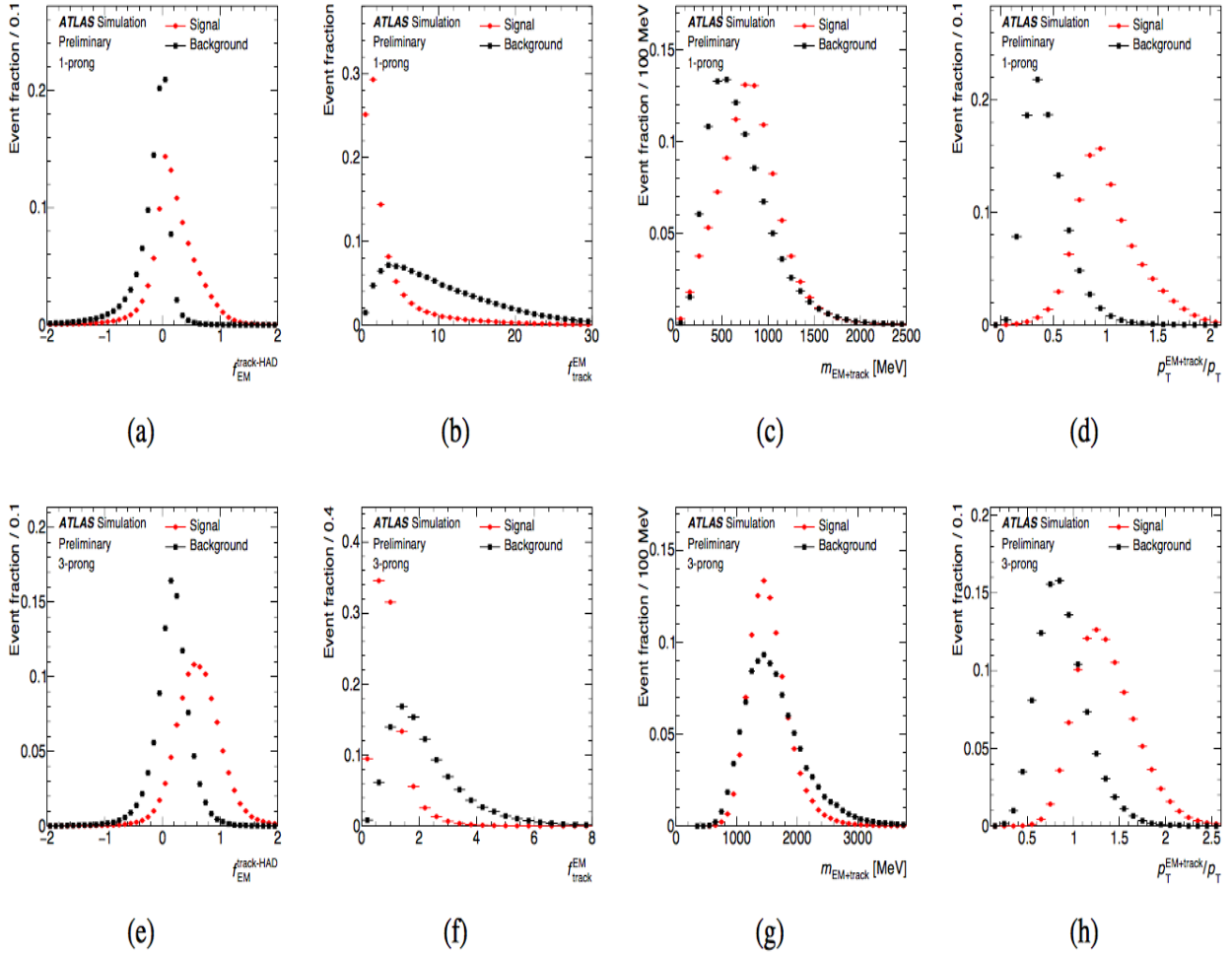


Fig. 4.1: Distribution of identification variables for tau leptons and QCD jets (a)  $f_{EM}^{track-HAD}$  (b)  $f_{track}^{EM}$  (c)  $m_{EM+track}$  (d)  $p_T^{EM+track}/p_T$  for one-prong (top plots) and (e)  $f_{EM}^{track-HAD}$  (f)  $f_{track}^{EM}$  (g)  $m_{EM+track}$  (h)  $p_T^{EM+track}/p_T$  for three-prong (bottom plots) ([127])

Pileup corrections are applied to these discriminating variables. The BDTs are trained using different set of identification variables for single and multi-prong taus. Three separate working points: the loose, the medium and the tight, are considered based on the efficiencies of 70%, 60% and 40% with background rejection of 10, 50 and 100 respectively [128] (Background rejection factor of about 100 means that only 1 jet out of 100 is identified as a tau lepton).

#### 4.4.7 Muon Reconstruction

Muon reconstruction begins with information only from the muon spectrometer (description of the muon spectrometer is provided in section 3.2.3). Straight line segments are formed from multiple hits within a given monitored drift tubes (MDT) or cathode strip chambers (CSC). These Segments are combined to create “stand-alone” muon tracks. The tracks are then extrapolated to the primary vertex accounting for the energy loss in the calorimeter which ranges from 1-100 GeV.

In the next step, tracks are matched between the inner detector and the muon spectrometer. If a match is found with a small  $\chi^2$ , the result is a “combined” muon. Finally, an attempt is made to match the ID tracks with the segments in the muon spectrometer which have not formed tracks. If a match is formed, the result is a “segment-tagged” muon. In the analysis, an event where a muon is in the final state, only combined muon is considered. However, the segment-tagged and stand-alone muons are used to resolve ambiguities between overlapping objects. To reject muons from decaying hadrons, candidates are required to be isolated from other nearby activity in the detector [129].

#### 4.4.8 Missing Transverse Energy

Conservation of momentum in the plane transverse to the beam axis implies that the vector sum of all particles’ momenta should be zero. An imbalance in the sum is known as “missing transverse momentum” or simply “missing transverse energy ( $E_T^{miss}$ )” (in the ultra-relativistic limits  $E = \sqrt{m_0^2 c^4 + p^2 c^2} \approx pc$ , or  $E \approx p$  in natural units). Weakly interacting particles, like neutrinos, deposit no energy in the detector and give rise to

the missing transverse energy.

The reconstruction of  $E_T^{miss}$  uses reconstructed and calibrated objects in an event. The component  $E_{T_{x(y)}}^{miss}$  is calculated as:

$$E_{T_{x(y)}}^{miss} = E_{T_{x(y)}}^{miss,e} + E_{T_{x(y)}}^{miss,\gamma} + E_{T_{x(y)}}^{miss,\tau} + E_{T_{x(y)}}^{miss,jets} + E_{T_{x(y)}}^{miss,\mu} + E_{T_{x(y)}}^{miss,soft} \quad (4.4)$$

Each term in the right side of above equation is the negative of the vector sum of the momenta of the respective calibrated objects.  $E_{T_{x(y)}}^{miss,soft}$  is reconstructed from the transverse momentum deposited in the detector but not associated with any reconstructed hard objects.

The magnitude of  $E_T^{miss}$  and the azimuthal angle  $\phi^{miss}$  is calculated as:

$$E_T^{miss} = \sqrt{(E_{T_x}^{miss})^2 + (E_{T_y}^{miss})^2} \quad (4.5)$$

$$\phi^{miss} = \tan^{-1} \left( \frac{E_{T_y}^{miss}}{E_{T_x}^{miss}} \right) \quad (4.6)$$

The measurement of  $E_T^{miss}$  is affected by the poor reconstruction of the energy deposited by particles.

#### 4.4.9 b-tagging

The b-jet reconstruction is divided into three main steps: reconstruction of the tracks of charged particles, the primary vertex reconstruction and the use of a b-tagging algorithm. The track and vertex reconstruction is summarized in [4.4.1](#) and [4.4.2](#) respectively. In order to reduce the processing time in b-jet triggering, tracking is performed in a smaller Region of Interest (ROI) (half the size in  $\eta$  and  $\phi$  of the L1 jet ROI).

## b-tagging algorithm

Most of the b-tagging algorithms exploits the relatively long lifetime of b-jets that results in a secondary vertex which is noticeably displaced from the primary interaction point. In Run-2, flavour tagging benefits from the new IBL and a new multivariate technique, MV2, was created which provides 30-50% better light jet rejection at the same b-tagging efficiency compared to the Run-1 multivariate tagger MV1.

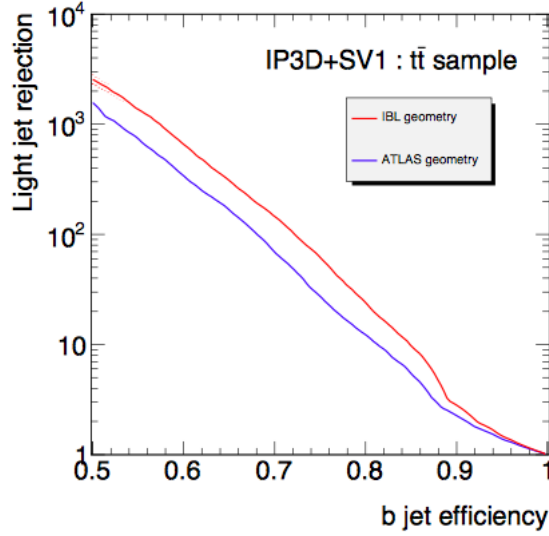


Fig. 4.2: The light-jet rejection versus b-jet efficiency with and without the IBL ( [130])

MV2 makes use of the impact parameter based algorithm (IP3D), secondary vertex based algorithm (SV1) and the decay chain multi-vertex algorithm (JetFitter) by combining the output of these three basic taggers with a boosted decision tree (BDT) algorithm. A brief overview of these taggers is provided below (for details see [131]):

- **IP3D:** This algorithm uses the signed impact parameters significance (SIPS) of tracks matched to the jet. The sign is positive (negative) if the point of closest approach of the track to the primary vertex is in front of (behind) the primary vertex with respect to the jet direction. The probability distribution functions ( $P_b/P_{light}$ ) of the SIPS of these tracks are built from simulation for the b- and

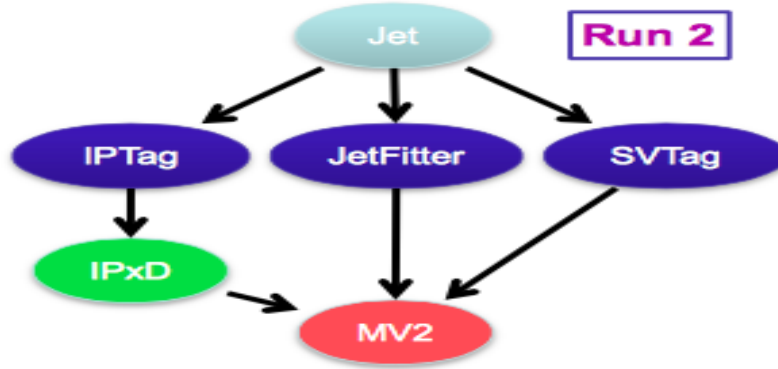


Fig. 4.3: Schematic view of the workflow of MV2 algorithm ( [130])

light-flavour jet hypotheses and then combined in a single log likelihood ratio (LLR) discriminant ( $w_{jet}$ ).

$$w_{track} = \frac{P_b}{P_{light}} \quad (4.7)$$

$$w_{jet} = \sum_{tracks} \log(w_{track}) \quad (4.8)$$

IP3D uses both the transverse and longitudinal impact parameters taking into account their correlations. The output of IP3D algorithm is shown in figure 4.4. If no tracks are found in the jet, a large negative value is assigned as the algorithm output [131].

- **SV:** SV1 aims to reconstruct displaced secondary vertex within the jet using candidate tracks. The tracks are rejected if they form a secondary vertex which seems likely to be originating from the decay of a long-lived particle (such as kaons), hadronic interactions or photon conversions in the detector's material [131]. After reconstructing the secondary vertex, the properties of the secondary vertex such as the invariant mass of the tracks emerging from the vertex, the number of tracks associated to the secondary vertex and the energy fraction of the tracks fitted to the vertex to all tracks in the jet, are used as final discriminants between b-, c- and light-flavoured jets (see figure 4.5).
- **JetFitter:** The JetFitter uses the topological structure of b- and c-hadron decays

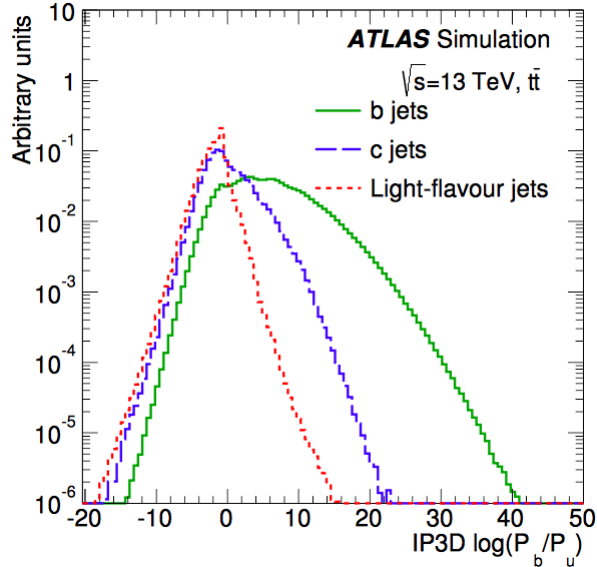


Fig. 4.4: Final discriminant of IP3D algorithm for b-, c- and light-flavoured jets in  $t\bar{t}$  events ( [131])

inside the jet and aims to reconstruct the Primary Vertex  $\rightarrow b \rightarrow c$ -hadron decay chain. A Kalman Filter algorithm is used to find a common line on which the primary vertex and the bottom and charm vertices lie. The line is approximated as the b-hadron flight path. JetFitter uses the same discriminating variables as used by the SV1 but adds the decay topology in it ( [131]). Figure 4.6 shows the distributions of some of the output variables.

Outputs from these three basic algorithms are provided as inputs to MV2 which uses a boosted decision tree (BDT) algorithm to discriminate b-jets from the light (u,d,s-quarks or gluon jets) and c-jets. The training is performed on large  $t\bar{t}$  events. The kinematic properties ( $p_T$  and  $\eta$ ) of jets are included in the training to take advantage of correlations with the other input variables. Figure 4.7 shows the output of MV2 for b-, c- and light-flavour jets in  $t\bar{t}$  events. Figure 4.8 shows the comparison between the performance of default Run-1 b-tagging algorithm, MV1c, which uses the Run-1 detector and the reconstruction software compared to the default Run-2 b-tagging algorithm, MV2c20, which uses the Run-2 detector and the reconstruction software.

A single cut value on the MV2 output distribution provides a specific b-jet efficiency on a  $t\bar{t}$  sample (termed as operating point). For the analysis, the MV2 tagger with operating

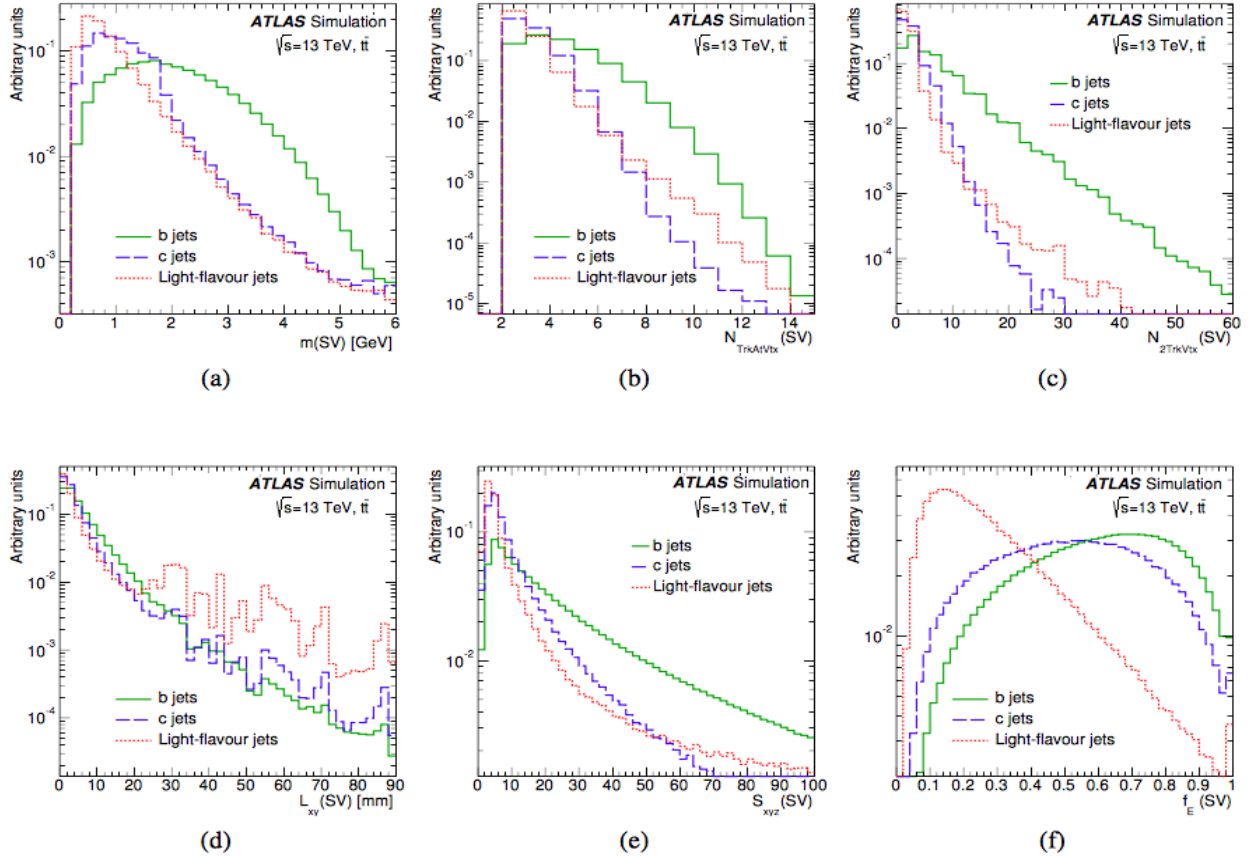


Fig. 4.5: Properties of the secondary vertices reconstructed by the SV algorithm for b-, c- and light-flavoured jets in  $t\bar{t}$  events: (a) the invariant mass, (b) the number of tracks, (c) number of 2-track vertices, (d) transverse decay length, (e) 3D decay length significance, and (f) the energy fraction of tracks in the secondary vertex to all tracks reconstructed within the jet ([131])

point  $> -0.0436$  is used (using ATLAS flavour tagging group's recommendations) which gives 70% b-jet efficiency on a  $t\bar{t}$  sample.

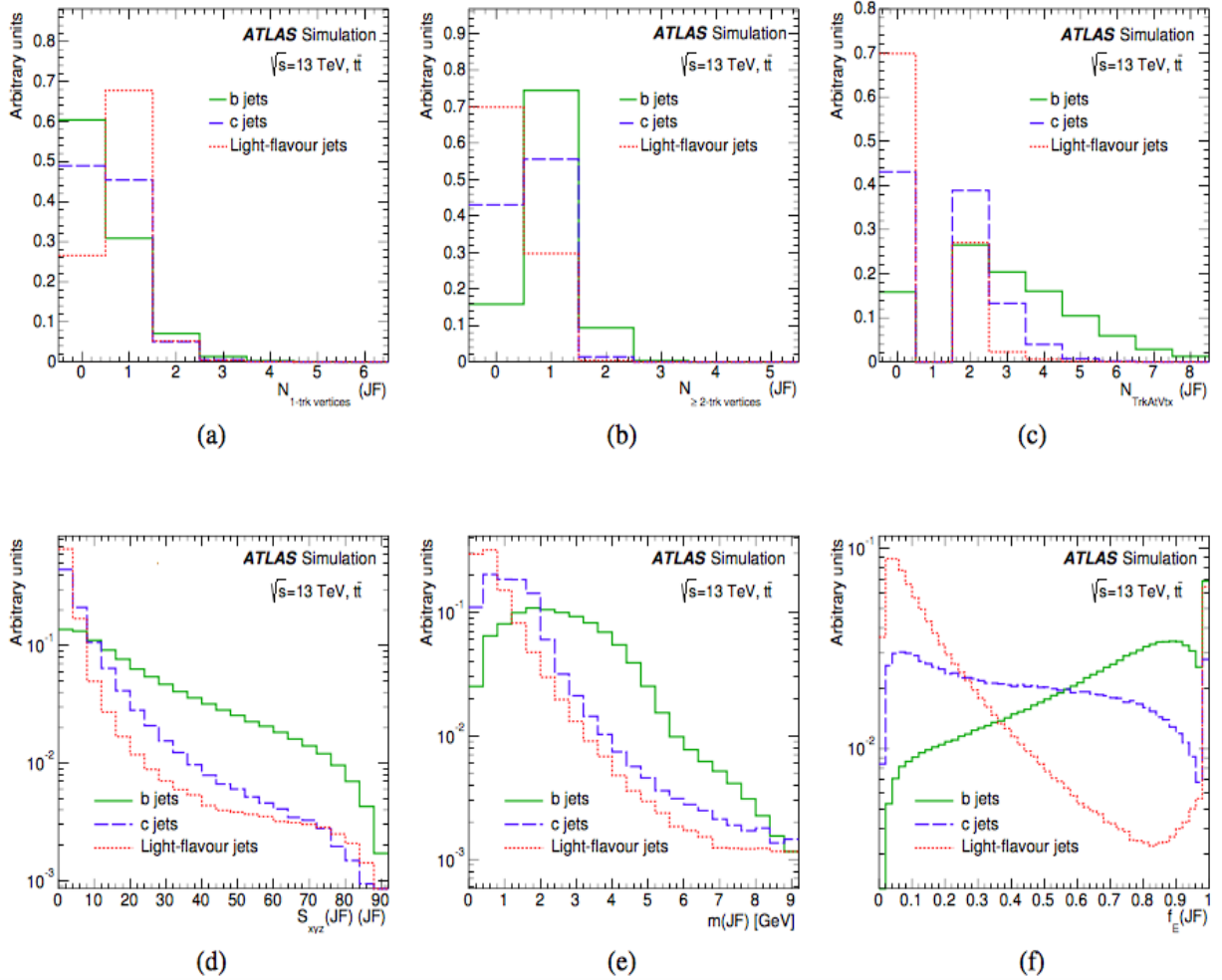


Fig. 4.6: Properties of the decay toplogy and secondary vertices reconstructed by the JetFitter algorithm for b-, c- and light-flavoured jets in  $t\bar{t}$  events: (a) the number of 1-track vertices, (b) the number of vertices with at least two tracks, (c) the number of tracks from vertices with at least two tracks, (d) the average flight length significance of the reconstructed vertices, (e) the invariant mass of tracks fitted to one or more displaced vertices, and (f) the energy fraction of tracks in the secondary vertex to all tracks reconstructed within the jet ([131])

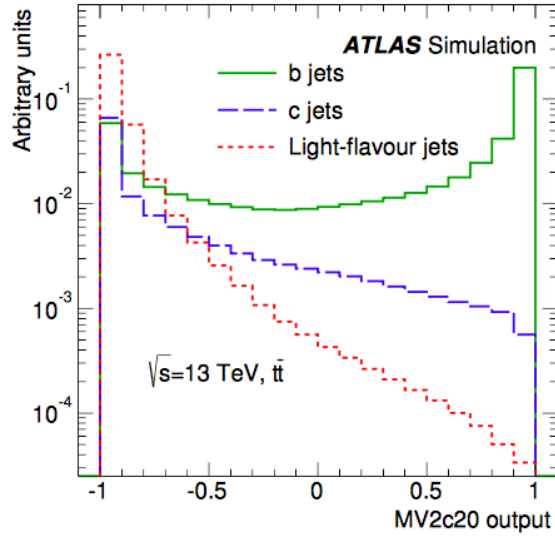


Fig. 4.7: The output of MV2c20 for b-, c- and light-flavour jets in  $t\bar{t}$  events ( [131]). In MV2c20 algorithm, the BDT training is performed assigning b-jets as signal and a mixture of 80% light-flavour jets and 20% c-jets as background.

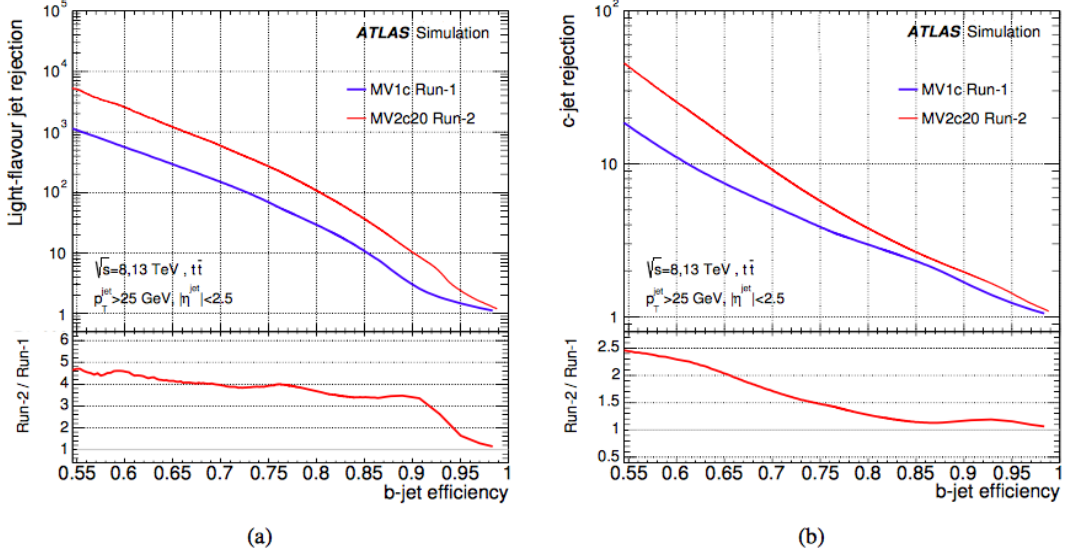


Fig. 4.8: a) The light-flavour jet rejection b) c-jet rejection versus b-jet efficiency for Run-1 and Run-2 default taggers ( [131])

---

## CHAPTER 5

# Events Selection and the Background Estimation for $A/H \rightarrow \tau_{lep}\tau_{had}$

The aim of this analysis is to search neutral MSSM Higgs boson ( $A/H$ ) decaying into di-taus where one tau decays leptonically ( $\tau_{lep}$ ) and the other tau decays hadronically ( $\tau_{had}$ ). The two dominant modes of production of the MSSM Higgs boson, gluon fusion and associated production with b-quarks are considered, with the latter mode dominant for high  $\tan\beta$  values.

The analysis is split into two categories, b-tag where one or more b-jets are identified and b-veto where no b-jet is identified in the event by the b-tagging algorithm. Event selection occurs in two stages. In pre-selection, basic cuts are applied to reduce the number of events to process later. This is followed by the event selection cuts required to separate MSSM Higgs boson events from the processes with similar final states (see section 4.1.2). Estimation of these backgrounds is performed in control regions chosen to enrich particular background events. Table 5.1 lists all control regions that are used in the analysis. The analysis used the first 978  $\text{pb}^{-1}$  of the data for the b-tag category and first 413  $\text{pb}^{-1}$  of the data for the b-veto category to check the performance of the background estimation in the signal region. Once satisfied with the performance, rest of the 2015 data was unblinded in the signal region.

### 5.1 Pre-selection

Pre-selection refers to basic quality criteria applied to an event. Such as, events that were recorded when not all parts of the detector were fully operational or objects that

W+jets/top control region	$\tau_{had}$ and $e/\mu$ with opposite signs $\tau_{had}$ passing “medium” identification requirement [128] Isolated $e/\mu$ passing “medium” identification requirement [125] $\Delta\phi(\tau_{had}, e/\mu) > 2.4$ $m_T(e/\mu, E_T^{miss}) > 70(60)$ GeV/ $c^2$ for electron (muon) channels $80 < m_{\tau, e/\mu} < 110$ GeV/ $c^2$ is vetoed Number of b-jets = 0 (b-veto category, for W+jets events) Number of b-jets $\geq 1$ (b-tag category, for $t\bar{t}$ events)
QCD control region	$\tau_{had}$ and $e/\mu$ with opposite signs invert $e/\mu$ isolation requirement $\tau_{had}$ and leptons ( $e/\mu$ ) passing “medium” identification requirement $\Delta\phi(\tau_{had}, e/\mu) > 2.4$ $m_T(e/\mu, E_T^{miss}) < 40$ GeV/ $c^2$ $80 < m_{\tau, e/\mu} < 110$ GeV/ $c^2$ is vetoed
Fake lepton control region	$\tau_{had}$ and $e/\mu$ with opposite signs no isolation requirement on $e/\mu$ leptons ( $e/\mu$ ) passing “medium” identification requirement no $\tau_{had}$ passing loose identification $\Delta\phi(\tau_{had}, e/\mu) > 2.4$ $m_T(e/\mu, E_T^{miss}) < 30$ GeV/ $c^2$ $80 < m_{\tau, e/\mu} < 110$ GeV/ $c^2$ is vetoed Number of jets $\geq 1$ (b-veto category) Number of jets $\geq 2$ (b-tag category)
Anti- $\tau_{had}$ control region	$\tau_{had}$ and $e/\mu$ with opposite signs $\tau_{had}$ fail “medium” identification requirement Isolated $e/\mu$ passing “medium” identification requirement $\Delta\phi(\tau_{had}, e/\mu) > 2.4$ $m_T(e/\mu, E_T^{miss}) < 40$ GeV/ $c^2$ $80 < m_{\tau, e/\mu} < 110$ GeV/ $c^2$ is vetoed
Electrons fake taus control region	In electron channel only with cuts: $\tau_{had}$ and electron with opposite signs $\tau_{had}$ passing “medium” identification requirement Isolated electrons passing “tight” identification requirement $\Delta\phi(\tau_{had}, e) > 2.4$ $m_T(e, E_T^{miss}) < 40$ GeV/ $c^2$ $80 < m_{\tau, e} < 110$ GeV/ $c^2$ for 1-prong $\tau_{had}$ $90 < m_{\tau, e} < 100$ GeV/ $c^2$ for 3-prong $\tau_{had}$

Table 5.1: List of control regions used in the analysis for b-veto and b-tag categories and in the electron and muon channels.

Channel	Triggers
Electron	HLT_e24_lhmedium_L1EM20VH (for data)
	HLT_e24_lhmedium_L1EM18VH (for Monte Carlo Samples)
	HLT_e60_lhmedium
	HLT_e120_lhloose
Muon	HLT_mu20_loose_L1MU15
	HLT_mu50

Table 5.2: List of triggers used in the electron and the muon channel. The electron and muon trigger conditions are provided in [132] and [133]

correspond to noisy cells are killed. In the analysis, the pre-selection cuts applied to events are:

- **Good Run List:**

The data we use should satisfy certain quality constraints to be called "good". The data are not "good" if LHC beam was not stable during the data taking, magnets were off or ramping, one or more sub-detectors were off and/or there were too many noisy cells inside the calorimeters. The data taking runs are divided into intervals of time called lumi blocks. Only "good" lumi blocks are listed in the XML format Good Run Lists (GRLs) and events are checked to confirm that they are from one of these lumi blocks.

- **Trigger:**

Events are selected by either a single electron or a single muon trigger. For the electron channel ( $e\tau_{had}$ ), electron triggers with  $p_T$  thresholds of 24 GeV/c, 60 GeV/c and 120 GeV/c are used. For the muon channel ( $\mu\tau_{had}$ ), muons with  $p_T > 55$  GeV/c are required to pass a muon trigger with  $p_T$  threshold of 50 GeV/c, and muons with  $p_T < 55$  GeV/c are required to pass a muon trigger with  $p_T$  threshold of 20 GeV/c. The list of triggers used in the analysis are provided in the table 5.2:

- **Vertex:**

An event is selected if there is at least one primary vertex with at least four tracks.

- **Jet Cleaning:**

Jet cleaning is done to remove those jets that are in bad regions of the detector, noise bursts in the calorimeter and jets coming from non-collision sources. To

remove these jets, certain cleaning cuts are applied according to the recommendations from ATLAS Jet and missing  $E_T$  combined performance group [134]. This includes application of a JVT cut which is the output of the jet vertex tagger algorithm: a method that allows for the identification and selection of jets originating from the hard-scatter interaction through the use of tracking and vertexing information (for details see [135]). A jet whose  $p_T < 50$  GeV/c and  $|\eta| < 2.4$  is required to have a  $|JVT| > 0.64$ . Other cuts include rescaled jet  $p_T > 20$  GeV/c where the energy of the jet is corrected through the jet energy scale calibration.

- **Di-lepton Veto:**

Events with more than one electron or muon are rejected. This reduces the background from Drell-Yan processes  $Z/\gamma^*$ .

- **Lepton Selection:**

At least one isolated electron or muon is required with  $p_T > 30$  GeV/c and  $|\eta| < 2.5$ . The “medium” electron or muon identification criteria are used.

- **Hadronic Tau Selection:**

Events with exactly one tau passing the medium tau identification criteria are selected with  $p_T > 25$  GeV/c and  $|\eta| < 2.3$  and not within the gap between the barrel and endcaps (i.e.  $1.37 < |\eta| < 1.52$ ). For  $|\eta| > 2.3$ , events are mostly background and there is a large mis-modelling of electron to tau fake rate (see section 5.4.1 for details). In events where there is more than one tau candidate the tau with the highest  $p_T$  is selected.

- **Overlap Removal:**

Objects with a geometrical overlap, based on  $\Delta R = \sqrt{(\Delta\phi)^2 + \Delta\eta^2}$  are removed in the following order:

1. Jet axis within  $\Delta R \leq 0.2$  of the leading tau.
2. Jet axis within  $\Delta R \leq 0.2$  of an electron or a muon.
3. Tau axis within  $\Delta R \leq 0.2$  of an electron or a muon.
4. Electron axis within  $\Delta R \leq 0.2$  of a muon.

- **Opposite sign:**

The electron or muon and the hadronic tau have opposite signs.

## 5.2 Event Selection

After preselection cuts are applied, a simple cut based event selection is applied. The event selection consists of the following requirements:

- $\Delta\phi(\tau_{had}, e/\mu) > 2.4$ . The leptonically and hadronically decaying taus follow approximately back-to-back topology. This requirement on the  $\Delta\phi(\tau_{had}, e/\mu)$  reduces the SM background (by nearly 40%) with little loss ( $\sim 1$ -2%) of the signal.
- A cut on the transverse mass between the electron or muon ( $e/\mu$ ) and the missing transverse energy ( $E_T^{miss}$ ). The transverse mass is defined as:

$$m_T(e/\mu, E_T^{miss}) = \sqrt{2p_T(e/\mu)E_T^{miss}(1 - \cos \Delta\phi(e/\mu, E_T^{miss}))} \quad (5.1)$$

We require  $m_T(e/\mu, E_T^{miss}) < 40$  GeV/ $c^2$ . This requirement on  $m_T(e/\mu, E_T^{miss})$  kills the W+jet events significantly (by nearly 80%) and enhances the signal significance. The W+jets background features a Jacobian peak in  $m_T(e/\mu, E_T^{miss})$  at about 80 GeV/ $c^2$ . However, the signal is from a heavy Higgs boson produced with typically low  $p_T$  and decays into two tau leptons where the leptonically decaying tau has one extra neutrino compared to the hadronically decaying tau so the missing energy  $E_T^{miss}$  is close to the electron or muon giving a smaller  $\Delta\phi(e/\mu, E_T^{miss})$  and resulting in smaller  $m_T(e/\mu, E_T^{miss})$  (from equation 5.1).

- The region where  $80 < m_{\tau, e/\mu} < 110$  GeV/ $c^2$  is vetoed in the electron channel only to reduce the  $Z \rightarrow ee$  events where an electron is misidentified as a tau (as explained in the section 5.4.1).

Events satisfying the above selection requirements are categorized into two types depending on whether a b-jet is found in the event:

- b-veto: number of b-jets = 0
- b-tag: number of b-jets  $\geq 1$

The b-tagged jets are required to pass the same selection cuts ( $p_T$ ,  $\eta$  and the Jet Vertex tagger (JVT) cuts) as all other jets. In the b-veto category, the signal selection efficiency

varies between 0.5% at  $m_A=200$  GeV/ $c^2$  to 1% at  $m_A=1.2$  TeV/ $c^2$  for the gluon-fusion production. In the b-tag category, the signal selection efficiency varies between 0.01% at  $m_A=200$  GeV/ $c^2$  to 0.02% at  $m_A=1.2$  TeV/ $c^2$  for the b-associated production. Events passing each cutflow level are shown in tables 5.3 and 5.4.

Cut: Backgrounds	Top	$Z \rightarrow \tau\tau$ +jets	$W$ +jets	Diboson	$Z \rightarrow ee/\mu\mu$ +jets
events	$4.52 \times 10^6$	$1.03 \times 10^6$	$8.42 \times 10^6$	$1.37 \times 10^6$	$7.68 \times 10^6$
pre-selection	$3316.2 \pm 11.2$	$7102.3 \pm 54.5$	$12258.0 \pm 146.4$	$524.4 \pm 5.6$	$1796 \pm 29$
$\Delta\phi(\tau, e/\mu) > 2.4$	$1354.4 \pm 7.1$	$5516.2 \pm 47.8$	$6340.7 \pm 105.5$	$261.1 \pm 3.6$	$1377 \pm 26$
$m_T(e/\mu, E_T^{miss})$	$221.0 \pm 2.9$	$4286.2 \pm 42.2$	$1142.8 \pm 44.8$	$53.3 \pm 1.8$	$920 \pm 21$
b-veto	$51.9 \pm 1.4$	$4216.5 \pm 41.7$	$1116.3 \pm 44.0$	$51.2 \pm 1.7$	$907 \pm 21$
b-tag	$160.6 \pm 2.4$	$36.3 \pm 4.2$	$16.5 \pm 6.6$	$1.4 \pm 0.5$	$5.7 \pm 2.0$
Cut: Signal	ggH200	ggH300	ggH400	ggH500	ggH600
events	14889	19397	21823	23679	19555
pre-selection	$52.8 \pm 1.4$	$105.0 \pm 2.0$	$144.5 \pm 2.4$	$166.8 \pm 2.6$	$181.0 \pm 3.0$
$\Delta\phi(\tau, e/\mu) > 2.4$	$45.4 \pm 1.3$	$96.2 \pm 1.9$	$137.7 \pm 2.4$	$160.1 \pm 2.5$	$173.8 \pm 2.9$
$m_T(e/\mu, E_T^{miss})$	$31.2 \pm 1.1$	$60.5 \pm 1.5$	$89.8 \pm 1.9$	$103.2 \pm 2.0$	$108.8 \pm 2.3$
b-veto	$30.7 \pm 1.1$	$58.9 \pm 1.5$	$87.0 \pm 1.9$	$99.8 \pm 2.0$	$105.2 \pm 2.3$
b-tag	$0.2 \pm 0.1$	$0.6 \pm 0.2$	$1.3 \pm 0.2$	$1.6 \pm 0.3$	$1.6 \pm 0.3$
Cut: Signal	ggH700	ggH800	ggH1000	ggH1200	
events	19714	19770	19349	19760	
pre-selection	$182.5 \pm 3.0$	$187.9 \pm 3.0$	$177.5 \pm 2.9$	$167.9 \pm 2.8$	
$\Delta\phi(\tau, e/\mu) > 2.4$	$176.9 \pm 2.9$	$182.3 \pm 3.0$	$172.1 \pm 2.9$	$163.7 \pm 2.8$	
$m_T(e/\mu, E_T^{miss})$	$112.2 \pm 2.3$	$113.9 \pm 2.4$	$101.7 \pm 2.2$	$95.3 \pm 2.1$	
b-veto	$108.5 \pm 2.3$	$109.0 \pm 2.3$	$97.4 \pm 2.1$	$90.7 \pm 2.1$	
b-tag	$1.5 \pm 0.3$	$2.5 \pm 0.4$	$2.1 \pm 0.3$	$2.4 \pm 0.3$	
Cut: Signal	bbH200	bbH300	bbH400	bbH500	bbH600
events	263138	341364	507632	400204	345886
pre-selection	$53.0 \pm 1.6$	$106.0 \pm 2.3$	$139.2 \pm 2.3$	$157.3 \pm 2.8$	$169.6 \pm 3.5$
$\Delta\phi(\tau, e/\mu) > 2.4$	$48.0 \pm 1.5$	$99.2 \pm 2.2$	$131.5 \pm 2.2$	$149.4 \pm 2.7$	$163.0 \pm 3.4$
$m_T(e/\mu, E_T^{miss})$	$33.1 \pm 1.2$	$65.7 \pm 1.8$	$81.9 \pm 1.8$	$92.2 \pm 2.1$	$102.4 \pm 2.7$
b-veto	$25.5 \pm 1.1$	$46.0 \pm 1.5$	$53.6 \pm 1.4$	$61.4 \pm 1.7$	$65.1 \pm 2.1$
b-tag	$7.0 \pm 0.6$	$18.3 \pm 0.9$	$26.4 \pm 0.9$	$28.9 \pm 1.2$	$34.9 \pm 1.5$
Cut: Signal	bbH700	bbH800	bbH1000	bbH1200	
events	343107	348260	454194	326243	
pre-selection	$170.3 \pm 3.3$	$168.8 \pm 3.2$	$164.6 \pm 2.8$	$151.7 \pm 3.0$	
$\Delta\phi(\tau, e/\mu) > 2.4$	$164.1 \pm 3.2$	$163.1 \pm 3.2$	$159.4 \pm 2.7$	$148.1 \pm 3.0$	
$m_T(e/\mu, E_T^{miss})$	$100.2 \pm 2.5$	$97.2 \pm 2.4$	$89.6 \pm 2.0$	$81.9 \pm 2.2$	
b-veto	$59.9 \pm 2.0$	$57.4 \pm 1.9$	$53.5 \pm 1.6$	$48.0 \pm 1.7$	
b-tag	$37.9 \pm 1.4$	$37.2 \pm 1.4$	$33.9 \pm 1.2$	$31.7 \pm 1.3$	

Table 5.3: The electron channel cutflow in the signal region. The uncertainties provided are only statistical.

Cut: Backgrounds	Top	$Z \rightarrow \tau\tau$ +jets	$W$ +jets	Diboson	$Z \rightarrow ee/\mu\mu$ +jets
events	$4.52 \times 10^6$	$1.03 \times 10^6$	$8.42 \times 10^6$	$1.37 \times 10^6$	$7.68 \times 10^6$
pre-selection	$3914.7 \pm 11.7$	$8599.8 \pm 58.5$	$17590 \pm 190$	$615.9 \pm 5.7$	$2465 \pm 32$
$\Delta\phi(\tau, e/\mu) > 2.4$	$1559.5 \pm 7.4$	$6859.5 \pm 52.1$	$9937 \pm 140$	$314.0 \pm 3.9$	$2050 \pm 29$
$m_T(e/\mu, E_T^{mis})$	$258.9 \pm 3.0$	$5145.7 \pm 45.2$	$1538 \pm 55$	$61.9 \pm 1.8$	$931 \pm 19$
b-veto	$61.3 \pm 1.4$	$5072.5 \pm 44.7$	$1504 \pm 54$	$60.1 \pm 1.8$	$920 \pm 19$
b-tag	$187.8 \pm 2.5$	$35.5 \pm 4.0$	$22.0 \pm 7.2$	$0.7 \pm 0.2$	$5.3 \pm 1.4$
Cut: Signal	ggH200	ggH300	ggH400	ggH500	ggH600
events	14889	19397	21823	23679	19555
pre-selection	$68.5 \pm 1.6$	$112.3 \pm 2.0$	$135.9 \pm 2.2$	$158.7 \pm 2.4$	$169.0 \pm 2.8$
$\Delta\phi(\tau, e/\mu) > 2.4$	$59.6 \pm 1.5$	$102.4 \pm 1.9$	$129.0 \pm 2.2$	$152.0 \pm 2.4$	$163.0 \pm 2.7$
$m_T(e/\mu, E_T^{mis})$	$39.9 \pm 1.2$	$64.7 \pm 1.5$	$83.0 \pm 1.8$	$96.1 \pm 1.9$	$101.9 \pm 2.2$
b-veto	$39.2 \pm 1.2$	$62.9 \pm 1.5$	$80.7 \pm 1.7$	$93.0 \pm 1.8$	$98.3 \pm 2.1$
b-tag	$0.2 \pm 0.1$	$0.7 \pm 0.2$	$1.0 \pm 0.2$	$1.3 \pm 0.2$	$1.5 \pm 0.3$
Cut: Signal	ggH700	ggH800	ggH1000	ggH1200	
events	19714	19770	19349	19760	
pre-selection	$178.3 \pm 2.8$	$184.0 \pm 2.9$	$179.2 \pm 2.8$	$178.4 \pm 2.8$	
$\Delta\phi(\tau, e/\mu) > 2.4$	$172.7 \pm 2.8$	$178.5 \pm 2.8$	$172.7 \pm 2.8$	$173.4 \pm 2.8$	
$m_T(e/\mu, E_T^{mis})$	$107.0 \pm 2.2$	$110.5 \pm 2.2$	$105.3 \pm 2.2$	$101.0 \pm 2.1$	
b-veto	$102.5 \pm 2.1$	$105.9 \pm 2.2$	$100.6 \pm 2.1$	$96.0 \pm 2.0$	
b-tag	$2.3 \pm 0.3$	$2.3 \pm 0.3$	$2.3 \pm 0.3$	$2.7 \pm 0.4$	
Cut: Signal	bbH200	bbH300	bbH400	bbH500	bbH600
events	263138	341364	507632	400204	345886
pre-selection	$65.4 \pm 1.7$	$109.7 \pm 2.2$	$132.6 \pm 2.1$	$146.0 \pm 2.6$	$159.9 \pm 3.2$
$\Delta\phi(\tau, e/\mu) > 2.4$	$58.9 \pm 1.6$	$101.2 \pm 2.1$	$124.6 \pm 2.1$	$137.7 \pm 2.5$	$152.1 \pm 3.1$
$m_T(e/\mu, E_T^{mis})$	$39.1 \pm 1.3$	$65.4 \pm 1.7$	$79.0 \pm 1.6$	$82.5 \pm 2.0$	$93.8 \pm 2.4$
b-veto	$28.7 \pm 1.1$	$45.6 \pm 1.4$	$51.1 \pm 1.3$	$53.0 \pm 1.6$	$57.9 \pm 1.9$
b-tag	$9.6 \pm 0.6$	$18.4 \pm 0.9$	$26.0 \pm 0.9$	$27.5 \pm 1.1$	$33.6 \pm 1.4$
Cut: Signal	bbH700	bbH800	bbH1000	bbH1200	
events	343107	348260	454194	326243	
pre-selection	$170.4 \pm 3.0$	$172.9 \pm 3.0$	$171.7 \pm 2.6$	$166.6 \pm 3.0$	
$\Delta\phi(\tau, e/\mu) > 2.4$	$163.5 \pm 3.0$	$166.2 \pm 3.0$	$166.0 \pm 2.6$	$162.3 \pm 2.9$	
$m_T(e/\mu, E_T^{mis})$	$99.6 \pm 2.3$	$97.8 \pm 2.3$	$96.3 \pm 1.9$	$89.9 \pm 2.1$	
b-veto	$62.2 \pm 1.8$	$58.7 \pm 1.8$	$57.4 \pm 1.5$	$55.2 \pm 1.6$	
b-tag	$35.0 \pm 1.3$	$36.8 \pm 1.3$	$36.6 \pm 1.2$	$32.5 \pm 1.3$	

Table 5.4: The muon channel cutflow in the signal region. The uncertainties provided are only statistical.

### 5.3 Di-tau Mass Reconstruction

The mass of the di-tau system is used as a final discriminant between the signal and the background. Due to the presence of neutrinos from the tau decays, the true di-tau mass reconstruction is challenging. Therefore, in this analysis mass the total transverse mass is used. This is defined as:

$$m_T^{tot} = \sqrt{m_T^2(E_T^{miss}, e/\mu) + m_T^2(E_T^{miss}, \tau_h) + m_T^2(e/\mu, \tau_h)} \quad (5.2)$$

where  $m_T(a, b)$  is defined as:

$$m_T(a, b) = \sqrt{2p_T(a)p_T(b)(1 - \cos \Delta\phi(a, b))} \quad (5.3)$$

$m_T^{tot}$  is chosen as the final variable due to the fact that it is less complicated and does not take much computation time as compared to other mass reconstruction algorithms such as the missing mass calculator (described in ref. [136]) and the MOSAIC (Matrix-element Oriented SAMpling Calculator) algorithm which reconstructs tau lepton pair events using the matrix-element of tau lepton decay and which is still in an early stage of development.

## 5.4 Background Estimation

In the analysis, background estimation is categorized based on whether the hadronic tau and/or the  $e/\mu$  are real or faked by jets. Backgrounds where both the tau and the electron or muon are real or where electrons are misidentified as taus are estimated through simulation. A dedicated data-driven method is used for estimation of background for the processes where taus or both electrons or muons and taus are misidentified. The contribution of backgrounds where only the electron or muon is misidentified is negligible.

### 5.4.1 Background Estimation Through Simulation

#### Backgrounds with correctly identified taus and electrons or muons

Backgrounds with real hadronic taus and electrons or muons are estimated through Monte Carlo simulated samples. These backgrounds are  $Z/\gamma^* \rightarrow \tau\tau$ , where one tau decays leptonically and the other hadronically, top ( $t\bar{t} \rightarrow W^-W^+b\bar{b} \rightarrow \tau_{had}l\nu\bar{b}b$ ) and the diboson events (WW, ZZ, WZ). The Monte Carlo simulated samples are corrected

using the recommended ATLAS data-driven scale factors for trigger, reconstruction and identification efficiencies.

### Electron faking tau

The main source of this background comes from  $Z/\gamma^* \rightarrow ee$  events, where the electron or muon is genuine and the hadronic tau ( $\tau_{had}$ ) is faked by an electron. The cut on  $\tau - e/\mu$  mass ( $m_{\tau,e/\mu}$ ) from 80-110 GeV/c<sup>2</sup> in the signal region aims to reduce this background.

When compared with the data, the simulated samples have large mis-modelling for the electron faking  $\tau_{had}$  as a function of  $\tau_{had}$   $\eta$ . Electron mis-modelling rate increases significantly in the  $\eta > 2$  and  $\eta \sim 0$  regions. A control region enriched in  $Z/\gamma^* \rightarrow ee$  events is defined (as described in table 5.1 on page 89) to derive scale factors that are applied to the simulation to correct for difference between the simulation and the data. The control region cuts use a requirement on the invariant mass between the hadronic tau and the lepton ( $e/\mu$ ):  $80 < m_{\tau,e/\mu} < 110$  GeV/c<sup>2</sup> (for 1-prong taus) or  $90 < m_{\tau,e/\mu} < 100$  GeV/c<sup>2</sup> (for 3-prong taus). In the 3-prong case, the  $\tau - e/\mu$  mass window is smaller in order to reduce the backgrounds which are larger relative to the 1-prong case.

The scale factor is calculated using:

$$SF = \frac{P_{mis}(Data)}{P_{mis}(MC)} \quad (5.4)$$

where  $P_{miss}$  is the misidentification rate of electrons that are reconstructed as taus, calculated using a tag and probe method on  $Z \rightarrow ee$  events in which a tight electron acts as a “tag” and the other electron is used as a “probe” to check if it is reconstructed as an hadronic tau. The misidentification rate calculated as:

$$P_{mis} = \frac{N(\text{probe passing “medium” tau ID})}{N(\text{probe})} \quad (5.5)$$

For the 3-prong  $\tau_{had}$ , a constant scale factor of  $1.15 \pm 0.50$  is applied as there was no good evidence of the eta dependence (as shown in figure 5.1). The scale factor for 1-prong  $\tau_{had}$  varies with  $\eta$  and is shown in the figure 5.2.

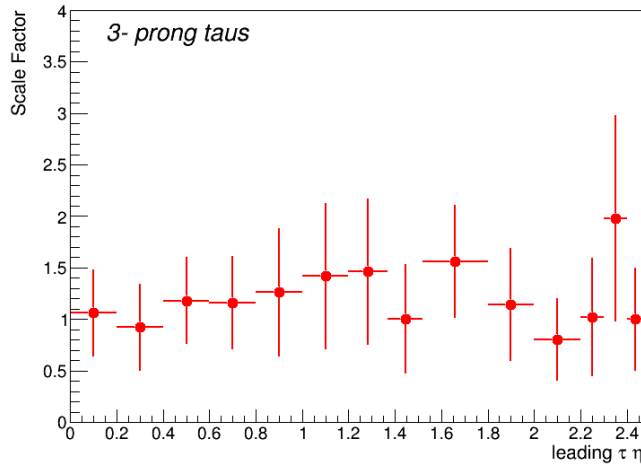


Fig. 5.1: Scale factor for electron faking 3- prong  $\tau_{had}$  as a function of leading  $\tau_{had} \eta$

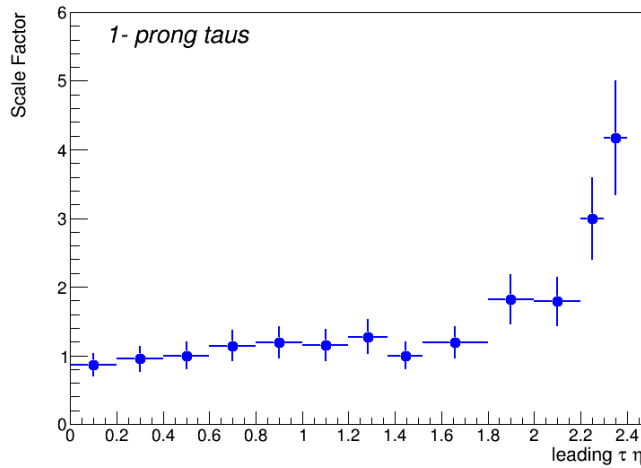


Fig. 5.2: Scale factor for electron faking 1- prong  $\tau_{had}$  as a function of leading  $\tau_{had} \eta$ . Monte Carlo simulation has large mis-modelling near  $\eta > 2.3$ , therefore events with  $\tau_{had} \eta > 2.3$  are vetoed in the signal region.

#### 5.4.2 Data-Driven Background Estimation: The Combined Fake Factor Method

In Monte Carlo event generation, simplified QCD models are used to simulate processes such as the hard interaction, parton showering and hadronization that occur in the real collision. Therefore, the rate of jets being misidentified as electrons, muons or  $\tau_{had}$  is not well modelled in simulation. This is why, a data-driven method is used to estimate

these background events. The fake factor method calculates the misidentification rate of a certain background by calculating this rate in a control region enriched with particular background events. The main sources of background where jets fake one or both of the final particles ( $e/\mu$  and  $\tau_{had}$ ) are QCD multijets, W+jets and top ( $t\bar{t}$  and single top) for the b-tag category. The W+jets events are mostly composed of light quark jets whereas jets from QCD multi-jet processes are mostly gluon-initiated jets which tend to have lower fake rates to taus compare to quark-initiated jets. This is because in the hadronization process, quark-initiated jets spread out less than gluon-initiated jets and therefore have a narrow shower width, similar in appearance to a tau. Hence separate fake factors for W+jets  $FF(W+jets)$  and QCD  $FF(QCD)$  are calculated using the respective control regions defined in table 5.1. The contributions of other backgrounds are very small in those regions so we can assume minimal cross contamination. Once the fake factors are calculated, a combined fake factor is determined and subsequently applied in the anti-tau region which has the same criteria as the signal region except that the  $\tau_{had}$  is required to fail the “medium” identification requirement, defined in table 5.1, by weighting the events with this factor. This gives an estimate of the total fake rate from jets in the signal region.

The combined fake factor ( $FF_{comb}$ ) is defined as:

$$FF_{comb} = FF(W + jets) \times (1 - r_{QCD}) + FF(QCD) \times r_{QCD} \quad (5.6)$$

where,  $r_{QCD}$  is the fraction of QCD multijet events in the anti-tau region.  $1 - r_{QCD}$  refers to contributions from W+jets and top in the b-tag category. Contributions from all other electroweak processes, such as Drell Yan Process, are negligible. Details of fake factors related to QCD, W+jets and the fraction  $r_{QCD}$  are provided in following sections.

### **Background with an Electron or Muon and a Jet Faking a Tau : FF (W+jets)**

In this category, the electron or muon is real while a quark or gluon initiated jet fakes  $\tau_{had}$ . This background is dominated by W+jets and top (single top and  $t\bar{t}$ ) events in the b-veto and b-tag categories respectively. A smaller contribution also comes from

$Z/\gamma^*$ +jets events. In W+jets event, the light quark initiated jets are mis-identified as  $\tau_{had}$  whereas in  $t\bar{t}$  events,  $\tau_{had}$  can also be faked by the b-quark initiated jets. Therefore, separate fake rates are calculated for W+jets and top events in their respective control regions (as defined in table 5.1) to check the effects of jet flavour composition.

The fake factor in W+jets (top) control region is defined as:

$$FF(\text{W+jets (top)}) = \frac{N(\text{pass "medium" tau ID})}{N(\text{fail "medium" tau ID and jet BDT} > 0.35)} \quad (5.7)$$

where  $N(\text{pass "medium" tau ID})$  is the number of  $\tau_{had}$  candidates that pass "medium" tau identification criteria and  $N(\text{fail "medium" tau ID and jet BDT} > 0.35)$  is the number of  $\tau_{had}$  candidates that fail "medium" tau identification criteria but have a jet BDT score  $> 0.35$ .

Table 5.5 and 5.6 show the W+jets control region composition for the electron and muon channel in the b-veto category and b-tag category respectively. The uncertainty shown here is only due to the finite number of generated events in the simulated samples.

	Electron Channel	Muon Channel
Data	56020	100071
W+jets	$40643 \pm 266$	$85068 \pm 414$
Top	$263 \pm 9$	$358 \pm 12$
$Z \rightarrow ll$	$1170 \pm 22$	$2411 \pm 31$
$Z \rightarrow \tau\tau$	$192 \pm 8$	$778 \pm 17$
Diboson	$534 \pm 11$	$837 \pm 9$
Total non-W+jets bkg (except QCD)	$2159 (\sim 5\%)$	$4384 (\sim 5\%)$

Table 5.5: W+jets control region composition for the electron and muon channel in the b-veto category. The remainder corresponds to the multijet background that is estimated through data.

The purity of the W+jets background in the b-veto category of the control region is about 95%, while in the b-tag category both the W+jets and  $t\bar{t}$  processes contribute and W+jets are nearly 15% of the total events.

Events with real electron or muon, real electron or muon faking tau and the real  $\tau_{had}$  are subtracted from the data using the simulation. Fake factors calculated using equation (5.7) in W+jets control region is shown in figure 5.3. In the b-tag category, fake-factors

	Electron Channel	Muon Channel
Data	4081	5927
Top	$2782 \pm 10$	$3972 \pm 12$
W+jets	$342 \pm 25$	$506 \pm 32$
$Z \rightarrow ll$	$15 \pm 2$	$21 \pm 3$
$Z \rightarrow \tau\tau$	$4 \pm 1$	$8 \pm 2$
Diboson	$20 \pm 1$	$34 \pm 2$
Total non-W+jets/Top bkg (except QCD)	39 ( $\sim 1\%$ )	63 ( $\sim 1\%$ )

Table 5.6: W+jets control region composition for the electron and muon channel in the b-tag category. The remainder corresponds to the multijet background that is estimated through data.

without b-tag requirement (figure 5.4) are used in the analysis to improve statistical precision. Additionally, fake factors for the combined electron and muon channels are used because there is no significant difference observed between the factors measured in the two channels.

## Background from Jets Misidentified as Leptons

In this category, both identified  $e/\mu$  and  $\tau_{had}$  are quark or gluon initiated jets. This type of background is dominated by QCD multi-jet processes. Separate fake factors for jets faking electrons or muons and jets faking taus are calculated.

### 1. Jet to Tau Fake Factor: $FF(QCD)$

A multijet enriched control region is defined (as described in table 5.1) with selection cuts similar to the signal region cuts except that the isolation requirement on the electron or the muon is inverted. Table 5.7 and 5.8 show the QCD control region composition for the electron and muon channel in the b-veto and b-tag category respectively. The purity of multi-jet events in this control region is  $\sim 97-98\%$ .

The fake factors in a QCD control region are calculated using:

$$FF(QCD) = \frac{N(\text{pass "medium" tau ID})}{N(\text{fail "medium" tau ID and jet BDT} > 0.35)} \quad (5.8)$$

Fake factors for the b-veto and b-tag categories are shown in figure 5.5 and 5.6. Separate fake factors for the electron and muon channel are also calculated: but

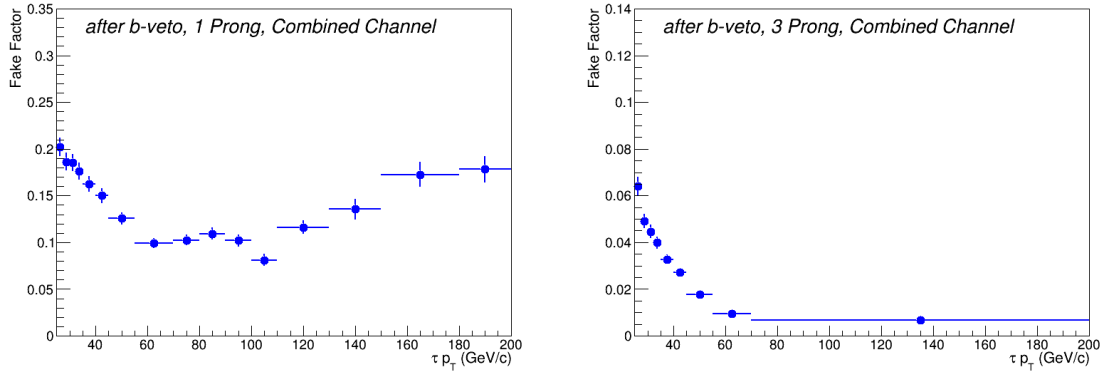


Fig. 5.3: Fake factors from the W+jets control region in the b-veto category for 1-prong (left) and 3-prong (right) taus. The error bars correspond to statistical uncertainties only.

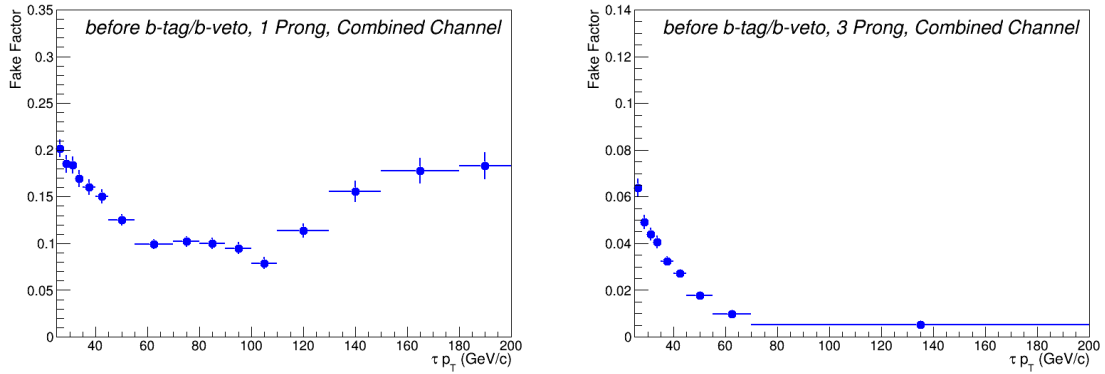


Fig. 5.4: Fake factors from the W+jets control region before the b-veto/b-tag (the inclusive category) for 1-prong (left) and 3-prong (right) taus. The error bars correspond to statistical uncertainties only.

these agreed within statistical uncertainty, therefore only combined channel is considered.

## 2. Jet to Lepton ( $e/\mu$ ) Fake Factor: FF(Lep)

A fake lepton control region is defined (as described in table 5.1) to contain enhanced number of events with jets misidentified as electrons or muons. These cuts are designed to reduce the contamination from real electrons or muons and to bring the selection of the control region close to the signal region selection. The cut on  $m_T(l, E_T^{miss})$  reduces the W+jets backgrounds and makes the event

	Electron Channel	Muon Channel
Data	83662	64402
W+jets	$978 \pm 41$	$1326 \pm 54$
Top	$37 \pm 1$	$60 \pm 1$
$Z \rightarrow ll$	$191 \pm 9$	$116 \pm 7$
$Z \rightarrow \tau\tau$	$305 \pm 11$	$414 \pm 13$
Diboson	$15 \pm 1$	$17 \pm 1$
Total non-multijet bkg	1526 ( $\sim 2\%$ )	1933 ( $\sim 3\%$ )

Table 5.7: The QCD control region composition for the electron and muon channel in the b-veto category. The uncertainty shown here are only statistical. The remaining events are QCD multijets.

	Electron Channel	Muon Channel
Data	3816	5799
W+jets	$5 \pm 3$	$24 \pm 7$
Top	$77 \pm 2$	$115 \pm 2$
$Z \rightarrow ll$	$2 \pm 1$	$1 \pm 1$
$Z \rightarrow \tau\tau$	$4 \pm 2$	$6 \pm 2$
Diboson	$1 \pm 0$	$1 \pm 0$
Total non-multijet bkg	89 ( $\sim 2\%$ )	147 ( $\sim 2\%$ )

Table 5.8: The QCD control region composition for the electron and muon channel in the b-tag category. The uncertainty shown here are only statistical. The remaining events are QCD multijets.

selection similar to the signal. The requirement of at least one selected jet (in addition to the b-tagged jet for the b-tag category) enhances the fraction of QCD di-jet events. The fake lepton control region composition is provided in tables 5.9 and 5.10 for the b-veto and b-tag categories in the electron and muon channels.

	Electron Channel	Muon Channel
Data	2511210	507760
W+jets	$244500 \pm 1700$	$67700 \pm 900$
Top	$3020 \pm 40$	$1366 \pm 27$
$Z \rightarrow ll$	$174700 \pm 700$	$5130 \pm 120$
$Z \rightarrow \tau\tau$	$10700 \pm 180$	$4340 \pm 110$

Table 5.9: The fake lepton control region composition for the electron and muon channel in the b-veto category. The remainder corresponds to the QCD multijet background that is estimated through data.

The lepton fake factor ( $FF_{lep}$ ) is calculated using the “gradient” lepton isolation requirement. The “gradient” isolation is  $p_T$  and  $\eta$  dependent and is based on the calorimeter and track information as described in [137] and [138]. This working

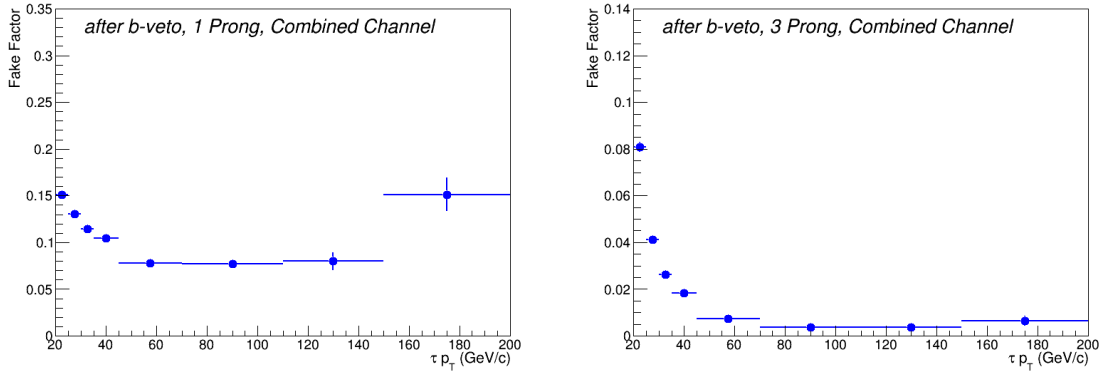


Fig. 5.5: Fake factors from the QCD control region in the b-veto category for 1-prong (left) and 3-prong (right) taus. The error bars correspond to statistical uncertainties only.

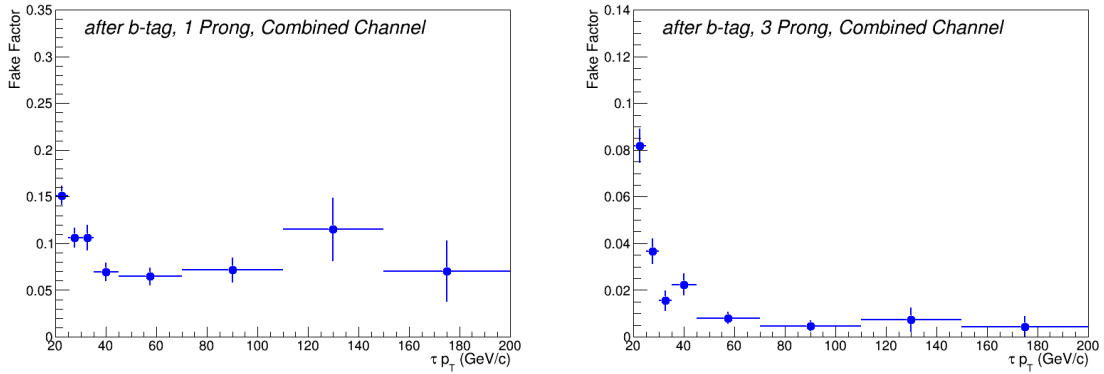


Fig. 5.6: Fake factors from the QCD control region in the b-tag category for 1-prong (left) and 3-prong (right) taus. The error bars correspond to statistical uncertainties only.

point is defined with efficiency and fake lepton rejection intermediate between the loose and tight isolation selections.  $FF_{lep}$  is calculated using the formula:

$$FF_{lep} = \frac{N(\text{pass "gradient" lepton isolation})}{N(\text{fail "gradient" lepton isolation})} \quad (5.9)$$

where  $N(\text{pass "gradient" lepton isolation})$  is the number of leptons passing the "gradient" lepton isolation requirement whereas  $N(\text{fail "gradient" lepton isolation})$  is the number of leptons failing the "gradient" lepton isolation criterion of the signal region.

	Electron Channel	Muon Channel
Data	103572	42587
W+jets	$2860 \pm 190$	$810 \pm 100$
Top	$2870 \pm 40$	$1378 \pm 28$
$Z \rightarrow ll$	$1400 \pm 70$	$91 \pm 18$
$Z \rightarrow \tau\tau$	$360 \pm 40$	$101 \pm 18$

Table 5.10: The fake lepton control region composition for the electron and muon channel in the b-tag category. The remainder corresponds to the QCD multijet background that is estimated through data.

The true electron or muon contamination in this region is subtracted from the data using the simulated samples. The fake factors are parametrized in lepton eta ( $\eta$ ) and separated into two lepton  $p_T$  bins in the muon channel. Separate fake factors are calculated in the b-veto and b-tag categories. The lepton fake factors are shown in figure 5.7 and 5.8 for the electron and muon channels.

$FF_{lep}$  is applied in the anti- $\tau_{had}$  region when estimating fraction of multijet events ( $r_{QCD}$ ) as described below.

### Parameterization Test on FF (QCD) and FF (W+jets)

Since the fake factors are parameterized only in  $p_T$  of the  $\tau_{had}$ , it could lead to imperfect modelling of other variables. Therefore a test is performed in both QCD and W+jets control region, in which the jet to tau fake factors (FF (QCD) and FF (W+jets)) are applied back to the same regions where they were derived by re-weighting the events which fail the “medium” tau ID requirement by these fake factors. The ratio plots between the number of events which failed “medium” tau ID but weighted with the fake factors to the number of events passed “medium” tau ID are shown in figure 5.9 and 5.10 for QCD and W+jets. These ratios are parametrized in  $\Delta\phi(e/\mu, E_T^{miss})$  and  $\Delta\phi(\tau_{had}, E_T^{miss})$  in the QCD and W+jets control regions respectively. Ideally, these ratios should be one but this was not the case. Therefore, discrepancies in the ratio plots are used as systematic uncertainties in the fake factor estimation and full details about the systematic uncertainties included in this thesis are provided in the next chapter.

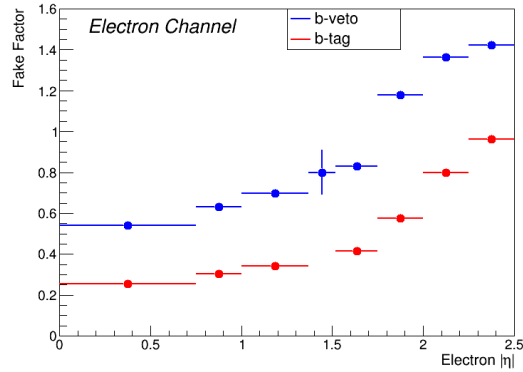


Fig. 5.7: Fake factors from the fake lepton control region in the electron channel for the b-veto and b-tag categories. The error bars correspond to statistical uncertainties only. The unusual behaviour near  $\eta = 1.5$  correspond to the transition region between the barrel and endcap electromagnetic calorimeters at  $1.37 < |\eta| < 1.52$

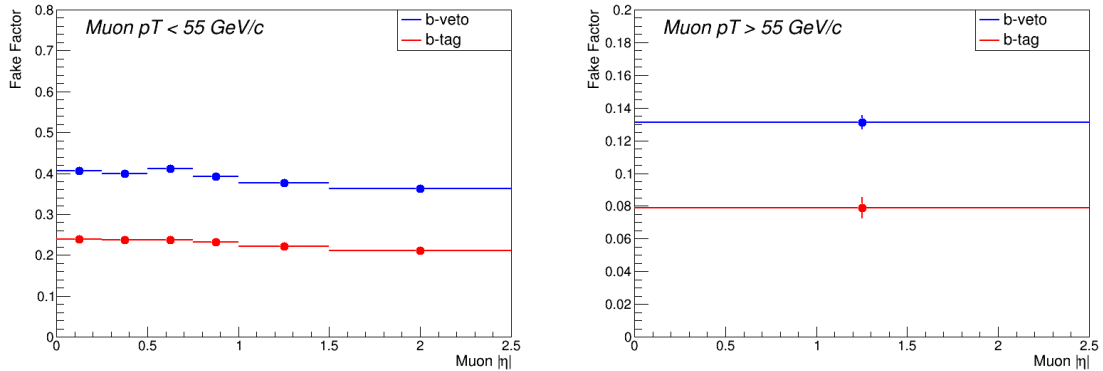


Fig. 5.8: Fake factors from the fake lepton control region in the muon channel with  $p_T < 55 \text{ GeV}/c$  (left) and  $p_T > 55 \text{ GeV}/c$  (right) for the b-veto and b-tag categories. The error bars correspond to statistical uncertainties only. Due to low statistics in lepton control region with muon  $p_T > 55 \text{ GeV}/c$ , fake factors in only one bin are considered

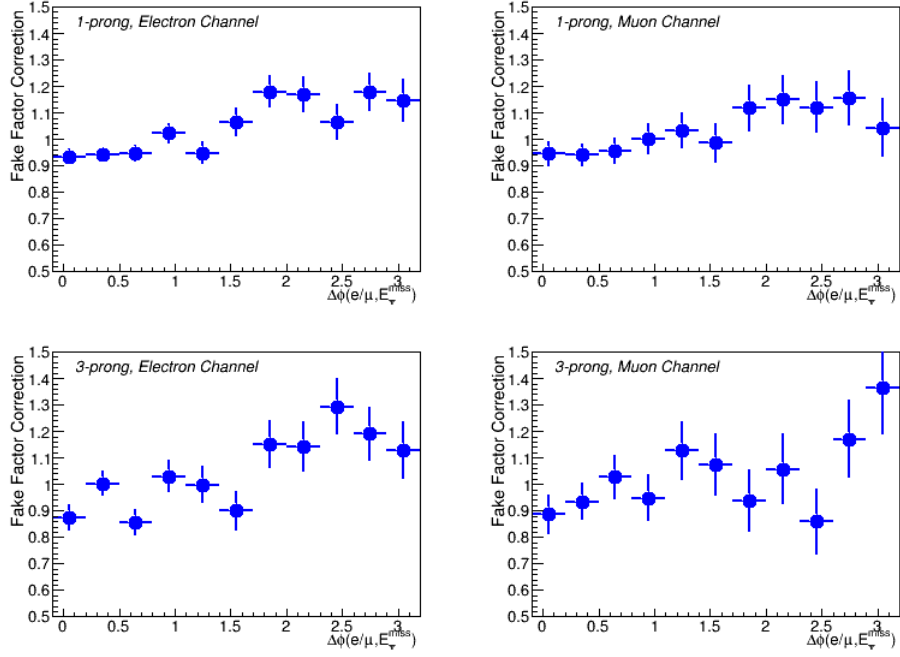


Fig. 5.9: Ratio plots of the parametrization test on FF(QCD) as a function of  $\Delta\phi(e/\mu, E_T^{miss})$  in electron and muon channels and for 1- and 3- prong taus.

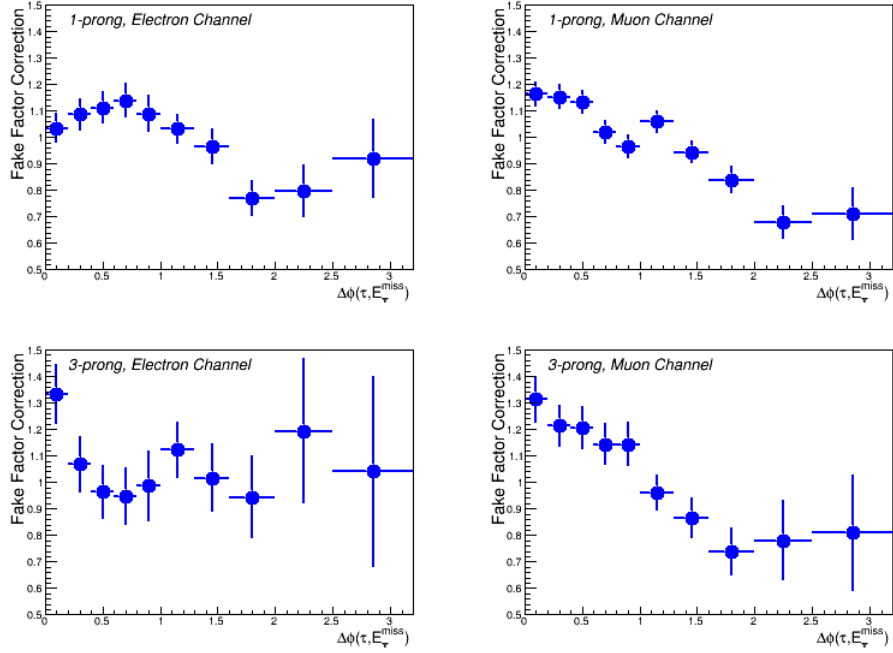


Fig. 5.10: Ratio plots of the parametrization test on FF(W+jets) as a function of  $\Delta\phi(\tau_{had}, E_T^{miss})$  in electron and muon channels and for 1- and 3- prong taus.

### Multijet Fraction in the Anti- $\tau_{had}$ Region: ( $r_{QCD}$ )

The  $r_{QCD}$  is a measure of the fraction of events arising from QCD multijet processes in the anti- $\tau_{had}$  region. It is defined as:

$$r_{QCD} = \frac{N(\text{data}) - N(\text{true } \tau_{had}, \text{MC})_{\text{anti-iso, anti-tau region}}}{N(\text{data}) - N(\text{true } \tau_{had}, \text{MC})_{\text{anti-tau region}}} \quad (5.10)$$

The anti-isolated and anti-tau region in the numerator is same as the signal region except for the lepton isolation requirement and the “medium” tau identification criteria of the signal region which are inverted. The anti-isolated is weighted by the jet to lepton ( $e/\mu$ ) fake factors ( $FF_{lep}$ ). The QCD multijet fraction  $r_{QCD}$  is parametrized in the  $p_T$  of the tau candidate and determined separately for the b-veto and b-tag categories as well as the electron and muon channels (shown in figures 5.11 and 5.12).

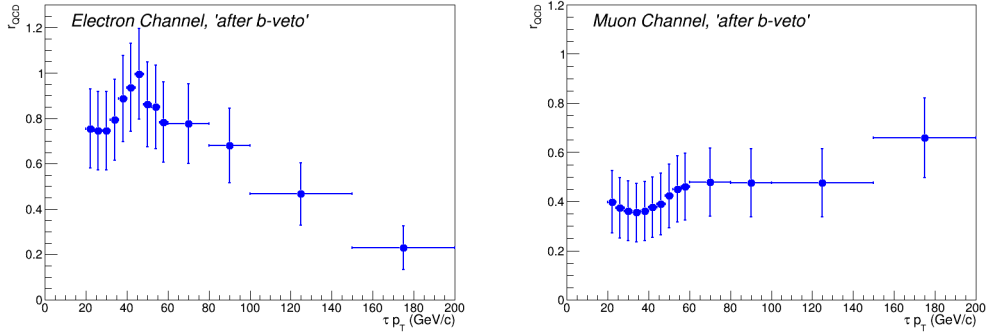


Fig. 5.11: The fraction of QCD multijet events ( $r_{QCD}$ ) in the b-veto category for the electron and muon channels.

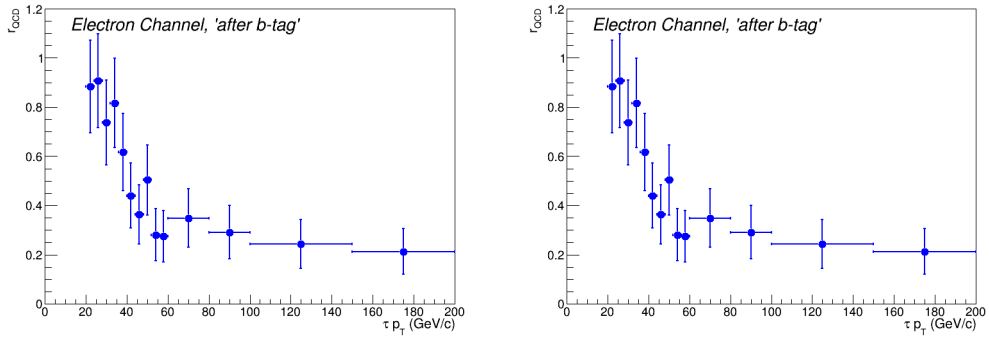
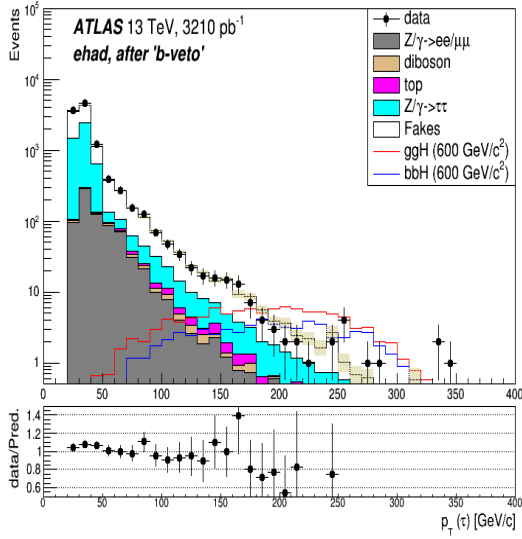


Fig. 5.12: The fraction of QCD multijet events ( $r_{QCD}$ ) in the b-tag category for the electron and muon channels.

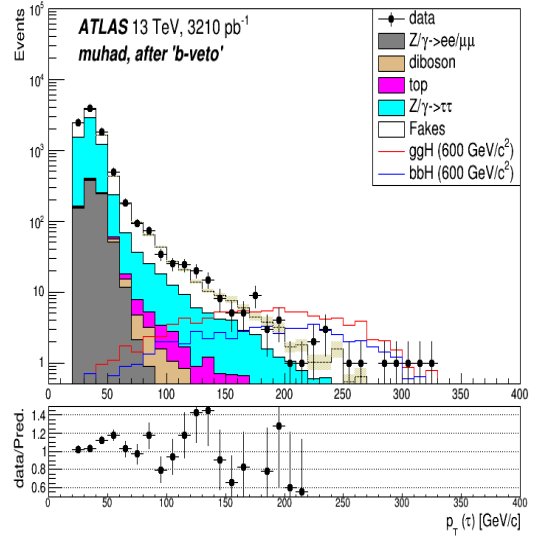
## 5.5 Validation of the Signal Region

Once total background in the signal region is estimated, the region is unblinded using the full 2015 data corresponding to  $3.21 \text{ fb}^{-1}$  with no change in the signal selection cuts. The predicted background matches the data and no statistically significant difference consistent with a signal is observed as seen in figures 5.13 and 5.14 where the distributions of the transverse momentum ( $p_T$ ) of the hadronic tau ( $\tau_{had}$ ) for the b-veto and b-tag categories in the electron and muon channels are shown. To illustrate, Monte Carlo signal samples normalized to a cross section of 1 pb and an integrated luminosity of  $3.21 \text{ fb}^{-1}$  are also shown. The uncertainties provided in the figures (shaded regions) are only statistical uncertainties associated with the total background prediction.

Other important distributions of the signal region are provided in the next chapter (figures 6.11 to 6.18) where the systematic uncertainties associated with the background estimation are also shown. The signal region yields of the data and the Monte Carlo signal and background events with the statistical and systematic uncertainties are also provided in the next chapter (tables 6.7 and 6.8), for all categories.

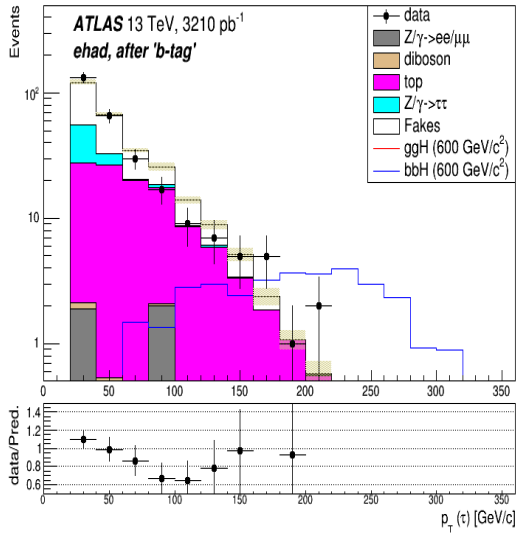


(a) Electron Channel

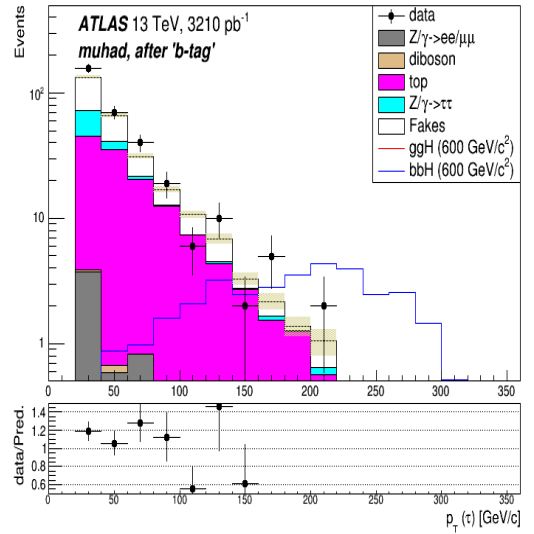


(b) Muon Channel

Fig. 5.13: Distribution of the transverse momentum ( $p_T$ ) of the tau candidate in the signal region, in the b-veto category for the electron (left) and the muon (right) channel



(a) Electron Channel



(b) Muon Channel

Fig. 5.14: Distribution of the transverse momentum ( $p_T$ ) of the tau candidate in the signal region, in the b-tag category for the electron (left) and the muon (right) channel

---

## CHAPTER 6

# Systematic Uncertainties

In addition to statistical uncertainties, several sources of systematic uncertainties could significantly affect our measurements such as the background modelling in the signal region, the predicted signal, background event yields and the expected shape of the total transverse mass distributions. In this analysis, the systematic uncertainties are divided into four categories: systematics related to the background estimation methods; systematics related to the luminosity and theoretical cross section measurements; systematics related to the detector simulation; and systematics related to the Monte Carlo (MC) modelling.

## 6.1 Background Estimation Systematics

The combined fake factor method used to predict backgrounds (see section 5.4.2) have several sources of systematic errors which are discussed below:

### 6.1.1 QCD Fake Factors

QCD fake factors calculate the probability that jets fake hadronic taus and leptons ( $e/\mu$ ). The systematic uncertainties involved in the QCD fake factor calculations include:

1. **Subtraction of real hadronic taus ( $\tau_{had}$ ):** In the data-driven fake factor method, the real hadronic taus ( $\tau_{had}$ ) are estimated using simulated Monte Carlo samples and then subtracted from the data. The anti-isolated region, where the QCD fake factors are measured, is dominated by fake hadronic taus and the contamination from events with real hadronic taus is of the order of 1-2% percent. Therefore, tiny variations on the simulated real hadronic taus have no noticeable

effect on the fake factors. This is why, a high variation of 50% on the subtraction of simulated events with true  $\tau_{had}$  is considered.

2. **Selection cuts:** The QCD fake factor is measured in a region with inverted isolation cuts on the leptons ( $e/\mu$ ). A systematic is considered to take into account whether the inverted lepton isolation cut biases the fake factors. In order to test this, fake factors are calculated in a control region that has same selection cuts as in the QCD control region except the events are required to have isolated electrons or muons and the hadronic tau and the lepton (electron or muon) have the same electric charge. The difference between the fake factors measured in this region and in the nominal QCD control region are taken as a systematic uncertainty.
3.  $\Delta\phi(e/\mu, E_T^{miss})$  **correction:** QCD fake factors are parametrized in the transverse momentum of the  $\tau_{had}$  that could cause errors when modelling other variables. A parametrization test (as described in section 5.4.2) is performed in which the ratio of events that pass the tau identification to the events that fail the tau identification requirement but weighted with the QCD fake factors is calculated, and is parameterized in  $\Delta\phi(e/\mu, E_T^{miss})$ . On the average, the ratio varies about 10% from 1 (see plot 5.9) therefore an overall uncertainty of 10% is considered from this correction.

These systematics are calculated with different selection cuts and have minimal event overlap. Therefore, they are un-correlated and added in quadrature. Figure 6.1 and 6.2 show the QCD fake factor distributions for b-veto and b-tag category respectively (the error bars show the statistical uncertainties, and the shaded regions show the systematic uncertainties).

### 6.1.2 W+Jets/Top Fake Factors

W+jets/top fake factors provide the probability of a jet faking hadronic taus. The effect of the following systematics are considered:

1. **Extrapolation from high to low  $m_T$ :** The fake factors in the W+jets control region are derived in the high  $m_T(e/\mu, E_T^{miss})$  region. The control region definition assumes that these fake factors are the same in the low  $m_T(e/\mu, E_T^{miss})$  signal

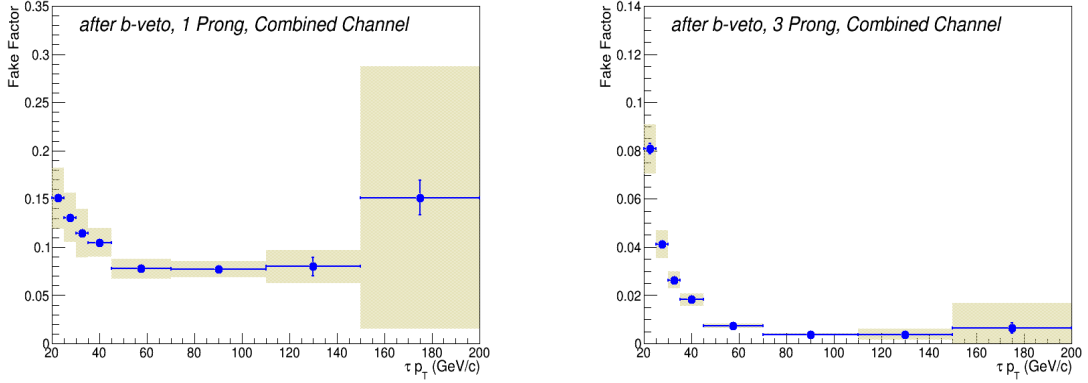


Fig. 6.1: QCD fake factors for 1- and 3-prong taus in the b-veto category. The error bars show the statistical error while the shaded regions show the systematic error.

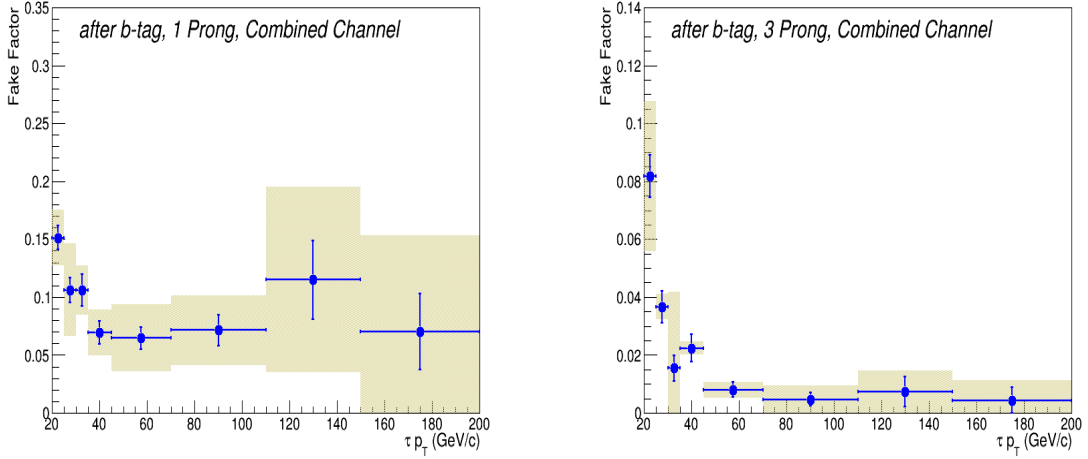


Fig. 6.2: QCD fake factors for 1- and 3-prong taus in the b-tag category. The error bars show the statistical error while the shaded regions show the systematic error.

region. This extrapolation gives rise to an associated systematic uncertainty. In order to determine the systematics,  $W$ +jets fake factors ( $FF(W + jets)$ ) are calculated using the Monte Carlo  $W$ +jets events in the  $W$ +jets control region. Since fake factor aims to calculate the ratio of the number of events passing the signal region to the number of events passing the anti- $\tau_{had}$  region. Therefore, the ratio of the Monte Carlo  $W$ +jets events in the signal region over the anti- $\tau_{had}$  region ( $FF_{SR/Anti-\tau}$ ) are also calculated. The relative difference between these two fake factors ( $FF(W + jets)$  and  $FF_{SR/Anti-\tau}$ ) is calculated using the following relation:

$$\Delta_{rel} = \frac{FF(W + jets) - FF_{SR/Anti-\tau}}{FF(W + jets)} \quad (6.1)$$

The relative difference is shown in the table 6.1 for 1- and 3-prong taus:

$p_T$ (GeV/c)	1-prong (%)	3-prong (%)
25-30	$30 \pm 5$	$15 \pm 9$
30-45	$16 \pm 5$	$30 \pm 9$
45-200	$21 \pm 5$	$23 \pm 12$

Table 6.1: The relative difference between the Monte Carlo W+jets events in the signal region over the anti- $\tau_{had}$  region to the W+jets control region fake factors calculated through the Monte Carlo samples. The error provided here are statistical

Only three bins are used to minimize statistical errors. A systematic of about 20% (average of numbers across three  $p_T$  bins) is considered.

- 2. Contamination from other backgrounds:** The impurity of the W+jets control region can bias the calculation of the fake factor and is therefore taken as a systematic. The major contribution in the contamination which comes from QCD multi-jet events. To estimate the difference between the data and the total of the non-QCD Monte Carlo samples is taken as the QCD multi-jets contamination. The fake factor calculated in this region is assumed to follow the QCD multijet fake factors (as described in Section 5.4.2). The QCD fake factors ( $FF_{QCDW}$ ) in the W+jets control region (calculated using data minus all Monte Carlo non-multijet background including W+jets) are compared to the QCD fake factors ( $FF(QCD)$ ) calculated in the QCD control region. The relative difference between these fake factors (as calculated using equation 6.2) is taken as a systematic which is 3% for 1-prong and 1% for 3-prong.

$$\Delta_{rel} = \frac{FF(QCD) - FF_{QCDW}}{FF(QCD)} \quad (6.2)$$

- 3. Subtraction of real hadronic taus ( $\tau_{had}$ ):** In the fake factor calculation, the real hadronic taus are subtracted from the data using the Monte Carlo simulation. A 10% uncertainty in the number of simulated real  $\tau_{had}$  is assumed when subtracting through the data. This number is an estimation based on the effects of the  $\tau_{had}$  systematics on the Monte Carlo samples such the uncertainties in the reconstruction and identification techniques.

4.  $\Delta\phi(\tau, E_T^{miss})$  **correction:** A parameterization test, similar to the one performed for the QCD fake factors, is also implemented for the W+jets fake factors (as described in section 5.4.2). In this test, the ratio of number of events that pass the tau identification to the number of events that fail the tau identification requirement but weighted with the W+jets fake factors is calculated. This ratio is parameterized in  $\Delta\phi(\tau, E_T^{miss})$ . An overall uncertainty of 15% is considered from this correction as the ratio varies on average nearly 15% from 1 (see plot 5.10).

Similar to the systematics in the W+jets/Top fake factors, these systematics are also un-correlated and added in quadrature. Figure 6.3 and 6.4 show the fake factor distributions for b-veto and b-tag category respectively (the error bars show the statistical uncertainties, and the shaded regions show the systematic uncertainties).

### 6.1.3 Systematic uncertainties in the $r_{QCD}$ Calculations

The calculation of the QCD multijets fraction in the anti- $\tau_{had}$  region uses the lepton fake factors calculated in the lepton control region (as explained in 5.4.2). Therefore, the uncertainties associated to the lepton fake factors effect the  $r_{QCD}$  calculation in addition to the uncertainties in the anti- $\tau_{had}$  control region. The  $r_{QCD}$  systematics considered in the analysis are:

1. **Real lepton subtraction:** Similar to the real hadronic taus, real leptons are also subtracted from the data using the Monte Carlo simulation when calculating the lepton fake factors in the lepton control region. A 10% uncertainty in the number of subtracted simulated real leptons is considered. The number is estimated by taking into account effects of all relevant systematics associated to the simulated leptons such the uncertainties in the reconstruction and identification techniques.
2. **Systematics from the choice of  $m_T$  cut:** An uncertainty on the lepton fake factor due to varying the  $m_T$  cut by  $\pm 10$  GeV/ $c^2$  in the fake lepton control region is used to estimate systematic error from the  $m_T$  cut. This variation in the  $m_T$  cut was chosen such that we have enough statistics and does not enhance the contribution of the W+jets and top events.

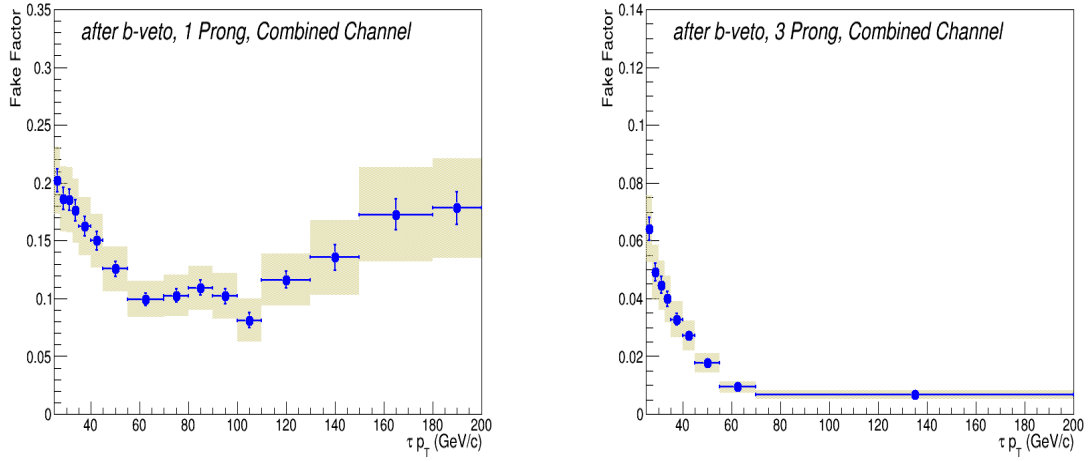


Fig. 6.3: The W+jets fake factors for 1- and 3-prong taus in the b-veto category. The error bars show the statistical error while the shaded regions show the systematic error.

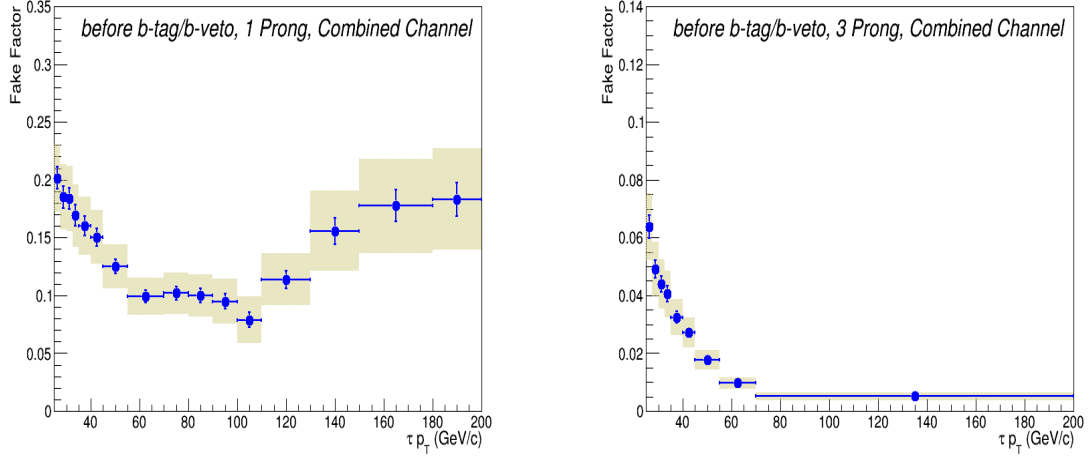


Fig. 6.4: The W+jets fake factors for 1- and 3-prong taus in the b-tag category. The error bars show the statistical error while the shaded regions show the systematic error.

3. **Contamination in the anti-tau region:** While calculating the  $r_{QCD}$  in the anti-tau region, the real leptons ( $e/\mu/\tau_{had}$ ) are subtracted from the data through the Monte Carlo simulation. The systematics associated to the simulated leptons effect the  $r_{QCD}$  calculation. Therefore, a 20% uncertainty on the number of simulated real leptons is taken which is sum of the systematics on the simulated hadronic taus and on the other simulated leptons ( $e/\mu$ ).

In addition, the statistical uncertainty in the lepton fake factor is also transmitted to the  $r_{QCD}$  calculations. Figures 6.5 and 6.6 show the  $r_{QCD}$  distributions in the b-veto

and b-tag category respectively (the error bars show the statistical uncertainties, and the shaded regions show the systematic uncertainties).

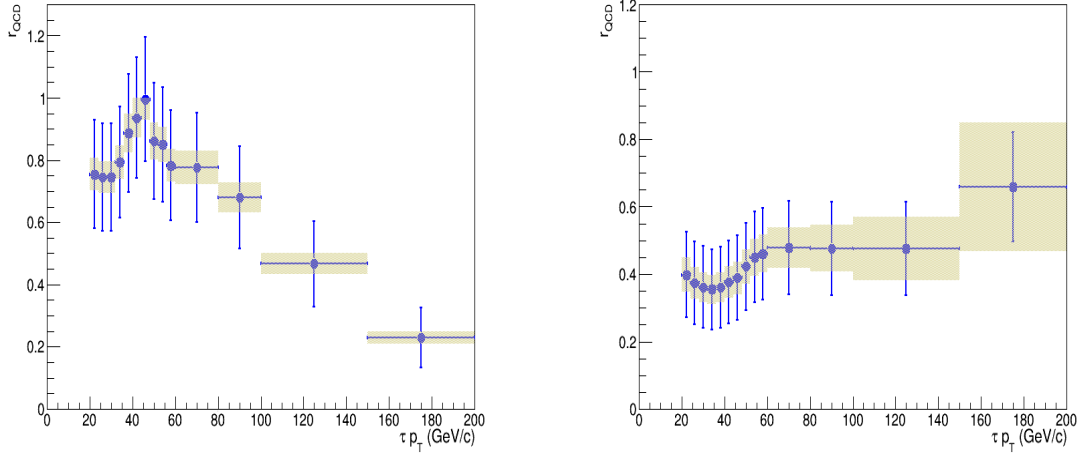


Fig. 6.5: The  $r_{QCD}$  shape in the b-veto category. The error bars show the statistical error while the shaded regions show the systematic error.

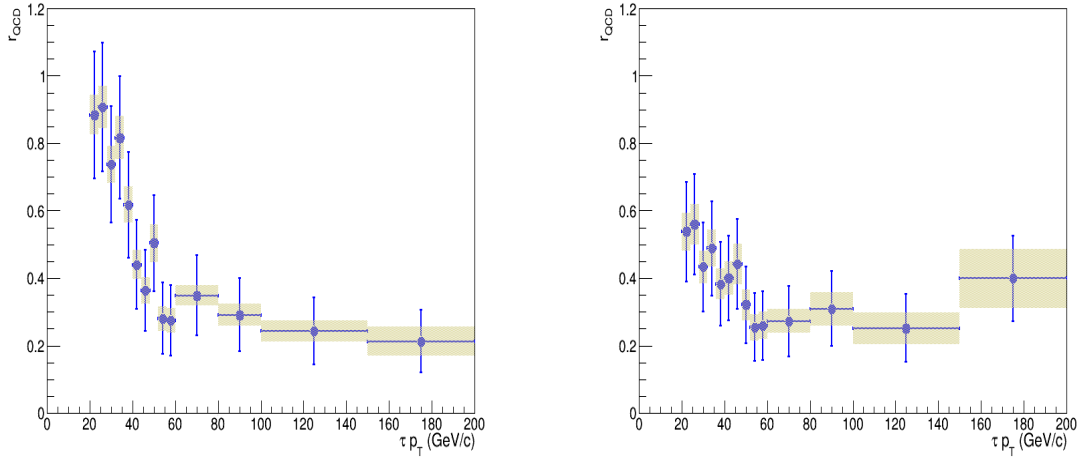


Fig. 6.6: The  $r_{QCD}$  shape in the b-tag category. The error bars show the statistical error while the shaded regions show the systematic error.

### 6.1.4 Electron to Tau Scale Factor

The misidentification rate of electrons faking taus is estimated using data as well as simulated samples. The simulated samples show large mis-modelling when compared to the data, therefore a scale factor is defined which is used to re-weight simulated events

(the details provided in section 5.4.1). The systematics associated with the electron to tau scale factor is calculated by varying the number of simulated real hadronic taus which is subtracted from the data. By taking into account the systematics related to the simulated hadronic taus, a 20% uncertainty in the simulated hadronic taus is considered. The effect of this variation on the normalization of the total transverse mass distribution in the signal region is 22% for  $Z \rightarrow ee$  events, 1% for top events and 2% for diboson events (in the electron channel only).

## 6.2 Systematic Uncertainties on Luminosity and Theoretical Cross Section Measurements

The integrated luminosity has an uncertainty of 5% [143]. The dominant source of uncertainty in the luminosity measurements is the uncertainty of the absolute calibration of the various luminosity monitors. The normalization of all Monte Carlo samples is varied up and down by this amount.

The theoretical cross section uncertainties have been used for all backgrounds estimated using simulation which leaves only  $Z$ +jets, diboson,  $t\bar{t}$  and single top production. The uncertainties for  $Z$ +jets and diboson production is taken 5% and 6% respectively, combining parton distribution function (PDF),  $\alpha_s$  and the scale variation uncertainties in quadrature (details are provided in [139]). For  $t\bar{t}$  and single top production the uncertainties are taken 6% based on PDF and top-quark mass uncertainties (details are provided in [140], [141], [142]).

## 6.3 Detector-related Simulation Systematics

Detector-related simulation uncertainties are considered for all signal and backgrounds that are estimated using simulation. These uncertainties are:

1. Pileup: In simulation pileup, the average number of proton proton interaction per bunch crossing, is added by overlaying a generated event with a random number of

minimum bias events to correctly model the expected luminosity. In the analysis events in the Monte Carlo samples are re-weighted to match the measured luminosity profile of the data. The uncertainties in the pileup modelling (for details see [144]) introduces a systematic.

2. Electron: The electron trigger, reconstruction and identification efficiency uncertainties are measured by varying the efficiency scale factors, estimated from electrons from  $Z \rightarrow ee$  with a tag-and-probe method and used to correct the simulation to match the data efficiency [145]. In addition to these, the difference between the electromagnetic energy scales (and the resolution) in the data and simulation is also corrected through scale factors (for details see [146]). The uncertainties in these scale factors gives rise to systematic error.
3. Muon: These systematics consists of uncertainties in the trigger, reconstruction and identification efficiency; and the momentum scale and the resolution. The muon trigger, reconstruction and identification efficiency uncertainties are estimated by varying the efficiency scale factors, estimated from muons from  $Z \rightarrow \mu\mu$  and  $J/\psi \rightarrow \mu\mu$  with a tag-and-probe method and used to correct the simulation to match the data efficiency [147]. In addition to these, the uncertainties in the scale factors that are used to correct the muon momentum and the resolution measured through simulation are included.
4. Tau: The tau systematics consists of uncertainties in the scale factors related to the reconstruction, identification, electron-veto and the tau energy scale (TES) efficiencies which are derived to re-weight simulated events and provide agreement with the data (for details see [127]).
5. Jet: Uncertainties in the scale factors associated with jet energy scale and the resolution (see [148]) also taken into consideration.
6. Flavour-tagging (FT): Simulated events are corrected through the scale factors derived from the b-tagging efficiencies in the data and simulation of the  $t\bar{t}$  events (for details see [131]). Uncertainties in these scale factors effect both b-tag and b-veto events therefore effect of these uncertainties are considered in both categories.
7. ATLFast-II simulation (AF2): During the production of b-associated Monte Carlo signal samples, ATLFast-II was used for fast simulation of the generated

events and their interaction with the detector material (as described in section 4.3). The fast simulation is tuned against the data using scale factors (for details see [118]). The uncertainties in the scale factors are taken as systematics.

8. Missing Transverse Energy ( $E_T^{miss}$ ): The systematic uncertainties in the tau, electron, muon and jet energy scales propagate to the missing transverse energy calculations. Apart from these, uncertainties associated to energy scales and resolutions which are not associated to any physics objects also contribute in the total  $E_T^{miss}$  systematics (for details see [149]).

For each category listed above, the uncertainties are provided by the respective ATLAS working groups. The overall effect of systematics on the normalization of the reconstructed total transverse mass  $m_T^{tot}$  distribution are provided in the tables 6.2 to 6.5, for each MC sample used in the signal region and in the electron and the muon channels for the b-veto and b-tag categories. For each individual group the corresponding uncertainties are added in quadrature as they are un-correlated.

Electron Channel (effects shown in %, variations are $\pm$ )				
Category	$Z \rightarrow ll$	$Z \rightarrow \tau\tau$	top	Diboson
Pileup	1.91	3.30	3.13	2.88
Electron	1.99	1.27	1.48	1.43
Muon	0.00	0.00	0.11	0.06
Tau	0.03	11.03	12.00	11.35
Jet	2.58	2.51	5.23	1.79
Flavour-tagging	0.02	0.03	6.53	0.01
$E_T^{miss}$	1.35	0.67	1.13	0.89
Muon Channel (effects shown in %, variations are $\pm$ )				
Category	$Z \rightarrow ll$	$Z \rightarrow \tau\tau$	top	Diboson
Pileup	0.96	2.43	2.98	2.24
Electron	0.00	0.01	0.00	0.11
Muon	0.96	1.25	2.42	1.83
Tau	0.00	11.94	12.16	12.22
Jet	3.17	2.97	5.00	3.76
Flavour-tagging	0.07	0.03	6.26	0.01
$E_T^{miss}$	3.23	0.86	0.57	1.20

Table 6.2: The effect of the detector related systematic uncertainties in the Monte Carlo samples used for the background estimation in the b-veto category. The effect on the normalization is shown in %.

Electron Channel (effects shown in %, variations are $\pm$ )				
Category	$Z \rightarrow ll$	$Z \rightarrow \tau\tau$	top	Diboson
Pileup	31.95	8.87	2.98	4.27
Electron	12.33	0.00	0.00	0.00
Muon	0.00	0.00	0.00	0.00
Tau	0.00	15.31	16.41	10.33
Jet	25.00	15.89	0.20	11.78
Flavour-tagging	15.02	8.70	2.68	13.30
$E_T^{miss}$	1.61	1.82	0.62	13.93
Muon Channel (effects shown in %, variations are $\pm$ )				
Category	$Z \rightarrow ll$	$Z \rightarrow \tau\tau$	top	Diboson
Pileup	20.00	5.20	3.30	27.18
Electron	0.00	0.00	0.00	0.00
Muon	1.83	1.56	3.24	2.99
Tau	0.00	15.48	16.09	15.20
Jet	9.29	14.38	3.60	6.19
Flavour-tagging	9.98	10.18	2.27	15.44
$E_T^{miss}$	0.00	1.73	0.00	8.86

Table 6.3: The effect of the detector related systematic uncertainties in the Monte Carlo samples used for the background estimation in the b-tag category. The effect on the normalization is shown in %.

Electron Channel (effects shown in %, variations are $\pm$ )									
Category	ggH200	ggH300	ggH400	ggH500	ggH600	ggH700	ggH800	ggH1000	ggH1200
Pileup	2.17	5.61	1.42	3.71	1.90	1.81	0.78	5.10	3.35
Electron	0.94	1.22	0.99	1.14	1.26	1.43	1.51	1.74	1.78
Muon	0.00	0.00	0.00	0.00	0.00	0.00	0.00	0.00	0.00
Tau	14.18	10.55	9.33	7.71	8.31	8.34	9.05	9.25	9.04
Jet	2.75	3.21	1.87	2.07	2.41	2.26	1.95	2.07	2.58
Flavour-tagging	0.02	0.05	0.03	0.03	0.02	0.02	0.04	0.04	0.04
$E_T^{miss}$	1.22	1.23		0.51	0.61	0.51	0.54	1.09	0.74
Category	bbH200	bbH300	bbH400	bbH500	bbH600	bbH700	bbH800	bbH1000	bbH1200
Pileup	1.22	3.31	1.99	0.66	1.89	0.78	1.86	0.90	1.06
Electron	1.37	1.13	1.30	1.47	1.81	1.85	1.85	2.01	1.78
Muon	0.04	0.04	0.04	0.06	0.04	0.03	0.04	0.03	0.03
Tau	12.70	10.29	9.22	8.23	8.51	8.64	8.93	8.65	8.55
Jet	3.13	2.15	2.06	2.28	2.34	1.99	1.86	2.26	2.14
Flavour-tagging	1.64	1.83	1.81	1.79	1.56	1.78	1.82	1.73	1.68
AF2	3.69	2.48	2.35	2.22	2.12	2.22	2.19	2.17	2.17
$E_T^{miss}$	1.90	0.50	0.40	0.57	0.63	0.57	0.60	0.48	0.60
Muon Channel (effects shown in %, variations are $\pm$ )									
Category	ggH200	ggH300	ggH400	ggH500	ggH600	ggH700	ggH800	ggH1000	ggH1200
Pileup	0.88	1.69	0.63	1.33	2.67	2.78	3.40	3.96	3.94
Electron	0.00	0.00	0.00	0.00	0.00	0.00	0.00	0.00	0.00
Muon	1.84	2.31	2.70	2.83	2.90	3.04	3.13	3.32	3.16
Tau	12.30	10.03	9.16	8.62	9.11	9.07	8.97	9.36	9.24
Jet	2.22	2.71	2.43	2.13	2.32	2.47	2.59	2.31	2.26
Flavour-tagging	0.03	0.05	0.04	0.04	0.05	0.04	0.06	0.05	0.05
$E_T^{miss}$	0.56	0.60	1.06	0.55	0.54	0.58	0.57	0.58	0.58
Category	bbH200	bbH300	bbH400	bbH500	bbH600	bbH700	bbH800	bbH1000	bbH1200
Pileup	0.81	2.25	0.26	2.62	1.69	2.11	4.16	2.52	2.61
Electron	0.06	0.09	0.05	0.02	0.04	0.03	0.04	0.03	0.03
Muon	1.79	2.46	2.71	2.99	2.87	3.21	3.23	3.38	3.40
Tau	12.27	10.06	9.29	8.63	9.01	9.14	9.32	8.90	8.87
Jet	4.06	2.41	2.59	3.37	3.18	3.12	2.29	2.93	2.84
Flavour-tagging	1.50	1.73	1.76	1.81	1.82	1.94	1.96	1.84	1.87
AF2	2.91	2.57	2.49	2.43	2.38	2.31	2.22	2.20	2.20
$E_T^{miss}$	0.78	1.12	0.56	0.46	0.76	0.73	0.65	0.57	0.61

Table 6.4: The effect of the detector related systematic uncertainties in the Monte Carlo samples used for the signal in the b-veto category. The effect on the normalization is shown in %.

Electron Channel (effects shown in %, variations are $\pm$ )									
Category	ggH200	ggH300	ggH400	ggH500	ggH600	ggH700	ggH800	ggH1000	ggH1200
Pileup	19.975	37.48	18.04	12.33	7.38	29.12	6.44	5.69	6.34
Electron	1.03	1.10	1.21	1.27	1.37	1.52	1.59	1.71	1.92
Muon	0.00	0.00	0.00	0.00	0.00	0.00	0.00	0.00	0.00
Tau	16.49	19.03	15.83	16.00	12.08	10.77	13.93	14.27	13.15
Jet	33.55	3.66	8.7	5.71	3.55	18.64	5.71	7.33	6.90
Flavour-tagging	16.46	14.80	11.78	12.00	12.77	9.97	12.65	7.49	10.14
$E_T^{miss}$	2.67	11.15	4.35	5.16	6.57	4.18	3.94	2.21	2.72
Category	bbH200	bbH300	bbH400	bbH500	bbH600	bbH700	bbH800	bbH1000	bbH1200
Pileup	5.90	2.04	2.19	2.07	1.99	3.79	4.12	2.12	2.76
Electron	0.95	1.04	0.91	1.56	1.68	1.83	1.90	2.17	2.28
Muon	0.00	0.00	0.00	0.00	0.00	0.00	0.00	0.00	0.00
Tau	17.31	15.40	13.37	12.50	12.03	11.21	12.71	14.13	13.63
Jet	5.82	6.74	5.27	3.45	3.15	2.41	3.61	3.69	4.30
Flavour-tagging	5.80	5.70	5.15	4.67	4.06	3.94	4.27	3.67	3.99
AF2	2.99	2.41	2.16	2.32	2.61	2.46	2.57	2.45	2.58
$E_T^{miss}$	0.99	0.95	1.80	1.02	0.94	0.89	0.83	0.87	1.02
Muon Channel (effects shown in %, variations are $\pm$ )									
Category	ggH200	ggH300	ggH400	ggH500	ggH600	ggH700	ggH800	ggH1000	ggH1200
Pileup	5.78	15.38	25.07		20.37	4.50	5.87	12.37	14.11
Electron	0.00	0.00	0.00	0.00	0.00	0.00	0.00	0.00	0.00
Muon	2.45	2.43	4.14	5.13	3.97	4.24	4.92	3.85	4.83
Tau	18.69	12.94	13.24	14.87	21.06	12.26	14.00	10.92	16.49
Jet	8.78	17.63	11.54	9.16	3.98	3.12	4.30	11.68	13.52
Flavour-tagging	27.73	14.82	20.68	12.21	9.26	9.31	14.59	12.88	14.30
$E_T^{miss}$	1.67	5.56	1.78	4.31	1.93	6.17	4.85	3.84	1.87
Category	bbH200	bbH300	bbH400	bbH500	bbH600	bbH700	bbH800	bbH1000	bbH1200
Pileup	5.65	2.34	3.67	9.71	4.13	3.58	3.76	2.94	3.52
Electron	0.00	0.00	0.00	0.00	0.00	0.00	0.00	0.00	0.00
Muon	2.37	3.16	3.51	3.91	4.14	4.28	4.23	4.42	4.62
Tau	17.14	14.41	12.36	12.52	12.29	12.10	11.76	13.24	13.06
Jet	7.58	4.37	3.51	4.47	5.88	3.59	1.88	1.69	0.98
Flavour-tagging	6.14	6.27	5.09	5.19	4.77	4.28	3.87	3.81	3.78
AF2	2.79	2.46	2.23	2.33	2.64	2.43	2.61	2.41	2.57
$E_T^{miss}$	2.13	0.78	0.65	0.68	0.71	1.67	0.85	0.83	0.81

Table 6.5: The effect of the detector related systematic uncertainties in the Monte Carlo samples used for the signal in the b-tag category. The effect on the normalization is shown in %.

## 6.4 Systematics Uncertainties on the Monte Carlo Modelling

In section 4.1, production of the Monte Carlo signal and background samples is described with details of the generators used in the analysis. Systematic errors from Monte Carlo modelling are estimated by producing Monte Carlo samples with varied configurations such as changing the initial and final state radiation, the parton distribution function (PDF), and the factorization ( $\mu_F$ ) and the renormalization ( $\mu_R$ ) scales of perturbative QCD. Only Monte Carlo samples for the signal and top background are considered as the effects of these systematics on other background samples were negligible.

### 6.4.1 Modelling of the Monte Carlo Signal Samples

Uncertainties on the signal acceptance include:

1. Scaling up and down the factorization ( $\mu_F$ ) and the renormalization ( $\mu_R$ ) scales of the perturbative QCD, by doubling and halving these factors which is a conservative choice as minimal variations have no significant effect. The up and down variations in the signal acceptance are found to be symmetrical.
2. Uncertainties due to the modelling of the initial- and final-state radiation, as well as the multiple parton interactions for the signal are also taken into account. These uncertainties are estimated from the PYTHIA8 A14 tune [89] for the b-associated production and the AZNLO PYTHIA8 tune [87] for the gluon-gluon fusion production. The final uncertainty due to the tune variations is taken as the average of the uncertainties associated with each tune variation.
3. For the b-associated production, PDF sets NNPDF30\_nlo\_as\_0118\_nf4 [150], MSTW2008nlo68cl\_nf4 [151], CT10nlo\_nf4 [90] and CT14nlo\_NF4 [91] are used whereas for the gluon-gluon fusion production PDF4LHC15\_nlo\_100 [152] set is used to estimate the uncertainty associated due to the PDF variation. The total PDF uncertainty is taken as the largest difference in the signal acceptance of any PDF variation.

Uncertainties (given in %) on the signal acceptance of the b-associated and the gluon-gluon fusion signal in the b-veto and the b-tag categories are listed in table 6.6.

Signal	$M_{A/H}$ (GeV/ $c^2$ )	Tune	Scale	PDF	Total
b-associated (b-veto category)	200	5.8	19.1	5.7	20.8
	500	6.7	20.2	6.5	22.2
	1000	1.4	25.7	12.9	28.8
b-associated (b-tag category)	200	4.7	17.6	5.9	19.1
	500	3.9	18.7	6.5	20.2
	1000	3.7	20.0	12.3	23.8
gluon-gluon fusion (b-veto category)	200	3.9	17.4	4.1	18.3
	500	1.6	15.5	4.8	16.3
	1000	1.8	15.1	4.3	15.8
gluon-gluon fusion (b-tag category)	200	38.8	22.0	5.3	44.9
	500	15.1	22.2	6.4	27.6
	1000	32.4	18.9	4.5	37.8

Table 6.6: Uncertainties (given in %, variations are  $\pm$ ) on the signal acceptance of the gluon-gluon fusion and the b-associated signal in the b-veto and b-tag category

The total uncertainties for 200, 500 and 1000 GeV/ $c^2$  mass points are fitted linearly. This linear fit is used to estimate uncertainties in all the mass points of the signal samples. The fit gives:

$$\Delta(m_{A/H}) = \pm(18.06 + 10.367 \times 10^{-3}m_{A/H})\% \quad (6.3)$$

$$\Delta(m_{A/H}) = \pm(17.68 + 5.986 \times 10^{-3}m_{A/H})\% \quad (6.4)$$

for the b-associated production in the b-veto and b-tag category respectively and

$$\Delta(m_{A/H}) = \pm(18.45 - 2.908 \times 10^{-3}m_{A/H})\% \quad (6.5)$$

$$\Delta(m_{A/H}) = \pm(40.10 - 5.888 \times 10^{-3}m_{A/H})\% \quad (6.6)$$

for the gluon-gluon fusion production in the b-veto and b-tag category respectively. The mass of the MSSM Higgs boson,  $m_{A/H}$ , is given in units of GeV/ $c^2$ .

## 6.4.2 Monte Carlo Top Modelling

Backgrounds from top events with truth  $\tau_{had}$  in the final state are modelled by the Monte Carlo simulation. The modelling uncertainties are estimated by comparing the Monte Carlo samples with different configurations (for details see [153]). These include:

1. The modelling uncertainty of the initial state radiation which is estimated by comparing the Monte Carlo samples generated with enhanced or reduced initial state radiation. This is done by varying the `hdamp` parameter value in POWHEG-BOX v2, which controls the amount of radiation produced by the parton shower.
2. The modelling uncertainty of the hard scattering, estimated by comparing the POWHEG plus HERWIG++ [154] and the aMC@NLO plus HERWIG++ generators.
3. The systematic uncertainty on the fragmentation modelling is estimated by comparing  $t\bar{t}$  events generated with the POWHEG-BOX v2 interfaced to either HERWIG++ or PYTHIA6.

In the b-tag category, the effect of these systematics on the acceptance in the signal region are: 6.5% (4.5%) in showering and 4.5% (3%) in radiation for electron (muon) channels. The effect of these systematics in b-veto case is negligible.

## 6.5 Comparison of the Statistical and Systematic Errors in Fakes

Once systematic errors in the data-driven fake estimation are calculated (section 6.1), a comparison of the systematic and statistical errors is made. Figures 6.7 and 6.8 show the distributions (in all categories) of the transverse momentum of the tau of the total expected background in the signal region with error bars corresponding to the statistical uncertainties and the shaded regions corresponding to the systematic errors. With exception of the muon b-veto category, statistical errors dominate the systematics. Therefore, analysis can be improved with more statistics available in 2016 run.

Another comparison between the statistical and systematic errors in the fake estimation, and the data in the signal region is made in figures 6.9 and 6.10 which show the distributions (in all categories) of the transverse momentum of the tau. The error bars correspond to the statistical uncertainties and the shaded regions correspond to the systematic errors. In all categories, the expected background matches with the data within uncertainties.

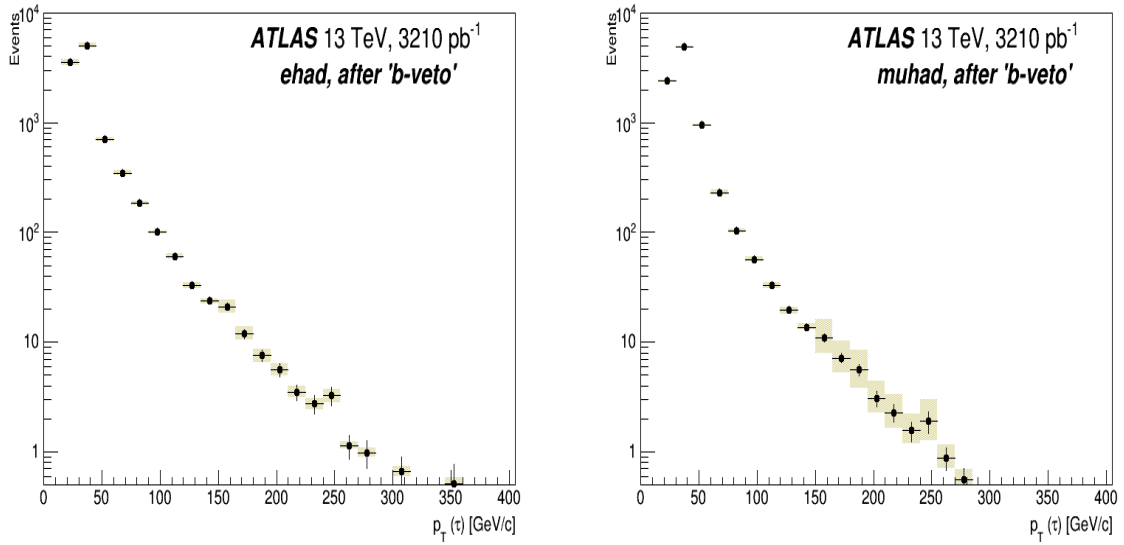


Fig. 6.7: Comparison between the statistical (error bars) and the systematic (shaded region) uncertainties associated with the data-driven fake estimation in the signal region is provided in the b-veto category for the electron (left) and the muon (right) channel.

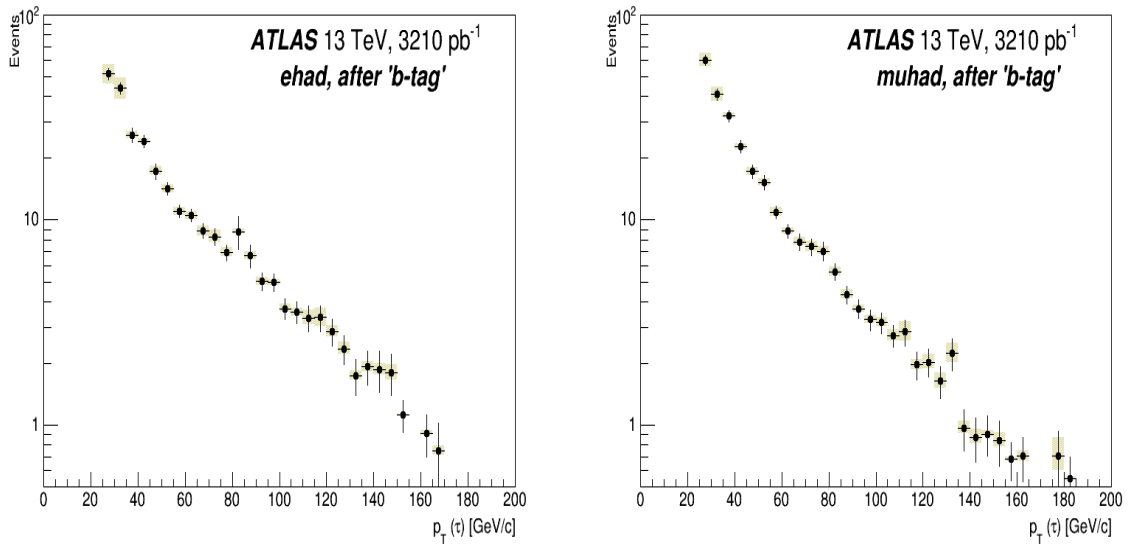


Fig. 6.8: Comparison between the statistical (error bars) and the systematic (shaded region) uncertainties associated with the data-driven fake estimation in the signal region is provided in the b-tag category for the electron (left) and the muon (right) channel.

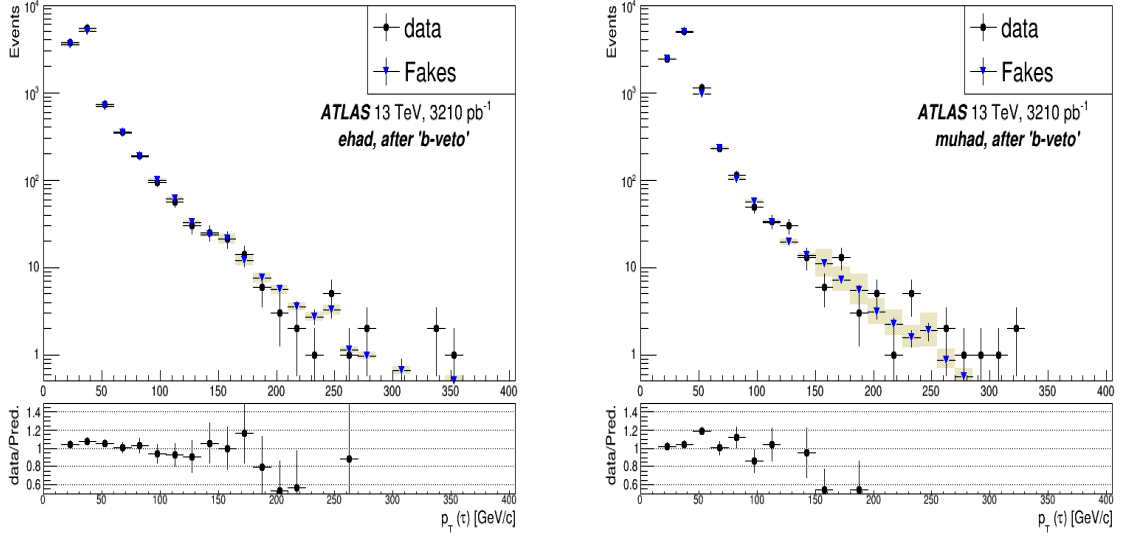


Fig. 6.9: Comparison between the data and the predicted background in the signal region is provided in the b-veto category for the electron (left) and the muon (right) channel. Statistical errors are shown as error bars and the systematic errors are shown as the shaded region.

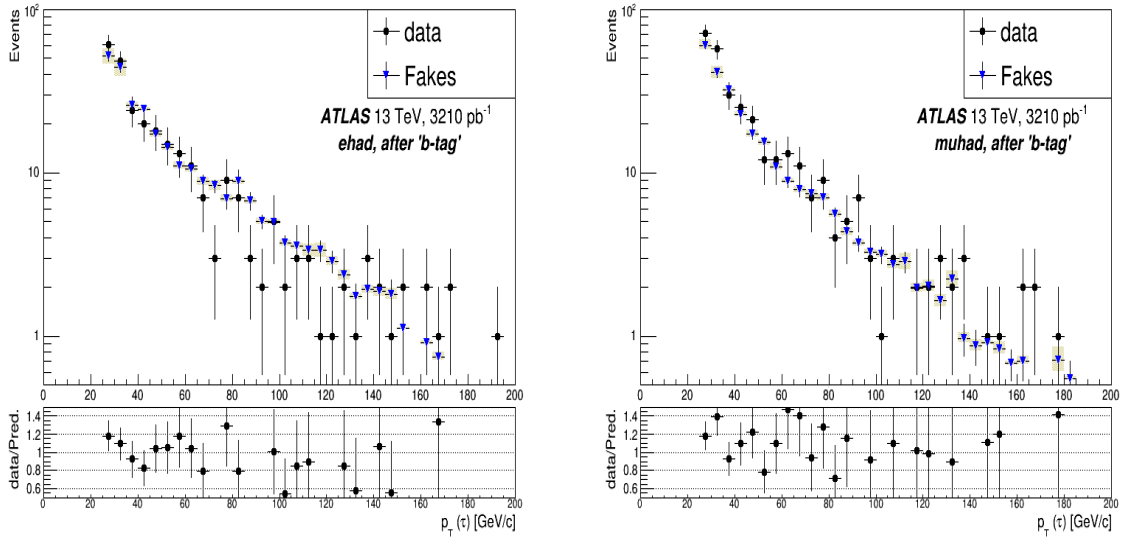


Fig. 6.10: Comparison between the data and the predicted background in the signal region is provided in the b-tag category for the electron (left) and the muon (right) channel. Statistical errors are shown as error bars and the systematic errors are shown as the shaded region.

## 6.6 Signal Region Yields with Full Systematics

The effects of statistical and systematic uncertainties on the signal region yields are shown in tables 6.7 and 6.8 for b-veto and b-tag category respectively, in the electron and muon channels. In addition, the signal region distributions of the transverse momentum of the tau candidate ( $p_T(\tau)$ ); the transverse momentum of the lepton ( $p_T(e/\mu)$ ); the visible mass ( $m_{\tau,e/\mu}$ ) of the tau and the lepton ( $e/\mu$ ); and the missing transverse energy ( $E_T^{miss}$ ) are shown in figures. 6.11 to 6.18. The shaded regions show the statistical plus systematic uncertainties in the combined data-driven fake estimation in the signal region. In all these distributions, the total expected background matches with the data.

Table 6.7: The signal region yields in the b-veto category for the electron and muon channels with full systematics.

Electron Channel	Nominal	Stat.	Lumi	Xsec.	e fakes	Detector	Fakes	MC Modelling	Combined Sys.
$Z \rightarrow ll + \text{jets}$	747.5	$\pm 19.4$	$\pm 37$	$\pm 37.37$	$\pm 164.45$	$\pm 30$	...	...	$\pm 175.24$
$Z \rightarrow \tau\tau + \text{jets}$	4186	$\pm 41.6$	$\pm 209$	$\pm 209.3$	...	$\pm 494$	...	...	$\pm 575$
$t\bar{t}$ and single top	33.1	$\pm 1.1$	$\pm 1.7$	$\pm 1.98$	$\pm 0.33$	$\pm 5$	...	$\pm 2.6$	$\pm 6.20$
Diboson	41.3	$\pm 1.3$	$\pm 2.1$	$\pm 2.47$	$\pm 0.83$	$\pm 5$	...	...	$\pm 6.02$
Fakes	5100	$\pm 24$	...	...	...	...	$\pm 730$	...	$\pm 730$
Total prediction	10108	$\pm 51.8$	$\pm 212.3$	$\pm 212.63$	$\pm 164.45$	$\pm 495$	$\pm 730$	$\pm 2.6$	$\pm 946$
Data	10619	...	...	...	...	...	...	...	...
ggH ( $\tan \beta = 20, m_{H/A} = 600 \text{ GeV}/c^2$ )	105.198	$\pm 2.26$	$\pm 5.26$	...	...	$\pm 10.1$	...	$\pm 0.167$	$\pm 11.38$
bbH ( $\tan \beta = 20, m_{H/A} = 600 \text{ GeV}/c^2$ )	63.148	$\pm 1.91$	$\pm 3.16$	...	...	$\pm 5.7$	...	$\pm 0.24$	$\pm 6.52$
Muon Channel	Nominal	Stat.	Lumi	Xsec.	e fakes	Detector	Fakes	MC Modelling	Combined Sys.
$Z \rightarrow ll + \text{jets}$	839	$\pm 18.4$	$\pm 42$	$\pm 41.95$	...	$\pm 39.64$	...	...	$\pm 71.38$
$Z \rightarrow \tau\tau + \text{jets}$	5035.3	$\pm 44.5$	$\pm 252$	$\pm 251.76$	...	$\pm 636$	...	...	$\pm 728.90$
$t\bar{t}$ and single top	37.1	$\pm 1.1$	$\pm 1.85$	$\pm 2.22$	...	$\pm 5.6$	...	$\pm 1.8$	$\pm 6.55$
Diboson	49.1	$\pm 1.4$	$\pm 2.45$	$\pm 2.95$	...	$\pm 6.5$	...	...	$\pm 7.54$
Fakes	2760	$\pm 18$	...	...	...	...	$\pm 340$	...	$\pm 340$
Total prediction	8720.7	$\pm 51.4$	$\pm 255.5$	$\pm 255.26$	...	$\pm 637.3$	$\pm 340$	$\pm 1.8$	$\pm 807$
Data	9163	...	...	...	...	...	...	...	...
ggH ( $\tan \beta = 20, m_{H/A} = 600 \text{ GeV}/c^2$ )	98.29	$\pm 2.1$	$\pm 5$	...	...	$\pm 9.5$	...	$\pm 0.167$	$\pm 10.7$
bbH ( $\tan \beta = 20, m_{H/A} = 600 \text{ GeV}/c^2$ )	58.22	$\pm 1.74$	$\pm 3$	...	...	$\pm 5.2$	...	$\pm 0.24$	$\pm 6.00$

Table 6.8: The signal region yields in the b-tag category for the electron and muon channels with full systematics.

Electron Channel		Nominal	Stat.	Lumi	Xsec.	e fakes	Detector	Fakes	MC Modelling	Combined Sys.
$Z \rightarrow ll + \text{jets}$	4.6	$\pm 1.8$	$\pm 0.23$	$\pm 1.01$	$\pm 1.58$	...	...	...	$\pm 1.90$	
$Z \rightarrow \tau\tau + \text{jets}$	35.8	$\pm 4.2$	$\pm 1.8$	...	$\pm 5.52$	...	...	...	$\pm 6.07$	
$t\bar{t}$ and single top	109	$\pm 1.9$	$\pm 5.45$	$\pm 1.09$	$\pm 12.58$	...	$\pm 8.7$	...	$\pm 17.53$	
Diboson	0.77	$\pm 0.2$	$\pm 0.04$	$\pm 0.01$	$\pm 0.2$	...	...	...	$\pm 0.2$	
Fakes	129.7	$\pm 3.5$	...	...	...	$\pm 18$	...	...	$\pm 18$	
Total prediction	279.87	$\pm 6.06$	$\pm 5.74$	$\pm 1.5$	$\pm 13.83$	$\pm 18$	$\pm 8.7$	...	$\pm 25.9$	
Data	275	...	...	...	...	...	...	...	...	
ggH ( $\tan \beta = 20, m_{H/A} = 600 \text{ GeV}/c^2$ )	1.634	$\pm 0.29$	$\pm 0.08$	...	$\pm 0.15$	...	$\pm 0.36$	...	$\pm 0.39$	
bbH ( $\tan \beta = 20, m_{H/A} = 600 \text{ GeV}/c^2$ )	34.165	$\pm 1.37$	$\pm 1.7$	...	$\pm 3.1$	...	$\pm 0.21$	...	$\pm 3.54$	
Muon Channel		Nominal	Stat.	Lumi	Xsec.	e fakes	Detector	Fakes	MC Modelling	Combined Sys.
$Z \rightarrow ll + \text{jets}$	5.2	$\pm 1.4$	$\pm 0.26$	$\pm 0.26$	$\pm 1.13$	...	...	...	$\pm 1.18$	
$Z \rightarrow \tau\tau + \text{jets}$	34.8	$\pm 4$	$\pm 1.74$	...	$\pm 5.12$	...	...	...	$\pm 5.68$	
$t\bar{t}$ and single top	126	$\pm 2$	$\pm 6.3$	$\pm 7.56$	$\pm 15.26$	...	$\pm 6.3$	...	$\pm 19.21$	
Diboson	0.35	$\pm 0.1$	$\pm 0.018$	$\pm 0.02$	$\pm 0.18$	...	...	...	$\pm 0.18$	
Fakes	108	$\pm 3.1$	...	...	...	$\pm 14$	...	...	$\pm 14$	
Total prediction	274.35	$\pm 5.6$	$\pm 6.54$	$\pm 7.76$	$\pm 16.14$	$\pm 14$	$\pm 6.3$	...	$\pm 24.46$	
Data	312	...	...	...	...	...	...	...	...	
ggH ( $\tan \beta = 20, m_{H/A} = 600 \text{ GeV}/c^2$ )	1.53	$\pm 0.25$	$\pm 0.08$	...	$\pm 0.13$	...	$\pm 0.36$	...	$\pm 0.39$	
bbH ( $\tan \beta = 20, m_{H/A} = 600 \text{ GeV}/c^2$ )	33.814	$\pm 1.26$	$\pm 1.7$	...	$\pm 3.07$	...	$\pm 0.21$	...	$\pm 3.51$	

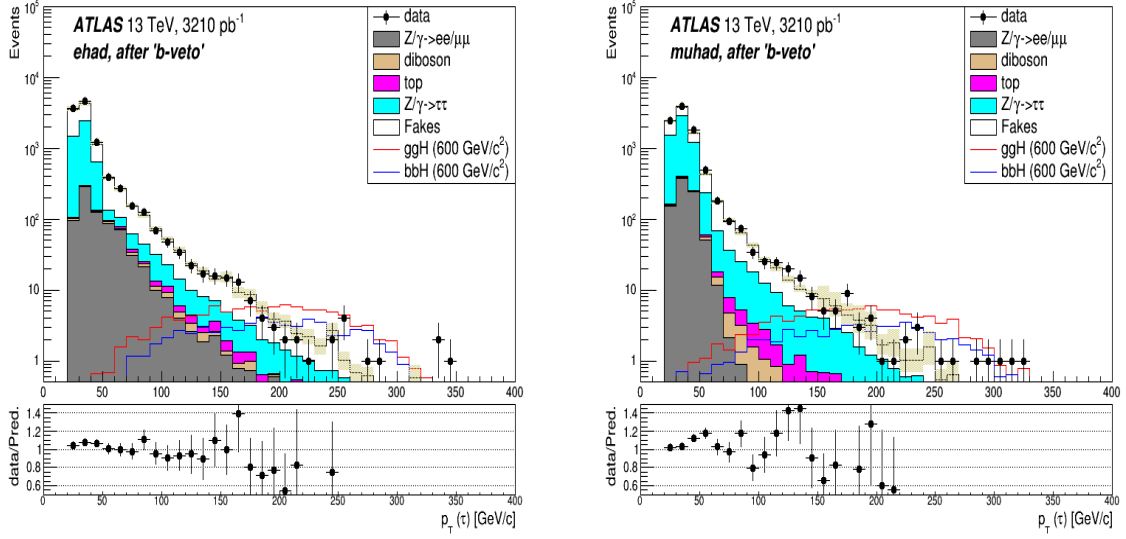


Fig. 6.11: Distribution of the transverse momentum ( $p_T$ ) of the tau candidate in the signal region, in the b-veto category for the electron (left) and the muon (right) channel. The error bars show the statistical uncertainties and the shaded region shown the total error (statistical plus systematic) on the fake estimation in the signal region.

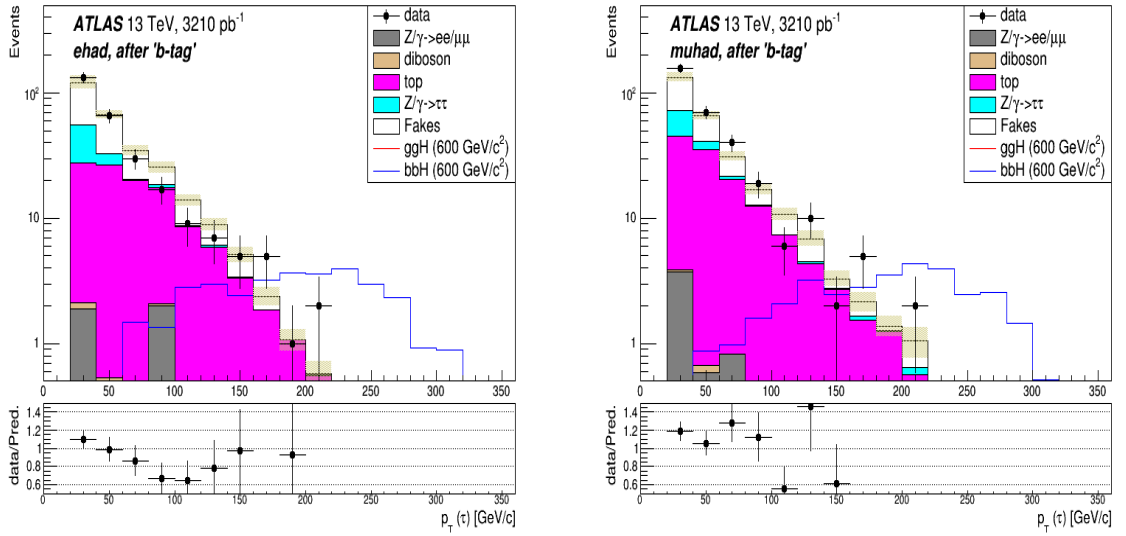


Fig. 6.12: Distribution of the transverse momentum ( $p_T$ ) of the tau candidate in the signal region, in the b-tag category for the electron (left) and the muon (right) channel. The error bars show the statistical uncertainties and the shaded region shown the total error (statistical plus systematic) on the fake estimation in the signal region.

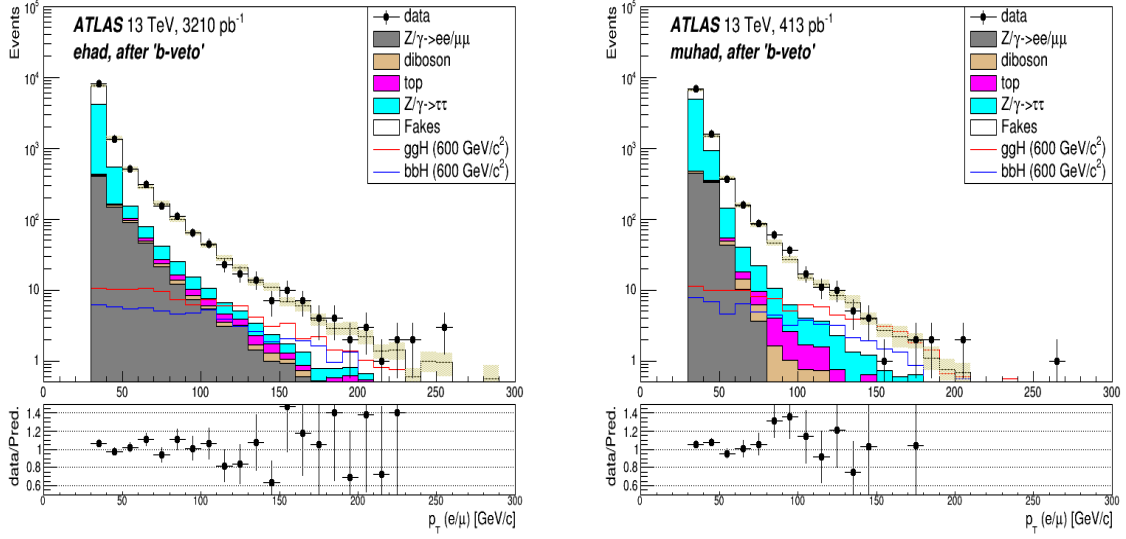


Fig. 6.13: Distribution of the transverse momentum ( $p_T$ ) of the lepton ( $e/\mu$ ) candidate in the signal region, in the b-veto category for the electron (left) and the muon (right) channel. The error bars show the statistical uncertainties and the shaded region shown the total error (statistical plus systematic) on the fake estimation in the signal region.

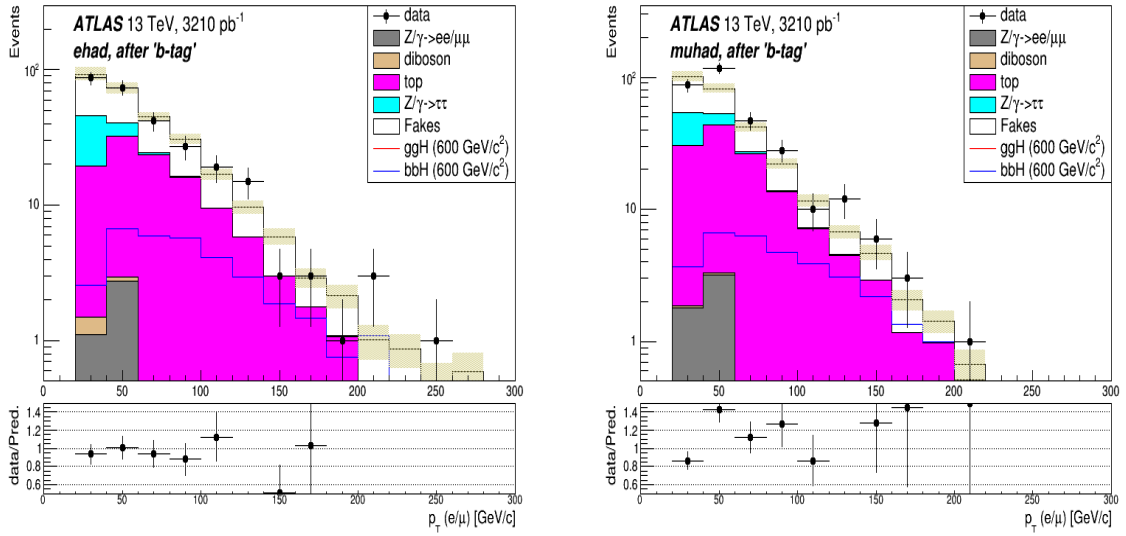


Fig. 6.14: Distribution of the transverse momentum ( $p_T$ ) of the lepton ( $e/\mu$ ) candidate in the signal region, in the b-tag category for the electron (left) and the muon (right) channel. The error bars show the statistical uncertainties and the shaded region shown the total error (statistical plus systematic) on the fake estimation in the signal region.

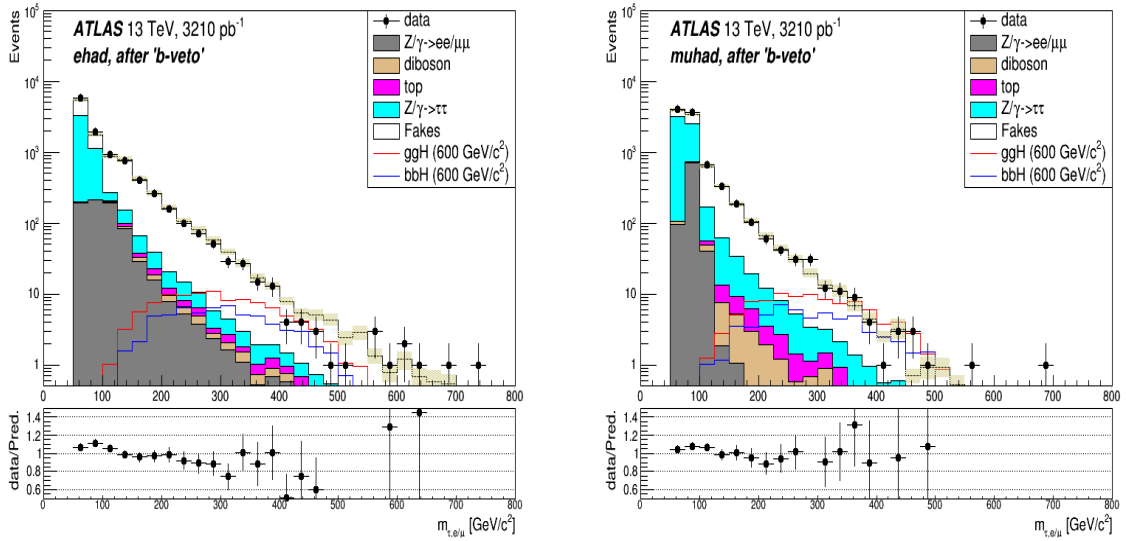


Fig. 6.15: Distribution of the visible mass ( $m_{\tau, e/\mu}$ ) of the lepton ( $e/\mu$ ) and the tau candidate in the signal region, in the b-veto category for the electron (left) and the muon (right) channel. The error bars show the statistical uncertainties and the shaded region shown the total error (statistical plus systematic) on the fake estimation in the signal region.

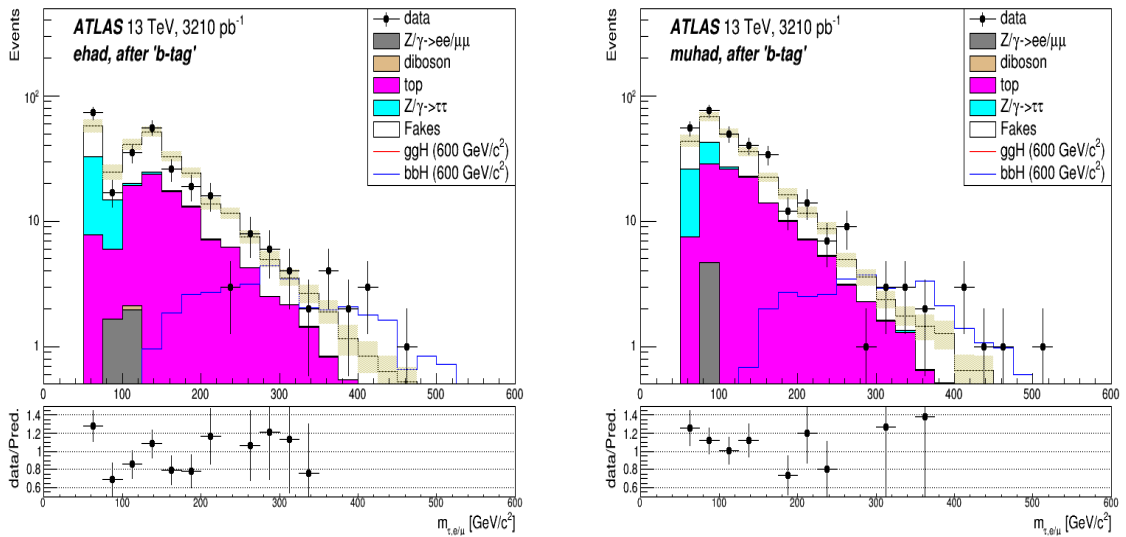


Fig. 6.16: Distribution of the visible mass ( $m_{\tau, e/\mu}$ ) of the lepton ( $e/\mu$ ) and the tau candidate in the signal region, in the b-tag category for the electron (left) and the muon (right) channel. The error bars show the statistical uncertainties and the shaded region shown the total error (statistical plus systematic) on the fake estimation in the signal region.

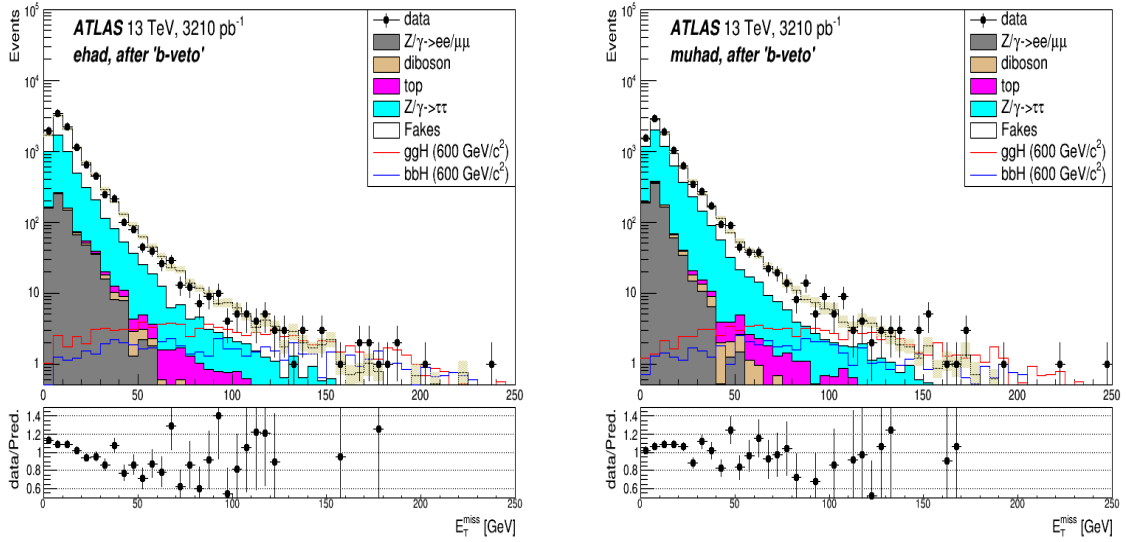


Fig. 6.17: Distribution of the missing transverse energy ( $E_T^{miss}$ ) in the signal region, in the b-veto category for the electron (left) and the muon (right) channel. The error bars show the statistical uncertainties and the shaded region shown the total error (statistical plus systematic) on the fake estimation in the signal region.

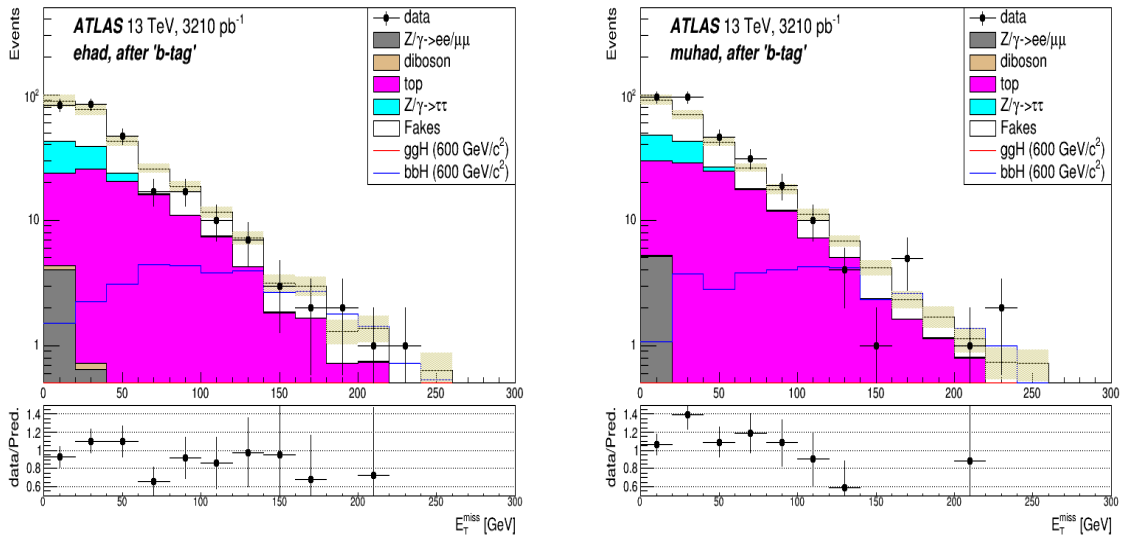


Fig. 6.18: Distribution of the missing transverse energy ( $E_T^{miss}$ ) in the signal region, in the b-tag category for the electron (left) and the muon (right) channel. The error bars show the statistical uncertainties and the shaded region shown the total error (statistical plus systematic) on the fake estimation in the signal region.

---

## CHAPTER 7

# Statistical Procedure for Limit Settings and Results

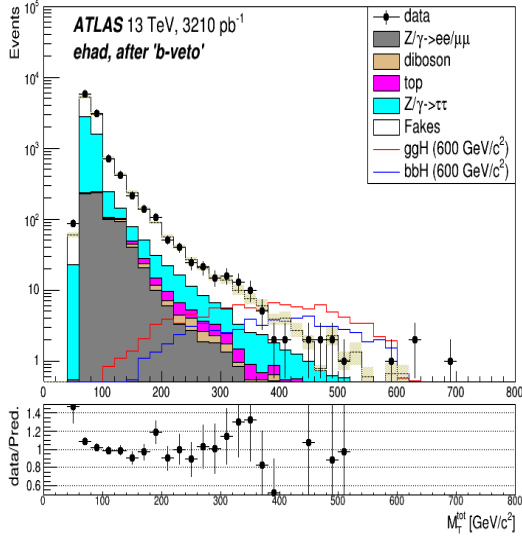
In the analysis, the mass of di-tau system ( $m_T^{tot}$ ) is used as a final discriminant between the signal and the background (as described in section 5.3). The invariant mass distributions are shown in figure 7.1 for combined channel (electron+muon) in the b-veto and b-tag categories. No statistically significant excess over the Standard Model background is seen. Although no evidence of supersymmetric neutral heavy Higgs boson has been observed, the results are used to set upper limits on the parameter  $\tan\beta$  as well as on the cross section times branching ratio ( $\sigma \times BR$ ) as a function of the MSSM Higgs mass ( $m_{A/H}$ ). The statistical procedure used for limit settings and the upper limit plots are presented in this chapter.

### 7.1 Limit Settings

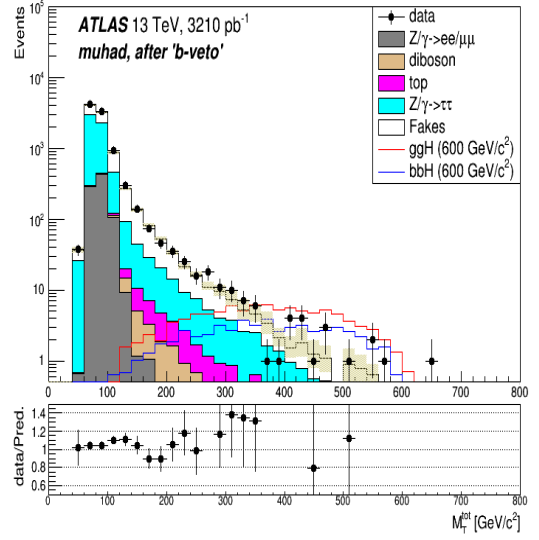
In order to test the signal and background hypotheses, the binned  $m_T^{tot}$  distributions are used to construct likelihood functions for each category. These likelihood functions are used to measure the compatibility of the data with a given hypothesis, also known as signal strength ( $\mu$ ). This parameter is defined as:

$$\mu = \frac{\sigma \times BR_{\text{observed}}}{\sigma \times BR_{\text{expected}}} \quad (7.1)$$

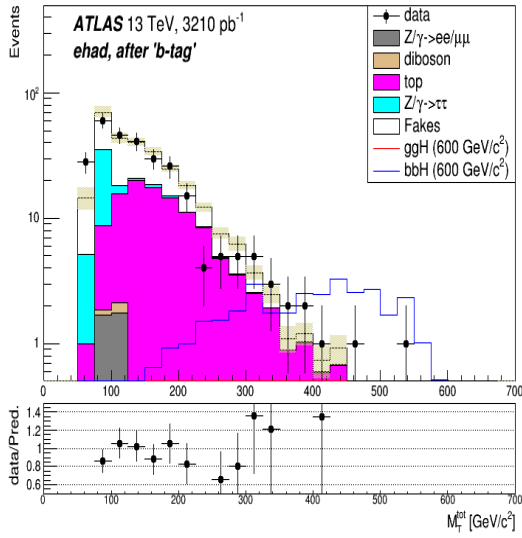
$\mu = 0$  corresponds to background only hypothesis while  $\mu = 1$  gives signal prediction. Since no significant excess over the Standard Model background expectations is observed therefore upper limits on the signal strength  $\mu$  is computed as a function of the Higgs mass  $m_{A/H}$ . For this, a method is implemented that uses a sample or toy data to compute upper limits on  $\mu$  with a certain confidence level such as the signal hypothesis may



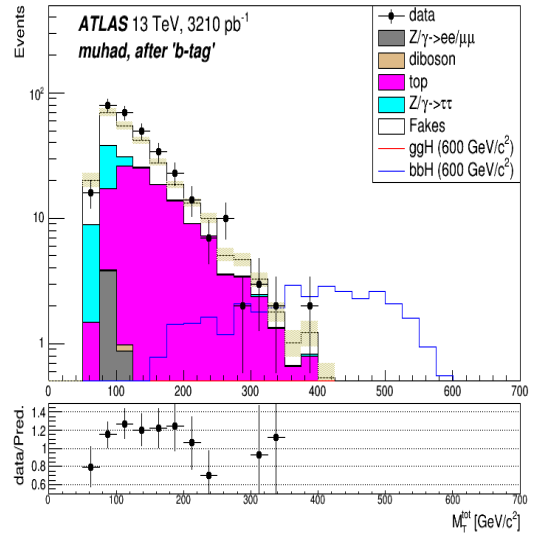
(a) electron channel, b-veto category



(b) muon channel, b-veto category



(c) electron channel, b-tag category



(d) muon channel, b-tag category

Fig. 7.1: Distribution of the total invariant mass ( $m_T^{tot}$ ) in the signal region. Each category is shown separately. The shaded region shows the uncertainties (statistical plus systematic) in the total fake estimation in the signal region.

be excluded if  $\mu = 1$  is disfavoured at the 95% confidence level. The detail description of the statistical procedure used in the analysis and to compute upper limits is provided below:

### 7.1.1 Likelihood Function ( $\mathcal{L}$ )

The binned likelihood function of the signal strength given the set of nuisance parameters (the parameters that are not under investigation in an experiment but still have an impact on the predictions) constructed from the bins of the  $m_T^{tot}$  distribution is product of a poisson and a gaussian probability function, as given below:

$$\mathcal{L}(\mu, \theta) = \prod_{j=bin} \mathcal{F}_P(N_j | \mu \cdot s_j(\theta_1, \theta_2, \dots, \theta_n) + b_j(\theta_1, \theta_2, \dots, \theta_n)) \prod_{\theta_i} \mathcal{F}_G(\theta_i | 0, 1) \quad (7.2)$$

where

$\mu$ : the signal strength

$N_j$ : observed number of events in bin j

$s_j$ : expected events from signal in bin j

$b_j$ : expected events from background in bin j

$\mathcal{F}_P(N_j | \mu \cdot s_j(\theta) + b_j(\theta))$ : probability of  $N_j$  events from the poisson distribution with mean  $\mu \cdot s_j + b_j$

$\theta_i$ : nuisance parameter

In the statistical procedure, systematic uncertainties are parametrized as nuisance parameters and are constrained using gaussian probability distributions ( $\mathcal{F}_G(\theta_i | \bar{\theta}_i, \sigma_i)$ ) with mean  $\bar{\theta}_i$  and variance  $\sigma_i$  for each individual nuisance parameter  $\theta_i$ . Both signal and background yields are functions of nuisance parameters (i.e.,  $s_j(\theta_1, \theta_2, \dots, \theta_n)$  and  $b_j(\theta_1, \theta_2, \dots, \theta_n)$ ). Separate likelihood functions are taken for each analysis category (the b-tag and b-veto as well as the electron and muon channels)

### 7.1.2 Test Statistics

A test statistics ( $\tilde{q}_\mu$ ) is defined that computes the probability (p-value) that the background could fluctuate to the level of the observed data or higher. The test statistics

is:

$$\tilde{q}_\mu = \begin{cases} -2 \ln\left(\frac{\mathcal{L}(\mu, \hat{\theta}_\mu)}{\mathcal{L}(\hat{\mu}, \hat{\theta})}\right), & \text{if } 0 \leq \hat{\mu} \leq \mu \\ 0, & \text{if } \hat{\mu} > \mu \end{cases} \quad (7.3)$$

where  $\hat{\mu}$  and  $\hat{\theta}$  correspond to those values of  $\mu$  and  $\theta$  that maximize the likelihood while  $\hat{\theta}_\mu$  corresponds to the conditional maximum likelihood of a given  $\mu$ . If the signal strength ( $\mu$ ) is smaller than the value corresponding to the global maximum of the likelihood  $\hat{\mu}$  then that values of the signal strength can never not be excluded.

In order to exclude an hypothesis based on the observed data, the p-value must be calculated. To reject signal hypotheses at 95% confidence-level, the upper limit on the signal strength must be such that the p-value  $< \alpha$  (where  $\alpha = 0.05$ ). To evaluate p-value for background and signal + background hypotheses, the full expected distribution of the test statistics is required. This can be done by running several pseudo experiments for different  $\mu$  and nuisance parameter values and then observing the resulting distribution of the test statistic. However, this requires large computing time, therefore an asymptotic approximation to the test statistics is used (details are provided in reference [156]). The validity of the approximation was tested using pseudo experiments at a number of points. In this approximation

$$p_\mu = 1 - \Phi(\tilde{q}_\mu) \quad (7.4)$$

and in particular for background only hypothesis,

$$p_0 = 1 - \Phi(q_0) \quad (7.5)$$

where  $\Phi(q)$  is the cumulative distribution function of the gaussian distribution defined as:

$$\Phi(q) = \frac{1}{\sqrt{2\pi}} \int_{-\infty}^q e^{-t^2/2} dt \quad (7.6)$$

### 7.1.3 $CL_s$ Method

Exclusion of models to which one has little or no sensitivity occurs, for example, if the data fluctuate very low relative to the expectation of the background only hypothesis, In this case, the upper limit on the signal strength becomes very small. This problem

is solved by using the modified frequentist approach known as  $CL_s$ .  $CL_s$  is defined as a ratio of two p-values. That is:

$$CL_s = \frac{p_\mu}{1 - p_0} \quad (7.7)$$

where  $p_0$  is the p-value of the background only hypothesis. A point in the parameter space is regarded as excluded if one finds  $CL_s < \alpha$ . The denominator in the eq. 7.7 is always less than or equal to unity. If the experimental sensitivity to a given value of  $\mu$  is very low, then  $p_\mu$  decreases and so does the denominator. Thus the condition  $CL_s < \alpha$  is prevented from being satisfied and the exclusion of parameters in the case of low sensitivity is suppressed.

### 7.1.4 Exclusion Limits

Once observed  $CL_s$  limits on  $\mu$  are obtained, these are compared with the expected signal + background limits using a simplified Monte Carlo generated dataset (often called the “asimov” dataset) which uses the median values of the nuisance parameters. The asimov dataset is replaced by the actual data, and then the full statistical procedure stated above is performed. In addition to this, the uncertainty on the expected limits are also obtained using asymptotic formulae, as derived in [156]. These uncertainties are shown as 1 and 2  $\sigma$  bands in the limit plots.

## 7.2 Results

For calculating the upper limits on allowed values of  $\tan \beta$  in the  $m_{A/H} - \tan \beta$  plane, other SUSY parameters are specified using the  $m_h^{mod+}$  scenario (see section 2.7.1) as it provides the most stringent MSSM parameter space constraints for the Higgs boson search. Here, cross sections and branching ratios assume that the MSSM Higgs boson is produced via either gluon-gluon fusion or in association of b-quarks. The cross sections and branching ratios of both heavy neutral Higgs bosons ( $A$  and  $H$ ) are added. The results from the electron and muon channels are combined to improve the sensitivity. A 95% confidence limit is set on the signal strength parameter  $\mu$ . If  $\mu = 1$  is excluded with 95% confidence level, then that point in the  $m_{A/H} - \tan \beta$  plane is excluded. The

hypothesis runs on grid of points on the  $m_{A/H} - \tan\beta$  plane where mass points are 200, 300, 400, 500, 600, 700, 800, 1000, 1200 GeV/c<sup>2</sup> and  $\tan\beta$  runs from 1 to 60. Extrapolation is performed if the upper limit on  $\tan\beta$  exceeds 60. Figure 7.2 shows the  $m_{A/H} - \tan\beta$  exclusion limits obtained from the b-tag and b-veto analyses. Figure 7.3 shows upper limits on  $\tan\beta$  as a function of  $m_{A/H}$  in the inclusive category (no b-tag or b-veto requirements).

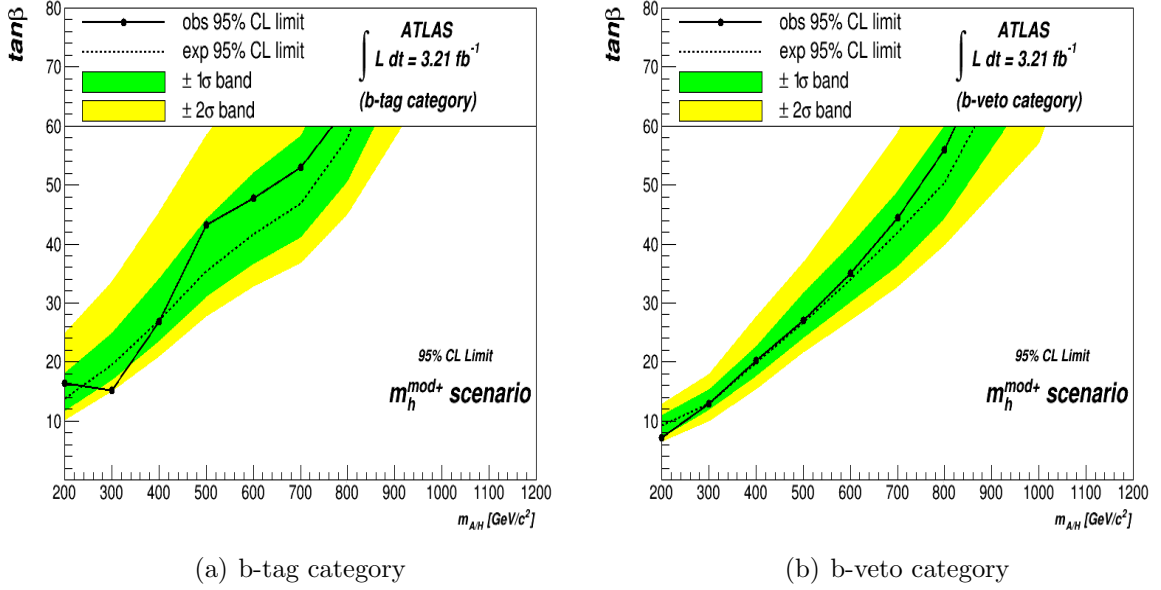


Fig. 7.2: The 95% CL upper limit on the  $m_{A/H} - \tan\beta$  plane of the MSSM parameter space in the  $m_h^{mod+}$  scenario. The b-tag category (a) and the b-veto category (b) are shown separately.

In this analysis,  $m_h^{max}$  scenario (see section 2.7.1) is used as a reference scenario to compare thesis results with the previous searches from LEP (combined results from ALEPH, DELPHI, L3, OPAL are presented in [157]), Tevatron (results from CDF and D0 are presented here [158], [159]) and the LHC experiments (the combined ( $\tau_{lep}\tau_{had} + \tau_{had}\tau_{had}$ ) Run-1 results from the ATLAS and CMS experiments are provided in [43] and [160]). Figure 7.4 shows upper limits for the  $m_{A/H} - \tan\beta$  plane in the  $m_h^{max}$  scenario. For comparison LEP, Tevatron and the ATLAS Run-1 excluded regions are also drawn. The analysis extends the previous results from LEP and Tevatron, while provides comparative results with the previous ATLAS searches. The CMS results in

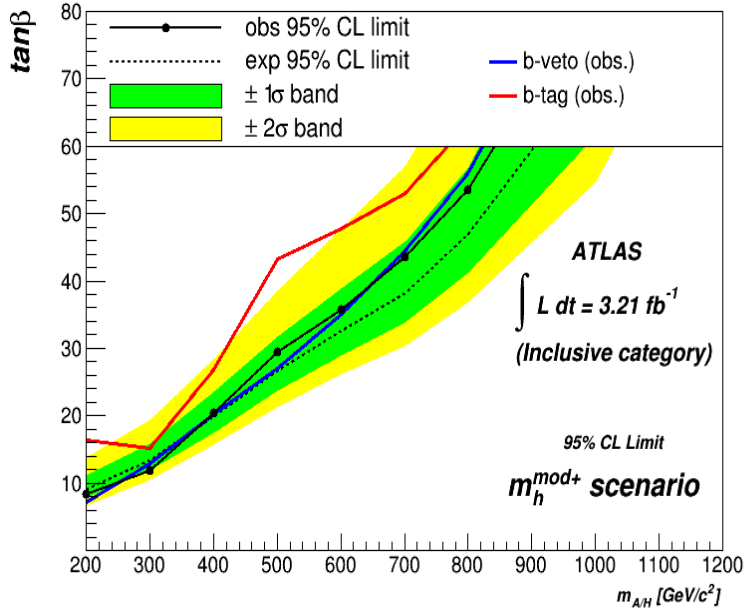


Fig. 7.3: The 95% CL upper limit on the  $m_{A/H} - \tan \beta$  plane of the MSSM parameter space in the  $m_h^{mod+}$  scenario. The limits are obtained from the inclusive (before b-tag and b-veto requirement) analysis.

the combined Run-1 analysis ( $\tau_{lep}\tau_{had} + \tau_{had}\tau_{had}$ ) are comparable to the ATLAS results (CMS exclusion limits are shown in figure 7.5). The combined ATLAS Run-2 analysis ( $\tau_{lep}\tau_{had} + \tau_{had}\tau_{had}$ ) with 2015 data is more sensitive than the Run-1 analysis in the entire mass range being considered (presented in figure 7.6). These results (without b-tagging) have been published (see [161]).

The above results use a specific set of SUSY parameters. In order to make results applicable to wider range of models, an additional interpretation of the analysis is performed. In this interpretation, the signal model is assumed to be an additional scalar boson that is produced via gluon-gluon fusion or b-associated production and decays into di-taus. An upper limit on the cross-section times branching ratio as a function of the boson mass is set. Figure 7.7 shows the upper limits on the cross section times branching ratio for the b-veto and b-tag categories and in the gluon-gluon fusion and b-associated production mechanisms.

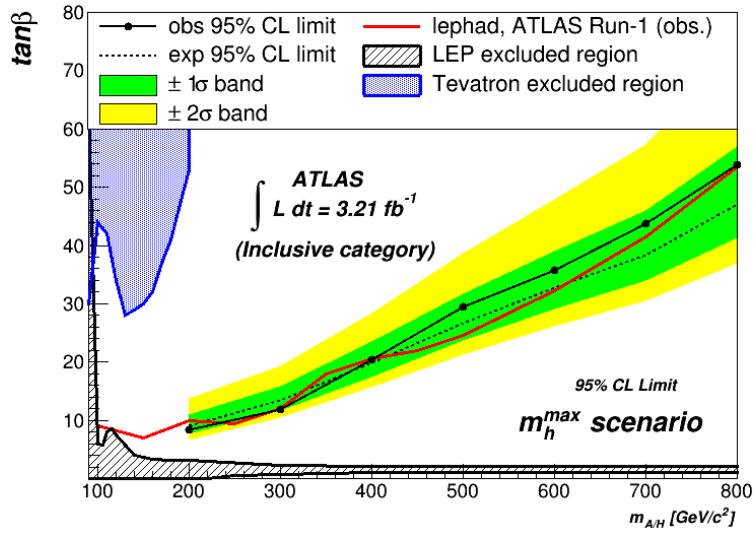


Fig. 7.4: Comparison of the 95% CL upper limits on  $m_{A/H} - \tan\beta$  the plane of the MSSM parameter space in the  $m_h^{max}$  scenario with LEP, Tevatron and the ATLAS Run-1 exclusion limits.

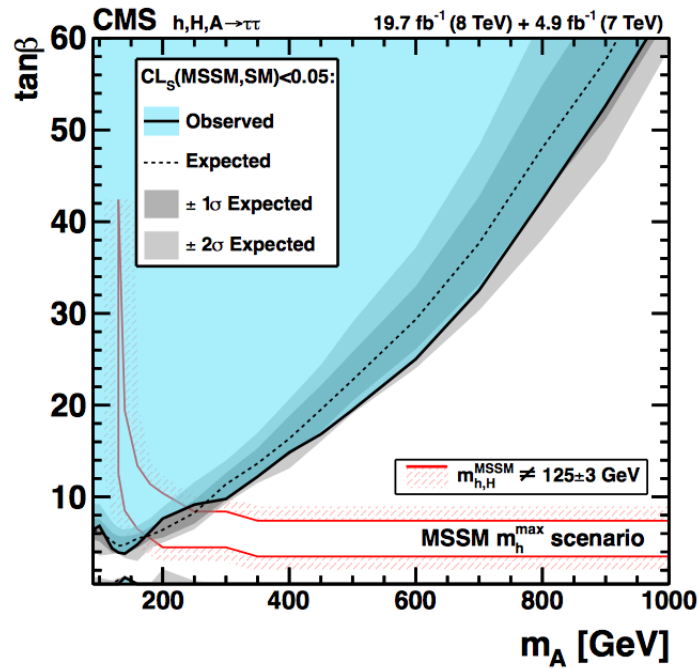


Fig. 7.5: CMS exclusion limits in the  $m_{A/H} - \tan\beta$  plan (in the  $m_h^{max}$  (see section 2.7.1)) for the combined analysis ( $\tau_{lep}\tau_{had} + \tau_{had}\tau_{had}$ ) using Run-1 data [160].

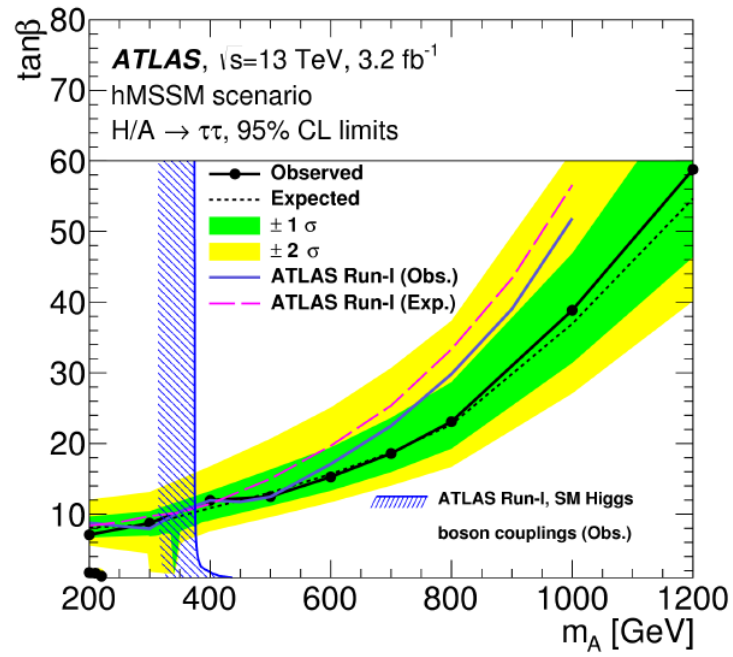
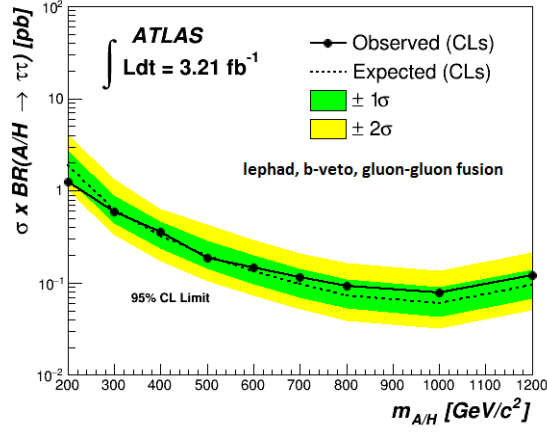
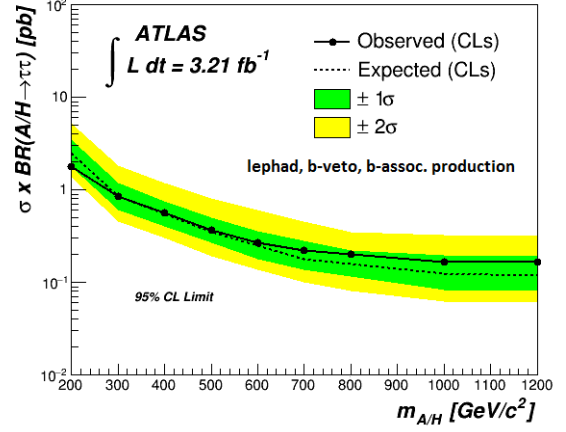


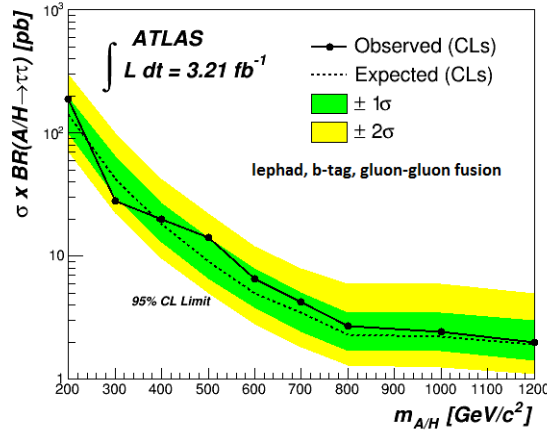
Fig. 7.6: Comparison of the exclusion limits in the  $m_{A/H} - \tan \beta$  plan (in the hMSSM scenario (see section 2.7.1)) for the combined  $(\tau_{lep}\tau_{had} + \tau_{had}\tau_{had})$  Run-2  $H/A \rightarrow \tau\tau$  search with the 2015 data [161].



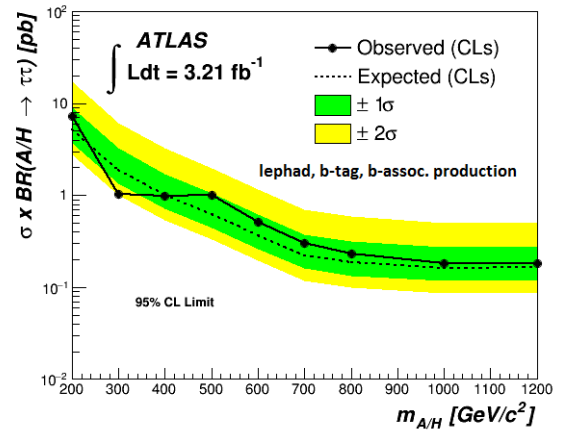
(a) b-veto category, gluon-gluon fusion



(b) b-veto category, b-associated production



(c) b-tag category, gluon-gluon fusion



(d) b-tag category, b-associated production

Fig. 7.7: The 95% CL upper limit on the production cross section times branching ratio to  $\tau_{lep}\tau_{had}$  of a single scalar boson produced via gluon-gluon fusion or b-associated production. Each category is shown separately.

---

## CHAPTER 8

# Summary and Conclusion

The analysis presented in this thesis searched for the neutral MSSM Higgs boson (A/H) decaying into a pair of taus where one tau decays into leptons ( $e/\mu$ ) and the other tau decays into hadrons. When the Standard Model predictions are compared to data no statistically significant excess in the data over the expected background is seen. Although no hint of the MSSM Higgs boson is found, the results set 95% confidence level (CL) upper limits on the parameter  $\tan\beta$  as a function of the MSSM Higgs mass  $m_{A/H}$  in the  $m_h^{mod+}$  scenario for both b-tag and b-veto categories (figure 7.2), with significant regions of the relevant parameter space being excluded. The excluded region ranges from  $\tan\beta > 7.2$  for  $m_{A/H} = 200 \text{ GeV}/c^2$  to  $\tan\beta > 56$  for  $m_{A/H} = 800 \text{ GeV}/c^2$  in the b-veto category and  $\tan\beta > 16.3$  for  $m_{A/H} = 200 \text{ GeV}/c^2$  to  $\tan\beta > 53$  for  $m_{A/H} = 700 \text{ GeV}/c^2$  in the b-tag category.

The exclusion limits are compared with the previous searches at LEP, Tevatron and the ATLAS experiment (see figure 7.4). The analysis expands the exclusion limits that were provided by LEP and the Tevatron while it shows comparable results to the ATLAS Run-1 searches that used data with  $20.3 \text{ fb}^{-1}$  integrated luminosity and the centre of mass energy of 8 TeV. With nearly double the energy in Run-2 and almost one sixth of the total integrated luminosity, similar results have been achieved. In addition, Run-2 data have excluded more parameter space as compared to Run-1 when the combined ( $\tau_{lep}\tau_{had} + \tau_{had}\tau_{had}$ ) analysis is performed, (see figure 7.6). In Run-1, CMS performed a similar search to that presented here in the combined ( $\tau_{lep}\tau_{had} + \tau_{had}\tau_{had}$ ) analysis (see figure 7.5) with exclusion limits similar to the ATLAS Run-1 limits. Therefore, the results presented in the analysis are also consistent with the previous CMS search.

The 95% CL upper limits on the production cross section times the branching ratio for a scalar boson produced via gluon-gluon fusion or in association with b-quarks are

also presented (figure 7.7). The lowest excluded cross section times branching fraction values range from 1.25 pb at  $m_{A/H} = 200 \text{ GeV}/c^2$  to 0.12 pb at  $m_{H/A} = 1200 \text{ GeV}/c^2$  for a scalar boson produced via gluon-gluon fusion in the b-veto category and 190 pb at  $m_{A/H} = 200 \text{ GeV}/c^2$  to 2 pb at  $m_{H/A} = 1200 \text{ GeV}/c^2$  in the b-tag category. Similarly, for the b-associated production mechanism the lowest excluded values range from 1.8 pb at  $m_{A/H} = 200 \text{ GeV}/c^2$  to 0.165 pb at  $m_{A/H} = 1200 \text{ GeV}/c^2$  in the b-veto category and 7.28 pb at  $m_{A/H} = 200 \text{ GeV}/c^2$  to 0.18 pb at  $m_{A/H} = 1200 \text{ GeV}/c^2$  in the b-tag category.

The LHC has delivered more data in 2016 with ATLAS collecting nearly  $25 \text{ fb}^{-1}$  integrated luminosity which is about eight times higher than of 2015 run. It is expected that the final results from 2016 run will show an increase in the limits by roughly a factor of 2 and preliminary results have already shown a gain in the limits. It is also expected that the systematic errors calculated in the analysis will drop with more data. In figures 6.7 and 6.8 effects of the systematics associated with the background estimations are compared with the statistical errors. With the exception of the muon b-veto category, the statistical error dominates showing that more data from 2016 run and onward will clearly improve the results. Even for the muon b-veto category, part of the total background is estimated from data. Therefore, some of the systematic errors in this channel will also decrease with more data and improvement is still expected.

The current Run-2 will end in 2018 with delivering data in two more years with the integrated luminosity per year comparable to that of 2016. Run-3 will start in 2020 for three years with no major upgrades. Then in 2024, LHC and the experiments will have phase-2 upgrade to prepare for the High Luminosity LHC (HL-LHC) when LHC will deliver data with nearly  $250 \text{ fb}^{-1}$  integrated luminosity per year for up to 10 years. Thus, it can be presumed that the results presented here will be improved with the new LHC data coming in future runs albeit at a far slower rate because the centre of mass energy will remain similar to that of Run-2.

Plenty of other SUSY searches are on going at the LHC providing limits on other supersymmetric particle masses at the TeV scale using the simplified models and also providing bounds on the SUSY parameter space. LHCb's measurement of the rate of the rare  $B_s$  meson decay into a pair of muons that requires any new contribution to the

decay amplitude from new physics has to be small compared to the Standard Model. This result has been interpreted as a blow to SUSY. However, while these results have ruled out a large region of constrained SUSY scenarios like mSUGRA, the constraints are far weaker to non-minimal SUSY models. Therefore, SUSY remains a viable theory to explain the light Higgs mass and may be in reach of the LHC in the future.

---

# Bibliography

- [1] P. W. Higgs, “Broken symmetries, massless particles and gauge fields”, **Phys.Rev.Lett. 12 (1964) 132-133**
- [2] P. W. Higgs, “Broken Symmetries and the Masses of Gauge Bosons”, **Phys.Rev.Lett. 13 (1964) 508-509**
- [3] P. W. Higgs, “Spontaneous Symmetry Breakdown without Massless Bosons”, **Phys.Rev. 145 (1966) 1156-1163**
- [4] The ATLAS Collaboration, “Observation of a New Particle in the Search for the Standard Model Higgs Boson with the ATLAS Detector at the LHC”, **Phys. Lett. B 716 (2012) 1-29**
- [5] The CMS Collaboration, “Observation of a New boson at a mass of 125 GeV with the CMS experiment at the LHC”, **Phys. Lett. B 716 (2012) 30**
- [6] The ATLAS Collaboration, “Study of the spin and parity of the Higgs boson in diboson decays with the ATLAS detector”, **Eur.Phys.J. C75 (2015) no.10, 476**
- [7] The ATLAS Collaboration, “Determination of spin and parity of the Higgs boson in the  $WW^* \rightarrow e\nu\mu\nu$  decay channel with the ATLAS detector”, **Eur.Phys.J. C75 (2015) no.5, 231**
- [8] The CMS Collaboration, “Precise determination of the mass of the Higgs boson and tests of compatibility of its couplings with the Standard Model predictions using proton collisions at 7 and 8 TeV”, **Eur. Phys. J. C (2015) 75: 212.**
- [9] G. Bertone, D. Hooper and J. Silk, “Particle dark matter: Evidence, candidates and constraints”, **FERMILAB-Pub-04/047-A**
- [10] C. Rovelli, “Quantum Gravity”, Cambridge University Press 2004, **ISBN 978-0-511-75580-4.**

- [11] M. Dine and A. Kusenko, “The Origin of the matter - antimatter asymmetry”, **Rev. Mod. Phys.** **76**, **1**
- [12] S. P. Martin, “A Supersymmetry Primer”, **High Energy Phys.** **21 (2010) 1-153**
- [13] M. Gomez-Bock, et al., “Concepts of Electroweak Symmetry Breaking and Higgs Physics”, [arXiv:0712.2419v1 \[hep-ph\]](https://arxiv.org/abs/0712.2419v1), (2007).
- [14] The ATLAS Collaboration, “The ATLAS Experiment at the CERN Large Hadron Collider”, **JINST** **3 (2008) S08003**.
- [15] David Griffiths, “Introduction to Elementary Particles”, Wiley, (2008).
- [16] S. L. Glashow, “Partial-Symmetries of Weak Interactions”, **Nucl.Phys.** **22 (1961) 579-588**
- [17] S. Weinberg, “A Model of Leptons”, **Phys. Rev. Lett.** **19 (1967) 1264-1266**.
- [18] A. Salam and J. C. Ward, “Weak and Electromagnetic Interactions”, **Conf.Proc. C680519 (1968) 367-377**
- [19] J. Beringer et. al. (Particle Data Group), “Review of Particle Physics”, **Phys. Rev. D** **86, 010001**
- [20] The ATLAS Collaboration, “Evidence for the Higgs-boson Yukawa coupling to tau leptons with the ATLAS detector”, **JHEP** **1504 (2015) 117**
- [21] Francis Helzen, Alan D. Martin, “Quarks and Leptons: An Introductory Course in Modern Particle Physics”, (1984), John Wiley & Sons, Inc.
- [22] Carl D. Anderson, “The Positive Electron”, **Phys. Rev.** **43, 491**
- [23] Michael E. Peskin, Daniel V. Schroeder, “An Introduction to Quantum Field Theory”, Westview Press, (1995).
- [24] A. Pich, “Quantum Chromodynamics”, [arXiv:hep-ph/9505231](https://arxiv.org/abs/hep-ph/9505231)
- [25] J. H. Christenson, J. W. Cronin, V. L. Fitch, and R. Turlay, “Evidence for the  $2\pi$  Decay of the  $K_2^0$  Meson”, **Phys. Rev. Lett.** **13, 138**

- [26] A. Pich, “The Standard Model of Electroweak Interactions”, [arXiv:0705.4264 \[hep-ph\]](#)
- [27] [http://www.nature.com/nphys/journal/v7/n1/fig\\_tab/nphys1874\\_F1.html](http://www.nature.com/nphys/journal/v7/n1/fig_tab/nphys1874_F1.html)
- [28] The LEP Collaboration: ALEPH, DELPHI, L3, OPAL and the LEP EW Working Group, “A Combination of Preliminary Electroweak Measurements and Constraints on the Standard Model”, [CERN-PH-EP-2006-042](#)
- [29] The ATLAS Collaboration, “Observation of a new particle in the search of the Standard Model Higgs boson with the ATLAS detector at the LHC”, [Phys.Lett. B716 \(2012\) 1-29](#)
- [30] <http://www.atlas.ch/news/images/stories/july31-2012-plot.jpg>
- [31] The CMS Collaboration, “Combination of standard model higgs boson searches and measurements of the properties of the new boson with a mass near 125 GeV”, [CMS PAS HIG-12-045](#)
- [32] The ATLAS and CMS Collaborations, “Combined Measurement of the Higgs Boson Mass in  $pp$  Collision at  $\sqrt{s} = 7$  and 8 TeV with the ATLAS and CMS Experiments”, [Phys.Rev.Lett. 114 \(2015\) 191803](#)
- [33] C.N. Yang, “Selection Rules for the Dematerialization of a Particle into Two Photons”, [Phys. Rev. 77, 242](#)
- [34] Irvin Isenberg, “The Virial Theorem and the Variation Principle”, [Phys. Rev. 79, \(1950\) 737](#)
- [35] The LEP Collaboration: ALEPH, DELPHI, L3, OPAL and the LEP EW Working Group for Higgs Boson Searches, “Search for neutral MSSM Higgs boson at LEP”, [Eur.Phys.J. C47 \(2006\) 547-587](#).
- [36] A. Djouadi, “The anatomy of electroweak symmetry breaking Tome II: The Higgs bosons in the Minimal Supersymmetric Model”, [Phys.Rept. 459 \(2008\) 1-241](#)
- [37] M. Carena, S. Heinemeyer, O. Stal, C.E.M. Wagner, G. Weiglein, “MSSM Higgs Boson Searches at the LHC: Benchmark Scenarios after the Discovery of a Higgs-like Particle”, [Eur.Phys.J. C73 \(2013\) no.9, 2552](#)

- [38] A. Djouadi, S. Rosier-Lees, “The Minimal Supersymmetric Standard Model: Group Summary Report”, [arXiv:hep-ph/9901246](#)
- [39] A. Djouadi et. al., “Fully covering the MSSM Higgs sector at the LHC”, [arXiv:1502.05653 \[hep-ph\]](#)
- [40] Marcela Carena, Howard E. Haber, “Higgs Boson Theory and Phenomenology”, **Prog.Part.Nucl.Phys. 50 (2003) 63-152**
- [41] Robert V. Harlander, William B. Kilgore, “Higgs boson production in bottom quark fusion at next-to-next-to-leading order”, **Phys.Rev. D68 (2003) 013001**
- [42] The ATLAS Collaboration, “Search for the neutral Higgs boson of the Minimal Supersymmetric Standard Model in pp collision at  $\sqrt{s} = 7$  TeV with the ATLAS detector”, **JHEP02 (2013) 095**
- [43] The ATLAS Collaboration, “Search for neutral Higgs boson of the Minimal Supersymmetric Standard Model in pp collision at  $\sqrt{s} = 8$  TeV with the ATLAS detector”, [arXiv:1409.6064\[hep-ph\]](#), **JHEP11(2014)056**
- [44] A. L. Read, “Presentation of search results: the  $CL_s$  technique”, **J.Phys. G: Nucl. Part. Phys. 28 (2002) 2693**.
- [45] K. Schindl., “The injector chain for the LHC” , Workshop on LEP-SPS Performance, Chamonix, (1999), **CERN/PS 99- 018(DI)**
- [46] <http://te-epc-lpc.web.cern.ch/te-epc-lpc/machines/pagesources/Cern-Accelerator-Complex.jpg>
- [47] The ATLAS Collaboration, “ATLAS detector and physics performance: Technical Design Report”, **CERN-LHCC-99-014**
- [48] The CMS Collaboration, ”The CMS Experiment at the CERN Large Hadron Collider”, **JINST 3 (2008) S08004**.
- [49] The ALICE Collaboration, ”The ALICE Experiment at the CERN Large Hadron Collider”, **JINST 3 (2008) S08002**.
- [50] The LHCb Collaboration, ”LHCb Experiment at the CERN Large Hadron Collider”, **JINST 3 (2008) S08005**.

- [51] Lyndon Evans and Philip Bryant, “LHC Machine”, **JINST 3 (2008) S08001**
- [52] R. Bruce et.al., “LHC RUN 2: Results and Challenges”, **Proceedings of HB2016**, Malmö, Sweden
- [53] Mike Lamont, “Status of the LHC”, **Journal of Physics: Conference Series 455 (2013) 012001**
- [54] The ATLAS Collaboration, “ATLAS magnet system: Technical Design Report”, **CERN-LHCC-97-018**
- [55] The ATLAS Collaboration, “ATLAS central solenoid: Technical Design Report”, **CERN-LHCC-97-021**
- [56] The ATLAS Collaboration, “ATLAS end-cap toroids: Technical Design Report”, **CERN-LHCC-97-020**
- [57] The ATLAS Collaboration, “ATLAS barrel toroid: Technical Design Report”, **CERN-LHCC-97-19**
- [58] G. Ad. et al., “The ATLAS Inner Detector commissioning and calibration”, (2010), **arXiv:1004-5293v2**.
- [59] [https://mediastream.cern.ch/MediaArchive/Photo/Public/2008/0803014/0803014\\_01/0803014\\_01-A4-at-144-dpi.jpg](https://mediastream.cern.ch/MediaArchive/Photo/Public/2008/0803014/0803014_01/0803014_01-A4-at-144-dpi.jpg)
- [60] [https://atlas.web.cern.ch/Atlas/GROUPS/PHYSICS/PUBNOTES/ATL-PHYS-PUB-2015-018/fig\\_01.png](https://atlas.web.cern.ch/Atlas/GROUPS/PHYSICS/PUBNOTES/ATL-PHYS-PUB-2015-018/fig_01.png)
- [61] [http://atlas.ch/inner\\_detector1.html](http://atlas.ch/inner_detector1.html)
- [62] Y. Takubo, “The Pixel Detector of the ATLAS experiment for the Run2 at the Large Hadron Collider”, (2015), **JINST 10 C02001**.
- [63] <https://kjende.web.cern.ch/kjende/en/atlas.htm>
- [64] [http://atlas.ch/inner\\_detector3.html](http://atlas.ch/inner_detector3.html)
- [65] [www.hep.lu.se/atlas/thesis/egede/thesis-node43.html](http://www.hep.lu.se/atlas/thesis/egede/thesis-node43.html)

- [66] The ATLAS Collaboration, “ATLAS calorimeter performance: Technical Design Report”, **CERN-LHCC-96-40**
- [67] Zhaoxia Meng, “Performance of the ATLAS liquid argon calorimeter”, Institute of Physics, Academia Sinica, on behalf of the ATLAS Liquid Argon Calorimeter Group, **5th conference: Physics at the LHC 2010**.
- [68] The ATLAS Collaboration, “ATLAS muon spectrometer: Technical Design Report”, **CERN-LHCC-97-022**.
- [69] <http://www.atlas.ch/photos/muons-combined.html>
- [70] F. Pastore, “The ATLAS Trigger System: Past, Present and Future”, Royal Holloway, University of London (UK), on behalf of the ATLAS Collaboration, **Nucl.Part.Phys.Proc. 273-275 (2016) 1065-1071**
- [71] A. Borga et al., “Evolution of the ReadOut System of the ATLAS experiment”, **PoS (TTPP2014) 205**
- [72] Joern Mahlstedt, “The ATLAS Hadronic Tau Trigger”, on behalf of the ATLAS collaboration, **J.Phys:Conf. Ser. 513 (2014) 012021**.
- [73] <http://inspirehep.net/record/798323/plots>
- [74] Yuki Sakurai, “The ATLAS Tau Trigger Performance during LHC Run 1 and Prospects for Run 2”, Waseda University (Japan), on behalf of the ATLAS Collaboration, **arXiv:1409.2699 [hep-ex]**
- [75] K. Benslama et al., “Tau trigger at the ATLAS experiment”, 34<sup>th</sup> International Conference on High Energy Physics, Philadelphia, (2008), **arXiv:0810.0465 [hep-ex]**
- [76] Andrea Coccaro, “Track Reconstruction and b-jet Identification for the ATLAS Trigger System”, **J.Phys.Conf.Ser. 368 (2012) 012034**.
- [77] [http://atlas.web.cern.ch/Atlas/GROUPS/PHYSICS/CONFNOTES/ATLAS-CONF-2010-042/fig\\_01.png](http://atlas.web.cern.ch/Atlas/GROUPS/PHYSICS/CONFNOTES/ATLAS-CONF-2010-042/fig_01.png)
- [78] <http://home.web.cern.ch/about/computing/grid-system-tiers>

- [79] C. Leggett et al., “The Athena Control Framework in Production, New Developments and Lessons Learned”, LBNL, Berkeley, USA, <https://cdsweb.cern.ch/record/865624/files/p456.pdf>
- [80] Torbjorn Sjostrand, Patrik Eden, et al., “High-Energy-Physics Event Generation with Pythia 6.1”, [arXiv:hep-ph/0010017](https://arxiv.org/abs/hep-ph/0010017).
- [81] Stefano Frixione, Fabian Stoeckli, et al., “The MCNLO 4.0 Event Generator”, [arXiv:1010.0819](https://arxiv.org/abs/1010.0819) [hep-ph].
- [82] S. Moretti, “HERWIG: an event generator for MSSM processes”, [arXiv:hep-ph/1215105](https://arxiv.org/abs/hep-ph/1215105).
- [83] D. Costanzo, A. Dell Acqua, et al., “The Geant4-Based Simulation Software of the ATLAS Detector”, **Nuclear Science Symposium Conference Record, 2006, IEEE (Volume 1)**.
- [84] P. Nason, “A New method for combining NLO QCD with shower Monte Carlo algorithms”, [arXiv:hep-ph/0409146](https://arxiv.org/abs/hep-ph/0409146).
- [85] S. Alioli et al., “A general framework for implementing NLO calculations in shower Monte Carlo programs: the POWHEG BOX”, **JHEP 06 (2010) 043**, [arXiv:1002.2581](https://arxiv.org/abs/1002.2581) [hep-ph].
- [86] Torbjorn Sjostrand et al., “An introduction to PYTHIA 8.2”, [arXiv:1410.3012v1](https://arxiv.org/abs/1410.3012v1) [hep-ph].
- [87] The ATLAS Collaboration, “Measurement of the  $Z/\gamma^*$  boson transverse momentum distribution in pp collisions at  $\sqrt{s} = 7$  TeV with the ATLAS detector”, [arXiv:1406.3660](https://arxiv.org/abs/1406.3660) [hep-ex].
- [88] M. Wiesemann et al., “Higgs production in association with bottom quarks”, **JHEP 02 (2015) 132**, [arXiv:1409.5301](https://arxiv.org/abs/1409.5301) [hep-ph].
- [89] The ATLAS Collaboration, “ATLAS Run 1 Pythia8 tunes”, **ATL-PHYS-PUB-2014-021**
- [90] H.-L. Lai et al., “New parton distributions for collider physics”, [arXiv:1007.2241](https://arxiv.org/abs/1007.2241) [hep-ph].

- [91] S. Dulat et al., “New parton distribution functions from a global analysis of quantum chromodynamics”, [arXiv:1506.07443 \[hep-ph\]](#).
- [92] R. V. Harlander, S. Liebler and H. Mantler, “SusHi: A program for the calculation of Higgs production in gluon fusion and bottom-quark annihilation in the Standard Model and the MSSM”, **Comp. Phys. Commun.** **184** (2013) 1605, [arXiv:1212.3249 \[hep-ph\]](#).
- [93] R. Harlander and W. B. Kilgore, “Higgs boson production in bottom quark fusion at next-to-next-to-leading order”, **Phys. Rev. D** **68** (2003) 013001, [arXiv:hep-ph/0304035](#)
- [94] S. Dittmaier, M. Krämer and M. Spira, “Higgs radiation off bottom quarks at the Tevatron and the LHC”, **Phys. Rev. D** **70** (2004) 074010, [arXiv:hep-ph/0309204](#).
- [95] S. Dawson, C. B. Jackson, L. Reina and D. Wackerath, “Exclusive Higgs boson production with bottom quarks at hadron colliders”, **Phys. Rev. D** **69** (2004) 074027, [arXiv:hep-ph/0311067](#).
- [96] R. Harlander, M. Kramer and M. Schumacher, “Bottom-quark associated Higgs-boson production: reconciling the four- and five-flavour scheme approach”, (2011), [arXiv:1112.3478 \[hep-ph\]](#).
- [97] S. Heinemeyer, W. Hollik and G. Weiglein, “FeynHiggs: A Program for the calculation of the masses of the neutral CP even Higgs bosons in the MSSM”, **Comput. Phys. Commun.** **124** (2000) 76, [arXiv:hep-ph/9812320](#).
- [98] LHC Higgs Cross Section Working Group, “Handbook of LHC Higgs Cross Sections: 3. Higgs Properties”, [arXiv:1307.1347 \[hep-ph\]](#).
- [99] Torbjorn Sjostrand, Stephen Mrenna, Peter Skands, “A brief introduction to PYTHIA 8.1”, [arXiv:0710.3820 \[hep-ph\]](#).
- [100] E. Barberio, B. V. Eijk and Z. Was, “PHOTOS - a universal Monte Carlo for QED radiative corrections in decays”, **Comput. Phys. Commun.** **66** (1991) 115.
- [101] N. Davidson, T. Przedzinski and Z. Was, “PHOTOS Interface in C++: Technical and Physics Documentation”, [arXiv:1011.0937 \[hep-ph\]](#).

- [102] T. Przedzinski, E. Richter-Was, Z. Was, “TauSpinner: a tool for simulating CP effects in H to tau tau decays at LHC”, [arXiv:1406.1647\[hep-ph\]](#)
- [103] R. Gavin et al., “FEWZ 2.0: A code for hadronic Z production at next-to-next-to-leading order”, [arXiv:1011.3540 \[hep-ph\]](#).
- [104] C. Anastasiou et al., “High precision QCD at hadron colliders: Electroweak gauge boson rapidity distributions at NNLO”, **Phys. Rev. D** **69** (2004) 094008, [arXiv:hep-ph/0312266](#).
- [105] P. Artoisenet et al., “Automatic spin-entangled decays of heavy resonances in Monte Carlo simulations”, [arXiv:1212.3460 \[hep-ph\]](#).
- [106] T. Sjostrand, S. Mrenna and P. Skands, “PYTHIA 6.4 physics and manual”, **JHEP** **05** (2006) 026, [arXiv:hep-ph/0603175](#).
- [107] P. Skands, “Tuning Monte Carlo Generators: The Perugia Tunes”, **Phys. Rev. D** **82** (2010) 074018, [arXiv:1005.3457 \[hep-ph\]](#).
- [108] M. Czakon and A. Mitov, “Top++: A Program for the Calculation of the Top-Pair Cross-Section at Hadron Colliders”, [arXiv:1112.5675 \[hep-ph\]](#).
- [109] N. Kidonakis, “Next-to-next-to-leading-order collinear and soft gluon corrections for t-channel single top quark production”, **Phys. Rev. D** **83** (2011) 091503, [arXiv:1103.2792 \[hep-ph\]](#).
- [110] N. Kidonakis, “NNLL resummation for s-channel single top quark production”, **Phys. Rev. D** **81** (2010) 054028, [arXiv:1001.5034 \[hep-ph\]](#).
- [111] N. Kidonakis, “Two-loop soft anomalous dimensions for single top quark associated production with a W- or H-”, **Phys. Rev. D** **82** (2010) 054018, [arXiv:1005.4451 \[hep-ph\]](#).
- [112] T. Gleisberg et al., “Event generation with SHERPA 1.1”, [arXiv:0811.4622 \[hep-ph\]](#).
- [113] R.D. Ball et al., “Parton distributions with LHC data”, [arXiv:1207.1303 \[hep-ph\]](#).

- [114] D. J. Lange, “The EvtGen particle decay simulation package”, *Nucl. Instrum. Meth. A* **462** (2001) 152.
- [115] The ATLAS Collaboration, “Summary of ATLAS Pythia 8 tunes”, ATL-PHYS-PUB-2012-003, (2012), <http://cdsweb.cern.ch/record/1474107>.
- [116] A. D. Martin et al., “Parton distributions for the LHC”, *Eur. Phys. J. C* **63** (2009) 189, [arXiv:0901.0002](https://arxiv.org/abs/0901.0002).
- [117] S. Agostinelli et al., “GEANT4 Collaboration, GEANT4 - a simulation toolkit”, *Nucl. Instrum. Meth. A* **506** (2003) 250.
- [118] The ATLAS collaboration, “The ATLAS Simulation Infrastructure”, *Eur. Phys. J. C* **70** (2010) 823, [arXiv:1005.4568](https://arxiv.org/abs/1005.4568) [[physics.ins-det](https://arxiv.org/archive/physics)].
- [119] Ramsey Faragher, “Understanding the basis of the Kalman Filter via a simple and intuitive Derivation”, <https://www.cl.cam.ac.uk/~rmf25/papers/Understanding%20the%20Basis%20of%20the%20Kalman%20Filter.pdf>
- [120] V. Lacuesta, “Track and vertex reconstruction in the ATLAS experiment”, *JINST* **8 C02035** (2013).
- [121] The ATLAS Collaboration, “Vertex reconstruction performance of the ATLAS detector at  $\sqrt{s} = 13$  TeV”, ATL-PHYS-PUB-2015-026, <https://cds.cern.ch/record/2037717?ln=en>.
- [122] W. Lampl et al., “Calorimeter clustering algorithms: Description and performance”, ATL-LARG-PUB-2008-002, <https://cds.cern.ch/record/1099735?ln=en>.
- [123] The ATLAS Collaboration, “Electron performance measurements with the ATLAS detector using the 2010 LHC proton-proton collision data”, [arXiv:1110.3174](https://arxiv.org/abs/1110.3174) [[hep-ex](https://arxiv.org/archive/hep)].
- [124] The ATLAS Collaboration, “Electron reconstruction and identification efficiency measurements with the ATLAS detector using the 2011 LHC proton-proton collision data”, [arXiv:1404.2240](https://arxiv.org/abs/1404.2240) [[hep-ex](https://arxiv.org/archive/hep)].

- [125] The ATLAS Collaboration, “Expected performance of the ATLAS experiment detector, trigger and physics”, [arXiv:0901.0512 \[hep-ex\]](#)
- [126] Gavin P. Salam, “Towards Jetography”, [arXiv:0906.1833 \[hep-ph\]](#).
- [127] The ATLAS Collaboration, “Reconstruction, energy calibration, and identification of hadronically decaying tau leptons in the ATLAS experiment for Run-2 of the LHC”, ATL-PHYS-PUB-2015-045, <https://cds.cern.ch/record/2064383>
- [128] Felix Friedrich, “Reconstruction and Identification Techniques for Tau Leptons at the ATLAS Detector at LHC”, **Journal of Physics: Conference Series 490 (2014) 012228**.
- [129] R. Nicolaidou et al., “Muon identification procedure for the ATLAS detector at the LHC using Muonboy reconstruction package and tests of its performance using cosmic rays and single beam data”, **J. Phys.: Conf. Ser. 219 (2010) 032052**.
- [130] Jovan Mitrevski , “Preparing ATLAS reconstruction software for LHC’s Run 2”, **J. Phys: Conf. Ser. 664 (2015) 072034**.
- [131] The ATLAS Collaboration, “Expected Performance of the ATLAS b-tagging algorithms in Run-2”, ATL-PHYS-PUB-2015-022, <http://cds.cern.ch/record/2037697>.
- [132] <https://twiki.cern.ch/twiki/bin/view/AtlasPublic/EgammaTriggerPublicResults>
- [133] <https://twiki.cern.ch/twiki/bin/view/AtlasPublic/MuonTriggerPublicResults>
- [134] The ATLAS Collaboration, “Selection of jets produced in 13TeV proton-proton collisions with the ATLAS detector”, **ATLAS-CONF-2015-029**
- [135] The ATLAS Collaboration, “Tagging and suppression of pileup jets with the ATLAS detector”, ATLAS-CONF-2014-018, 2014, <https://cds.cern.ch/record/1700870>.
- [136] A. Elagin et al., “A New Mass Reconstruction Technique for Resonances Decaying to di-tau”, **Nucl.Instrum.Meth. A654 (2011) 481-489**, [arXiv:1012.4686 \[hep-ex\]](#).

- [137] The ATLAS Collaboration, “Electron efficiency measurements with the ATLAS detector using the 2015 LHC proton-proton collision data”, **ATLAS-CONF-2016-024**
- [138] The ATLAS Collaboration, “Muon reconstruction performance of the ATLAS detector in proton-proton collision data at  $\sqrt{s} = 13$  TeV”, **Eur. Phys. J. C76 (2016) 292**, [arXiv:1603.05598 \[hep-ex\]](#)
- [139] J Butterworth et al., “Single Boson and Diboson Production Cross Sections in pp Collisions at  $\sqrt{s} = 7$  TeV”, ATL-COM-PHYS-2010-695, <https://cds.cern.ch/record/1287902>.
- [140] M. Czakon and A. Mitov, “Top++: A Program for the Calculation of the Top-Pair Cross-Section at Hadron Colliders”, **Comput. Phys. Commun. 185 (2014) 2930**, [arXiv:1112.5675 \[hep-ph\]](#).
- [141] M. Aliev et al., “HATHOR: HAdronic Top and Heavy quarks crOss section calculator”, **Comput. Phys. Commun. 182 (2011) 1034**, [arXiv:1007.1327 \[hep-ph\]](#).
- [142] P. Kant et al., “HATHOR for single top-quark production: Updated predictions and uncertainty estimates for single top-quark production in hadronic collisions”, **Comput. Phys. Commun. 191 (2015) 74**, [arXiv:1406.4403 \[hep-ph\]](#).
- [143] <https://twiki.cern.ch/twiki/bin/view/AtlasPublic/LuminosityPublicResultsRun2>
- [144] Zachary Marshall, “Simulation of Pile-up in the ATLAS Experiment ”, on behalf of ATLAS Collaboration, **Journal of Physics: Conference Series 513 (2014) 022024**
- [145] Gabriella Pasztor, “The Upgrade of the ATLAS Electron and Photon Triggers towards LHC Run 2 and their Performance”, on behalf of the ATLAS Collaboration, **ATL-DAQ-PROC-2015-053**
- [146] The ATLAS Collaboration, “Electron and photon energy calibration with the ATLAS detector using data collected in 2015 at  $\sqrt{s} = 13$  TeV”, **ATL-PHYS-PUB-2016-015**

- [147] The ATLAS Collaboration, “Muon reconstruction performance in ATLAS at Run-2”, **ATL-PHYS-PROC-2015-157**
- [148] The ATLAS Collaboration, “Jet Calibration and Systematic Uncertainties for Jets Reconstructed in the ATLAS Detector at  $\sqrt{s} = 13$  TeV”, **ATL-PHYS-PUB-2015-015**
- [149] The ATLAS Collaboration, “Performance of missing transverse momentum reconstruction for the ATLAS detector in the first proton-proton collisions at  $\sqrt{s} = 13$  TeV”, **ATL-PHYS-PUB-2015-027**
- [150] R. D. Ball et al., “Parton distributions for the LHC Run II”, **JHEP 04 (2015) 040**, [arXiv:1410.8849 \[hep-ph\]](#).
- [151] A. Martin et al., “Heavy-quark mass dependence in global PDF analyses and 3- and 4-flavour parton distributions”, **Eur. Phys. J. C 70 (2010) 51**, [arXiv:1007.2624 \[hep-ph\]](#).
- [152] R. D. Ball et al., “Parton distributions for the LHC Run II”, **JHEP 04 (2015) 040**, [arXiv:1410.8849 \[hep-ph\]](#).
- [153] ATLAS Collaboration, “Simulation of top-quark production for the ATLAS experiment at  $\sqrt{s} = 13$  TeV”, ATL-PHYS-PUB-2016-004, <http://cds.cern.ch/record/2120417>
- [154] M. Bahr et al., “Herwig++ Physics and Manual”, **Eur. Phys. J. C 58 (2008) 639**, [arXiv:0803.0883 \[hep-ph\]](#)
- [155] A.L. read, “Presentation of search results: the CLs technique”, **J. Phys. G 28 (2002) 2693**
- [156] G. Cowan, K. Cranmer, E. Gross and O. Vitells, “Asymptotic formulae for likelihood-based tests of new physics”, **Phys. J. C (2011) 71: 1554**
- [157] ALEPH, DELPHI, L3, OPAL Collaborations, and the LEP Working Group for Higgs Boson Searches Collaboration, “Search for the Standard Model Higgs Boson at LEP”, **Phys. Lett. B 565 (2003) 61**

- [158] The CDF Collaboration, “Search for Higgs Bosons Predicted in Two-Higgs-Doublet Models via Decays to Tau Lepton Pairs in 1.96 TeV  $p\bar{p}$  Collisions”, **Phys. Rev. Lett.** **103**, 201801
- [159] The D0 Collaboration, “Search for Higgs bosons decaying to  $\tau^+\tau^-$  pairs in 1.96 TeV  $p\bar{p}$  Collisions”, **Phys. Lett. B** **707**, 323 (2012)
- [160] The CMS Collaboration, “Search for additional neutral Higgs bosons decaying to a pair of tau leptons in  $pp$  collisions at  $\sqrt{s} = 7$  and 8 TeV”, **CMS-PAS-HIG-14-029**
- [161] The ATLAS Collaboration, “Search for Neutral Minimal Supersymmetric Standard Model Higgs Bosons  $H/A \rightarrow \tau\tau$  produced in the  $pp$  collisions at  $\sqrt{s} = 13$  TeV with the ATLAS Detector”, **Eur. Phys. J. C** **76** (2016) 585

# Appendices

---

# APPENDIX A

## Signal and Background MC Samples

Monte Carlo samples used in the analysis for signal and backgrounds are listed below with their dataset identification numbers (DID) and sample names. These samples can be browsed on [Panda Monitor](#) and the [ATLAS Metadata Interface](#) (AMI) and can be downloaded using the [DQ2Clients](#) and [RucioClients](#) tools. The signal samples for gluon-gluon fusion and b-associated production of the MSSM Higgs boson are generated for several mass points and with  $\tan\beta = 20$ . Both signal and background Monte Carlo samples are listed below:

DID	Sample name
342305	ggH200_tautaulh
342310	ggH300_tautaulh
342312	ggH350_tautaulh
342314	ggH400_tautaulh
342316	ggH500_tautaulh
342318	ggH600_tautaulh
342320	ggH700_tautaulh
342322	ggH800_tautaulh
342326	ggH1000_tautaulh
342330	ggH1200_tautaulh

Table A.1: List of MC15 ggH signal samples used in the analysis.

DID	Sample name
341858	bbH200_yb2_tautaulh
341860	bbH300_yb2_tautaulh
341861	bbH350_yb2_tautaulh
341862	bbH400_yb2_tautaulh
341863	bbH500_yb2_tautaulh
341864	bbH600_yb2_tautaulh
341865	bbH700_yb2_tautaulh
341866	bbH800_yb2_tautaulh
341868	bbH1000_yb2_tautaulh
341870	bbH1200_yb2_tautaulh

Table A.2: List of MC15 bbH signal samples used in the analysis.

DID	Sample name
301090	PowhegPythia8EvtGen_AZNLOCTEQ6L1_Wminenu_2000M2250
301081	PowhegPythia8EvtGen_AZNLOCTEQ6L1_Wminenu_180M250
301095	PowhegPythia8EvtGen_AZNLOCTEQ6L1_Wminenu_3500M4000
301086	PowhegPythia8EvtGen_AZNLOCTEQ6L1_Wminenu_1000M1250
301084	PowhegPythia8EvtGen_AZNLOCTEQ6L1_Wminenu_600M800
301094	PowhegPythia8EvtGen_AZNLOCTEQ6L1_Wminenu_3000M3500
301082	PowhegPythia8EvtGen_AZNLOCTEQ6L1_Wminenu_250M400
301098	PowhegPythia8EvtGen_AZNLOCTEQ6L1_Wminenu_5000M
301083	PowhegPythia8EvtGen_AZNLOCTEQ6L1_Wminenu_400M600
301097	PowhegPythia8EvtGen_AZNLOCTEQ6L1_Wminenu_4500M5000
301089	PowhegPythia8EvtGen_AZNLOCTEQ6L1_Wminenu_1750M2000
301091	PowhegPythia8EvtGen_AZNLOCTEQ6L1_Wminenu_2250M2500
301080	PowhegPythia8EvtGen_AZNLOCTEQ6L1_Wminenu_120M180
301096	PowhegPythia8EvtGen_AZNLOCTEQ6L1_Wminenu_4000M4500
301088	PowhegPythia8EvtGen_AZNLOCTEQ6L1_Wminenu_1500M1750
301093	PowhegPythia8EvtGen_AZNLOCTEQ6L1_Wminenu_2750M3000
301092	PowhegPythia8EvtGen_AZNLOCTEQ6L1_Wminenu_2500M2750
301085	PowhegPythia8EvtGen_AZNLOCTEQ6L1_Wminenu_800M1000
301087	PowhegPythia8EvtGen_AZNLOCTEQ6L1_Wminenu_1250M1500
301122	PowhegPythia8EvtGen_AZNLOCTEQ6L1_Wminenu_250M400
301133	PowhegPythia8EvtGen_AZNLOCTEQ6L1_Wminenu_2750M3000
301124	PowhegPythia8EvtGen_AZNLOCTEQ6L1_Wminenu_600M800
301125	PowhegPythia8EvtGen_AZNLOCTEQ6L1_Wminenu_800M1000
301129	PowhegPythia8EvtGen_AZNLOCTEQ6L1_Wminenu_1750M2000
301121	PowhegPythia8EvtGen_AZNLOCTEQ6L1_Wminenu_180M250
301127	PowhegPythia8EvtGen_AZNLOCTEQ6L1_Wminenu_1250M1500
301131	PowhegPythia8EvtGen_AZNLOCTEQ6L1_Wminenu_2250M2500
301126	PowhegPythia8EvtGen_AZNLOCTEQ6L1_Wminenu_1000M1250
301138	PowhegPythia8EvtGen_AZNLOCTEQ6L1_Wminenu_5000M
301135	PowhegPythia8EvtGen_AZNLOCTEQ6L1_Wminenu_3500M4000
301128	PowhegPythia8EvtGen_AZNLOCTEQ6L1_Wminenu_1500M1750
301136	PowhegPythia8EvtGen_AZNLOCTEQ6L1_Wminenu_4000M4500
301134	PowhegPythia8EvtGen_AZNLOCTEQ6L1_Wminenu_3000M3500
301120	PowhegPythia8EvtGen_AZNLOCTEQ6L1_Wminenu_120M180
301132	PowhegPythia8EvtGen_AZNLOCTEQ6L1_Wminenu_2500M2750
301123	PowhegPythia8EvtGen_AZNLOCTEQ6L1_Wminenu_400M600
301130	PowhegPythia8EvtGen_AZNLOCTEQ6L1_Wminenu_2000M2250
301137	PowhegPythia8EvtGen_AZNLOCTEQ6L1_Wminenu_4500M5000
301172	PowhegPythia8EvtGen_AZNLOCTEQ6L1_Wminenu_2500M2750
301163	PowhegPythia8EvtGen_AZNLOCTEQ6L1_Wminenu_400M600
301171	PowhegPythia8EvtGen_AZNLOCTEQ6L1_Wminenu_2250M2500
301178	PowhegPythia8EvtGen_AZNLOCTEQ6L1_Wminenu_5000M
301165	PowhegPythia8EvtGen_AZNLOCTEQ6L1_Wminenu_800M1000
301177	PowhegPythia8EvtGen_AZNLOCTEQ6L1_Wminenu_4500M5000
301173	PowhegPythia8EvtGen_AZNLOCTEQ6L1_Wminenu_2750M3000
301167	PowhegPythia8EvtGen_AZNLOCTEQ6L1_Wminenu_1250M1500
301164	PowhegPythia8EvtGen_AZNLOCTEQ6L1_Wminenu_600M800
301170	PowhegPythia8EvtGen_AZNLOCTEQ6L1_Wminenu_2000M2250
301162	PowhegPythia8EvtGen_AZNLOCTEQ6L1_Wminenu_250M400
301160	PowhegPythia8EvtGen_AZNLOCTEQ6L1_Wminenu_120M180
301174	PowhegPythia8EvtGen_AZNLOCTEQ6L1_Wminenu_3000M3500
301168	PowhegPythia8EvtGen_AZNLOCTEQ6L1_Wminenu_1500M1750
301166	PowhegPythia8EvtGen_AZNLOCTEQ6L1_Wminenu_1000M1250
301176	PowhegPythia8EvtGen_AZNLOCTEQ6L1_Wminenu_4000M4500
301169	PowhegPythia8EvtGen_AZNLOCTEQ6L1_Wminenu_1750M2000
301175	PowhegPythia8EvtGen_AZNLOCTEQ6L1_Wminenu_3500M4000
301161	PowhegPythia8EvtGen_AZNLOCTEQ6L1_Wminenu_180M250
301078	PowhegPythia8EvtGen_AZNLOCTEQ6L1_Wplusenu_5000M
301060	PowhegPythia8EvtGen_AZNLOCTEQ6L1_Wplusenu_120M180
301076	PowhegPythia8EvtGen_AZNLOCTEQ6L1_Wplusenu_4000M4500
301075	PowhegPythia8EvtGen_AZNLOCTEQ6L1_Wplusenu_3500M4000

Table A.3: List of MC15 W+jets samples used in the analysis

DID	Sample name
301073	PowhegPythia8EvtGen_AZNLOCTEQ6L1_Wplusenu_2750M3000
301061	PowhegPythia8EvtGen_AZNLOCTEQ6L1_Wplusenu_180M250
301066	PowhegPythia8EvtGen_AZNLOCTEQ6L1_Wplusenu_1000M1250
301067	PowhegPythia8EvtGen_AZNLOCTEQ6L1_Wplusenu_1250M1500
301065	PowhegPythia8EvtGen_AZNLOCTEQ6L1_Wplusenu_800M1000
301077	PowhegPythia8EvtGen_AZNLOCTEQ6L1_Wplusenu_4500M5000
301068	PowhegPythia8EvtGen_AZNLOCTEQ6L1_Wplusenu_1500M1750
301062	PowhegPythia8EvtGen_AZNLOCTEQ6L1_Wplusenu_250M400
301072	PowhegPythia8EvtGen_AZNLOCTEQ6L1_Wplusenu_2500M2750
301071	PowhegPythia8EvtGen_AZNLOCTEQ6L1_Wplusenu_2250M2500
301063	PowhegPythia8EvtGen_AZNLOCTEQ6L1_Wplusenu_400M600
301064	PowhegPythia8EvtGen_AZNLOCTEQ6L1_Wplusenu_600M800
301074	PowhegPythia8EvtGen_AZNLOCTEQ6L1_Wplusenu_3000M3500
301069	PowhegPythia8EvtGen_AZNLOCTEQ6L1_Wplusenu_1750M2000
301070	PowhegPythia8EvtGen_AZNLOCTEQ6L1_Wplusenu_2000M2250
301109	PowhegPythia8EvtGen_AZNLOCTEQ6L1_Wplumunu_1750M2000
301108	PowhegPythia8EvtGen_AZNLOCTEQ6L1_Wplumunu_1500M1750
301107	PowhegPythia8EvtGen_AZNLOCTEQ6L1_Wplumunu_1250M1500
301118	PowhegPythia8EvtGen_AZNLOCTEQ6L1_Wplumunu_5000M
301115	PowhegPythia8EvtGen_AZNLOCTEQ6L1_Wplumunu_3500M4000
301101	PowhegPythia8EvtGen_AZNLOCTEQ6L1_Wplumunu_180M250
301111	PowhegPythia8EvtGen_AZNLOCTEQ6L1_Wplumunu_2250M2500
301104	PowhegPythia8EvtGen_AZNLOCTEQ6L1_Wplumunu_600M800
301106	PowhegPythia8EvtGen_AZNLOCTEQ6L1_Wplumunu_1000M1250
301110	PowhegPythia8EvtGen_AZNLOCTEQ6L1_Wplumunu_2000M2250
301113	PowhegPythia8EvtGen_AZNLOCTEQ6L1_Wplumunu_2750M3000
301116	PowhegPythia8EvtGen_AZNLOCTEQ6L1_Wplumunu_4000M4500
301112	PowhegPythia8EvtGen_AZNLOCTEQ6L1_Wplumunu_2500M2750
301117	PowhegPythia8EvtGen_AZNLOCTEQ6L1_Wplumunu_4500M5000
301105	PowhegPythia8EvtGen_AZNLOCTEQ6L1_Wplumunu_800M1000
301114	PowhegPythia8EvtGen_AZNLOCTEQ6L1_Wplumunu_3000M3500
301103	PowhegPythia8EvtGen_AZNLOCTEQ6L1_Wplumunu_400M600
301100	PowhegPythia8EvtGen_AZNLOCTEQ6L1_Wplumunu_120M180
301102	PowhegPythia8EvtGen_AZNLOCTEQ6L1_Wplumunu_250M400
301153	PowhegPythia8EvtGen_AZNLOCTEQ6L1_Wplustaunu_2750M3000
301141	PowhegPythia8EvtGen_AZNLOCTEQ6L1_Wplustaunu_180M250
301144	PowhegPythia8EvtGen_AZNLOCTEQ6L1_Wplustaunu_600M800
301148	PowhegPythia8EvtGen_AZNLOCTEQ6L1_Wplustaunu_1500M1750
301158	PowhegPythia8EvtGen_AZNLOCTEQ6L1_Wplustaunu_5000M
301145	PowhegPythia8EvtGen_AZNLOCTEQ6L1_Wplustaunu_800M1000
301146	PowhegPythia8EvtGen_AZNLOCTEQ6L1_Wplustaunu_1000M1250
301147	PowhegPythia8EvtGen_AZNLOCTEQ6L1_Wplustaunu_1250M1500
301140	PowhegPythia8EvtGen_AZNLOCTEQ6L1_Wplustaunu_120M180
301143	PowhegPythia8EvtGen_AZNLOCTEQ6L1_Wplustaunu_400M600
301142	PowhegPythia8EvtGen_AZNLOCTEQ6L1_Wplustaunu_250M400
301154	PowhegPythia8EvtGen_AZNLOCTEQ6L1_Wplustaunu_3000M3500
301152	PowhegPythia8EvtGen_AZNLOCTEQ6L1_Wplustaunu_2500M2750
301157	PowhegPythia8EvtGen_AZNLOCTEQ6L1_Wplustaunu_4500M5000
301155	PowhegPythia8EvtGen_AZNLOCTEQ6L1_Wplustaunu_3500M4000
301156	PowhegPythia8EvtGen_AZNLOCTEQ6L1_Wplustaunu_4000M4500
301151	PowhegPythia8EvtGen_AZNLOCTEQ6L1_Wplustaunu_2250M2500
301149	PowhegPythia8EvtGen_AZNLOCTEQ6L1_Wplustaunu_1750M2000
301150	PowhegPythia8EvtGen_AZNLOCTEQ6L1_Wplustaunu_2000M2250
361100	PowhegPythia8EvtGen_AZNLOCTEQ6L1_Wplusenu
361101	PowhegPythia8EvtGen_AZNLOCTEQ6L1_Wplumunu
361102	PowhegPythia8EvtGen_AZNLOCTEQ6L1_Wplustaunu
361103	PowhegPythia8EvtGen_AZNLOCTEQ6L1_Wminusenu
361104	PowhegPythia8EvtGen_AZNLOCTEQ6L1_Wminusunu
361105	PowhegPythia8EvtGen_AZNLOCTEQ6L1_Wminustaunu

Table A.4: List of MC15 W+jets samples used in the analysis

DID	Sample name
361106	PowhegPythia8EvtGen_AZNLOCTEQ6L1_Zee
361107	PowhegPythia8EvtGen_AZNLOCTEQ6L1_Zmumu
301015	PowhegPythia8EvtGen_AZNLOCTEQ6L1_DYee_3500M4000
301005	PowhegPythia8EvtGen_AZNLOCTEQ6L1_DYee_800M1000
301017	PowhegPythia8EvtGen_AZNLOCTEQ6L1_DYee_4500M5000
301003	PowhegPythia8EvtGen_AZNLOCTEQ6L1_DYee_400M600
301013	PowhegPythia8EvtGen_AZNLOCTEQ6L1_DYee_2750M3000
301002	PowhegPythia8EvtGen_AZNLOCTEQ6L1_DYee_250M400
301011	PowhegPythia8EvtGen_AZNLOCTEQ6L1_DYee_2250M2500
301008	PowhegPythia8EvtGen_AZNLOCTEQ6L1_DYee_1500M1750
301004	PowhegPythia8EvtGen_AZNLOCTEQ6L1_DYee_600M800
301007	PowhegPythia8EvtGen_AZNLOCTEQ6L1_DYee_1250M1500
301001	PowhegPythia8EvtGen_AZNLOCTEQ6L1_DYee_180M250
301000	PowhegPythia8EvtGen_AZNLOCTEQ6L1_DYee_120M180
301010	PowhegPythia8EvtGen_AZNLOCTEQ6L1_DYee_2000M2250
301006	PowhegPythia8EvtGen_AZNLOCTEQ6L1_DYee_1000M1250
301012	PowhegPythia8EvtGen_AZNLOCTEQ6L1_DYee_2500M2750
301009	PowhegPythia8EvtGen_AZNLOCTEQ6L1_DYee_1750M2000
301018	PowhegPythia8EvtGen_AZNLOCTEQ6L1_DYee_5000M
301016	PowhegPythia8EvtGen_AZNLOCTEQ6L1_DYee_4000M4500
301014	PowhegPythia8EvtGen_AZNLOCTEQ6L1_DYee_3000M3500
301027	PowhegPythia8EvtGen_AZNLOCTEQ6L1_DYmumu_1250M1500
301026	PowhegPythia8EvtGen_AZNLOCTEQ6L1_DYmumu_1000M1250
301031	PowhegPythia8EvtGen_AZNLOCTEQ6L1_DYmumu_2250M2500
301021	PowhegPythia8EvtGen_AZNLOCTEQ6L1_DYmumu_180M250
301020	PowhegPythia8EvtGen_AZNLOCTEQ6L1_DYmumu_120M180
301038	PowhegPythia8EvtGen_AZNLOCTEQ6L1_DYmumu_5000M
301022	PowhegPythia8EvtGen_AZNLOCTEQ6L1_DYmumu_250M400
301023	PowhegPythia8EvtGen_AZNLOCTEQ6L1_DYmumu_400M600
301030	PowhegPythia8EvtGen_AZNLOCTEQ6L1_DYmumu_2000M2250
301033	PowhegPythia8EvtGen_AZNLOCTEQ6L1_DYmumu_2750M3000
301024	PowhegPythia8EvtGen_AZNLOCTEQ6L1_DYmumu_600M800
301028	PowhegPythia8EvtGen_AZNLOCTEQ6L1_DYmumu_1500M1750
301035	PowhegPythia8EvtGen_AZNLOCTEQ6L1_DYmumu_3500M4000
301025	PowhegPythia8EvtGen_AZNLOCTEQ6L1_DYmumu_800M1000
301037	PowhegPythia8EvtGen_AZNLOCTEQ6L1_DYmumu_4500M5000
301034	PowhegPythia8EvtGen_AZNLOCTEQ6L1_DYmumu_3000M3500
301032	PowhegPythia8EvtGen_AZNLOCTEQ6L1_DYmumu_2500M2750
301029	PowhegPythia8EvtGen_AZNLOCTEQ6L1_DYmumu_1750M2000
301036	PowhegPythia8EvtGen_AZNLOCTEQ6L1_DYmumu_4000M4500

Table A.5: List of MC15  $Z/\gamma^*(\rightarrow ee/\mu\mu)+\text{jets}$  samples used in the analysis

DID	Sample name
410000	PowhegPythiaEvtGen_P2012_ttbar_hdamp172p5_nonallhad
410011	PowhegPythiaEvtGen_P2012_singletop_tchan_lept_top
410012	PowhegPythiaEvtGen_P2012_singletop_tchan_lept_antitop
410013	PowhegPythiaEvtGen_P2012_Wt_inclusive_top
410014	PowhegPythiaEvtGen_P2012_Wt_inclusive_antitop
410025	PowhegPythiaEvtGen_P2012_SingleTopSchan_noAllHad_top
410026	PowhegPythiaEvtGen_P2012_SingleTopSchan_noAllHad_antitop

Table A.6: List of MC15 single top and  $t\bar{t}$  samples used in the analysis

DID	Sample name
361063	Sherpa_CT10_llll
361064	Sherpa_CT10_lllvSFMinus
361065	Sherpa_CT10_lllvOFMinus
361066	Sherpa_CT10_lllvSFPlus
361067	Sherpa_CT10_lllvOFPlus
361068	Sherpa_CT10_llvv
361084	Sherpa_CT10_WqqZll
361085	Sherpa_CT10_WqqZvv
361086	Sherpa_CT10_ZqqZll
361087	Sherpa_CT10_ZqqZvv
361091	Sherpa_CT10_WplvWmqq
361092	Sherpa_CT10_WpqqWmlv
361093	Sherpa_CT10_WlvZqq

Table A.7: List of MC15 diboson samples used in the analysis

DID	Sample name
361108	PowhegPythia8EvtGen_AZNLOCTEQ6L1_Ztautau
301045	PowhegPythia8EvtGen_AZNLOCTEQ6L1_DYtautau_800M1000
301053	PowhegPythia8EvtGen_AZNLOCTEQ6L1_DYtautau_2750M3000
301058	PowhegPythia8EvtGen_AZNLOCTEQ6L1_DYtautau_5000M
301044	PowhegPythia8EvtGen_AZNLOCTEQ6L1_DYtautau_600M800
301041	PowhegPythia8EvtGen_AZNLOCTEQ6L1_DYtautau_180M250
301057	PowhegPythia8EvtGen_AZNLOCTEQ6L1_DYtautau_4500M5000
301054	PowhegPythia8EvtGen_AZNLOCTEQ6L1_DYtautau_3000M3500
301048	PowhegPythia8EvtGen_AZNLOCTEQ6L1_DYtautau_1500M1750
301050	PowhegPythia8EvtGen_AZNLOCTEQ6L1_DYtautau_2000M2250
301042	PowhegPythia8EvtGen_AZNLOCTEQ6L1_DYtautau_250M400
301049	PowhegPythia8EvtGen_AZNLOCTEQ6L1_DYtautau_1750M2000
301047	PowhegPythia8EvtGen_AZNLOCTEQ6L1_DYtautau_1250M1500
301055	PowhegPythia8EvtGen_AZNLOCTEQ6L1_DYtautau_3500M4000
301040	PowhegPythia8EvtGen_AZNLOCTEQ6L1_DYtautau_120M180
301043	PowhegPythia8EvtGen_AZNLOCTEQ6L1_DYtautau_400M600
301051	PowhegPythia8EvtGen_AZNLOCTEQ6L1_DYtautau_2250M2500
301056	PowhegPythia8EvtGen_AZNLOCTEQ6L1_DYtautau_4000M4500
301052	PowhegPythia8EvtGen_AZNLOCTEQ6L1_DYtautau_2500M2750
301046	PowhegPythia8EvtGen_AZNLOCTEQ6L1_DYtautau_1000M1250

Table A.8: List of MC15  $Z/\gamma^*(\rightarrow \tau\tau)$ +jets samples used in the analysis